TRANSPORT AND BUDGET OF **CARBON, NUTRIENTS AND OXYGEN** IN THE **NORTH ATLANTIC**

Marcos Fontela

PhD Thesis 2018

IIM Instituto de Investigaciones Marinas de Vigo

CSIC Consejo Superior de Investigaciones Científicas

Universidade Vigo

Cover design courtesy of Laura Martins

Universidade Vigo

International Doctoral School

Marcos Morente Fontela

DOCTORAL DISSERTATION

"Transport and budget of carbon, nutrients and oxygen in the North Atlantic"

Supervised by:
Fiz Fernández Pérez
Guillermo Francés Pedraz

2018

Universidade Vigo

International Doctoral School

Fiz Fernández Pérez and Guillermo Francés Pedraz,

DECLARE that the present work, entitled "Transport and budget of carbon, nutrients and oxygen in the North Atlantic", submitted by Marcos Morente Fontela to obtain the title of Doctor, was carried out under their supervision in the PhD international programme "Marine Science, Technology and Management (Do*Mar)".

Vigo, January 2018.

The supervisors,

Dr. Fiz Fernández Pérez

Dr. Guillermo Francés Pedraz

Memoria de tesis presentada por el Lcdo. en Ciencias del Mar y Lcdo. en Biología, Marcos Morente Fontela, para optar al grado de Doctor por la Universidad de Vigo.

La presente Tesis Doctoral fue realizada dentro del CO_2 *group* del Departamento de Oceanografía (Grupo de Oceanoloxía) del Instituto de Investigaciones Marinas (IIM) de Vigo, perteneciente al Consejo Superior de Investigaciones Científicas (CSIC). El autor fue beneficiario de la convocatoria de ayudas para contratos predoctorales para la formación de doctores 2014 (BES-2014-070449) del Programa Estatal de Promoción del Talento y su Empleabilidad en I+D+i, financiada por el Gobierno de España a través del Ministerio de Economía y Competitividad y cofinanciada por el Fondo Europeo de Desarrollo Regional 2007–2012 (FEDER). Así mismo, fue beneficiario de ayudas a la movilidad predoctoral para la realización de estancias breves en centros de I+D durante el año 2016 (EEBB-I-2016-10591) y 2017 (EEBB-I-2017-12010). Los trabajos recogidos en esta memoria se desarrollaron dentro del proyecto "*Biennial Observation of Carbon, Acidification, Transport and Sedimentation in the North Atlantic*" (BOCATS) (CTM2013-41048-P), financiado por el Ministerio de Economía y Competitividad, cofinanciado por el Fondo Europeo de Desarrollo Regional 2007–2012 (FEDER). Esta Tesis Doctoral se enmarca dentro del programa interuniversitario de doctorado "*Marine Science, Technology and Management*" (DO*MAR) y fue realizada en la Universidad de Vigo.

IIM Instituto de Investigaciones Marinas de Vigo

CSIC Consejo Superior de Investigaciones Científicas

Grupo de Oceanoloxía · I.I.M. · Vigo · C.S.I.C.

Unión Europea
Fondo Social Europeo
"El FSE invierte en tu futuro"

Universidade Vigo

DO*MAR PhD Program in Marine Science, Technology and Management

MF.

Vigo, 8 de enero de 2018

Table of contents

Thesis layout

This thesis project is structured in five parts subdivided in eight chapters and four appendices, whose contents, results and main findings are briefly summarized below.

Part I introduces the state of the art in the research field and sets the aim of the PhD thesis. It is subdivided in four chapters. This introductory part starts in the **Chapter 1** with a general background of marine biogeochemical cycles, putting emphasis on the oceanic carbon cycle. The physical oceanography of the North Atlantic it is summarized in **Chapter 2**, with a detailed description of the eastern subpolar region that is the main area of study in this thesis. This chapter also address the large scale circulation in the Atlantic, the main mode of climate variability and the current state of knowledge about the subpolar water masses. In **Chapter 3** the present concern about the implications of anthropogenic perturbations at geological scale is presented under the relatively new concept of Anthropocene, and chronology approaches in deep-sea sediments are suggested. At last, in **Chapter 4** the main and specific objectives of this thesis are provided.

From now on, each one of the subsequent parts of the thesis are related with specific objectives. With the exception of the introductory chapter in Part IV (Chapter 7), each chapter is designed as an independent entity, and structured in sections as a typical scientific publication.

In **Part II** the organic component of the carbon cycle is addressed. After an introduction to the dissolved organic carbon (DOC) in the ocean carbon cycle, in the **Chapter 5** is constructed a budget of DOC for the area of study combining water masses transports with source water type DOC characterizations. The budget is extended until subtropical latitudes (24ºN), where the implications of the Atlantic Meridional Overturning Circulation in the total exportation of DOC mediated by the Atlantic Ocean is evaluated for the first time.

In **Part III** a complete biogeochemical budget for the region of study is applied. **Chapter 6** update the actual state of knowledge of carbon, nutrients and oxygen cycling in the eastern subpolar North Atlantic. Combining long-term mass-balanced transports (2002-2016) across the OVIDE section with public available data from a wide range of sources, a total budget of the carbon cycle in the subpolar gyre that includes for the first time carbon variables, nutrients and oxygen was done. Under an inverse lineal model approach, a quantification of the exportation of organic and inorganic carbon as well as the oxygen flux in the eastern subpolar North Atlantic is given.

The geological part of the thesis dissertation is the **Part IV**. In the **Chapter 7** the methodological features of the innovative radiometric technique applied to date superficial deep-sea marine sediments is fully described. To our knowledge, this is the first time that high-resolution low level background gamma spectrometry with two simultaneous hyper-pure germanium (HPGe) detectors is used to measure radioactivity in deep-sea samples. In **Chapter 8** are showed the results of two superficial deep-sea cores located at different basins in the subpolar North Atlantic dated with the ^{210}Pb method. Joining geochronology information with geochemical characterization, carbon fluxes

to the sediments since the Anthropocene have been estimated. As an opening approach into carbon sedimentation in the subpolar North Atlantic, the projection of the results at basin-scale can give a first guess of the magnitude of carbon currently exported into the sediments.

The thesis dissertation ends with the main conclusions derived of this work in the **Part V**.

In order to ease the reading progress, all the references are grouped together as a separate section. Finally, the four **appendices** at the end of the volume provide: (I) a complete list of the acronyms, abbreviations and symbols used along with their explanations, (II) a comprehensive list of all the figures and (III) tables indicating the pages where they appear; and (IV) a summary of the thesis dissertation in Spanish.

PART I. Introduction and objectives

Chapter 1: Biogeochemical introduction

1.1. CO_2, climate change and oceanic carbon cycle

1.1.1. The anthropogenic perturbation

Climate on Earth is tightly interrelated with the biogeochemical cycling of major elements, and the composition of Earth's atmosphere is one of the most important coupling points. As a result of an unabated increase in anthropogenic greenhouse gases emissions, Earth's atmosphere composition has changed, and nowadays the planet's energy budget is not in balance. In words of the Intergovernmental Panel on Climate Change (IPCC) 5th Assessment Report: "*Warming of the climate system is unequivocal and anthropogenic greenhouse gas emissions are extremely likely to have been the dominant cause.*" Although there are other greenhouse gases—such as water vapor, ozone, methane, nitrous oxide, and aerosols—, emissions of carbon dioxide (CO_2) are the most important drivers. By the year 2100, cumulative emissions of CO_2 will account for two or more times the warming attributed to all the other non-CO_2 greenhouse gases [*Gattusso et al.,* 2015].

The longest running record of direct measurements of atmospheric CO_2 concentrations is in the Mauna Loa (Hawaii) station [*Keeling*, 1960] (Figure 1). It starts in 1958, with a mean annual value of 315 parts per million (ppm) and went above 400 ppm for the first time in 10th May 2013. 2016 was the first year with a mean value higher than 400 ppm, a value not reached since 850,000 years (atmospheric CO_2 concentrations measured in Antarctic ice cores*; Siegenthaler et al.,* [*2005*]); and the maximum daily value ever recorded at present is 412.63 ppm on April 26, 2017 (NOAA-ESRL). A notably difference between atmosphere and ocean, is that the atmospheric concentration of CO_2 is relatively homogeneous across the globe. With a concentration of CO_2 in the atmosphere of approximately 277 ppm at the beginning of the industrial era in 1750 [*Joos and Spahni,* 2008], the increase is almost 130 ppm in less of 270 years. Currently, global emissions are tracking along the upper end of the IPCC scenarios, as represented by RCP8.5. The growth rate in atmospheric CO_2 level increased from 1.7±0.1 Pg-C·yr^{-1} in the 1960s to 4.5±0.1 Pg-C·yr^{-1} during 2006–2015 with important decadal variations [*Le Quéré et al.,* 2016].

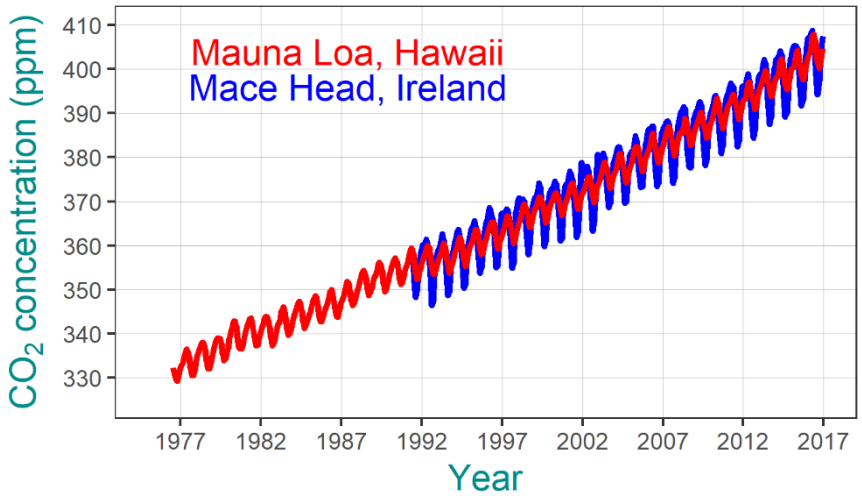

Figure 1. Time evolution of atmospheric CO_2 monthly averaged concentration in parts per million (ppm) measured in flask samples at Mauna Loa, Hawaii (red color) since September 1976 and in Mace Head, Ireland (blue color) since June 1991. Source: author elaboration with data from www.esrl.noaa.gov.

The emission of CO_2 into the atmosphere is the major driver for three important actual stressors of the global ocean: ocean warming, ocean deoxygenation and ocean acidification [*Gruber et al.,* 2011].

Ocean warming is the consequence of the ocean having taken up much of the extra heat accumulated, until 93% of the energy imbalance from 1971 to 2010 has been taken up by the ocean [*Rhein et al.,* 2013]. Although the upper ocean has taken up most of that excess heat, approximately 19% has gone into the deep ocean (>2000 m). This differential heating of the water column enhances the density gradient between the surface and mid-depth waters increasing the stratification. Stratification-induced shoaling of the mixed layer would have heterogeneous impact on global ocean productivity as it affects nutrient supply and light availability. The predicted response from the different biomes of low/high latitudes present still significant uncertainties. Since the ocean warming increase stratification, the reduce mixing and convection of upper waters tends to reduce the uptake of oxygen from the atmosphere, causing ocean deoxygenation. In fact, the magnitude of ocean deoxygenation is directly proportional to the oceanic heat uptake [*Bopp et al.,* 2002]. Furthermore, a rise in temperature suppose a decrease in the solubility of oxygen in seawater.

The uptake of CO_2 induces changes in seawater carbonate chemistry, reducing the concentration of carbonate ion ($[CO_3^{2-}]$) and increasing the concentration of protons ($[H^+]$), i.e. reducing the pH. The conjunction of these changes is commonly termed as ocean acidification, "*the other* CO_2

problem" [*Doney et al.,* 2009], and is going to be revisited in the section 1.1.2.2.4.- Ocean acidification.

The three stressors are driven by the same agent, the increase in atmospheric CO_2, but the resulting changes will have significant regional differences. For example, ocean acidification is expected to affect more at high latitudes while low latitudes are especially vulnerable to deoxygenation effect [*Orr et al.,* 2005*; Oschlies et al.,* 2017].

The condition of the future ocean depends on the amount of carbon emitted in the coming decades. Under the current track of emissions, the protection, adaptation, and repair options for the ocean become fewer and less effective [*Gattuso et al.,* 2015], and the multifaceted stressors of a warmer, higher-CO_2 world will impact biogeochemical cycles.

1.1.2. Oceanic carbon cycle

Along the document we will focus on the carbon cycle, given its central role in biogeochemical cycling and its interaction with climate. As any other biogeochemical cycle, the global carbon cycle can be represented as a series of fluxes connecting reservoirs in the Earth System. The main reservoirs and the associated fluxes between them are depicted in Figure 2 [*Ciais et al.,* 2013]. The carbon cycle circulates carbon between the reservoirs of the atmosphere, ocean, terrestrial biosphere and geologic reservoirs on timescales ranging from sub-daily to millennia.

It is noteworthy that the largest reservoir at global scale is the dissolved inorganic carbon (DIC) existent in intermediate and deep sea oceans, with an estimated pool of 37,100 Pg-C (1 Pg= 10^{15} g). The ocean large carbon reservoir is due to a combination of processes referred to as "*carbon pumps*" [*Volk & Hoffert,* 1985]. The amount of DIC present in the ocean is around twenty times the sum of all fossil fuel reserves (gas, oil and coal). The biggest reservoir of carbon in organic form is also present in the ocean, in form of dissolved organic carbon (DOC). The relevance of DOC cycling and its role in the carbon budget of the North Atlantic will be characterized in the PART II. Dissolved organic carbon.

At long-time scale, the record of ancient atmospheric CO_2 concentration inferred from the composition of air bubbles trapped in ice cores shows that the atmospheric CO_2 concentration of the last 800,000 years (800 kyr) was characterized by 100 kyr glacial-interglacial cycles [*EPICA community members,* 2004; *Lüthi et al.,* 2008]. The transition from glacial cycles having a 41 kyr period to a ~100 kyr period occurred about 800 kyr ago [*Tziperman & Gildor,* 2003]. At short-time scale, before preindustrial times, atmospheric carbon concentration has not changed over ten thousand years [*Hartmann et al.,* 2013], so the carbon cycle is understood to have been in balance and thus operated in steady state [*Sarmiento et al.,* 2000].

1.1.2.1 Global carbon budget

Biogeochemical budgets are conceptually represented with a set of fluxes circulating between different reservoirs. In Figure 2, red arrows and numbers denote changes due anthropogenic perturbations since 1750. Turnover times, defined as the ratio of the total pool of carbon and its rate of removal, range from a few years for the atmosphere pool to millennia for the major carbon domains in the ocean [*Ciais et al.,* 2013].

The average global CO_2 emissions for the period 2006-2015 is 9.3±0.5 Pg-C·yr^{-1}, with 91% of it corresponding to fossil fuel emissions. The total carbon emissions are accumulated in the atmosphere (44%), or absorbed by the ocean (26%), and land sinks (30%). The ocean CO_2 sink for the period 2006-2015 is 2.6±0.5 Pg-C·yr^{-1}, and presents a trend of increased uptake without important interannual variations –a difference with the more variable land sink- [*Le Quéré et al.,* 2016].

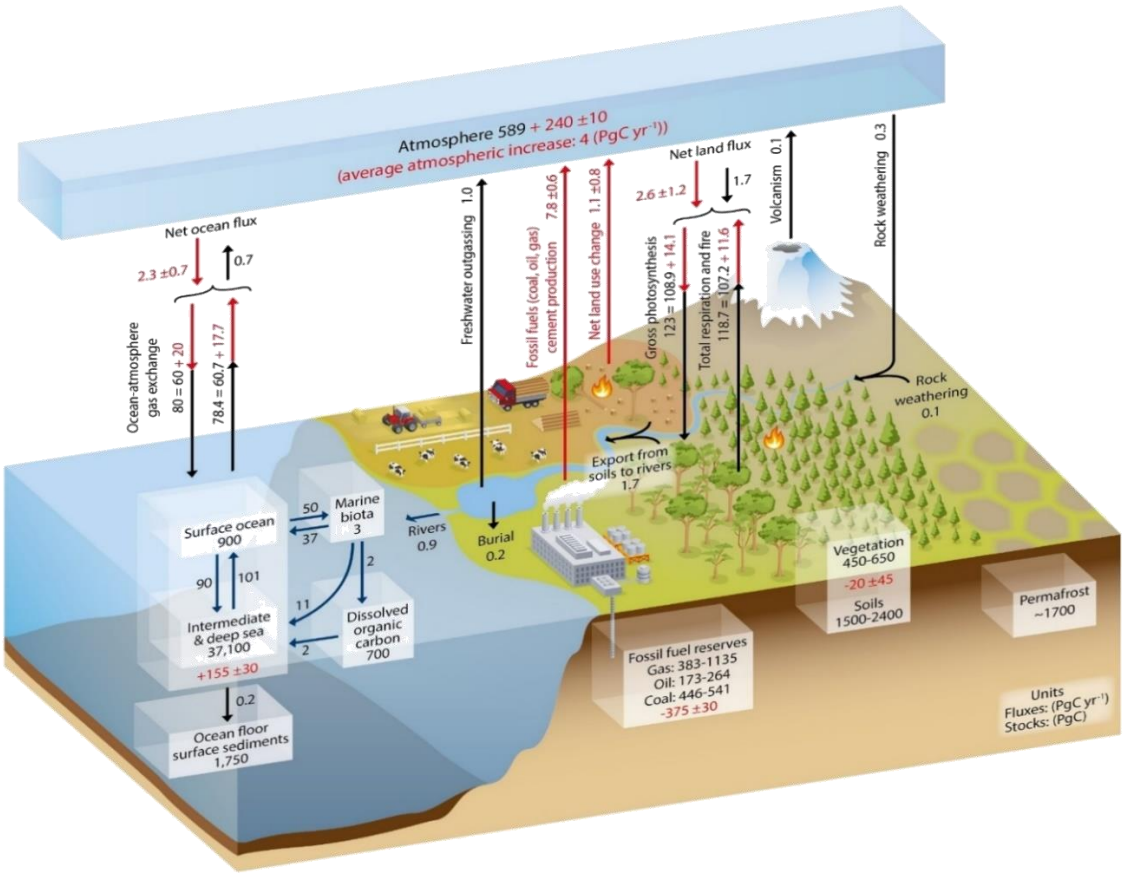

Figure 2. Conceptual schema of the global carbon budget. Carbon units: Pg-C. Numbers in white boxes represent the pool of carbon inside this reservoir. Numbers associated with black (red) arrows represents natural (anthropogenic) carbon fluxes. Source: *Ciais et al.,* [2013].

The ocean contains approximately 50 times more inorganic carbon than the atmosphere, but its ability to absorb atmospheric CO_2 is restricted by the rate of transport of carbon from the surface ocean (which communicates directly with the atmosphere) to the deep ocean. Long-term sequestration of carbon, as stipulated by the IPCC, requires removal from the atmosphere for over 100 years [*Hartmann et al.*, 2013]. On average, this criterion is met if carbon is transported below 1000 m depth [*Primeau,* 2005].

The inventory of deep ocean carbon is dependent on two types of processes that transport inorganic carbon against gradient: the solubility pump and the biological pump [*Raven & Falkowski,* 1999].

1.1.2.2. Solubility pump and seawater CO_2 system

We called solubility pump at the process whereby CO_2 is absorbed into cold, high latitude waters that sink into the ocean interior. The solubility or physical pump, is therefore dependent on physical and chemical processes and closely related with the large-scale ocean circulation (see Chapter 2: Oceanography of the North Atlantic). For all the gases, the solubility decreases with increasing temperature, so the uptake is driven by the increased solubility of CO_2 in cold waters at high latitudes.

Air-sea pCO_2 difference is the primary driver for the air-sea exchange of CO_2 (section 1.1.2.2.2.- Air-sea CO_2 fluxes). When CO_2 molecule enters the ocean, it reacts with seawater altering ocean chemistry (section 1.1.2.2.1.- Seawater CO_2 system). As a consequence of the uptake, DIC increases and pH descends (section 1.1.2.2.4.- Ocean acidification). The excess amount of DIC that is present in the water column due to the increasing pCO_2^{atm} is called anthropogenic carbon (C_{ant}) (section 1.1.2.2.3.- Anthropogenic carbon (C_{ant}) in the ocean).

1.1.2.2.1.- Seawater CO_2 system

When CO_2 molecule enters the ocean it reacts with water to produce carbonic acid (H_2CO_3), which then dissociates into carbonate (CO_3^{2-}) or bicarbonate (HCO_3^-), releasing protons (H^+) following the equations:

$$CO_2(gas) + H_2O \overset{k0}{\Leftrightarrow} H_2CO_3$$

$$H_2CO_3 \overset{k1}{\Leftrightarrow} HCO_3^- + H^+$$

$$HCO_3^- \overset{k2}{\Leftrightarrow} CO_3^{2-} + H^+$$

Where k_0 is the solubility of CO_2, and k_1 and k_2 are the dissociation constants of carbonic acid. The sum of all dissolved carbonate species is denoted as DIC. The proportion of inorganic carbon species in the current ocean is 90:9:1 for HCO_3^-, CO_3^{2-} and CO_2, respectively, i.e., the majority of DIC in the modern ocean is in the form of HCO_3^-.

In a more acid ocean even less [CO_3^{2-}] is expected (seawater DIC speciation in Figure 3–the so called Bjerrum plot-). The Bjerrum plot represents the shift in the partitioning of carbonate species and the associated modification of pH. The carbonate system is the natural buffer of seawater pH. When CO_2 dissolves in seawater, the CO_2 concentration in solution changes only slightly because the system is buffered by CO_3^{2-} ions. H_2CO_3 is a divalent acid; that is, it can undergo two de-protonation reactions: first to form bicarbonate ([HCO_3^-]), and then carbonate ([CO_3^{2-}]). The co-existence of weak acid and its conjugate base in seawater acts as a natural buffer system.

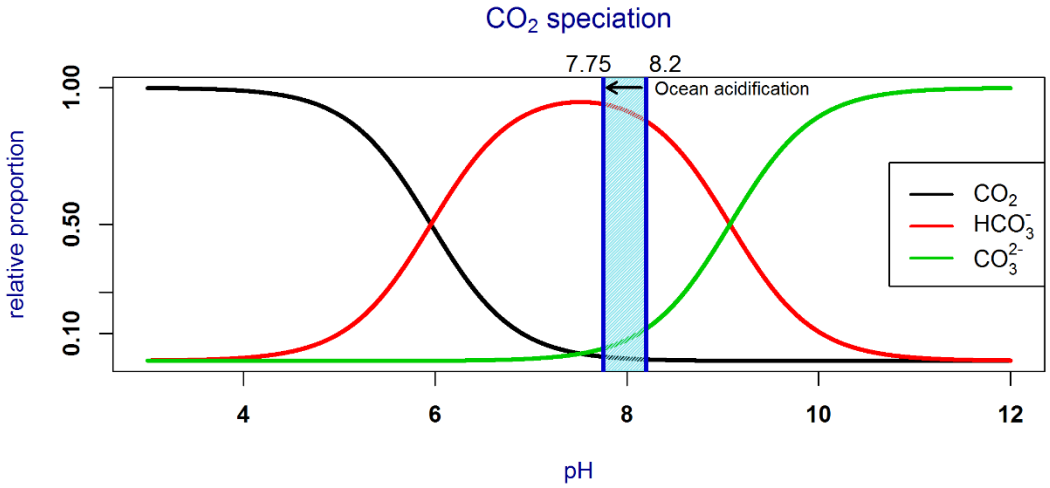

Figure 3. Relative proportions of the dissolved forms of the carbonate system in seawater as a function of pH. (so-called Bjerrum plot) The plot was made with a carbonate ΣCO_2 = 2000 µmol kg^{-1}, temperature T=15°C, salinity S=35, and pressure P=1 atm.

With increasing CO_2, the concentration of bicarbonate ion ([HCO_3^-]) increases, while that of carbonate ion ([CO_3^{2-}]) decreases. With declining [CO_3^{2-}], the stability of calcium carbonate ($CaCO_3$), the biomineral widely used by many organisms to build shells and skeletons, is reduced [*Zeebe,* 2012] along with the buffering capacity of seawater.

Another essential parameter to describe the carbonate system is the alkalinity, a measure of proton acceptors over proton donors, i.e. the charge balance in seawater [*Wolf-Gladrow et al.,* 2007]. Total alkalinity (TA) can be thought of as a measure of how well-buffered seawater is against changes in pH. DIC and TA are conservative quantities, i.e. their concentrations measured in

gravimetric units ($\mu mol \cdot kg^{-1}$) are unaffected by changes in pressure or temperature and they obey the linear mixing law, so they are optimal tracers in numerical models of the ocean's carbon cycle. A difference with the other variables is that TA is not affected by gas exchange [*Carter et al.* 2014].

Of all the carbon species and carbonate system parameters described above, only DIC, TA, pH and pCO_2 are routinely determined analytically. However, because of the relative consistency of the chemical constituents of seawater, the composition of the carbon dioxide system in any seawater sample can be completely specified knowing the salinity and temperature (and hence the values for all the various equilibrium constants), together with two other concentration-related parameters (any pair between DIC, TA, pH and pCO_2). It follows the fundamental rule that two carbonate system parameters are required to determine the carbonate chemistry [*Zeebe,* 2012].

1.1.2.2.2.- Air-sea CO_2 fluxes

The accurate estimation of net CO_2 fluxes through the air-sea interface (FCO_2) is a priority to reduce uncertainties in the global carbon budget [*Otero et al.,* 2013]. The direction of the carbon flux across the surface is determined by the CO_2 partial pressure (pCO_2) gradient across the air-sea interface, i.e. the difference between pCO_2 in seawater surface (pCO_2^{sw}) and atmosphere (pCO_2^{atm}). On a global scale pCO_2^{sw} generally increases at close to the same annual rate as the atmosphere, suggesting that the air-sea exchange flux is the dominant process regulating surface water CO_2 [*Takahashi et al.,* 2009]. The trend for the period 1986 to 2012 in pCO_2^{sw} and pCO_2^{atm} for our region of study is represented in the Figure 4, using data from an ensemble of methods participating in the Surface Ocean pCO_2 Mapping intercomparison (SOCOM) initiative [*Rödenbeck et al.,* 2015] for the pCO_2^{sw}; along with the pCO_2^{atm} of the station of Mace Head, Ireland, the closest atmospheric research station to our objective area that have continuous measurements in the same temporal data-frame.

The difference between pCO_2^{sw} and pCO_2^{atm} is the thermochemical driving potential for the net transfer of CO_2 across the sea surface [*Takahashi et al.,* 2002]. When pCO_2^{atm} is greater than pCO_2^{sw}, the ocean uptakes atmospheric CO_2. The net CO_2 flux across sea surface can be estimated knowing the partial pressures and using a gas-exchange coefficient, which depends mainly on the degree of turbulence near the interface and is typically parameterized through a relationship with wind speed [*Takahashi et al.,* 2009]. As we can see in the Figure 4, pCO_2^{atm} was always greater than pCO_2^{sw} in the eastern Subpolar North Atlantic, so it is expected to be a carbon sink area. Regardless, local physical or biological perturbation events can induce important spatial and temporal variability.

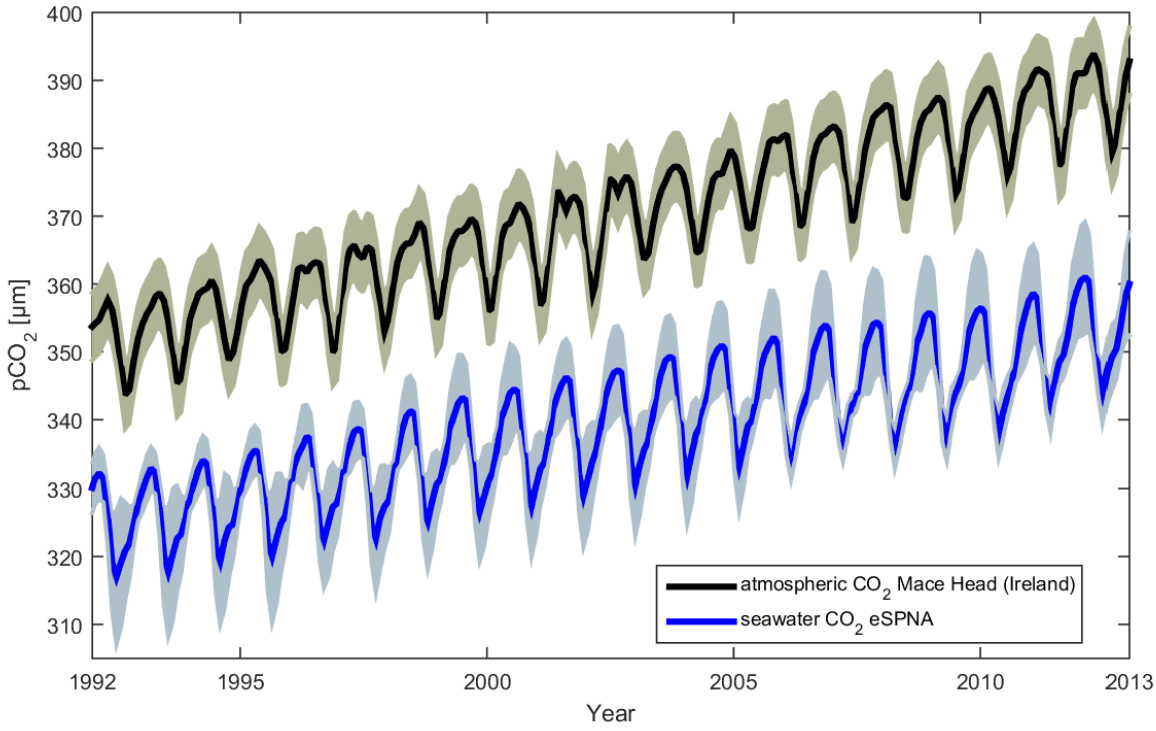

Figure 4. Time evolution (1992-2013) of the partial pressure of CO_2 (in µm) in seawater (blue) for the region of study in the eastern subpolar North Atlantic (eSPNA, which exact location will be defined in Chapter 2) from the data ensemble collection of the Surface Ocean pCO_2 Mapping intercomparison (SOCOM) [*Rödenbeck et al., 2015*]. Time evolution (1992-2013) of the partial pressure of CO_2 (in µm) in the atmosphere (black) at the closest land-based station with a time-series of CO_2 measurements long enough to cover the same temporal framework, the Mace Head station in Galway, Ireland. Data of atmospheric CO_2 flask measurements from https://www.esrl.noaa.gov.

The global ocean carbon sink is strongly influenced by natural variability. The ocean CO_2 sink increased from 1.2±0.5 Pg-C·yr^{-1} in the 1960's to 2.6±0.5 Pg-C·yr^{-1} during 2006–2015. [*Le Quéré et al.,* 2016]. Attending at the decadal variability of the last 40 years, the consensus is that in the 1980's there were a stationary sink, that diminished in the 1990's and is currently having a strong increase since the beginning of the 2000's [*Ländschutzer et al.,* 2016].

While the Atlantic has only 23% of the global ocean area, it takes up 41% of the annual global ocean flux [*Takahashi et al.,* 2009]. The pCO_2^{sw} in our area of study (Figure 4) reach its minimum value in summer due to biological drawdown (primary producers photosynthesis converts DIC in organic matter), and peaks in winter as a result of the enhanced vertical supply of carbon from the intermediate waters by deep convection [*Takahashi et al.,* 2009]. While the biological CO_2 drawdown regulates the seasonal cycle of CO_2 flux, the physical regulation is more important for interannual and decadal variations of CO_2 flux in the eastern Subpolar North Atlantic region [*Li et al.,* 2016].

1.1.2.2.3.- Anthropogenic carbon (C_{ant}) in the ocean

Anthropogenic carbon (C_{ant}) is defined as the excess amount of DIC that is present in the water column due to the increasing atmospheric concentration of CO_2 [*Khatiwala et al.,* 2013]. The estimation of the amount of C_{ant} in the ocean has inherent complications: (i) C_{ant} is not a directly measurable quantity since it has not any molecular difference at all; (ii) the C_{ant} signal in the ocean represents a small fraction (of around ~4% percent at most) over the natural or preindustrial background distribution of carbon; (iii) carbon in the ocean participates in biogeochemical processes, and (iv) finally, C_{ant} distribution in the ocean is highly heterogeneous, a significant difference with the rather homogeneous global pCO_2^{atm} distribution [*Kathiwala et al.,* 2013]. The ocean has constituted the only true net sink for anthropogenic CO_2 over the past 200 years and without its atmospheric uptake, CO_2 would be much higher today than observed [*Sabine et al.,* 2004].

The North Atlantic contains substantially higher C_{ant} concentrations than the other basins, storing 25% of the global oceanic C_{ant} inventory despite being only 11% of the global ocean volume [*García-Ibañez et al.,* 2016]. Due in part to its faster ventilation, but also because of a more favorable Revelle factor [*Sabine et al.,* 2004]. This factor determines how much C_{ant} can take up a particular water parcel upon equilibration with an atmospheric perturbation [*Sarmiento & Gruber,* 2006].

The total basin-wide accumulation for the North Atlantic Ocean shows significant decadal variability [*Woosley et al.,* 2016]. Strong relationships exists between the North Atlantic Oscillation (NAO, see section 2.3. North Atlantic Oscillation) and C_{ant} uptake rates in the Atlantic [*Pérez et al.,* 2008; 2010], with periods of high NAO index corresponding to periods of high C_{ant} storage [*Pérez et al.,* 2013]. The entire Atlantic presented much higher accumulation in the 2000's absorbing 8.1±1.6 Pg-C·yr^{-1}, compared to 5±1 Pg-C·yr^{-1} in the 1990's [*Woosley et al.,* 2016].

Surface waters in the upper limb of the meridional overturning circulation (MOC) undersaturated in C_{ant} progressively uptakes air-sea C_{ant} on its northward path, reaching C_{ant} saturation levels in the subpolar gyre and explaining why the air-sea C_{ant} flux in the subtropical region is higher than that observed in the subpolar region [*Pérez et al.,* 2013]. Practically, the entire air-sea C_{ant} uptake in the North Atlantic occurs in the subtropical region, where the contemporary air-sea CO_2 flux is mainly anthropogenic, whereas the natural component predominates in the subpolar region [*Zunino et al.,* 2015]. There is high uptake of C_{ant} in subtropical surface waters, while advection is the main contributor to the C_{ant} storage rate in subpolar waters [*Zunino et al.,* 2015]. At high latitudes, deeper penetration of C_{ant} occurs due intermediate and deep water formation processes [*Pérez et al.,* 2013]. Our region of study is an entrance portal for waters with high concentration of C_{ant} into the deep ocean through the overturning circulation [*Pérez et al.,* 2008], as a result of the formation and

downward spreading of Labrador Sea Water (LSW) and North Atlantic Deep Water (NADW) [*Sabine et al.,* 2004].

1.1.2.2.4.- Ocean acidification

Because climate change and ocean acidification are both consequence of increasing atmospheric CO_2, acidification is often referred to as "*the other CO_2 problem*" [*Doney et al.,* 2009]. Ocean uptake of anthropogenic CO_2 is a key service to society that moderates climate change, and ameliorate the rate of increase of atmospheric CO_2, although it comes at the cost of ocean acidification [*Gattuso et al.,* 2015].

The IPCC identified the pH ($-\log_{10}[H^+]$) as one of the principal climate drivers that affect marine ecosystem structure, functioning and adaptive capacity [*Pörtner et al.,* 2014]. Since the beginning of the Industrial Revolution, the sea surface has seen a 30% increase in hydrogen ion concentrations $[H^+]$, causing a decrease of surface waters by an average of 0.1 pH units (from 8.2 to 8.1, approx.). [*Caldeira & Wickett,* 2003*; Raven et al.,* 2005]. The pH in the surface has probably not been below 8.1 since 2 million years ago [*Hönisch et al.,* 2012], and the current acidification event is happening 100 times faster than any other seawater acidity change in the last 20 million years of Earth's history [*Pelejero et al.,* 2010]. An event of massive natural release of methane (CH_4) into the atmosphere occurred ~55 million years ago during the Paleocene-Eocene Thermal Maximum (PETM) [*Zachos et al.,* 2005]. The CH_4 emitted was rapidly oxidized to CO_2, altering ocean chemistry and shoaling the aragonite saturation horizon (ASH, the depth at which the calcium carbonate becomes thermodynamically unstable and tends to dissolve). The rate of shoaling of the ASH during the PETM was ~0.2 $m \cdot yr^{-1}$ [*Pelejero et al.,* 2010], and nowadays is between 4 and 7 $m \cdot yr^{-1}$ in the subpolar North Atlantic [*Vázquez-Rodríguez et al.,* 2012] and can be as high as 10-15 $m \cdot yr^{-1}$ in the Irminger Sea [*Pérez et al.,* 2018]. Today, the climate change-driven trend in pH already exceeds the bounds of natural variability in 99% (±0.5%) of the open ocean [*Henson et al.,* 2017], so marine life is currently exposed to surface pH values outside the range of natural variability that they have been adapted [*Sutton et al.,* 2016]. If CO_2 emissions continue unabated, surface ocean pH could decline by up to 0.5 units by the year 2100 [*Raven et al.,* 2005] and 0.7 units by the year 2300 [*Zeebe et al.,* 2008].

The uptake of C_{ant} by the ocean has been the main contributor to decreasing of pH over the last two decades [*Ríos et al.,* 2015*, Lauvset et al.,* 2015]. The trends of decreasing pH are stronger in basins with young waters recently formed, like the subpolar North Atlantic (SPNA) [*García-Ibañez et al.,* 2016]. The latest evaluation of ocean acidification trends in our region of study, with data spanning almost 25 years, found the greatest pH decreases in surface and intermediate waters,

with a rate of decrease observed for Subpolar Mode Water in the SPNA predicting a reduction of 0.17 units of pH in a century [*García-Ibañez et al.,* 2016].

Projecting the precise impact of ocean acidification on the diversity and functioning of marine organisms and ecosystems is challenging. A meta-analysis of 228 published studies revealed a decrease in calcification, growth, survival, development and abundance across a wide range of taxa, but also showed a certain degree of variability among groups suggesting different scales of sensitivity [*Kroeker et al.,* 2013]. Habitat suitability for stony colonial corals is going to be reduced in a near future: up to 85% of the Northeast Atlantic cold water corals habitats is going to be exposed to corrosive waters by 2060 [*Pérez et al.,* 2018]. Furthermore, there are other threats related with the acidification, as the impact on speciation of trace metals [*Millero et al.,* 2009], or the sound absorption of seawater [*Brewer & Hester,* 2009*; Ilyina et al.,* 2010] that are uncertain at present and require future research.

1.1.2.3. Biological pump

The biological carbon pump (BCP) is the export of biologically fixed CO_2 from the upper ocean to deep waters through the sinking of particulate biogenic material [*Broecker & Peng,* 1982]. The BCP mainly describes the fixation of DIC into organic carbon and its subsequent transfer to the deep ocean through sinking or subduction (Figure 5). If it were not for the BCP, the distribution of most chemicals in the ocean would be rather uniform [*Sarmiento & Gruber,* 2006].

Some authors consider the BCP to be formed by a “carbonate pump” and a “soft-tissue pump” [*Volk & Hoffert,* 1985*; Sarmiento & Gruber,* 2006*; Passow & Carlson,* 2012], while others separate it explicitly as individual pumps (Figure 6) [*Heinze et al.,* 2015*; Legendre et al.,* 2015]. Furthermore, new frameworks have been proposed recently and terms like “*microbial pump*” [*Jiao et al.,* 2010], “*lipid pump*” [*Jónasdóttir et al.,* 2015], or “*mixed-layer pump*” [*Gardner et al.,* 1995] have appeared. Despite its inherent peculiarities, all of them contribute to generate and maintain the vertical gradient of carbon in the ocean, which is attributed in two-thirds to the BCP and the rest due the solubility pump (Figure 6) [*Passow & Carlson,* 2012].

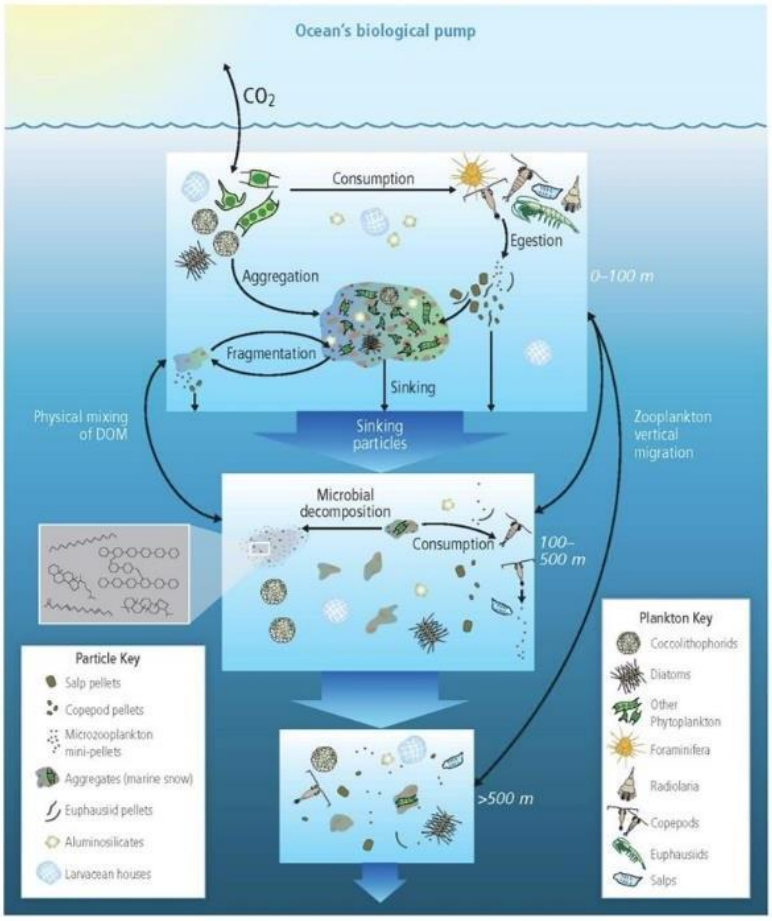

Figure 5. A schematic representation of the biological carbon pump with the main agents and processes represented. Biological and physical interactions between primary and secondary producers determines the final amount of carbon exported to depth. Note that depth-references are only approximations and cannot be taken as globally uniformed, and that the relative sizes of the organisms, particles, and particle building blocks are not presented to scale. Source: *Pörtner et al.,* [2014].

The soft-tissue pump, also called organic carbon pump, and used generally as a synonym of BCP, accounts for the export of particulate and dissolved organic carbon (POC and DOC). The carbonate pump represents the consume of inorganic carbon for the production of carbonate by marine calcifying organisms and its exportation as particulate inorganic carbon (PIC) into the ocean interior [*Rost & Riebesell,* 2004]. It is also called alkalinity pump or "carbon-counter pump" because the precipitation of $CaCO_3$ in the ocean is accompanied by a decrease in alkalinity and the release of CO_2 to surrounding waters, and thus the atmosphere, as shown by the theoretical calcification equation:

$$Ca_2^+ + 2HCO_3^- \rightarrow CaCO_3 + CO_2 + H_2O$$

In the ocean, different from the theoretical stoichiometry, there is a release of ~0.6 mol of CO_2 for each mole of $CaCO_3$ precipitated [*Frankignoulle et al.,* 1994]. Two effects of the carbonate pump contribute to maintain the vertical gradient: the release of CO_2 from the upper layer to the atmosphere decreasing surface DIC; and the sinking of $CaCO_3$ particles and subsequent dissolution at depth, increasing deep water DIC [*Legendre et al.,* 2015].

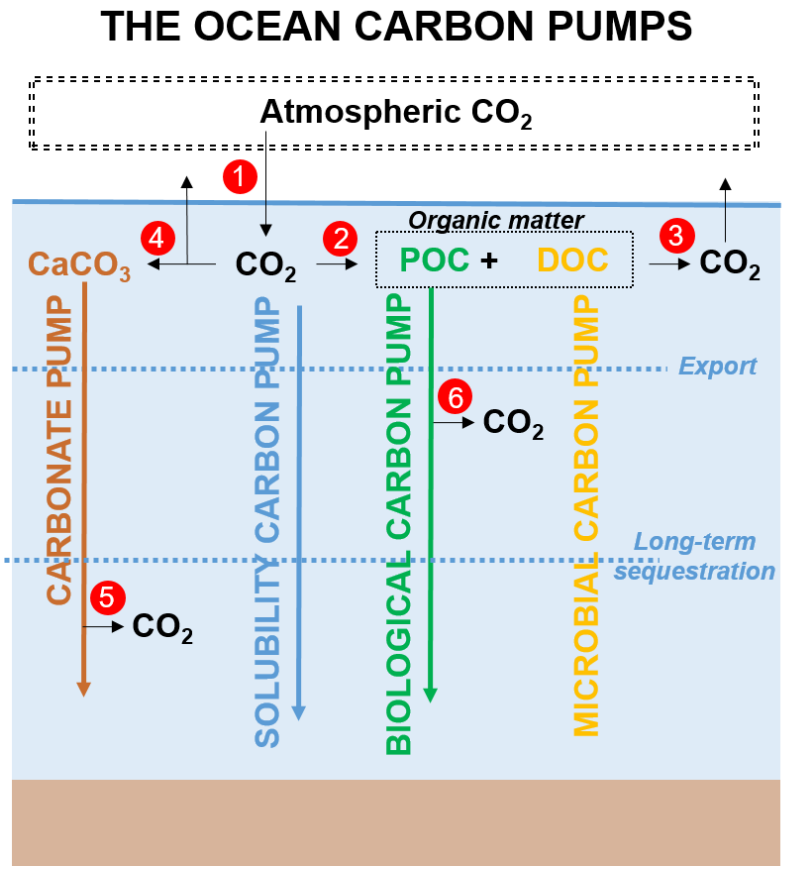

Figure 6. Schematization of the ocean carbon pumps. The dissolution of atmospheric CO_2 in surface waters (1) exported to depth is the solubility pump. Photosynthetic processes convert CO_2 (DIC) in organic matter (2) that is respired back to CO_2 (3) or exported as POC or DOC. The biological carbon pump is more related with the POC export whereas the microbial carbon pump it is with DOC. The generation of $CaCO_3$ in the upper layer (4) (which is accompanied by the release of CO_2) and its subsequent export to depth is the carbonate pump. During the sinking at depth, CO_2 is released in the water column by dissolution of part of the sinking $CaCO_3$ (5) and remineralisation of the organic carbon (6). Note that the mean depth of carbonate dissolution is greater than organic carbon remineralization. Also note that the long-term sequester by the microbial carbon pump is depth-independent. Source: author elaboration based in *Legendre et al., 2015*

The *microbial carbon pump* (MCP) is a modern conceptual framework for understanding the role of microbial processes in the production of recalcitrant DOC [*Jiao et al.,* 2010], i.e., DOC that is resistant to rapid microbial degradation [*Hansell,* 2013]. There are quite differences with the BCP. First, the vertical distribution of the carbon sequestered by the MCP is depth-independent because not imply any physical transportation to depth, it is based in the bacterially mediated chemical transformation of organic compounds to non-bioavailable forms which can persist at any depth in the water column [*Jiao et al.* 2010*; Legendre et al.,* 2015*; Polimene et al.,* 2017]. The fundamental driver of the BCP is primary production, whereas the MCP is driven by microbial heterotrophic activity [*Jiao et al.* 2010]. The MCP alters the chemical composition of dissolved organic matter (DOM), changing the stoichiometric ratios of carbon to nitrogen, phosphorus and other elements, enriching in carbon the recalcitrant DOM pool. The connection between MCP and BCP is the microbial loop, so the importance of the MCP can be strong in oligotrophic oceanic waters where the conventional BCP is very weak [*Jiao et al.,* 2010]. Proposal authors argue that sequestration from the MCP and the POC-based BCP are of the same order of magnitude [*Jiao et al.,* 2014]. The only quantitative estimate available for the magnitude of the MCP is 0.18 Pg-C $year^{-1}$ [*Legendre et al.,* 2015], inferior but in the same order of magnitude than BCP sequestration at 2000 m (0.33-0.66 Pg-C $year^{-1}$) [*Honjo et al.,* 2008*; Henson et al.,* 2012a*; Guidi et al.,* 2016].

Other biological mechanism, highly efficient at sequestering carbon into the deep ocean, has been recently discovered precisely in our region of study. The "*lipid pump*" [*Jónasdóttir et al.,* 2015] is based in the seasonal migrations in the life cycle of some species of copepods (*Calanus finmarchicus* in our area, predominantly). Carbon-rich lipids produced in surface waters are remineralized as energy reserves during the winter below the permanent thermocline (600-1400 m depth is the hibernation range of *C. finmarchicus*). This active transport and metabolism result in a downward export of carbon between 1-4 $g\text{-}C \cdot m^{-2} \cdot yr^{-1}$ [*Jónasdóttir et al.,* 2015], almost equivalent to the passively deep sinking POC flux. This process has no impact on the nutrient budget of the surface layer because the elemental composition of lipids is so carbon-enriched that there is almost not nutrient remove from the upper ocean, creating a decoupling between carbon and nutrients transport.

Another additional organic carbon source that can be a substantial component of the BCP is the seasonal entrainment of surface waters in deeper layers, a process termed *mixed-layer pump* [*Dall'Olmo et al.,* 2016]. Organic matter produced at the ocean surface is vertically transferred to depth by deep mixing and isolated by the development of a new mixed layer at shallower depths, i.e. variations in the depth of the surface mixed layer is the driver of carbon entrainment, mainly in dissolved form, into the ocean interior. If the mixed layers are deeper than the depth over which most of the remineralization takes place, the mixed-layer pump may be an efficient pathway for carbon export [*Dall'Olmo & Mork,* 2014].

The ocean's biological pump is hypothesized to have contributed to fluctuations in levels of pCO_2^{atm} during glacial–interglacial periods [*Sigman and Boyle,* 2000*; Kohfeld et al.,* 2005], and present day pCO_2^{atm} would be approximately 200 ppm (~50%) higher if the BCP did not exist [*Parekh et al.,* 2006]. How will the BCP respond to future anthropogenic climate change is uncertain [*Passow and Carlson,* 2012]. The projections are complicated by the synergy of multiple stressors of anthropogenic nature (ocean warming, acidification and deoxygenation will simultaneously alter temperature, vertical stratification and mixing, carbonate concentrations, nutrient availability…), combined with the natural variability (El Niño Southern Oscillation, NAO, Arctic Oscillation…) so at present it is not possible to predict with guarantee whether the biological pump will strengthen or weaken over the next century [*Turner, 2015*].

The amount of organic carbon exported out of the euphotic zone, and its rate of remineralization in the twilight mesopelagic zone, determines the total carbon sequestered in the deep ocean by the BCP [*DeVries & Weber, 2017*]. It is believed that the surface ocean is where the strength of the biological pump is set and the subsurface ocean where the efficiency is determined [*Buesseler & Boyd,* 2009]. A usual measure of the strength is the export ratio, the export flux at the euphotic zone divided by total primary production [*Lima et al.,* 2014]. The efficiency is quantified as the fraction of exported organic matter that reaches the deep ocean ("transfer efficiency") [*Francois et al.,* 2002]. Under these metrics, the North Atlantic represents an extremely strong and efficient biological pump, where about half of the net primary production is exported out of the euphotic zone, together with a low POC flux attenuation in the first 1000 m (NA in upper right corner of **Figure 7**) [*Buesseler & Boyd,* 2009]. As can also be seen in Figure 7, the strength and efficiency of the BCP as a carbon sink is not globally uniform [*Rosengard et al.,* 2015].

The accurate estimation of the export flux of organic matter out of the euphotic zone is important because it is one of the main drivers of ocean biogeochemical dynamics [*Dunne et al.,* 2007]. Current estimates of global carbon export out of the euphotic zone from a variety of measurement techniques range from 5 to 12 Pg-C·yr^{1} [*Laws et al.,* 2000*; Dunne et al.,* 2007*; Lutz et al.,* 2007*; Henson et al.,* 2011*; Siegel et al.,* 2014]., with an increasing consensus of estimates around 11±1 Pg-C yr^{1}. [*Henson et al.,* 2015]. Much of the variability in the export flux to depth is related to the abundance and composition of the overlying plankton community [*Guidi et al.,* 2009*; Henson et al.,* 2012a]. The fraction of the primary production exported to depth is not only controlled by physical forcing, the trophic uncoupling between producers and consumers in the planktonic food web and the amount of particulate organic matter remineralized by the pelagic community also influences the vertical flux [*Wassmann,* 1998]. In the early stages of the seasonal North Atlantic spring bloom there is a relatively uncoupling between primary and secondary producers, due the longer development time of zooplankton, that is associated with important export pulses [*Sanders et al.,* 2014]. So seasonal and geographical changes in plankton community structure (both phyto- and zooplankton) influences also the BCP at regional and local scale [*Guidi et al.,* 2009].

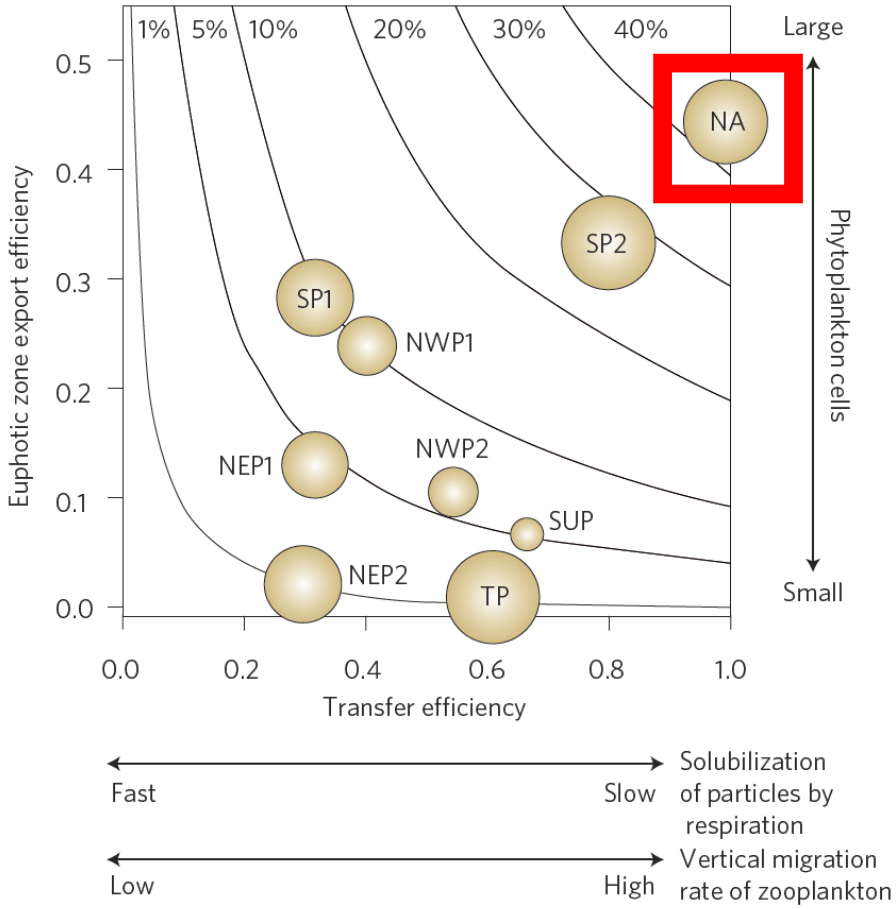

Figure 7. Plot of transfer efficiency versus export efficiency. The circle size is proportional to the net primary production in the North Atlantic (NA), South Pacific (SP), northwest Pacific (NWP), northeast Pacific (NEP), subtropical Pacific (SUP), tropical Pacific (TP). When for a given zone there is more than one site or season with data available, a number is added. The contour lines from 1 to 40% represent the flux of export production as a function of euphotic zone export and transfer efficiency. The North Atlantic (NA, red square) is characterized by high export and transfer efficiency, being the place where the biological carbon pump is more efficient in terms of the fraction of net primary production that exits the euphotic zone and that survives the transport at depth. Source: Based on *Buesseler & Boyd*, [2009] taken from *Herndl & Reinthaler,* [2013]

The downward flux of organic particles decays with increasing depth. The attenuation (i.e. remineralisation) has been usually parameterized with the equation proposed by *Martin et al.* [1987]. It is a power function that describe the decreasing flux of sinking organic carbon with depth ruled by a dimensionless exponent "*b*" with an average value of 0.87. Despite it was based on POC flux measurements that were made during short-term deployments (6–34 days) in the upper 2000 m at the northeast Pacific, the *Martin et al.* [1987]'s equation has been widely used to predict carbon flux at any depth. The use of power functions to describe the depth dependency of the flux

of organic carbon was criticized by *Armstrong et al.,* [2002] with his “ballast hypothesis”, proposed to reproduce the flux behavior due association of organic matter with ballast minerals. Their algorithm discriminates between the flux of organic carbon due a protected fraction associated with minerals, and an unprotected fraction which decreases exponentially with depth [*Armstrong et al.,* 2002]. The prediction of organic carbon flux at depth with multiple linear regression fits suggest that the flux increases with the amount of carbonate acting as ballast and decreases with depth and seasonality [*Francois et al.,* 2002]. Even under the consideration that all this algorithms ([*Martin et al.,* 1987*; Armstrong et al.,* 2002*, Francois et al.,* 2002*]*) are based on different premises, the fluxes predicted below 2000 m are rather similar and the differences do not exceed 15% [*Francois et al.,* 2002].

Vertical flux of particles is usually a combination of fecal pellets, marine snow, direct sedimentation of phytoplankton blooms or particles ballasted with mineral elements (particularly for carbonate, but also opal and terrigenous materials) [*Klaas & Archer,* 2002*; De La Rocha & Passow,* 2007*; Buesseler et al.,* 2008], with variable contributions at local and temporal scale [*Turner,* 2015]. There is also a growing body of literature underscoring the importance of slow-sinking particles contribution to total POC flux, not only in places where production is dominated by picoplankton and small-size classes [*Alonso-Gonzalez et al., 2010; Lomas & Moran,* 2011] but also in the eutrophic North Atlantic [*Riley et al.,* 2012*; Villa-Alfageme et al.,* 2016*; Baker et al.,* 2017]. Relatively new methodological approaches as the Underwater Vision Profile, the Marine Snow Catcher or the analysis of radioisotopic disequilibriums in the water column (^{234}Th, ^{210}Po); are proposed as an alternative to classical sediment traps to measure POC pools and fluxes, allowing the quantitative evaluation of the fast and slow sinking POC fluxes [*Riley et al.,* 2012]. By now, the principal tool that has been used to characterize quantitative and qualitatively the sinking particles is the sediment trap. It consists of a cylindrical or conical container with one open end that is placed on a mooring in a fixed depth for a period of time. An alternative to static sediment traps, less often used, are neutrally buoyant sediment traps with float capability at a controlled depth.

There are three common processes that may impact sediment trap results: hydrodynamic effects that alters the collection efficiency; the capture of motile zooplankton that enters the cup of the traps by its own (“swimmers”); and the loss of particulate elements due dissolution after collection in the trap (resolubilization) [*Buesseler et al.,* 2006]. Comparing two nearly moored sediment traps with identical configuration and even slightly tilt differences between them, the trapping efficiency can be range by a factor of nearly two [*Chiswell and Nodder,* 2016]. Despite the uncertainties, its use still prevails in POC flux determination because only deep tethered sediment traps can provide direct estimates of the magnitude of the sequestration flux into the deep ocean, how the flux changes with depth, the chemical nature of particles and even the seasonal and inter-annual variability [*Lampitt et al.,* 2008].

POC fluxes and concentrations exhibit the strongest gradient in the “twilight zone”, which is the part of the ocean located between the bottom of the euphotic zone and about ~1000 m [*Buesseler et al.,* 2008]. Carbon exported to the “midnight zone” (>1000 m) can be considered sequestered because it will be out of contact with the atmosphere for at least 100 years [*Primeau,* 2005*; Ciais et al.,* 2013]. The mechanisms of particle flux attenuation along the twilight zone are among the most uncertain ones in the state of knowledge of BCP, but there are at least three types of processes interacting: (i) heterotrophic degradation of passively sinking material; (i) zooplankton diel migration, and (iii) lateral advection [*Buesseler et al.,* 2008].

Observed variability in attenuation of vertical POC flux can largely be explained by temperature, with shallower remineralization occurring in warmer waters. Temperature effects are the more likely explanation for the increases in POC remineralization length scale observed with latitude [*Lima et al.,* 2014]. It is predicted that future increases in ocean temperature will likely lead to shallower remineralization of POC [*Marsay et al.,* 2015]. A shallower carbon remineralization depth would imply a redistribution of carbon inventory in the ocean with potential to impact atmospheric CO_2 concentrations [*Kwon et al.,* 2009].

Other direct loss of POC in the mesopelagic/twilight zone is via zooplankton respiration, fragmentation from “sloppy feeding” (cell breakage during feeding and subsequent release of DOC or suspended POC) [*Jumars et al.,* 1989], microbial gardening (the fragmentation of particles into smaller ones, increasing the surface area and stimulating the growth of microorganisms) [*Iversen and Poulsen,* 2007*; Mayor et al.,* 2014] and/or swimming activities [*Belcher et al.,* 2016].

The total carbon demand of heterotrophic metabolism (respiration) in the water column is very likely greater than the metabolic demands supported by sinking POC flux [*del Giorgio and Duarte,* 2002*; Steinberg et al.,* 2008]. The unbalance can result from deficient evaluations of POC flux and/or net metabolism; or the existence of additional sources of organic carbon to the dark ocean still unaccounted for [*Burd et al.,* 2010*; Giering et al.,* 2014].

The export flux in the North Atlantic represents less than 20% of the global export flux, ranging between 0.55–1.94 Pg-C yr^{-1}. with an average of 1.27 Pg-C·yr^{-1} [*Sanders et al.,* 2014]. Based on data from deep sediment traps, *Honjo et al.* [2008] estimated that the global ocean downward flux of POC at 2000 m was 0.43 Pg-C·yr^{-1}. Other estimates for the global POC flux at 2000 m are 0.34 Pg-C·yr^{-1} [*Lampitt and Antia,*1997], 0.66 Pg-C·yr^{-1} [*Henson et al.,* 2012a], 0.33 Pg-C·yr^{-1} [*Guidi et al.,* 2016]. Assuming a global primary production of 50 Pg-C·yr^{-1} [*Carr et al.,* 2006] the BCP mediated by POC at 2000 m would represent 0.6-1.3% of primary production [*Legendre et al.,* 2015]. The subpolar North Atlantic, our region of study, is characterized by a large flux of organic carbon at 2000 m that is often more than twice the global annual average (Figure 8) [*Scholten et al.,* 2001*; Antia et al.,* 2001*; Honjo et al.,* 2008].

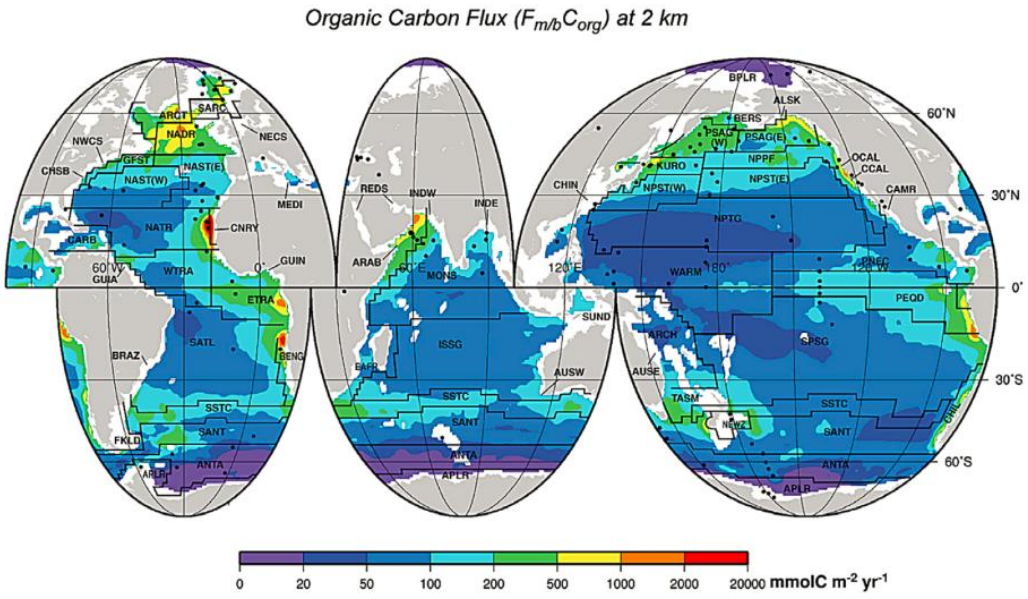

Figure 8. Global parameterization of the flux of organic carbon at 2000 m depth (in mmol-C·m^{-2}·yr^{-1}) based on deep sediment traps. Source: [*Honjo et al.,* 2008].

1.2. Nutrients and oxygen cycles

All organisms on Earth are made fundamentally of five major elements: H, C, O, N, and P. A biological group with important ecological role in oceanic environments, diatoms, also need silicon (Si) to complete his life cycle. The uptake of chemical forms of essential nutrients from the external environment constitute one of three principal resources required for life, along with energy and space to live [*Moore et al.,* 2013]. The quantitative relationships between chemical elements of a pool, stoichiometry, are key factors in ocean biogeochemical dynamics [*Sarmiento & Gruber,* 2006]. Most nutrients in seawater are in ionic form (HCO_3^-, NO_3^-, NH_4^+, HPO_4^-, SiO_4^{4-}) and they are found in approximately constant stoichiometric ratios in marine organisms. [*Redfield,* 1934*; Redfield et al.,* 1963] (see next section 1.2.1. Composition of organic matter: Redfield ratios). The understanding of nutrient cycling in marine systems is important to constrain rates of biological production and carbon export in the world's oceans [*Arrigo,* 2005].

Oceanic distribution of nutrients is not uniform precisely due the impact of organisms. The elements with reduced surface concentrations are generally related with biological processes or chemical scavenging by sinking particles [*Sarmiento & Gruber,* 2006]. *Broecker & Peng,* [1982] considered that the macronutrients almost depleted in surface water nitrogen (as nitrate),

phosphorus (as phosphate), and silicon (as silicic acid) are biolimiting elements. Curiously, they consider also as biolimiting elements the zinc (Zn^{2+}), cadmium (Cd^{2+}) and germanium (H_4GeO_4) [*Broecker and Peng,* 1982], and not the iron (Fe^{2+}), widely recognized now as the micronutrient that limits primary production in the high-nitrate low-chlorophyll regions [*Martin et al.* 1988*; Moore et al.,* 2013]. The vertical distribution of nutrients is controlled by its depletion at surface by organic matter production and its increase at depth by remineralization. The principal nutrient cycles are tightly coupled also as a consequence of biological activity, which links the cycles of elements at biogeochemical and molecular level as a result of the chemical structure of living organisms [*Gruber & Galloway,* 2008].

1.2.1. Composition of organic matter: Redfield ratios

A similarity between element ratios in the plankton biomass and deep-water nutrients was observed by Alfred Redfield more than 80 years ago, setting a cornerstone of marine biogeochemistry. The seminal papers of *Redfield* [*1934*] and *Redfield et al.,* [*1963*] proposed that on a global annual mean the organic matter is produced in constant molar element ratios and that biological processes controls the chemical composition of sea water. Marine primary producers fixed dissolved inorganic carbon, nitrogen and phosphorus into organic particles releasing oxygen under a constant stoichiometric ratio of 106 C:16 N:1 P:-138 O. In other words, for every phosphate atom fixed via primary production, 16 atoms of nitrogen and 106 atoms of carbon are also incorporated in the organic matter pool, whereas 138 oxygen atoms are removed. This are the classical Redfield ratio values. Posterior studies have evaluated the traditional values from alternative approaches, with a more appropriate formulation of organic matter [*Fraga et al.,* 1998], and the results are in agreement with the Redfield ratio, proposing only some slightly modifications [*Takahashi et al.,* 1985*; Peng & Broecker,* 1987*, Anderson & Sarmiento,* 1994; *Anderson,* 1995].

The connection of high and low latitudes mediated by the MOC it is believed to be the cause of the coincident value in the ratio of dissolved inorganic nutrients and the global mean composition of plankton [*Deutsch & Weber,* 2012]. Redfield ratios are particularly useful in oceanography: deviations from the expected ratio can give an insight for underlying biogeochemical processes [*Sarmiento & Gruber,* 2006], they allow to estimate the utilization of one nutrient from another [*Anderson & Sarmiento,* 1994], and they influence the efficiency of the ocean carbon sink [*Sanders et al.,* 2014].

1.2.2. Nitrogen cycle

Nitrogen has a critical role in controlling primary production in the biosphere. The N cycle is a drive component of the ocean biogeochemical dynamics because is often in short supply relative to other necessary macronutrients, acting as the major limiting nutrient [*Zehr & Kudela, 2010*].

If the largest reservoir of total nitrogen on Earth is the dinitrogen gas (N_2) present in the atmosphere, the largest for fixed nitrogen is present in the ocean [*Gruber, 2008*]. The relative rates of inputs and losses determine the N inventory, which in the end determines the total production of the ocean [*Zehr & Kudela,* 2011]. Balancing the oceanic N budget requires assumptions regarding homeostasis over time, that is, that N_2 fixation and denitrification have to be balanced over relatively short timescales [*Codispoti,* 2007]. The main approach to address this question is based on the N:P ratio of dissolved inorganic nutrients [*Tyrell,* 1999], because their distribution is expected to integrate the effects of remineralization over time and space [*Gruber & Sarmiento,* 1997].

Figure 9 represents a summary of the oceanic nitrogen budget. From a quantitative perspective, the most important process of the fixed nitrogen cycle in the ocean is the assimilation of NO_3^- and NH_4^+ into organic nitrogen in the euphotic zone. About 20% of the organic nitrogen formed in the euphotic zone is exported to the ocean's interior, where nearly all is nitrified back to NO_3^- in the water column, leading to a very small deposition flux of organic nitrogen to the seafloor (about 50 Tg-N·yr^{-1}).[*Gruber,* 2008] The largest natural source of fixed nitrogen to the ocean is N_2 fixation, estimated around 100-150 Tg-N·yr^{-1} [*Gruber,* 2004*; Gruber & Sarmiento,* 1997*; Galloway et al.,* 2004]. Nowadays, the anthropogenic perturbation of the global nitrogen cycle is such that inputs by rivers and through the atmosphere have reached the same order of magnitude as marine N_2 fixation [*Yang & Gruber,* 2016].

The ocean nitrogen cycle is biologically controlled and subject to change over fast timescales [*McElroy,* 1983]. It is a very dynamic cycle, with a residence time for fixed nitrogen of about 3,000 yr only, that contrasts with the residence time of PO_4^{3-} in the ocean, which is about 30,000 to 50,000 yr [*Delaney,* 1998].

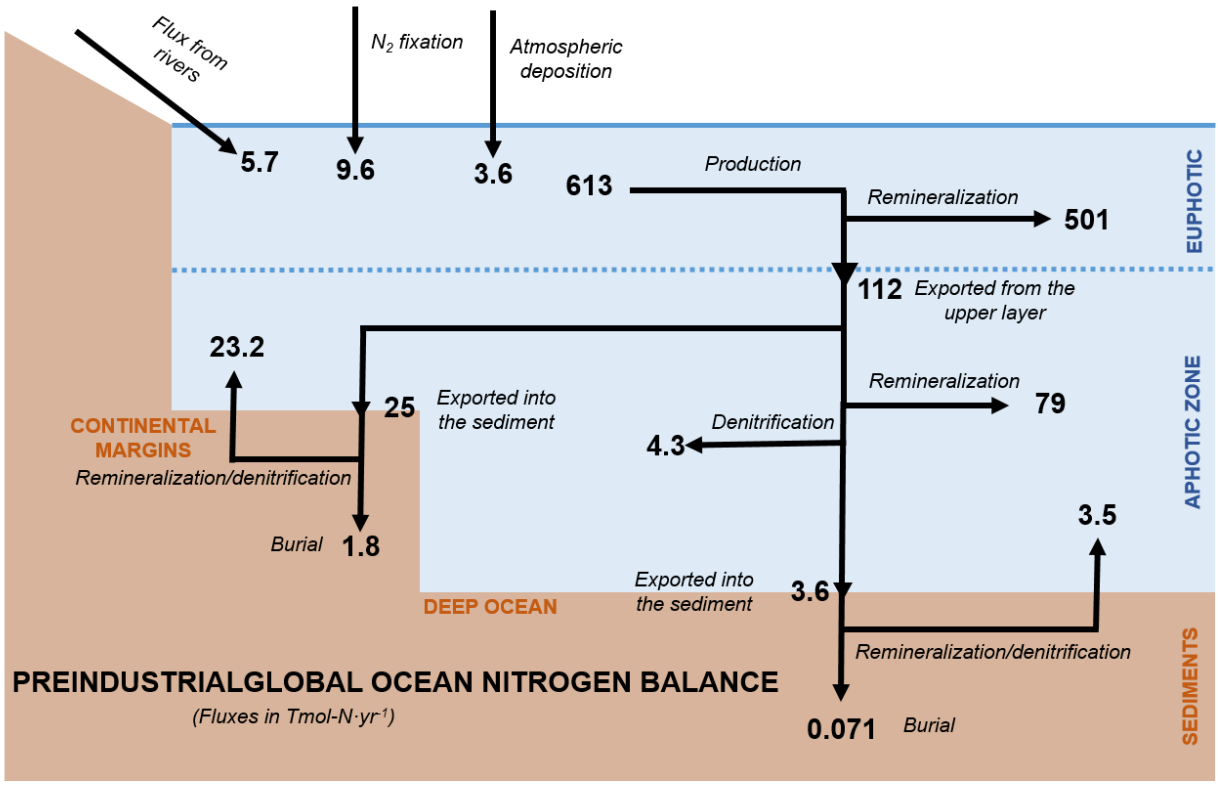

Figure 9. Preindustrial simplified nitrogen cycle in Tmol-N·yr^{-1} (1Tm=10^{12} mol). Source: author elaboration with data from *Gruber,* [2008].

Currently, the budget is out of balance between 9 and 22 Tg-N·yr^{-1} [*Yang & Gruber,* 2016]. The reason for the unbalance in the nitrogen marine cycle has been attributed to a massive increase in denitrification [*Codispoti et al.,* 2001], or a problem in the determination of the budget due poor constraint in the magnitudes of input (N_2 fixation, atmospheric deposition, river discharge) and output (denitrification) [*Zehr & Kudela,* 2011]. Instead, the most recent approaches agree that human activities have perturbed the marine nitrogen cycle due the increase in the source terms (atmospheric deposition), leading to an accumulation of fixed nitrogen in the upper ocean. [*Yang & Gruber,* 2016].

Nitrogen-based hypothesis to explain glacial-interglacial changes in the concentration of atmospheric CO_2 were questioned due the central role of nitrogen in the control of the primary production over great oceanic areas. However, it is unlikely that changes in the marine nitrogen cycle were the key drivers for the past changes in CO_2 levels, although they probably contributed to it [*Gruber & Galloway,* 2008].

1.2.3. Phosphorus cycle

The least known element cycle between the macronutrients, due its scarcity and methodological difficulties, is the phosphorus cycle. Phosphorus is an essential nutrient utilized by all organisms for energy transport and growth [*Froelich et al.,* 1982]. The global marine inventory of dissolved P is about 3.2 Pmol P (1 Pmol=10^{15} mol). [*Benitez-Nelson,* 2000]. The reservoir of oceanic P reflects primarily a balance between river input and sediment burial.

The continental weathering of crustal materials is the major source of riverine phosphorus that enters the oceans. The majority of the total P riverine input is in the particulate phase, so particles are removed quickly via sedimentation in the nearshore before reaches the open ocean [*Follmi,* 1996]*.* Hence, most of the riverine derived P which enters the oceanic cycle is in the dissolved phase [*Benitez-Nelson,* 2000]. The main processes in the removal mechanisms of P from the water column are organic matter burial, sorption and precipitation with clays or particles, the burial of phosphorites, and scavenging by hydrothermal activity [*Mach et al.,* 1987*; Delaney,* 1998]. The most important one is the organic matter sedimentary burial, exported from the upper water column to sediments through biological uptake and incorporation into sinking particles [*Benitez-Nelson,* 2000].

The majority of phosphorus associated with biogenic particles is recycled within the upper water column, and the amount that is finally accumulated in the sediment is less than 10% of that which reaches the seafloor, around 11 to 20 Gmol P yr^{-1}, (1 Gmol=10^{9} mol) [*Mach et al.,* 1987*; Delaney,* 1998]. Differences between calculations depend on either the amount chosen for organic C export or the ratio of P:C utilized [*Benitez-Nelson,* 2000]. Particulate organic C and organic P (acid-insoluble) are highly correlated in the sediment traps, implying that this operationally defined organic P is associated with organic C. However, these correlations do not yield the Redfield Ratio. The slopes for the equations relating organic C and organic P are significantly higher than the Redfield Ratio, with a range of ratios so large that could be as much as eight times higher than the Redfield ratio. P in sinking particulate matter has been preferentially regenerated relative to C when compared to C/P ratios in the living biomass [*Faul et al.,* 2005]. Same happens with its relationship with nitrogen: studies of the elemental stoichiometry of DOM and sinking organic matter suggest that dissolved organic P (DOP) is more reactive than dissolved organic N (DON), having faster turnover rates [*Clark et al.,* 1998].

The oceanic inventory of P is governed by geological processes and respond to changes in the Earth system on large timescales. The geologically controlled sources and sinks are small relative to the size of the P reservoir (primarily phosphate, PO_4^{3-}), so the residence time of P is on the order of 20,000 years [*Paytan & McLaughlin,* 2007; *Ruttenberg et al.,* 2013].

1.2.4. Silicon cycle

There are several organisms that needs silicon to form various types of structures, the most important being the diatom's frustule. Silicon exists in seawater primarily as silicic acid ([H_4SiO_4]), and is one of the major macronutrients of marine systems [*Tréguer et al.,* 1995], essential to the development of diatoms, radiolarians, silicoflagellates and some taxa of sponges [*Schlesinger & Bernhardt,* 2013].

In the ocean silica budget (Figure 10) there are several pathways as external sources of silicic acid to the ocean, all of which ultimately derive from the weathering of Earth's crust: rivers, groundwater discharge, aeolian deposit of particulate amorphous silica, dissolution of terrigenous silicates sediments of continental margins, or deep-sea hydrothermal vents. [*Tréguer & de la Rocha,* 2013]. The current residence time of silicon in the ocean is 15,000-17,000 years [*Tréguer et al.,* 1995*; Laruelle et al.,* 2009]. Rivers remain the dominant source of silicate inputs in the modern ocean, with a current best estimate of the discharge weighted average concentration of rivers of 158 μM [*Dürr et al.,* 2011].

Diatoms fabricate opal frustules from silicic acid in the surface layer, where the total gross production of biogenic silica is estimated in 240±40 Tmol-Si·yr^{-1} [*Nelson et al.,* 1995]. The global rate of biogenic silica production is equivalent to a mean production rate of 0.6–0.8 mol-Si·m^{-2} yr^{-1} or 1.5–2.1 mmol-Si m^{-2}·d^{-1}, but there is an enormous spatial and temporal variability. The difference between the lowest daily production rates in oligotrophic regions versus the high rates in coastal upwelling sites reach almost five orders of magnitude [*Ragueneau et al.,* 2000]. The amount of the biogenic silica exported from the euphotic layer is determined by the interplay between production and recycling in the upper surface waters. About 50% of gross production is returned to solution inside the upper ocean (Figure 10), while the rest is exported. Within the opal material exported from surface waters, the great majority is dissolved during the vertical sinking in the water column, and less than 25% of exported material reach the sediments [*Ragueneau et al.,* 2000; *Sarmiento & Gruber,* 2006]. Around a 12% of the opal gross reach the sediments, where dissolution processes still occur, reducing until the ~3% the quantity buried that eventually becomes sedimentary rock [*Sarmiento & Gruber,* 2006]. The preservation efficiency of biogenic silica in sediments is thirty times greater than carbon, favoring the use of silica as a proxy for export production [*Ragueneau et al.,* 2000; *Tréguer & de la Rocha,* 2013]. The global export of biogenic silica into the bathypelagic zone of open ocean areas is 34.4± 2.6 Tmol-Si·yr^{-1} [*Honjo et al.,* 2008], so the global export should be higher when coastal zones and continental slopes are included. Important local variability exists, and in average the silica flux is quite small in the Atlantic Ocean [*Honjo et al.,* 2008]. The global sink of silicate estimated from sediment data is about 220 kmol-Si·s^{-1} (6.9 Tmol-Si·yr^{-1}) which is close to the total input from river runoff, at 160 kmol-Si·s^{-1} (5 Tmol-Si·yr^{-1}) [*Tréguer et al.,* 1995].

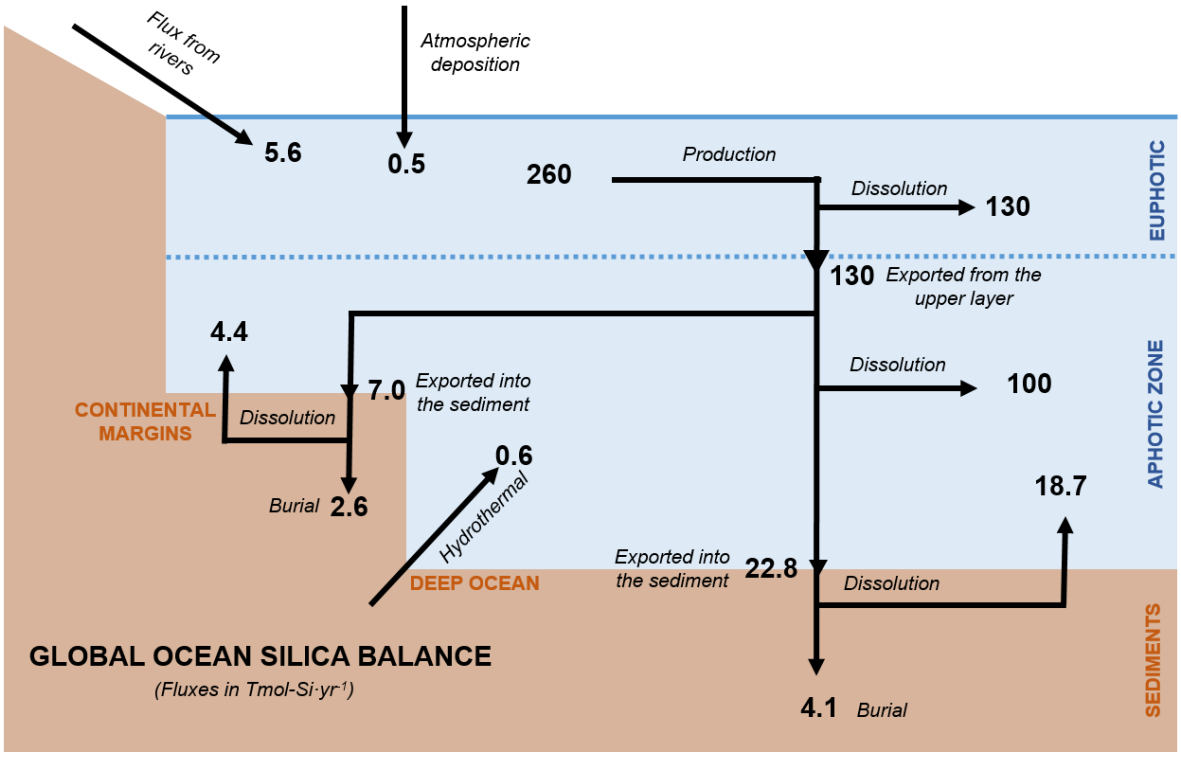

Figure 10. Silica cycle in Tmol-Si·yr^{-1} (1Tm=10^{12} mol). Author elaboration with data from *Sarmiento & Gruber,* [2006]. Note that during the text some slightly different numbers are given, but in the figure all the magnitudes are taken from *Sarmiento & Gruber,* [2006] for consistency purposes.

The recognition as sources of groundwater discharge and the dissolution of siliceous materials transferred from land to the continental margin [*Tréguer & de la Rocha,* 2013] had been ignored in previous silicate's budget [*Tréguer et al.,* 1995]. Lastly and significantly, the dissolution of biogenic silica appears to occur predominantly in the upper ocean and at the seabed, with only minor dissolution of biogenic silica occurring during its transit through the deep ocean [*Tréguer & de la Rocha,* 2013]. While some silica budgets for the global ocean supports the hypothesis that the marine silica cycle is not currently at steady state because total burial flux of biogenic silica due to diatoms in the coastal zone and the open ocean does not balance against an increased total input of silicate [*Tréguer & de la Rocha,* 2013], a recent approach revisiting the marine sedimentary Si cycle using cosmogenic isotopes (^{32}Si), claims that an important fraction of the missing silica sink is trapped in nearshore deposits as rapidly formed clay [*Rahman et al.,* 2017].

In our region of study, melting from Greenland's ice sheet play a more significant role in the global Si cycle than previously recognized, mainly via export of large quantities of potentially labile amorphous silica [*Hawkings et al.,* 2017].

1.2.5. Oxygen cycle

The air-sea exchange of oxygen in the ocean depends upon the partial pressure, that is controlled by (i) temperature and salinity [*Garcia & Gordon,* 1992], (ii) biological activity and (iii) physical processes such as advection, convection, upwelling/downwelling [*Ganachaud & Wunsch,* 2002]. The air-sea equilibration time of oxygen is extremely rapid –around a month, compared to a year for CO_2- so differences in partial pressures are quickly manifested as an oxygen flux.

(i) The influence of solubility on the air-sea gas exchange depends primarily on the temperature and, to a minor extent, salinity. As with any other gas, the solubility of O_2 in seawater is reduced with warming and increases in cold waters. Thus, if surface ocean saturated with a gas is cooled, the water will become undersaturated and will be uptake from the atmosphere [*Sarmiento & Gruber,* 2006].

(ii) Biological activity influences vertical distribution: photosynthesis produces oxygen in the upper layers and respiration consumes it all along the water column. The remineralization of organic matter at depth is responsible for the O_2 depletion of deeper waters (Oxygen Minimum Zone, OMZ) [*Bopp et al.,* 2002].

(iii) Changes in the dynamical field has associated changes in the oxygen inventory. A process of present concern is the warming-induced stratification, that leads to a decrease in the transport of dissolved oxygen from surface to subsurface waters [*Frölicher et al.,* 2009]. If stratification is strong enough to avoid the winter deepening of the mixed-layer, the supply of oxygen at intermediate depths will be reduced. Approximately 85% of the global oxygen decline can be explained by increased stratification, with the remainder explained by a warmer mixed-layer [*Helm et al.,* 2011].

There is a seasonal pattern in the oxygen cycle: in spring and summer the ocean releases O_2, by warming and by oxygen production from phytoplankton blooms. In fall and winter the ocean takes up O_2 by cooling and by undersaturated ingassing when the mixed layer deepens enough to put deeper waters in contact with the atmosphere [*Bopp et al.,* 2002].

At global scale the main pattern that emerges is uptake of oxygen in the high latitudes of both hemispheres and release of oxygen into the atmosphere in the low latitudes [*Gruber et al.,* 2001]. The general cooling and convection of waters at high latitudes increases the solubility of oxygen in the surface waters, thereby promoting an uptake of O_2 by the ocean [*Ganachaud & Wunsch,* 2002]. Also in high latitudes, O_2-depleted waters are mixed and transported to the surface from below. This undersaturation in O_2 is not compensated by O_2 biological production (incomplete nutrient utilization), thereby driving an O_2 flux from the atmosphere into the ocean [*Bopp et al.,* 2002]. The direction of oxygen transports is equatorward in the Indian and Pacific Oceans while the Atlantic basin has a net southward transport at all latitudes north of 36ºS [*Gruber et al.,* 2001]. Global

oxygen budget is in balance within uncertainty (900±1500 kmol-$O_2 \cdot s^{-1}$) [*Ganachaud & Wunsch,* 2002].

In the North Atlantic, the primary mechanism responsible for the southward flux of oxygen is the formation of North Atlantic Deep Water [*Rintoul & Wunsch,* 1991]. Subsurface waters poor in oxygen from subtropical areas progressively increase its oxygen content during its northward flow within the NAC [*Maze et al.,* 2012]. At high latitudes they are finally exposed at the sea surface, where equilibrates with the atmosphere as it is cooled and returns to the south at depth with a higher oxygen concentration [*Rintoul & Wunsch,* 1991].

An ensemble of models from the Coupled Model Intercomparison Project (CMIP5) comparative found that significant climate change trends in deoxygenation will emerge as soon as 2052 (±12 years) [*Henson et al.,* 2017]. In the North Atlantic the air-sea O_2 flux exhibits significant interannual and decadal variability. [*Bopp et al.,* 2002] being one of the regions where the natural variability of oxygen is so large that detection will be delayed on time [*Frölicher et al.,* 2009].

There are opposing views for the status of oxygen in the Atlantic Ocean. *Tanhua & Keeling,* [2012] showed that the mean trend for storage rate of oxygen is non-zero at the 95% confidence level, i.e., a deoxygenation is occurring in the Atlantic Ocean, and the trend is dominated by the subpolar region. On other side, *Stendardo & Gruber,* [2012] show that when the oxygen changes are integrated across all horizons and regions, the oxygen inventory shows no change, mainly because there is a near cancelation between a loss in the upper layers and a gain in the deeper layers.

1.2.6. Transport of nutrients and oxygen in the North Atlantic: State of the art

Nutrient and oxygen distribution in the ocean are controlled by the interplay of physical and biological processes. Biological processes lead to the transformation of nutrients between inorganic and organic forms, and also between dissolved and particulate forms: net nutrient consumption in the photic zone due photosynthesis and net remineralization of organic matter at depth. Physical processes redistribute tracers within the water column through transport and mixing: the dominant process is advection, but also diffusion, surface heat and freshwater fluxes. The combined role of biological and physical processes is reflected in the observed distributions of oxygen and nitrate, phosphate and silicate (macronutrients).

The balance between nutrient sources and sinks is related with export production. A downward flux of particles and dissolved organic matter creates a sink of dissolved nutrients in the upper layers by consumption, and a source in deep layers through remineralization. Photosynthesis and remineralization produce similar source terms in the oxygen budget, but with opposite sign, net production in the upper layer and consumption by respiration in depth. In addition, and unlike

nutrients, the oceanic oxygen balance includes the important physical process of air-sea fluxes [*Ganachaud & Wunsch,* 2002].

Assuming that basin-scale distribution of tracers intrinsically involves biogeochemical processes averages over time and space, a quantitative budget approach can be done combining horizontal transports because they are independent of assumptions about the biogeochemical behavior [*Ganachaud & Wunsch,* 2002]. Direct estimates of the advective transport of oxygen and nutrients provide an opportunity to investigate quantitatively the large-scale processes, which contribute to the basin scale balance of those relevant biogeochemical tracers. Basin-scale transports estimations of nutrients and oxygen published for the North Atlantic are summarized and discussed in the PART III: Biogeochemical budget.

Chapter 2: Oceanography of the North Atlantic

2.1. Area of study

The Atlantic Ocean occupies the North-South orientated basin that separates Europe and Africa to the east, and the Americas to the west. It goes from the northern limit with the Arctic Ocean to the Southern Ocean. A natural division, mediated topographically by the Mid-Atlantic Ridge, separates the Atlantic in Eastern and Western basins. A geographical separation, mediated by the Equator, separates it in North and South Atlantic. Although a wide vision of the global ocean is required to understand large-scale circulation processes, the North Atlantic domain that we are going to consider is represented in the Figure 11 and Figure 16. Important features like the anticyclonic subtropical gyre (~10-45ºN), the cyclonic subpolar gyre (~45-65ºN) or the North Atlantic Current (NAC) define the circulation in the upper layer flow.

The subtropical–subpolar gyre boundary is not fixed neither in time or space. Instead, a 'transition zone' exists, as observed in both the physical environment [*Pollard et al.,* 1996; *Eden & Willebrand,* 2001*; Marshall et al.,* 2001] and in the biogeochemical response [*Dutkiewicz et al.,* 2001*; Henson et al.,* 2009], where oceanographic conditions are neither purely subpolar nor subtropical, but rather a blend of the two.

2.1.1. OVIDE section

The key section where most of the data presented during this document come is the OVIDE section (represented as a red line in Figure 11). The OVIDE section runs from 40ºN latitude to 60ºN, from the shelf coast of Portugal to near Cape Farewell in Greenland. It was born as a French project (OVIDE: *Observatoire de la Variabilité Interannuelle à Décennale*) and it is repeated each summer biennially since 2002. In 2018 it is going to take place the ninth repetition. It is also called the WOCE A25 Greenland–Portugal section in the World Ocean Circulation Experiment (WOCE) project. Along its transit, the Iberian Abyssal Plain, the Western European Basin, the Iceland Basin and the Irminger Sea are crossed. The OVIDE section cross the summit of the Reykjanes Ridge at a depth of ~1450m, and other bathymetric features such as the Eriador Seamount and the Azores-Biscay Rise at ~3,000 and ~4,000 m depth respectively.

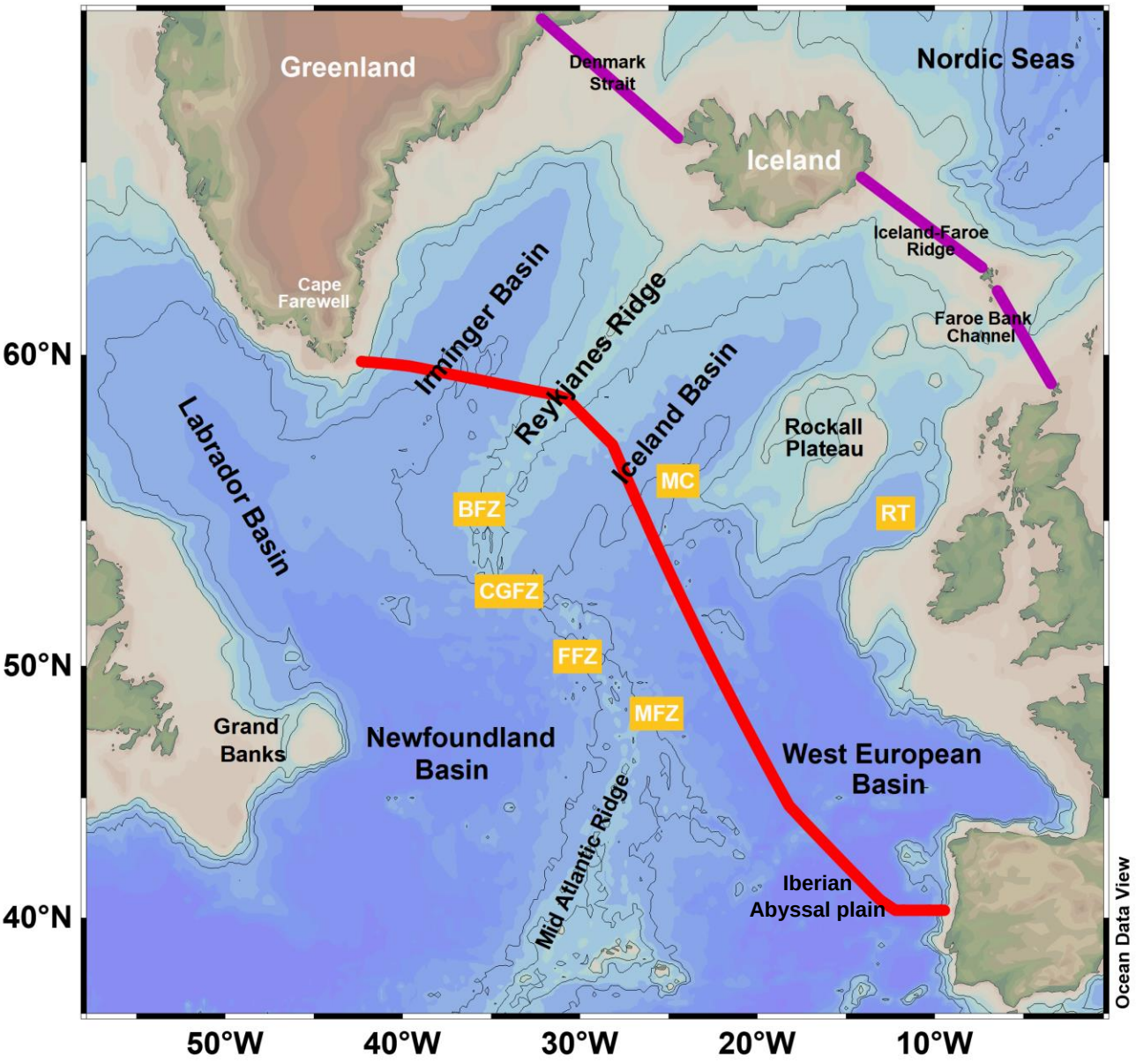

Figure 11. Subpolar North Atlantic topographic map. The red line between Iberian Peninsula and Cape Farewell, Greenland is the OVIDE section. The purple lines between Greenland and Scotland represents the Greenland–Iceland-Scotland Sills. Main basins and topographical features are written on black letters over its approximate location. Represented in yellow boxes are some topographical features that are mentioned along the memory: the Maury Channel (MC) in the Iceland Basin, the Rockall Trough (RT) east of the Rockall Plateau, and the main fracture zones across the Mid-Atlantic Ridge, from north to south, Bight Fracture Zone (BFZ), Charlie Gibbs Fracture Zone (CGFZ), Faraday Fracture Zone (FFZ) and Maxwell Fracture Zone (MFZ).

The OVIDE section was specifically designed to run perpendicularly across the main currents in order to minimize the transports due to eddies. Along a distance of 3,400 km, around 100 stations of hydrography and chemistry are done. The mean depth of the section is 3,200 m. The maximum depth sampled at the Irminger Sea, in the center of the basin is 3,100 m, at the Iceland Basin is 3,600 m and in the Iberian Abyssal Plain the deepest samples are taken at 5,300 m depth.

2.1.2. Greenland-Iceland-Scotland Sills

The limit north of our main region of study is defined by the Greenland-Iceland-Scotland Sills, (G-I-S sills, purple lines in Figure 11). It is the limit between Atlantic and Subarctic waters. The mean depth of the sill, around 500 m, limits the exchange of deep water with the North Atlantic. There are only few sections that allow relatively deep overflows (Figure 12), the Denmark Strait and the Faroe Bank Channel. The G-I-S sills impose a bathymetric restriction that narrows the variability in the circulation. The Denmark Strait is the gap between Greenland and Iceland, is relatively wide and reaches a depth of 640 m. The Faroe Bank Channel is 840 m deep and narrows to 10 km at its primary sill. Shallower overflows also occur across the Iceland- Faroe Ridge, a broad ridge of approximately 400 km wide with a crest depth varying around 450 m (deepening at the Faroese end), and the Wyville-Thomson Ridge between the Faroes and the Scotland shelf (depth ~600 m). The surface northward flow of warm and saline Atlantic water towards the Norwegian Sea (Figure 12) crosses the Greenland-Scotland Ridge in three Atlantic inflow branches: Iceland Branch, Faroe Branch and Shetland Branch. The Iceland branch goes through the Denmark Strait carrying ~10% of the Atlantic inflow volume flux with the other two branches carrying 45% each. The Faroe Branch pass over the ridge between Iceland and the Faroes. The Shetland Branch, crossing the sills through the Faroe-Shetland Channel west of Scotland, carried a slightly larger fraction of the salt (46%) and a considerably larger fraction (50%) of the heat flux.

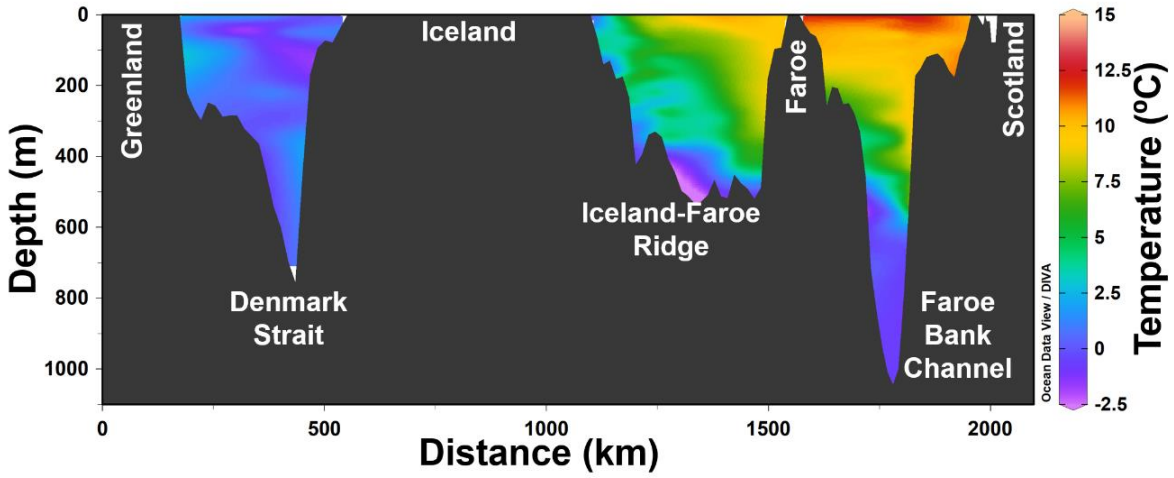

Figure 12. Vertical section of temperature at the Greenland-Iceland-Scotland Sills (G-I-S Sills) represented at linear y-scale in km from the Greenland coastline (68ºN) to the Orkney Islands (59ºN) in Scotland, passing through Iceland and the Faroe Islands. Named in the figure are the main topographic features that conditions the circulation. Source: author elaboration with GLODAPv2 data.

2.1.3. Reykjanes Ridge

The Mid-Atlantic Ridge(MAR) northern than 50ºN, the Reykjanes Ridge (RR), is the dominant bathymetric feature that strongly influences the circulation and the location of hydrographic fronts in the North Atlantic. The RR separates the Irminger Basin from the Iceland and West European Basins.

The RR clearly imposes a constraint on the spatial pattern of the subpolar gyre circulation [*Bower et al,* 2002] and water masses [*Thierry et al.,* 2008]. The RR extends along a southwest/northeast line from Iceland to the Bight Fracture Zone (BFZ) (Figure 11) at about 57°N and then along a more meridional line till the Charlie Gibbs Fracture Zone (CGFZ) at 52°N. The top of the ridge is at about 300 m depth at 63°N and deepens to about 3000 m at the CGFZ. The bottom topography is rather smooth northeast of about 59°N while troughs, fracture zones and seamounts are observed in the southwestern part of the ridge.

The ridge causes topographic steering, most notably through the CGFZ but also through the Faraday and Maxwell Fracture Zones (Figure 11) further to the south [*Bower et al.,* 2002*; Miller et al.,* 2013] and through the BFZ at north [*Kanzow & Zenk,* 2014]. The RR influences the main paths followed by the two limbs of the MOC and is the gate towards the deep convection areas for the warm water masses of the upper limb.

2.1.4. eastern Subpolar North Atlantic (eSPNA)

Using as boundaries the limits established in the previous sections, we are going to define a functional geographical area that we are going to name "*eastern Subpolar North Atlantic*" (eSPNA). The eSPNA is the marine region located northern of the OVIDE section and southern of the G-I-S sills (Figure 11). In the eSPNA, the Reykjanes Ridge acts as a natural topographic barrier, separating the Irminger Basin (IB) at the west from the Iceland and West European Basins at the east. The basins at the east of the Reykjanes Ridge can be combined with the denomination Eastern North Atlantic (ENA) (Figure 33). The eSPNA have an extension of 3.8×10^{12} m^2, with the ENA (IB) representing the 84% (16%) of the total area.

Along the thesis we are going to use this geographical naming convention. Some studies in this same region used similar geographical configurations [*Lherminier et al.,* 2010; *Maze et al.,* 2012; *García-Ibáñez et al.,* 2015], very useful in box-model approaches.

2.2. Large scale circulation

What drives ocean's circulation? Following *Wunsch,* [2002], I consider the ocean circulation as that of its mass, so oceanic circulation is driven mainly by the wind, and secondarily by tidal forcing. The terms meridional overturning circulation (MOC) and thermohaline circulation are sometimes used like synonyms, but they have very different meanings. MOC is a descriptive term of circulation in a meridional plane, as depicted by an overturning stream function, and does not refer to any particular driving mechanism. Contrary, the term thermohaline circulation is by definition the flow driven by mechanism of heat and salt [*Kuhlbrodt et al.,* 2007]. The overturning circulation is driven by remote and local wind and buoyancy forcing, the mixing supplied by tides and winds, and the impact of eddies on all these process [*Lozier et al.,* 2012].

The MOC is a key component of Earth's climate as it contributes to the redistribution of heat, salt and the cycling and storage of chemical species such as carbon in the world ocean. The global MOC connects all major World Ocean basins and explicitly accounts for water mass formation (Figure 13). Two global-scale counter-rotating meridional cells dominate the global overturning circulation [*Lumpkin & Speer,* 2007]. The deepest one, the "lower cell," originates from around Antarctica and supplies fluid to the abyssal ocean. The cell sourcing from the northern North Atlantic forms the "upper cell" of the ocean's MOC, and is called Atlantic Meridional Overturning Circulation [*Buckley & Marshall,* 2015].

An important inter-basin difference is that the Atlantic overturns is mostly sourced from the surface layer and is thus dyed by tracers indicating young age (high oxygen, low nutrients), while the

Pacific and Indian deep layers are almost entirely sourced from upwelled bottom waters, and hence are dyed by tracers indicating much greater age (low oxygen, high nutrients). [*Talley,* 2013]

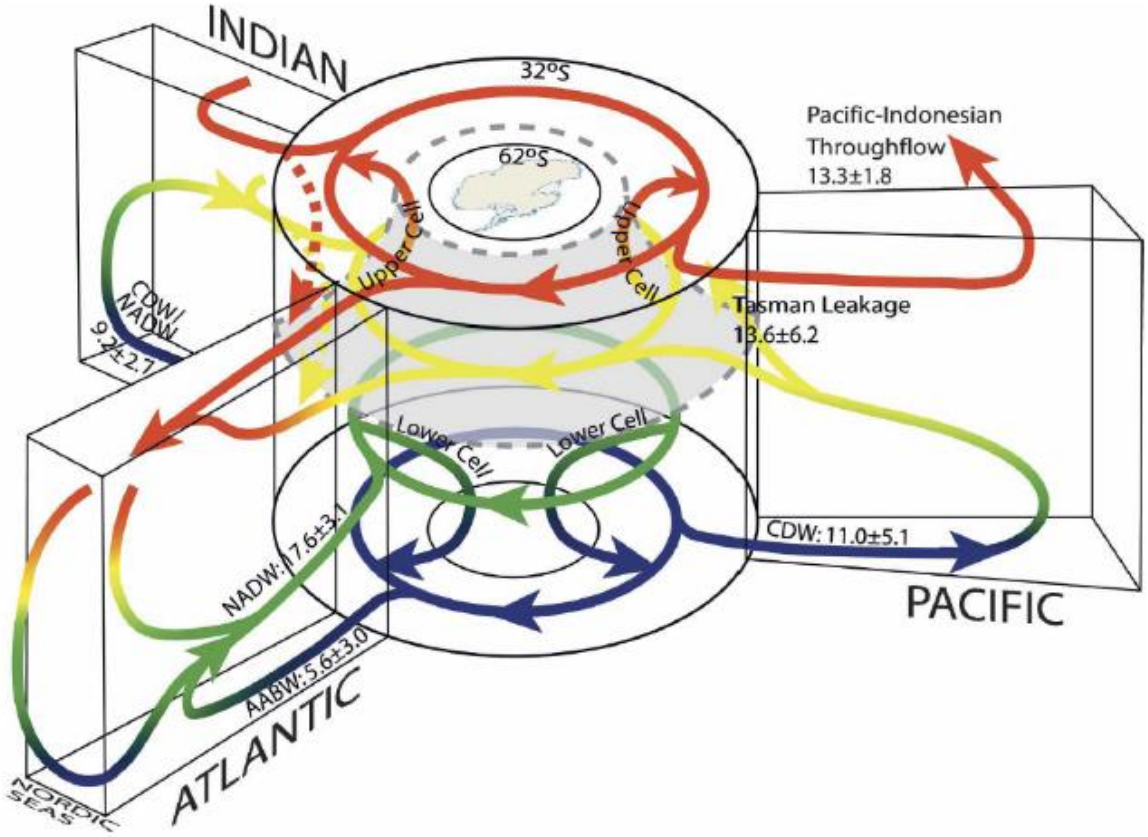

Figure 13. Schematic three-dimensional representation of the global meridional overturning circulation (MOC). The three slices represent the Atlantic, Indian and Pacific Ocean and their connection with the Antarctic domain. The color of the arrows represents surface (red), intermediate (yellow), deep (green) and bottom (blue) currents. Accronyms: CDW: Circumpolar Deep Water, AABW: Antarctic Bottom Water, NADW: north Atlantic Deep Water Source: adapted from *Schmitz,* [1996] taken from *Lumpkin & Speer,* [2007].

2.2.1. Atlantic Meridional Overturning Circulation (AMOC)

In the AMOC, warm and saline surface waters move poleward to higher latitudes where they undergo buoyancy loss. Water near the surface becomes denser as it loses heat to the atmosphere or becomes saltier due to evaporation or ice formation [*Frajka-Williams et al.,* 2016]. The surface waters gain density and eventually sink, returning southward as cool and denser waters at depth. As the deep water returns southward across subtropical and tropical latitudes, its density decreases due to mixing [*Lumpkin & Speer,* 2007].

The last predictions of IPCC consider very likely that the AMOC will significantly weaken over the XXIth century as a consequence of human-induced climate change [*Houghton et al.,* 2001], but it is very unlikely that will collapse [*Solomon et al.,* 2007*; Meehl et al.,* 2014*; Kirtman et al.,* 2013]. The weakening of the AMOC results from a reduction in the heat loss to the atmosphere and an increase in the freshwater fluxes at high latitudes, both diminishing the buoyancy loss of surface waters [*Buckley & Marshall,* 2015]. Lighter surface waters may lead to a reduction or collapse of deep water formation in the high latitude sinking regions, affecting the strength of the AMOC [*Zhang et al.,* 2010].

Apart from the impact on climate due heat redistribution, the AMOC plays a role in the ocean carbon cycle. AMOC disruptions will have not only implications in the CO_2 sink, it would also impact the ocean primary productivity if there is a decrease in the northward flow of nutrients [*Palter and Lozier,* 2008] or in the supply of nutrients to the surface by convection and mixing [*Lozier et al.,* 2017].

Analyzing the responses of interdecadal variability of the AMOC under various scenarios of future global warming in multiple models, the AMOC will be significantly weakened in amplitude and shortened in period under future global warming, and these responses could be caused by the strengthened ocean stratification and, in turn, the speedup of baroclinic Rossby waves [*Cheng et al.,* 2016].

The AMOC has a key role in climate change by which excess heat and carbon can be transported from the surface to the deep ocean. Despite being confined to the rather small Atlantic Basin, the AMOC plays a central role in climate. On decadal timescales, variability of the AMOC has been linked to low-frequency variability of Atlantic sea surface temperatures, termed the Atlantic Multidecadal Oscillation/Variability, with a host of implications for climate variability over surrounding landmasses [*Buckley & Marshall,* 2015].

Obtain an adequate measure of the AMOC, a basin-scale phenomenon, it is a challenging task. *Bryden et al.* [2005]*,* using all available trans-Atlantic hydrographic sections at 24ºN (a total of five, only), concluded that the AMOC had slowed between 1957 and 2004 almost a 30%. Nowadays, there are a continuous basinwide monitoring program of the AMOC which began in 2004. The RAPID project has installed a system of trans-atlantic array of moored instruments measuring ocean transport across 26.5ºN with daily resolution [*Cunningham et al.,* 2007]. The value of the AMOC is defined as the maximum of the transport streamfunction [*McCarthy et al.,* 2012]. The overturning is computed from the sum of the directly measured Gulf Stream transport through the Florida Straits, the Ekman transport estimated from QuikSCAT winds, and the midocean geostrophic transport estimated from the moored array measurements [*Lozier et al.,* 2012].

The strength of the AMOC and meridional heat transport are estimated as 17.2±0.3 Sv and 1.25±0.21 PW respectively from April 2004 to October 2012 (Figure 14) [*McCarthy et al.,* 2015]. Since the first years the observations reveal a surprising degree of AMOC variability in terms of the intra-annual range, the amplitude and phase of the seasonal cycle, and the interannual changes in strength affecting the ocean heat content [*Srokosz & Bryden,* 2015]. The AMOC strength decreases suddenly between the years 2009-2010, representing a 30% decline with respect to the annually averaged MOC strength [*McCarthy et al.,* 2012]. The 2009-2010 dip in strength can be partially attributed to an extreme negative NAO winter that affected the wind field [*Srokosz & Bryden,* 2015]. However, the AMOC 2008-2015 has a strength of 16 Sv, much reduced on the strength prior to 2008 of 18.8 Sv (Figure 14) [*Smeed et al.,* 2016].

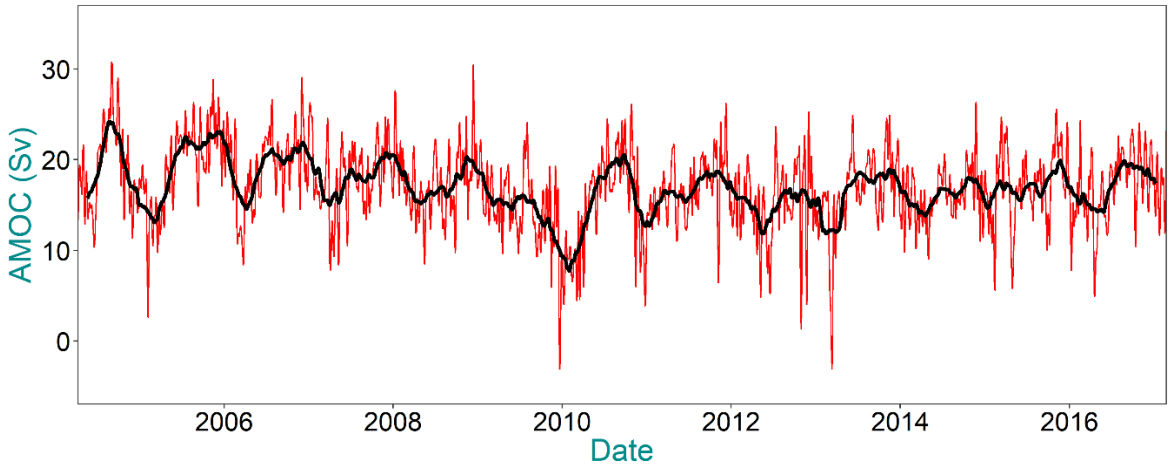

Figure 14. Time series of AMOC (26.5ºN) transport (Sv) at 12-hourly (red), and with a three month low-pass filtered (black) for the period April 2004 to February 2017. Source: author elaboration with data from the RAPID-WATCH MOC monitoring project freely available at www.rapid.ac.uk/rapidmoc.

Although maybe it is too soon to assign confidence to the decreasing trend proposed, it is now clear that AMOC involves the interaction between surface currents, deep currents, and eddy-driven circulations [*Buckley & Marshall,* 2015]. On an annual scale, the local wind forcing appears to influence the AMOC variability, while on decadal variability, a more complex interplay between wind-driven and buoyancy processes arise.

In the latitudes of OVIDE, a better measure of the overturning circulation is estimated in density space (MOC_σ) rather than in depth space. With the density separation, the warm and saline flowing northward waters are ascribed to the upper limb and the cold and fresher waters returning south are ascribed to the lower limb of the overturning cell [*Lherminier et al.,* 2010]. Under this approach, the magnitude MOC_σ quantifies the light-to-dense water mass conversion north of the section [*Grist*

et al., 2009]. Transports across OVIDE sections 2002-2016 integrated in density layers and accumulated from the bottom, with the estimate of MOC_σ at the maximum of each curve, are represented in Figure 15.

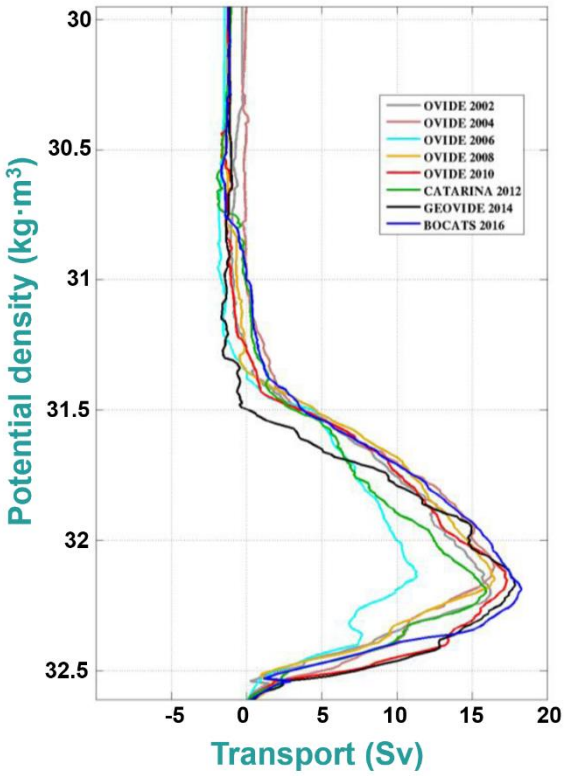

Figure 15. Transports (Sv) integrated in density layers (σ_1, potential density anomaly referenced to 1000 m) (kg·m^3) across all the OVIDE sections and accumulated from the bottom after a sign change. The density of the MOC_σ is at the maximum of the accumulated transport for each cruise.

The MOC_σ, defined as the net southward transport in the MOC_σ lower limb, varied between 11.4±2.4 Sv and 18.5±2.4 Sv with a mean value of 16.0±1 Sv (Figure 15). *Mercier et al.* [2015] constructed a monthly MOC_σ index built upon satellite data and Argo floats, and it was validated with good agreement against the estimates of the repeat OVIDE surveys. The MOC_σ index varies from less than 15 Sv to about 25 Sv [Figure 5 in *Mercier et al.,* 2015]. The intra-annual variability in the MOC_σ index shows a pronounced seasonal cycle with maximum in winter, minimum in summer and peak-to-peak amplitude of 4.3 Sv. Winter NAO leads the annual average MOC_σ index by 2 years, which is in line with previous results that relate the circulation in the eastern subpolar gyre with the NAO within a 2-year lag [*Bersch,* 2002*; Böning et al.,* 2006]. At the latitudes of OVIDE, same as 26.5ºN, heat transport and MOC intensity are strongly correlated.

2.2.2. Northern North Atlantic Ocean mean circulation

As can be inferred from previous section, mean ocean circulation in the northern North Atlantic is intrinsically related with the overturn process in the AMOC. The essential nature of the largescale circulation is as follows (Figure 16): the western-intensified boundary current Gulf Stream separates itself from the shelf at Cape Hatteras, and becomes a freely meandering jet in north-eastward direction until the Grand Banks. There, in the Northwest Corner region, the warm northward flowing waters of the Gulf Stream meet the cold southward flowing waters of the Labrador Current, the western boundary current of the cyclonic subpolar gyre. The majority of the near-surface waters from the Labrador Current join the Gulf Stream to form the North Atlantic Current (NAC) east of the Grand Banks [*Rossby et al.,* 1999]. The NAC is both the upper limb of the MOC, connecting subtropical and subpolar latitudes, and the southern limb of the cyclonic subpolar gyre [*Daniault et al.,* 2016]. As the NAC travels northward, an energetic eddy field is locked in place by topography, the most prevalent of which is the anticyclonic Mann Eddy (centered at 42ºN, 44ºW). The NAC follows its course across the North Atlantic as a broad baroclinic transport between 48º-52ºN, splitting into several branches strongly constrained by bathymetry. Three branches of the NAC have been reported associated mainly with gaps through the Mid-Atlantic Ridge: the CGFZ, (52.5ºN 31.5ºW), the FFZ, (50ºN 29ºW) and the MFZ (46.5ºN 27ºW) (Figure 11) [*Bower & von Appen,* 2008]. The central branch, that cross around ~50ºN, represents the Subarctic Front (SAF), a sharp salinity gradient between the northern and the southern branch. South to the SAF, the zone comprehended between European shelf and the mid-Atlantic Ridge, it is a weak circulation region that belongs neither subpolar or subtropical gyre, called the intergyre zone [*Pollard et al.,* 1996]. Overall, the circulation is cyclonic north of the NAC and anticyclonic south of the NAC. The net transport of the NAC measured between 2002-2012 is 41.8±3.7 Sv [*Daniault et al.,* 2016].

At latitudes >50ºN, the branches of a surface-intensified NAC flows northwestward through the Iceland Basin and Rockall Trough. An important part circulates cyclonically into the mean pattern of the subpolar gyre and only around ~8 Sv feed the Faroe and Shetland branches into the Nordic Seas. The flux stability variations in the branches of the NAC that cross to the Nordic Seas mainly resides in the existence of a negative correlation between the Shetland branch inflow and the other two branches [*Østerhus et al.,* 2005].

The topography of the Reykjanes Ridge itself imposes a general anticyclonic circulation from top-to-bottom. On the eastern flank of the ridge a highly barotropic current, the East Reykjanes Ridge Current (ERRC) flow southwestward, while on the western side of the ridge it is the surface-intensified Irminger Current. The southwest Irminger Basin presents its inner narrow cyclonic recirculation –the Irminger Gyre– [*Våge et al.,* 2011]. South of the Denmark Strait the Irminger

Current bifurcates: one branch continues northward through the strait, while the major fraction recirculates to the south.

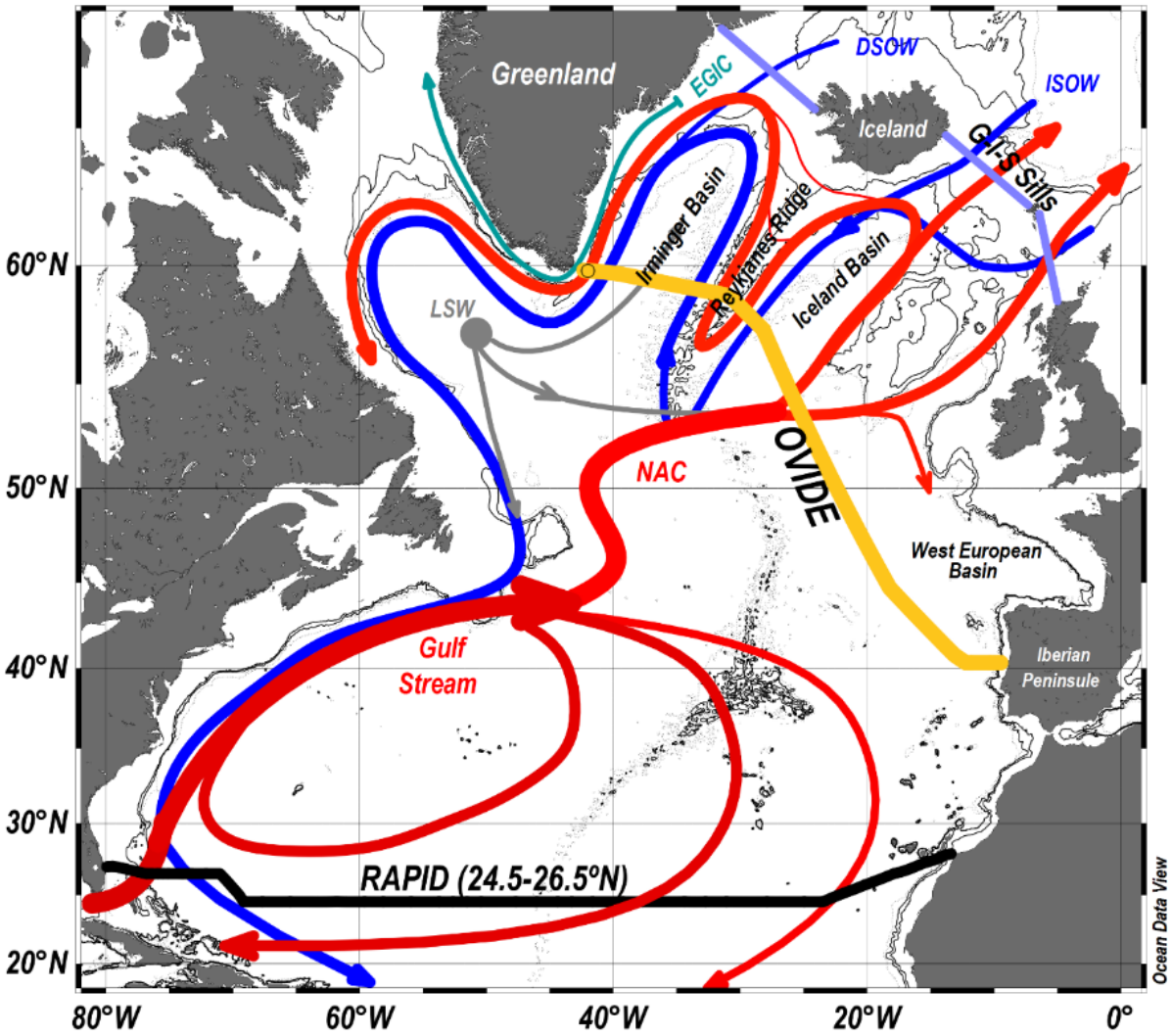

Figure 16. Map of the subpolar North Atlantic circulation with major topographical features included (the 1000, 1750 and 2500-m isobaths are plotted). Section tracks of the OVIDE (yellow thick line) and RAPID (24.5–26.5°N) (black thick line) cruises are indicated. The geographical domain eastern Subpolar North Atlantic (eSPNA) lies between the OVIDE section and the Greenland-Iceland-Scotland (G-I-S) sills (purple line). Abbreviations for the main currents and water masses are as follows: DSOW = Denmark Strait Overflow Water, ISOW = Iceland-Scotland Overflow Water, LSW = Labrador Sea Water, EGIC = East Greenland Irminger Current, NAC = North Atlantic Current. Schematic diagram of the large-scale circulation compiled from *Sarafanov et al.,* [2012]; *García-Ibañez et al.,* [2015]; *Lherminier et al.,* [2010], *Schmitz & McCartney*, [1993].

The inflowing of subarctic water is mainly by the overflows at the East and West of Iceland (Figure 16). The overflows don't present interannual variability or long-term trend declines, neither in the Denmark Strait [*Jochumsen et al.,* 2017] or Iceland-Scotland Ridge [*Hansen & Østerhus,* 2007].

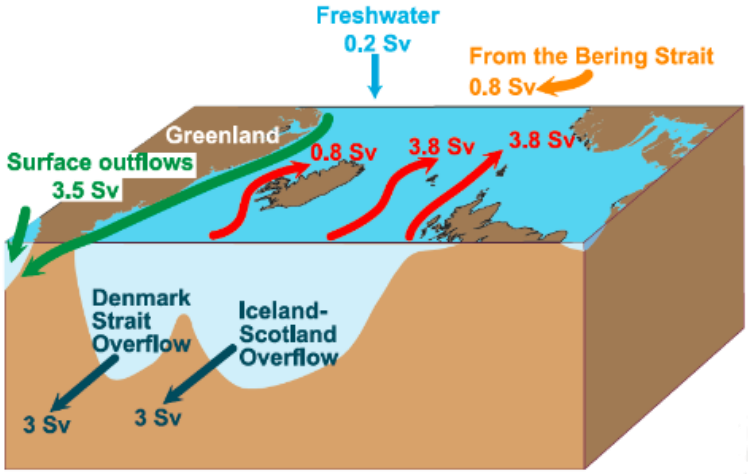

Figure 17. Mass (volume) budget of the Arctic Mediterranean. Source: *Hansen et al.,* [2008]

At Denmark Strait, mooring time series at the sill have shown that there is no significant seasonal signal of the overflow, and only weak interannual variability has been detected [*Dickson and Brown,* 1994*; Jochumsen et al.,* 2012; 2017]. Boluses, large lenses of weakly stratified overflow water that are periodically present in Denmark Strait, have become warmer and saltier over the last 22 years span of data coverage [*Mastropole et al.,* 2017]. With regards to the overflow water, the deepest part of the Denmark Strait trough is nearly all Arctic-Origin Water. To the west, in the vicinity of the Greenland shelfbreak, the overflow water is dominated by Atlantic-Origin Water, but there is also a significant amount of Polar Surface Water and Arctic-Origin Water [*Mastropole et al.,* 2017]. The eastern overflows are partitioned unequally between the two passages (Figure 12). The canonical estimates of overflow flux are 1.9±0.3 Sv and 1 Sv for the FBC and IFR, respectively [*Beaird et al.,* 2013].

Light-to-dense conversion processes occur during the cyclonical circulation in the subpolar gyre, so waters gain density due to cooling and overturns feeding the return lower limb of the MOC [*Sarafanov et al.,* 2012]. Together with the dense overflows from the Nordic Seas and the LSW formed in the Labrador and Irminger Sea [*Yashayaev et al.,* 2007*; de Jong & de Steur,* 2016], they together form the southwards Deep Western Boundary Current (DWBC) and the Deep Labrador Current. The DWBC is relatively stable and there is no evidence of slowdown or acceleration over the past five decades [*Sarafanov et al.,* 2009].

These deep waters are carried far into the southern hemisphere, ventilate the intermediate to deep ocean, and feed among others the formation of Circumpolar Deep Water, thus demonstrating the importance of North Atlantic water masses for the global ocean [*Schmitz,* 1996].

2.3. North Atlantic Oscillation

The North Atlantic Oscillation (NAO) is the dominant mode of climate variability on interannual to decadal timescales over the North Atlantic region. The NAO is a large scale seesaw in the displacement of the masses of atmospheric air in the corridor situated between the subtropical gyre, the high pressure Azores anticyclone, and the subpolar low pressure, situated near Iceland. The NAO index is the normalized Azores-to-Iceland sea level pressure difference (Figure 18) [*Hurrell,* 1995]. A high NAO means a stronger pressure difference over the central North Atlantic and hence enhanced westerly winds across the middle latitudes [*Yashayev et al.,* 2007]. During winter these strengthened winds bring colder, drier air from the North American continent over the warmer ocean, thereby enhancing air-sea temperature differences that lead to an increased flux of heat from the ocean to the atmosphere in subpolar region [*Visbeck et al.,* 2003].

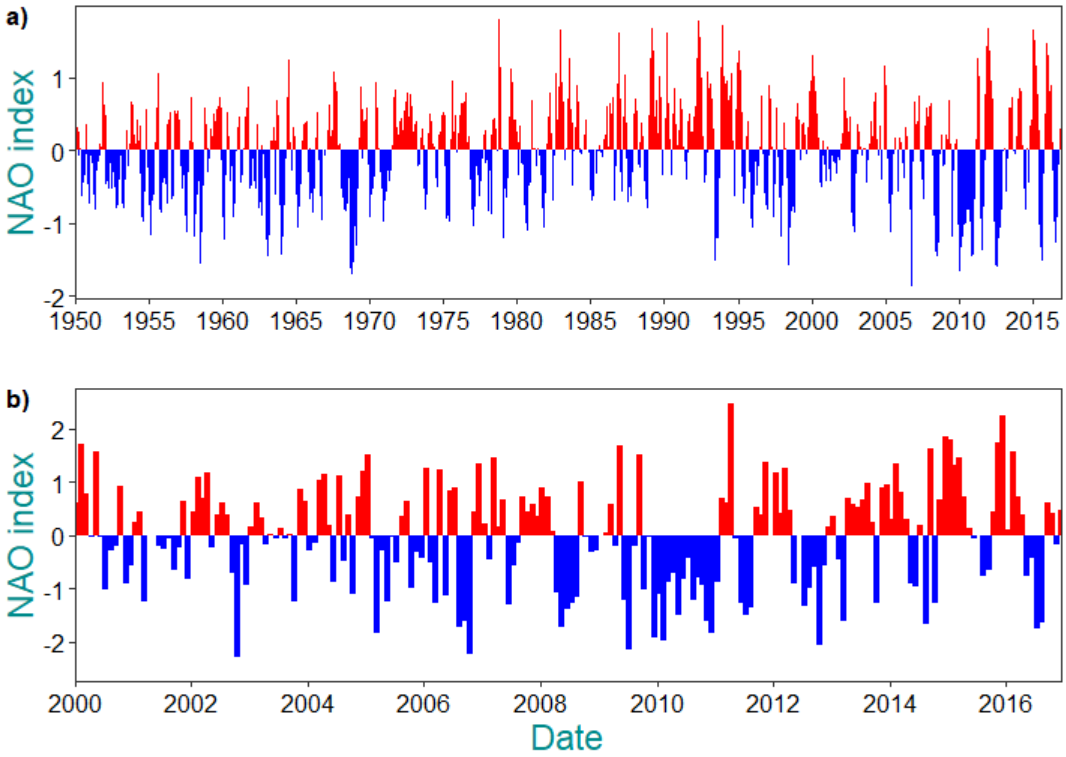

Figure 18. a) three monthly averaged monthly mean NAO index since the year 1950. b) monthly mean NAO index since the year 2000. Positive (negative) NAO phases are represented in red (blue). Both time series ends in December 2016. Source: author elaboration with data from www.cpc.noaa.gov.

This leads to colder, denser water in the upper ocean and enhanced deep water formation processes and convection events [*Delworth et al.,* 2016]. A predominance of high positive values of the NAO index is reflected in periods of cooling and freshening of the Labrador Sea associated with sustained renewal of the intermediate waters in the subpolar North Atlantic [*Yashayev et al.,* 2007]. A positive NAO tends to favor the occurrence of convective overturning in the southwest Irminger Sea, as it does in the Labrador Sea [*Pickart et al.,* 2003]. However, the agreement between convection and the NAO is not perfect for a number of reasons: NAO index has little auto-correlation between months, the ocean has thermal inertia, a strong NAO suppose stronger westerlies over the central North Atlantic, but not always stronger winds over the southwest Irminger Sea or the Labrador Sea [*Yashayev et al.,* 2007].

At decadal time scales, the ocean circulation [*Hakkinen and Rhines,* 2004], the deep water formation [*Dickson et al.,* 1996], the water mass property variability [*Hátún et al.* 2005] and even the timing and abundance of phytoplankton bloom [*Henson et al.,* 2012b] have been observed to show convincing correlations with the NAO.

2.4. Water masses in the subpolar North Atlantic

A water mass is a body of water with a common formation history, having its origin in a particular region of the ocean [*Tomczak,* 1999]. At the time of its formation they retain their thermohaline properties as distinctive features, and can be used as tracers to determine its displacement through the ocean interior. Water masses are physical entities with a measurable volume and therefore occupy a finite volume in the ocean so can be described mathematically by functional relationships between the hydrographic properties and by a set of standard deviations about those relationships [*Tomczak,* 1999]. Localized water mass formation regions act as windows to the deep ocean, as surface waters are transformed to intermediate and deep waters by a complex chain of physical processes, thus introducing characteristics previously imprinted at the surface into the deep ocean [*Kieke & Yashayaev,* 2015]. The water masses mix and interact, so that a given volume of seawater can be composed of several numbers of water masses.

In the North Atlantic Ocean, there are a large number of water masses due to the inputs of intermediate and deep waters formed in marginal seas. The recent published studies of *García-Ibañez et al.,* [2015, 2017] for the water mass distribution along the OVIDE line will be taken as a reference point for the present section. The subpolar gyre plays an important role in the climate system because it is the place where the properties of the water masses constituting the lower limb of the AMOC are set, and also where subtropical waters carried by the NAC are transformed into Subpolar Mode Waters [*Daniault et al.,* 2016].

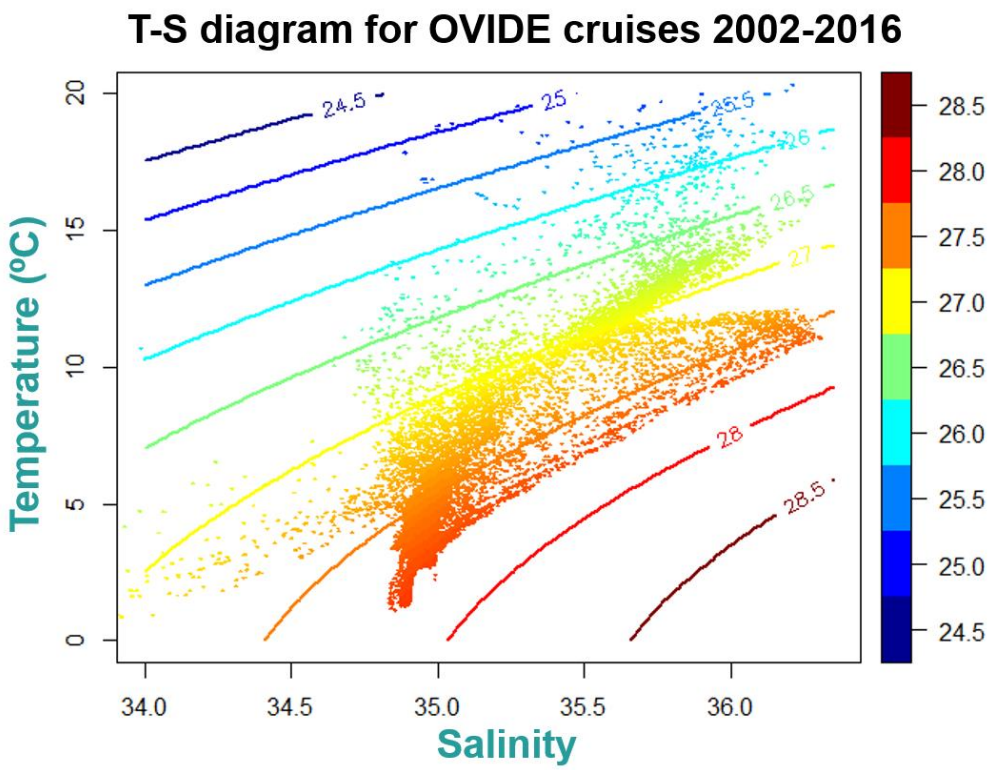

Figure 19. Temperature (ºC) versus salinity diagram for all the OVIDE cruises 2002-2016. Scatter points are colored according to the potential density referenced to 0 dbar.

The saltier waters of the OVIDE section are influenced by the Mediterranean Water (MW) that enters the North Atlantic from the Mediterranean Sea after overflowing the Strait of Gibraltar (Figure 19). The northward flow of MW along the Iberian Peninsula coast is visible in the body of water between 500-2000 m which show high salinity and low oxygen concentration centered at 1200 m depth off the shelf in the West European Basin (Figure 20f). The westward extension may result from meddy transport –intermediate anticyclonic Mediterranean eddies– [*Mazé et al.,* 1997] or may be associated with the Azores countercurrent [*Carracedo et al.,* 2014].

The warmer North Atlantic waters are influenced by the North Atlantic Central Waters (NACW) (Figure 20b). East of the Mid-Atlantic Ridge, the predominant variety of these waters is the East North Atlantic Central Water (ENACW), which is formed by winter convection in the intergyre region [*Pollard et al.,* 1996]. They occupy the upper eastern part of the OVIDE section until the Reykjanes Ridge.

The progressive renewal of the NAC waters during their cyclonic circulation in the Iceland and Irminger basins due air-sea interaction processes it is the origin of the Subpolar Mode Water (SPMW) [*Pollard et al.,* 1996*; Brambilla and Talley,* 2008*; Thierry et al.,* 2008]. SPMWs are surface

water masses with nearly uniform properties, confined between the ocean surface and the permanent pycnocline (Figure 20, c-d). [*Brambilla & Talley,* 2008]. The densest variety of SPMW is the LSW [*Daniault et al.,* 2016].

The intermediate water mass LSW is form by extreme winter heat losses combined with the subpolar gyre circulation mean in the Labrador [*Yashayaev et al.,* 2007] and Irminger Seas [*Pickart et al.,* 2003*; Fröb et al.,* 2016]. LSW shows relatively low salinity, high O_2 and a characteristic low potential vorticity [*García-Ibañez et al.,* 2015]. Formation of LSW is mandatory for ventilating and renewing water layers of the interior ocean [*Kieke & Yashayaev,* 2015]. Recently, there has been a progressive deepening of winter convection in the SPNA since 2012, resulting in the latest LSW pycnostad being the deepest, thickest, and densest LSW layer ever recorded since the period of 1987–1994 [*Yashayaev & Loder,* 2017]. After its formation, LSW fills the Labrador Sea and is advected at intermediate depths, becoming the dominant water mass in the OVIDE section (Figure 20, e) [*García-Ibañez et al.,* 2015].

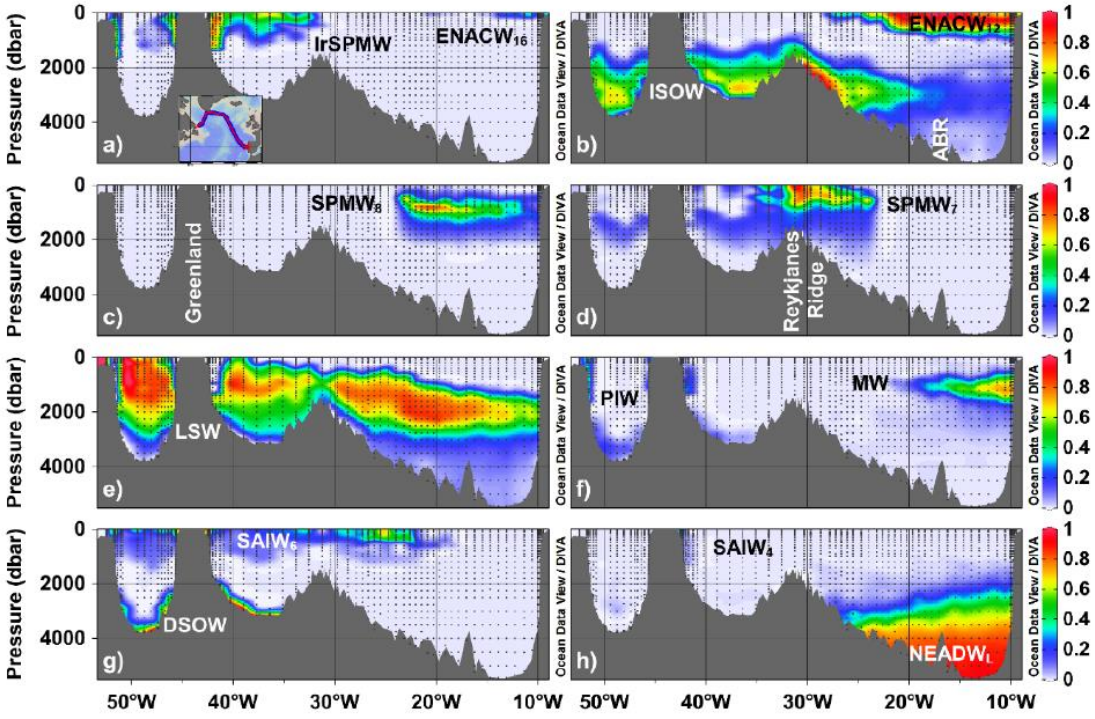

Figure 20. Water mass distribution resulting from the eOMP analysis for the 2014 GEOVIDE cruise (inset in subplot (a)), from Portugal (right) to Canada (left). The water mass contributions are expressed on a per unit basis. Starting from the upper right, Irminger Subpolar Mode Water (IrSPMW), Eastern north Atlantic Central Water of 16ºC ($ENACW_{16}$), Iceland-Scotland Overflow Water (ISOW), Eastern north Atlantic Central Water of 12ºC ($ENACW_{12}$), Subpolar Mode Water of 8 and 7ºC ($SPMW_8$ and $SPMW_7$), Labrador Sea Water (LSW), Polar Intermediate Water (PIW), Mediterranean Water (MW), Denmark Starit Overflow Water (DSOW), Subarctic intermediate Water of 6 and 4ºC ($SAIW_6$ and $SAIW_4$) and lower North East Atlantic Deep Water ($NEADW_L$). Sample locations appear as black dots. The ABR refers to Azores–Biscay Rise. Source: *García-Ibañez et al.,* [2017].

There is another intermediate water mass, the relatively fresh Subarctic Intermediate Water (SAIW), that is present in the upper layer of the Labradror Sea, over the Greenland Slope and in the eastern side of the Reykjanes Ridge [*García-Ibañez et al.,* 2017]. SAIW is formed in the western boundary of the subpolar gyre by mixing between the warm saline waters of the NAC with the cold and fresher LSW, then subducts below the NAC and it is transported to the Iceland Basin where it mixes with SPMWs and Central Waters (Figure 20g) [*Arhan, 1990*].

The Iceland-Scotland Overflow Water (ISOW) and the Denmark Strait Overflow Water (DSOW) are deep overflows from the Nordic Seas. The ISOW is formed during the entrainment of warm saline Atlantic waters by the overflow waters after the sills of the Iceland-Scotland Ridge. The ISOW is found near the bottom on both sides of the ridge below 2000 m. In the Iceland basin, the southward boundary flow of ISOW through the eastern flank of the Reykjanes Ridge partially recirculates northward after cross the ridge by gaps, then the fate of the ISOW northward flow is to recirculate southwestward and join the DWBC in the Irminger Sea (Figure 20b) [*Sarafanov et al.,* 2012].

DSOW forms a cold (θ<2ºC), highly oxygenated and dense (σ>27.8 kg m^{-3}) subsurface water mass in the deep channel in Denmark Strait, but also extends as a bottom layer far onto the Greenland shelf (Figure 20g) [*Jochumsen et al.,* 2017]. DSOW forms after the deep waters of the Nordic Seas overflow the Greenland–Iceland sill and entrain Atlantic waters (SPMW and LSW) [*Yashayaev and Dickson,* 2008]. Downstream of the sill of Denmark Strait, mixing rapidly transforms the properties of the dense DSOW plume [*Jochumsen et al.,* 2015]. Intrusions of low-salinity anomalies occurring in the Deep Western Boundary Current are likely injected from the East Greenland shelf, as dense shelf water cascading events [*Falina et al.,* 2012]. DSOW is denser than ISOW [*Smethie et al.,* 2001].

The different entrainments that suffers ISOW along its journey through the Iceland Basin, lead to the formation of the North East Atlantic Deep Water (NEADW) [*van Aken et al.,* 2000]. NEADW recirculates in the Iberian Basin and mixes with the surrounding waters (Figure 20h), including the deeper Antarctic Bottom Water (AABW) coming from the Southern Ocean.

With exception of the AABW, these deep water masses are precursors of the North Atlantic Deep Water (NADW). The major components are formed in the northern regions of the North Atlantic Ocean: LSW, ISOW, DSOW [*Smethie et al.,* 2001]. NADW is exported from convective regions through the DWBC and complex interior pathways [*Buckey & Marshall,* 2015]. Although deep water formation is proposed as a regulator of the AMOC, the true is that the linkage between deep water formation and MOC variability measured outside of the subpolar basin becomes all the more tenuous [*Lozier et al.,* 2012].

Chapter 3: Anthropocene: the geological imprint of global change

3.1. Anthropocene definition

The consideration of the current geological epoch as 'Anthropocene' (from *anthropos* 'human being' and *kainos* 'new') was first proposed by Paul Crutzen and Eugene Stoermer to emphasize the central role of mankind in geology and ecology [*Crutzen & Stoermer,* 2000]. They suggested that Humanity alters Earth-system behavior modifying natural processes such as biogeochemical cycles, ocean-atmosphere interactions, biological extinctions, and the flux of sediments, affecting long-term global geologic processes. The Anthropocene implies that the Earth is now moving out of its current geological epoch (Holocene) and that human activity is largely responsible for this, i.e., that humankind has become a global geological force by its own [*Steffen et al.,* 2011].

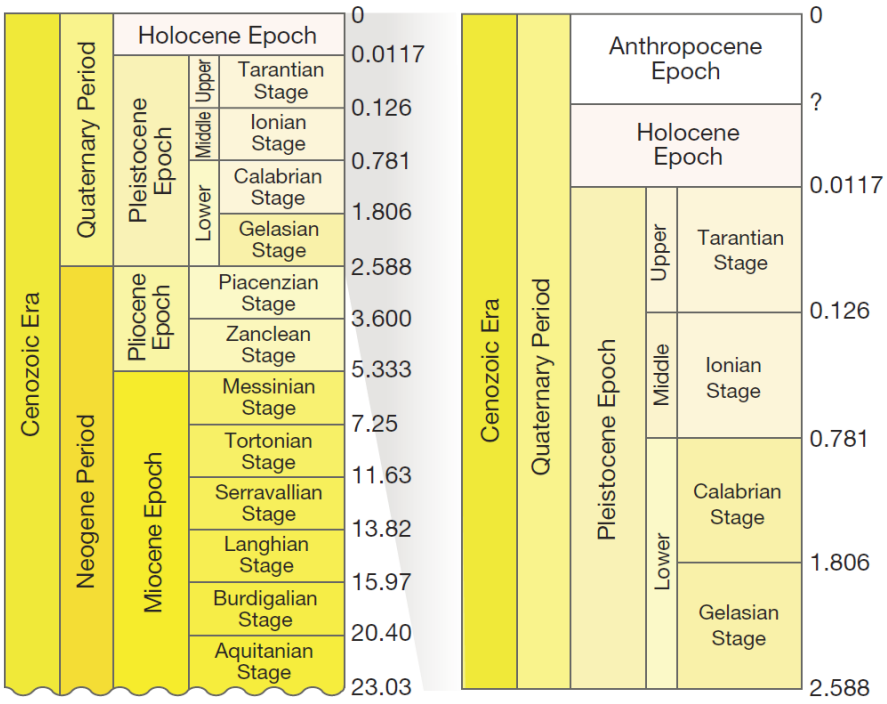

Figure 21. Current Geologic Time Scale [*Gradstein et al.,* 2012] with the proposal Anthropocene epoch included. Boundaries marked in millions of years. Source: *Lewis et al.,* [2015].

There are multiple proposals for the onset of the Anthropocene: (i) an "early Anthropocene" associated with the advent of early agriculture, animal domestication, and forest clearance around 7,000 years ago [*Ruddiman et al.,* 2003, 2013]; (ii) the arrival of Europeans in the Americas in 1492 CE, and the exchange of Old World and New World species associated with the colonization [*Lewis et al.,* 2015]; (iii) the beginning of the Industrial Revolution at ~1800 CE [*Crutzen & Stoermer,* 2000*, Crutzen,* 2002]… Some authors remark the importance of the phase of enhanced population growth, industrialization, and mineral and energy use termed as the "Great Acceleration" [*Steffen et al.,* 2011], while others point the focus in the atomic bombs detonation and the subsequent radiogenic fallout [*Waters et al.,* 2016]. Recent publications appear to favor an onset of the Anthropocene at the mid-20th century, when the worldwide impact of the Industrial Revolution became both global and near-synchronous [*Zalasiewicz et al.,* 2015*; Waters et al.,* 2016*; Zalasiewicz et al.,* 2017]. Setting the boundary at the mid-20th century is consistent with Charles Lyell's approach in defining subdivisions within the Tertiary based on percentage or degree of change rather than simply on presence or absence of change [*Steffen et al.,* 2016].

The Anthropocene Working Group (AWG) of the Subcommission on Quaternary Stratigraphy (SQS) is assessing since 2009 if the Anthropocene could be considered a potential chronostratigraphic/geochronologic unit within the hierarchical level of epoch/series. If the proposal is accepted and becomes a formal part of the Geological Time Scale, we will still live in the Quaternary Period but no longer in the Holocene Epoch, we will live in a new epoch called Anthropocene (Figure 21). Formally, geological time units are defined by their lower boundary, that is, their beginning. There are two types of boundary to define the lower limit of the Anthropocene. In stratigraphy, a Global Standard Stratigraphic Age (GSSA) defines a boundary by its absolute age [*Zalasiewicz et al.,* 2017]. The AWG has proposed a specific moment as GSSA for the beginning of the Anthropocene at the detonation of the Trinity A-bomb at Alamogordo, New Mexico, at 11:29:21 July 16, 1945. [*Zalasiewicz et al.,* 2015]. Rather than a GSSA, the geological community would prefer a Global boundary Stratotype Section and Point (GSSP) [*Finney and Edwards,* 2016]. This kind of GSSP boundary defines a colloquial "golden spike", a single physical manifestation of a change recorded at a particular location in a stratigraphic section [*Lewis et al.,* 2015]. One of the main caveats in Anthropocene onset election it is that a stratigraphic time boundary, however arbitrary, needs to be singular, globally synchronous and commonly understood [*Zalasiewicz et al.,* 2015]. Currently, the AWG has not yet proposed a candidate for GSSP election, but is gaining strength the idea that a ~1950 CE radionuclide signal associated with the "bomb spike" would provide the sharpest and most globally widespread signal [*Zalasiewicz et al.,* 2017].

Nowadays, despite that there are significant evidences of stratigraphically relevance and a criterion to recognize the Anthropocene consistent with those used to define other Quaternary stratigraphic units [*Waters et al.,* 2014*;* 2016*; Zalasiewick et al.,* 2015], neither the International Commission on

Stratigraphy or the International Union of Geological Sciences has officially approved the term. There are authors opposed to the concept, who consider that the recognition of the Anthropocene is a political decision rather than a scientific one [*Finney & Edwards,* 2016]. In summary, to define a new geological time unit, formal criteria must be met and at present, there is no formal agreement in the existence and timing of the Anthropocene.

Independently of a formal recognition or not, the utilization of the concept Anthropocene is growing exponentially since its proposal in the year 2000 (Figure 22) and it is becoming a common term in the debate about distinguishing human effects from natural variability in climate and biogeochemical cycles [*Falkowski et al.,* 2000*; Codispoti et al.,* 2001*; Andersson et al.,* 2006*; Lamborg et al.,* 2014b*; Landolfi et al.,* 2017].

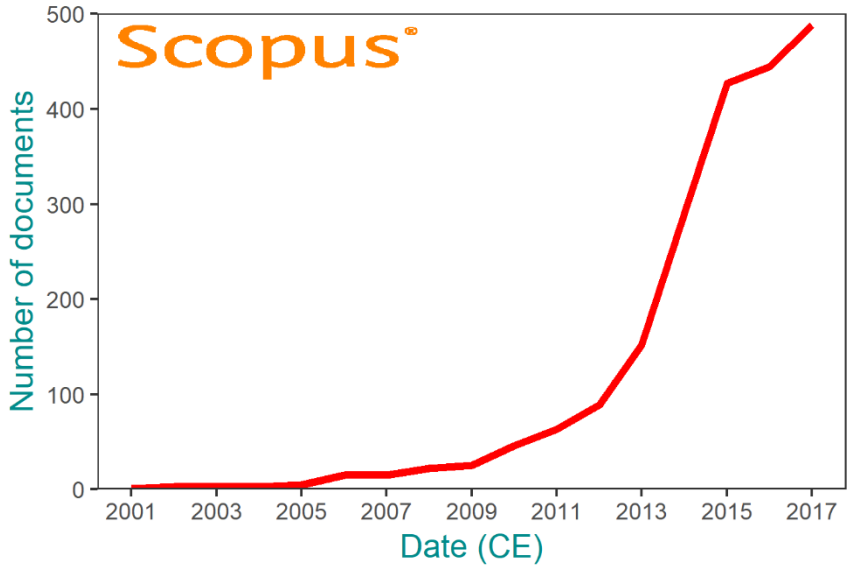

Figure 22. Time evolution of the number of documents in which the term Anthropocene appears in its article title, abstract or keywords since its proposal in the year 2000 until 2017. Source: author elaboration from Scopus® database.

In that current context of debate about the Anthropocene, high-resolution regional studies can provide key information to assess the magnitude, timing and spatial scale at which the human-mediated transformations of the geological record occurred [*Irabien et al.,* 2015]. In summary, humans changed the Earth to such an extent that recent and currently forming geological deposits, like marine sediments, include a signature that is distinguishable from those of the Holocene and earlier epochs.

3.2. Quaternary geochronology for dating the Anthropocene

Marine sediments act as reliable paleoenvironmental archives, but sedimentation rates in deep-sea ecosystems are in general so low that an appropriate detection of the onset of the Anthropocene needs to be associated with a high resolution chronostratigraphy.

The science of dating the time sequence in a geological record is called chronostratigraphy. In the election of an absolute dating technique (geochronometry), two principal criteria that reflect the quality and appropriateness of the technique must be considered: accuracy and precision. Accuracy refers to the degree of correspondence between the true age of a sample and that obtained by the dating process. In other words, it refers to the degree of bias in an age measurement. Precision relates to the statistical uncertainty that is associated with any analysis that is used as a basis for dating [*Walker,* 2005]. There is no dating method without uncertainties and all the techniques have their own distinctive set of advantages/disadvantages [*Noller et al.,* 2000]. As previously noted, in this study we are interested in the quantification of contemporary processes, so the election of the dating technique needs to be able to resolve with at least decennial resolution, the latest centuries

Among the Quaternary dating techniques (Figure 23), the contemporary temporal framework can be effectively dated with methods based on the accumulation of sediment or biological material through time (annual increments) or with some radiometric techniques. Among the group of annual increment's that can be counted, the most known is the dendrochronology, based on the successive growth rings of trees. There are more methods based on accumulations, like for example the annual deposition of sediment layers in lakes (varve chronology) or the formation of layers in glacier ice. Obviously, these techniques are valid only for continental environments. A valid alternative in marine systems is the use of the biological growth structures from corals or mollusks. Although this are real alternatives, they are not valid for evaluate deep-sea chronology, so nowadays the use of radiometric techniques is the main approach to obtain the absolute age of marine sediments.

Following Figure 23, the unique radiometric dating method that allows a continuous evaluation from present times through a century back it is based on ^{210}Pb. It is the technique selected in this study to assess the chronological characterization of deep-sea sediments, and the methodology it is going to be described in details below and in the Part IV: Sedimentation rates and carbon fluxes.

Figure 23. Temporal ranges for different dating techniques. Framed in red is the ^{210}Pb method chosen here for Anthropocene detection in marine sediments. Source: *Walker,* [2005].

3.2.1. Radiometric dating

The basis of the radiometric techniques relies at the knowledge of nuclear atomic processes. An atom is the smallest particle still characterizing a chemical element [*IUPAC,* 2014]. It consists of a positive charged nucleus which contain protons and neutrons and represent almost all its mass (more than 99.9%), and negative charged electrons spinning around the nucleus. Atoms of the same element with the same number of protons but different numbers of neutrons are referred to as isotopes. Individual isotopes of an element are referred to as nuclides [*Walker,* 2005]

Radiometric techniques are based on the fact that certain nuclides are radioactive (radionuclides) so they are unstable and undergo spontaneous nuclear transformations in order to achieve more stable atomic forms [*IUPAC,* 2014]. The three most commons types of radioactive decay are alpha (α), beta (β) and gamma-ray (γ-ray) decay [*Loveland et al.,* 2005]. This process is time-dependent, and leads to the production of a "daughter" nuclide by the disintegration of a "parent" nuclide [*Noller et al.,* 2000]. The half-life concept is fundamental to all forms of radiometric dating. For a single radioactive decay process, the half-life ($T_{1/2}$) of a radionuclide is the time required for the activity to decrease to half its value [*IUPAC,* 2014]. In all radioactive nuclides, the decay is not linear but exponential (Figure 24).

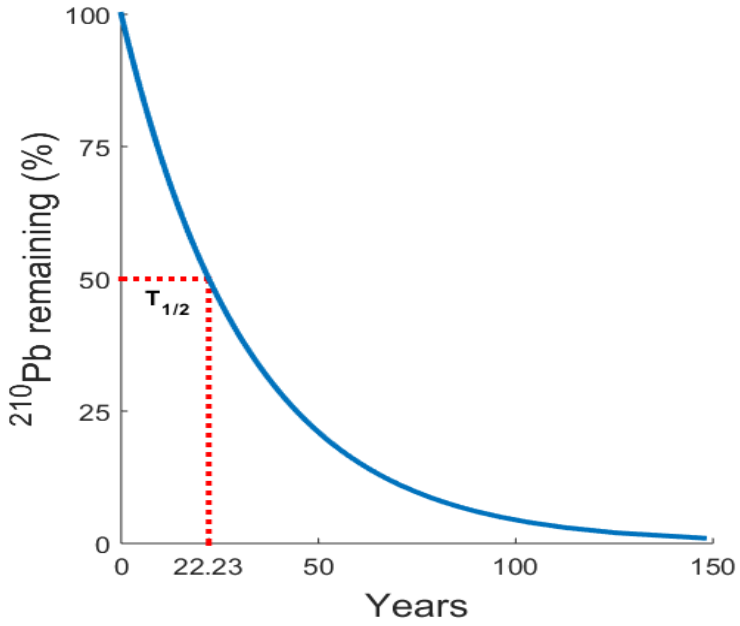

Figure 24. Radioactive decay of ^{210}Pb. Source: author elaboration.

As the radioactive decay proceeds at a specific rate, a geochronology (*t* in Equation 1) can be established by measuring the ratio of daughter (D) to parent (P) atoms. The disintegration constant of an isotope (λ), defined as the probability that a nuclei will decay per unit of time, is equals to $\lambda=\ln(2)/T_{1/2}$.

$$t = \frac{1}{\lambda}\ln\left(1 + \frac{D}{P}\right) \qquad \text{(Equation 1)}$$

The idealized isotope for radiometric dating is easy to measure, have a chemistry and a half-life well known and the initial amount of the isotope in the sample to be dated is known or can be estimated [*Gregory et al.,* 2011]. There are also assumptions in the standard radiometric methods, the most important being that radioactive isotopes are incorporated in the sample at the time of formation and no loss or gain of isotopes occurs except through decay [*Noller et al.,* 2000]. The last requisite, no less important, is that the isotope have an appropriate half-life for the scale of time investigated.

The objective of the radiochronology is the reconstruction of past events. Radionuclides can be used to obtain sediment geochronologies and accumulation rates. By far, the most known radiometric dating method involves the decay of ^{14}C (half-life 5730 years), but there are other methods based on long-lived (^{40}K/^{40}Ar, ^{39}Ar/^{40}Ar, Uranium-series, cosmogenic nuclides…) or short-lived radionuclides (^{210}Pb, ^{137}Cs, ^{32}Si, ^{7}Be).

3.2.1.1 Short-lived isotopes and marine sedimentation rates

In Quaternary chronology, short lived isotopes are those with half-lives in the order of decennial of years, like the natural radionuclide ^{210}Pb ($T_{1/2}$ ~22 years). The half-life of a radionuclide will condition the temporal range of processes than can be resolved by radiometric dating [*Geyh & Schleicher,* 1990]. Among the radioisotopes with shorter half-lives that can be used to date very recent events, ^{210}Pb is a suitable one for dating young sediments.

Marine sedimentation is the process of accumulating sediments in the form of layers at the seabed [*Seibold & Berger,* 2017]. Includes all the events that take place since particle formation and transport to the final deposition and preservation of the sedimentary particles [*Mulder et al.,* 2011]. As a general rule, sedimentation rates are typically almost ten times smaller in the deep-sea than on continental margins [*Seibold & Berger,* 2017], but there are great heterogeneity and sediment accumulation rates are inherently time-variant [*Sommerfield et al.,* 2006]. The main deep-sea sedimentary processes are the settling of pelagic biogenic particles through the water column (pelagic environment), the alongslope flow of bottom currents (Contourite Depositional Systems), and the downslope density currents with predominance of terrigenous sediments (deep-sea fans, slope aprons and wedges) [*Rebesco et al.,* 2014]. The rates of sedimentation in deep-sea sediments from studies of long length cores vary from values of 1-5 mm·kyr^{-1} [*Keen,* 1968] to sedimentation rates on sediment drifts of 5–20 cm kyr^{-1} [*McCave & Hall,* 2006]. Marine pelagic sedimentation rate depends on the intensity of primary production and biological processes, the quantity and quality of sediment settled onto the seabed, the depth of the seabed and its geological composition, along with hydrological and hydrodynamic effects.

The composition of marine pelagic sedimentary deposits depends mainly on three factors: biological productivity, preservation and dilution. Biogenic pelagic particles are affected by differential preservation processes according if they are calcareous or siliceous. $CaCO_3$ is more soluble with depth. The depth at which dissolution impacts become noticeable is termed the lysocline; and the depth at which the dissolution flux balances the rain flux of calcite to the sediments is known as the calcite compensation depth (CCD) [*Zeebe,* 2012]. No net accumulation of carbonate is possible below the CCD. Then, the formation of a calcareous sedimentary deposit it is limited to sea beds located above the CCD. The depth of the CCD is heterogeneous at global scale, with a current global mean of 4,800 m [*Tyrrel & Zeebe,* 2004], being deeper in the North Atlantic –more than 5,000 m [*Biscaye et al.,* 1976]– where relatively young water masses fill the deep ocean with waters whose carbon content does not favor the dissolution [*Jiang et al.,* 2015]. In pelagic zones, roughly one half of the deep-sea sediments are formed by calcareous ooze (biogenic sediments), largely shell material from coccolithophores and foraminifers [*Seibold & Berger,* 2017]. In contrast to carbonates, siliceous particles dissolve more easily in shallow waters. A siliceous sedimentary deposit, composed of biogenic silica, appears where surface plankton

productivity is high (important upwelling areas) and the seafloor lies below the CCD. The dilution factor refers to the relative abundance of material with pelagic, or marine-produced, origin versus a terrigenous, or land-derived, origin. The carbonate content in pelagic sediments is inversely related to dilution with terrigenous material [*Hays and Perruzza,* 1972], so the proportion of terrigenous have to be scarce to consider a sedimentary deposit as pelagic. In fact, the inorganic type of pelagic deposit (red clay or pelagic clay) is only formed below the CCD and in absence of biogenic siliceous inputs as the combination of all the insoluble residuals. Red clay sediments show one of the slowest sedimentation rates in the global ocean [*Seibold & Berger,* 2017].

The subpolar North Atlantic is a region characterized by a high occurrence of large sediment drifts deposits in the basins [*Rebesco et al.,* 2014]. In sediment drifts or contourite depositional systems, sedimentation rates can be exceptionally over 100 cm kyr^{-1} [*McCave & Hall,* 2006]. Contourite drifts are open ocean sedimentary bodies produced by the accumulation of sediment under the control of bottom currents [*Rebesco et al.,* 2016]. Contourite drifts are characterized by high lateral continuity, few hiatuses (periods of non-deposition or erosion that creates a gap in the amount of time and space preserved in a sediment sequence), and sedimentation rates higher than the average pelagic sedimentation [*Rebesco et al.,* 2014].

The use of ^{210}Pb as geochronometer for sediment accumulation has becomes the habitual technique for determining accumulation rates in coastal sediments [*Cochran & Masqué* 2004], but only few studies had used it in deep-sea sediments [*Orellana et al.,* 2008*; Lepore et al.,* 2009*; Jonkers et al.,* 2010a*; Moffa-Sánchez et al.,* 2014*; Chong et al.,* 2016]. The combination of a high-resolution chronology suitable to date superficial sediments, and the existence of sediment deposits in our area of study, the subpolar North Atlantic, with potentially high sedimentation rates can give us an insight in modern day deep-sea sedimentation processes and rates.

Chapter 4: Thesis objectives

Anthropogenic emissions of CO_2 are the main agents behind the unequivocal global change [*IPCC,* 2014]. Currently, 25-30% of that emissions had been absorbed by the ocean [*Sabine et al.,* 2004*; Khatiwala et al.,* 2013], changing the chemistry of the ocean [*Doney et al.,* 2009], but how long will the ocean act as sink? It is the natural carbon cycle in steady state? A robust assessment of the status of the carbon cycle is necessary to discern the anthropogenic perturbation from the natural variability of the biogeochemical carbon cycle.

The present doctoral dissertation was developed in the framework of the project BOCATS, Biennial Observation of Carbon, Acidification, Transport and Sedimentation in the North Atlantic (CTM2013-41048-P). The main objectives of BOCATS were the continuation of the biannual monitoring of the circulation and carbon cycle in the subpolar North Atlantic along the OVIDE section, and the evaluation of the variability of the subpolar gyre carbon cycle in its two components (natural and anthropogenic) including for the first time the interaction between sediments and water column.

The main objective of this thesis is to evaluate the carbon cycle in the subpolar North Atlantic under an integrated approach, taking advantage of the existence of a relatively long-term series (2002-2016) of high-quality observations for the water column. Furthermore, new Anthropogenic dated cores obtained under a novelty approach in the framework of this thesis can give a complementary insight into the most unconstrained flux in the ocean carbon cycle: the quantity incorporated into the deep-sea sediments.

The main objective is divided in the following specific objectives, that are fully developed during the chapters of this dissertation:

1- Evaluation of the budget of DOC in the subpolar gyre, and the quantititative assessment of its role in the total carbon cycle mediated by the AMOC (PART II. Dissolved organic carbon).
2- Evaluate the total budget of carbon (organic and inorganic) in the subpolar North Atlantic water column for the time framework 2002-2016 following an integrated approach that combines high-quality transports of carbon variables (DIC and alkalinity), nutrients (nitrate, phosphate and silicate) and oxygen under an inverse model optimization method (PART III. Biogeochemical budget).

3- Quantitative assessment of the amount of carbon incorporated in the sediments of our region of study since the onset of the Anthropocene (PART IV. Sedimentation rates and carbon fluxes).

This dissertation is part of the BOCATS project and directly contributes to accomplish the BOCATS synthesis objective: to elaborate a total budget of the carbon cycle in the subpolar gyre including, for the first time, all its components.

PART II. Dissolved organic carbon

Chapter 5: Dissolved organic carbon: the role of the North Atlantic Meridional Overturning circulation.

5.1. Introduction

5.1.1. Dissolved organic matter: introduction

Dissolved organic matter (DOM) is a complex mixture of uncharacterized reduced carbon molecules bound to heteroatoms such as oxygen, nitrogen, phosphorus, and sulfur [*Hansell,* 2013]. In the size-reactivity continuum of organic matter in the ocean [*Benner & Amon,* 2015], DOM it is operationally defined as the organic matter that passes through glass fiber filters with a nominal pore size of 0.7 μm. In the oceanographic community, reliable quantification of DOM was not reached until the beginning of the XXIth century with the development of suitable analytical techniques and the use of reference materials for intercalibration exercises [*Sharp et al.,* 2002]. DOM is mostly produced autochthonously in the surface ocean as part of primary production and subsequent food web interactions [*Martínez-Pérez et al.,* 2017]. DOM acts as a link between production and decay of organic matter in the water column [*Dittmar & Paeng,* 2009], with photosynthesis as the main source, and heterotrophic mineralization as the dominant sink. DOM plays a key role in multiple marine biogeochemical processes and in carbon storage on scales of several thousand years [*Medeiros et al.,* 2016].

As we consider the cycling of carbon through DOM, it is conceptually useful to isolate the carbon component of DOM, i.e., Dissolved Organic Carbon (DOC) [*Hansell et al.,* 2001]. DOC is the largest pool of organic matter in the ocean [*Hansell & Carlson,* 2015], it is produced in the euphotic zone by biological activity and can be exported, i.e. moved to the deep ocean, by physical processes where it is remineralized. Production of DOC is influenced by the composition of the plankton community [*Carlson & Ducklow,* 1995], and represents the fate of up to 50% of primary production [*Nagata,* 2008]. The majority of produced DOC is rapidly assimilated by the microbial community and only a small fraction resists or escapes rapid mineralization [*Hansell et al.,* 2015], it is this uncoupling between biological production and removal processes what represents the net production of DOC [*Hansell & Carlson,* 1998], fundamentally controlled by the input of new nutrients to the euphotic zone [*Romera-Castillo et al.,* 2016].

Closely conditioned by the few and inadequate measurements in the deep ocean it was the old idea that the DOC in the deep ocean was uniformly distributed and hence largely refractory to biological decay [*Martin & Fitzwater,* 1992]. This conception of the conservative nature of deep ocean DOC was challenged by *Hansell & Carlson,* [1998], revealing dynamic fractions in the DOC pool even in the deepest ocean, operating on time scales unable to be assessed with traditional incubation assays [*Hansell et al.,* 2009].

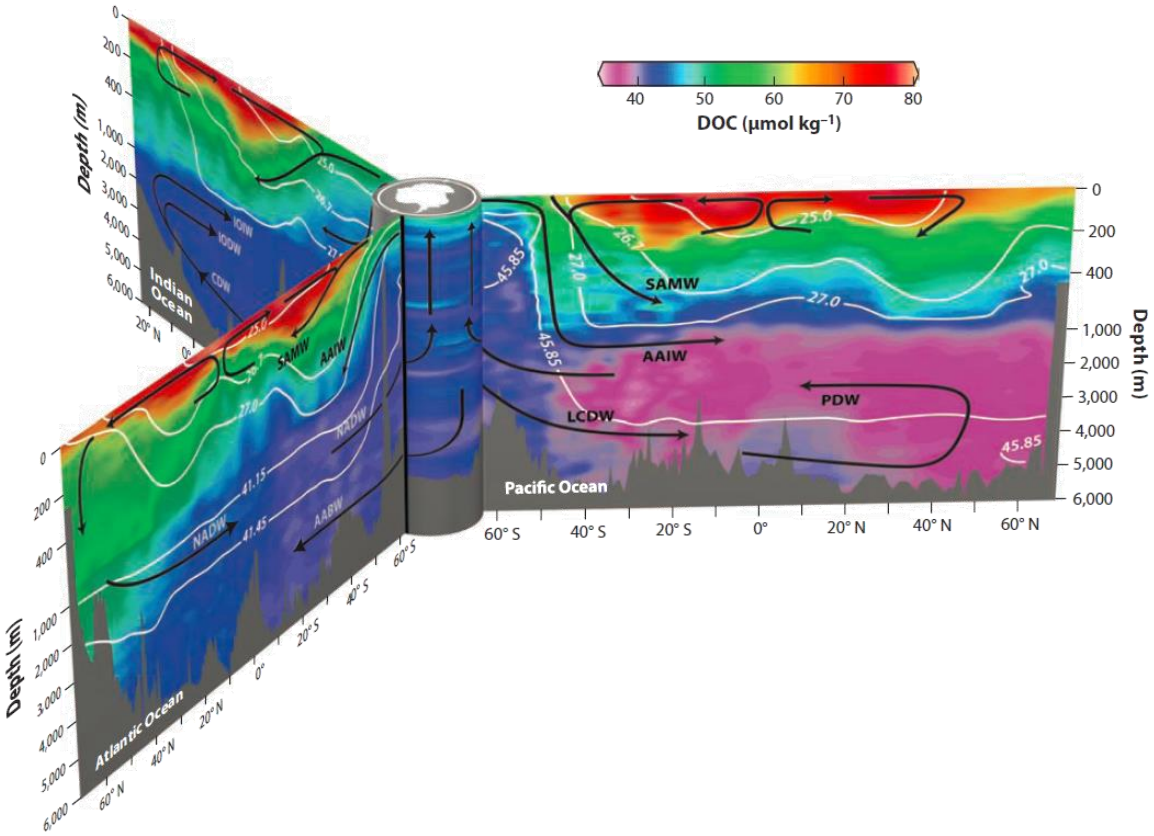

Figure 25. Vertical distributions of DOC (in µmol C kg^{-1}) in the central Atlantic, central Pacific, and eastern Indian Oceans, connected via the Antarctic circumpolar currents. Black arrows represents circulation; and white lines are isopycnal surfaces. Abbreviations: AABW, Antarctic Bottom Water; AAIW, Antarctic Intermediate Water; CDW, Circumpolar Deep Water; IODW, Indian Ocean Deep Water; IOIW, Indian Ocean Intermediate Water; LCDW, Lower Circumpolar Deep Water; NADW, North Atlantic Deep Water; PDW, Pacific Deep Water; SAMW, Subantarctic Mode Water. Source: *Hansell et al.,* [2013].

DOC concentrations in open ocean surface waters ranges between the high values of 70–80 µmol C kg^{-1} in tropical and subtropical systems to 40–50 µmol C kg^{-1} in subpolar seas [*Hansell et al.,* 2009]. Concentrations are controlled by primary production and vertical mixing processes [*Doval &*

Hansell, 2000]. The existence of vertical stratification in the upper layers of tropical and subtropical biomes favors the accumulation of DOC resistant to biological degradation [*Hansell et al.,* 2009], and hence the higher concentrations. In the subpolar seas, ventilation processes prevent the accumulation of DOC, and surface concentrations are lower [*Carlson et al.,* 2010].

Ocean interior distributions also shows variability (Figure 25). Northern latitude ocean basins, like the central Arctic Ocean, the Nordic Seas or the subpolar North Atlantic shows characteristics DOC concentrations higher than the global average [*Amon et al.,* 2003*; Amon & Benner,* 2003]. The no existence of the usual vertical gradient of DOC, with concentrations decreasing with depth, at latitudes northern than 35ºN is indicative of recent ventilation and water column renewal [*Carlson et al.,* 2010]. The changes in DOC concentration follows the deep path of the global overturning circulation, with lowest concentrations in the deep North Pacific (Figure 25), and with the northward transport of Antarctic Bottom Water (AABW) introducing low DOC in the deep North Atlantic appreciable at latitudes as far as 40ºN (Figure 30). The close relationship between ocean circulation and export processes it is going to be extended in the next sections.

5.1.2. DOC fractions based on reactivity

Same as happened with the size separation criteria to discriminate between dissolved and particulate organic matter, the classification of DOC fractions based on reactivities is operationally defined in the continuum reactivity spectrum to characterize portions of the bulk DOC with biogeochemical relevance [*Benner & Amon,* 2015]. Following the classification based on reactivity, understand as the susceptibility of a DOC fraction to being removed, proposed by *Hansell,* [2013], five different fractions are defined in function of its lability: labile (LDOC), semi-labile (SLDOC), semi-refractory (SRDOC), refractory (RDOC), and ultra-refractory (URDOC). The different characteristics between the fractions is such that between the LDOC and the URDOC there are more than seven orders of magnitude in lifetime, from hours to thousands of years [*Hansell,* 2013].

The fractions with relevance in the biological pump and that contribute to transport and export of carbon are SLDOC and SRDOC [*Hansell & Carlson,* 1998]. SLDOC is quantitatively the most important fraction in the contribution of DOC to the biological pump [*Hansell,* 2013], but it plays only a minor role in long-term carbon sequestration because the majority of this exported DOC is remineralized within the upper mesopelagic zone (100-500 m) [*Carlson and Hansell,* 2014]. The SRDOC fraction turns over on times scales of decades and is significantly important in the exportation mediated by the AMOC [*Carlson et al.,* 2011]. Contrary to what happened with the SLDOC fraction, the SRDOC have a minor contribution in the vertical export but a large proportion is remineralized below the permanent pycnocline, being long-term sequestered [*Carlson and Hansell,* 2014].

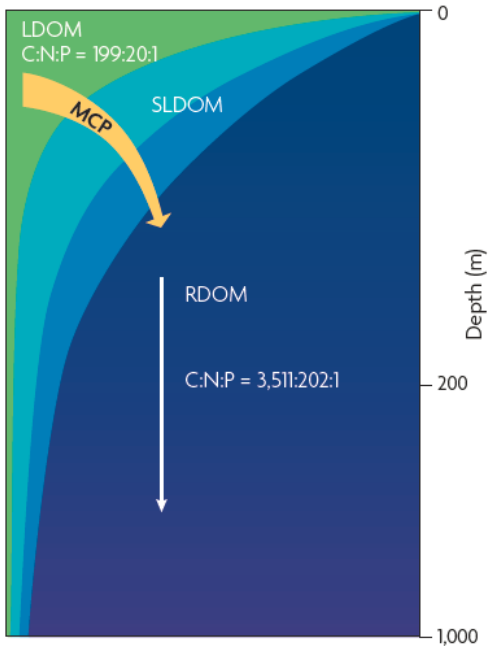

Figure 26. Schematization of the transformation of labile (LDOM) and semi.labile (SLDOM) into refractory dissolved organic matter (RDOM) mediated via the successive –and maybe repetitive- heterotrophic processing by the microbial carbon pump (MCP). The MCP increase the RDOM pool at the same time that alters the chemical composition of DOM, resulting in an increase in the stoichiometric ratios. Source: *Jiao et al.,* [2010].

In contrast to the labile fractions, the more refractory fractions (RDOC and the least understood URDOC), are present at all depths throughout the ocean [*Bauer et al.,* 1992] with mean concentrations of around ~40 μmol kg^{-1}. They constitute the great majority of DOC in the ocean (>95%), and with an average lifetime of 6000 years [*Druffel et al.,* 1992] they survive multiple meridional overturning cycles [*Bercovici & Hansell,* 2016]. The microbial carbon pump [*Jiao et al.,* 2010], transforms organic matter from the labile and semi-labile fractions to the refractory fraction via heterotrophic microbial processes (Figure 26).

With regard to pool size, the total inventory of 662 Pg-C is distributed between ~6±2 Pg-C of the labile and semi-labile fractions, 14±2 Pg-C of the semirefractory and ~642±32 Pg-C for the most refractory fractions.

5.1.3. DOC in the ocean carbon budget

The cycling of DOC with different reactivities along the global overturning circulation impacts significantly the ocean carbon cycle. DOC export and its consumption in deep waters have implications for the removal of DIC from the surface and the subsequent air-sea CO_2 interactions.

DOC accumulated in the surface ocean is redistributed by wind-driven circulation, and eventually exported to depth by overturning circulation [*Hansell et al.,* 2009*; Carlson et al.,* 2010], deep convection events [*Copin-Montégut & Avril,* 1993*; Carlson et al.,* 1994*; Tian et al.,* 2004] or subduction in the subtropical gyres [*Hansell & Carlson,* 2001*; Hansell et al.,* 2012].

In the North Atlantic, DOC produced and accumulated at the surface layer in tropical and subtropical biomes is transported northward by the NAC [*Walsh et al.,* 1992]. At higher latitudes the relatively fast downward transport of DOC with the AMOC fills the deep ocean with non-refractory DOC (mean concentrations around 50 μmol kg^{-1}), contributing to carbon sequestration during NADW formation. DOC is exported into the ocean interior in regions where deep isopycnal layers are ventilated [*Copin-Montégut & Avril,* 1993; *Doval & Hansell,* 2000], like the subpolar North Atlantic or the Nordic Seas. The injection of relatively labile DOC at the sites of deep water formation and its microbial remineralization at depth supposes that in a single global cycle of overturning circulation, the deep ocean DOC decreases from 50 μmol-C kg^{-1} to 34 μmol-C kg^{-1} [*Hansell & Carlson,* 1998*; Hansell et al.,* 2009].

In the global ocean only ~200 Tg-C yr^{-1} of the total exported DOC (1.8 Pg-C yr^{-1}) are not remineralized at depths > 500 m [*Hansell et al.,* 2009]. Of those, the whole Atlantic represents near the 50% with ~86 Tg-C yr^{-1} [*Hansell et al.,* 2009] mainly taking place in the interior of the North Atlantic, 81 Tg-C yr^{-1} [*Carlson et al.,* 2010]. In the next chapter we are going to evaluate the quantitative role of the AMOC in DOC exportation in the North Atlantic.

5.1.4. DOC in the AMOC

The Atlantic Meridional Overturning Circulation (AMOC) plays an active role in the cycling and storage of chemical species in the ocean because it is an entrance portal for chemical tracers into the deep ocean due to water mass formation processes [*Broecker,* 1991*; Kuhlbrodt et al.,* 2007]. In the North Atlantic, warm northward flowing surface waters cool and gain density due to strong air-sea interactions; they eventually sink, feeding the southward flowing lower limb of the AMOC [*Sarafanov et al.,* 2012*; Srokosz & Bryden,* 2015]. In the eastern subpolar North Atlantic (eSPNA), properties like dissolved inorganic carbon –DIC- [*Keeling & Peng,* 1995*; Gruber et al.,* 2009*; Takahashi et al.,* 2009*; Zunino et al.,* 2015], anthropogenic CO2 –C_{ant}– [*Sabine et al.,* 2004*; Pérez et al.,* 2013*; Zunino et al.,* 2014], trace metals like mercury [*Lamborg et al.,* 2014a], and dissolved organic carbon –DOC– [*Hansell et al.,* 2009] are transported to deeper layers as a result of water mass formation.

Oceanic DOC accumulated in the euphotic zone is redistributed horizontally by wind-driven surface circulation, then exported by (i) subduction in the subtropical gyres [*Hansell & Carlson* 2001; 2015*; Hansell et al.,* 2012], (ii) deep convection [*Copin-Montégut & Avril,* 1993*; Carlson et al.,* 1994*; Tian*

et al., 2004] or (iii) overturning circulation at high latitudes [*Hansell et al.,* 2009*; Carlson et al.,* 2010]. DOC export and its consumption in deep waters have implications for the removal of DIC from the surface, thus modifying air-sea CO_2 exchanges. *Hansell et al.* [2009] estimated a DOC export in the whole Atlantic (72ºS–63ºN) via water formation of 0.086 Pg-C·yr^{-1}, while *Carlson et al.* [2010] estimated it as 0.081 Pg-C·yr^{-1} for the North Atlantic (65ºN–9ºN).

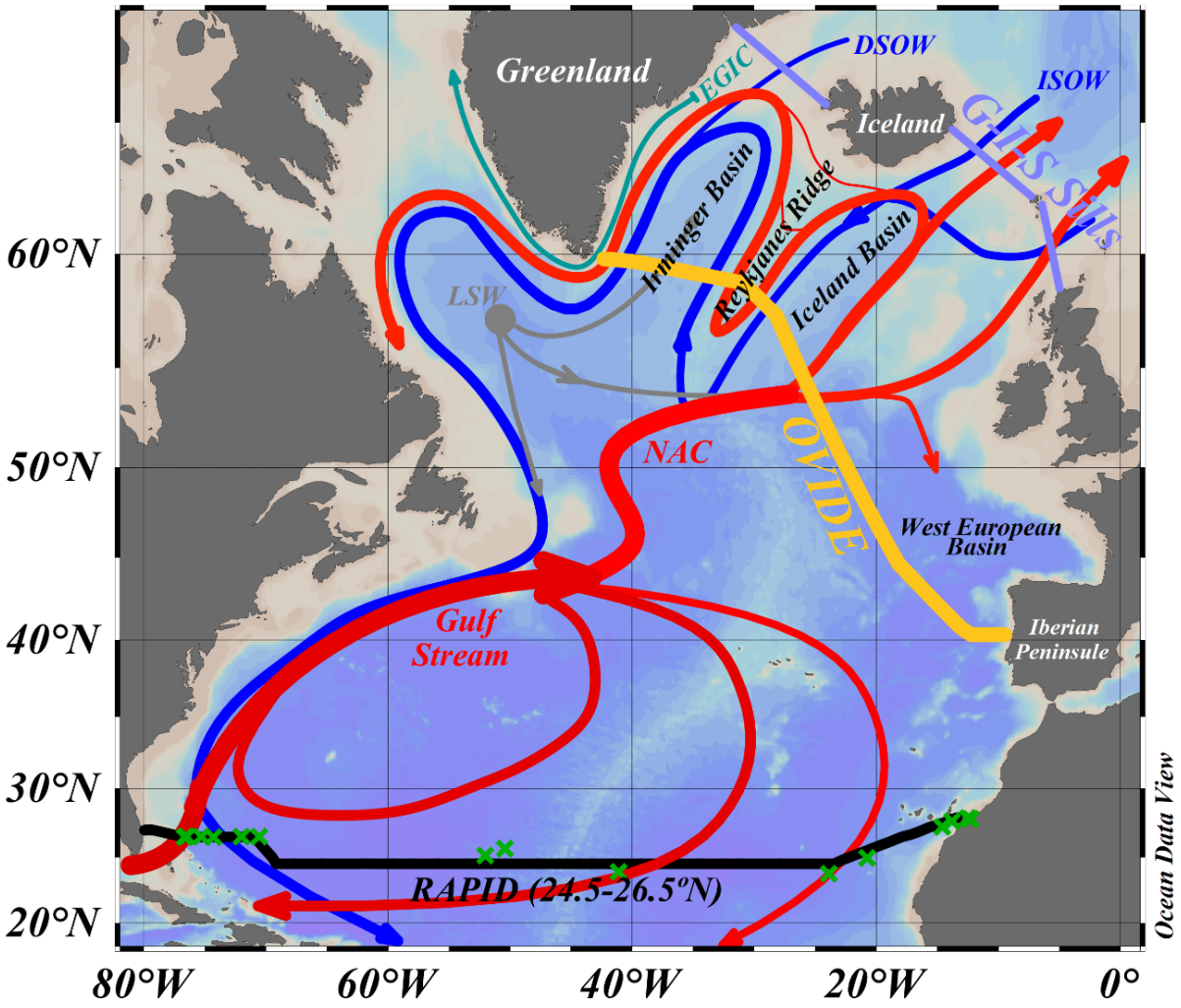

Figure 27. Map of the subpolar North Atlantic circulation with major topographical features included. Section tracks of the OVIDE (yellow thick line) and 24ºN (black thick line) cruises are indicated. The approximate location of the RAPID mooring array is represented with green crosses. The eSPNA domain is comprehended between the OVIDE section and the Greenland-Iceland-Scotland (G-I-S) sills (purple line). Abbreviations for the main currents and water masses are as follows: DSOW = Denmark Strait Overflow Water, ISOW = Iceland-Scotland Overflow Water, LSW = Labrador Sea Water, EGIC = East Greenland Irminger Current, NAC = North Atlantic Current. Schematic diagram of the large-scale circulation compiled from *Sarafanov et al.,* [2012]*; Lherminier et al.,* [2010]*, García-Ibañez et al.,* [2015]*; Schmitz & McCartney,* [1993].

5.2. Methods

We use an extended Optimum Multiparameter (eOMP) analysis as an objective tool to characterize the water mass DOC concentrations ([DOC]) along the OVIDE section (Figure 27). The OVIDE section crosses the main currents of the eastern-SPNA gyre and some regions where water mass formation takes place. Water mass characterization allows us to estimate DOC's horizontal transports across the section between 2002 and 2012 and their variability, even though DOC measurements were only performed in 2002 [*Álvarez-Salgado et al.,* 2013]. Estimating carbon fluxes within water masses characterized for carbon content allows an assessment of the significance of the AMOC in carbon export and the impact of its variability in the marine carbon cycle. The main objectives of the present chapter are (i) to estimate the DOC transport and budget in the eSPNA, and (ii) to disentangle the role of the AMOC in the DOC cycle.

5.2.1. OVIDE sampling program

The OVIDE section, a high-resolution hydrographic survey from Portugal to Greenland, has been repeated biennially during spring-summer since 2002 (Figure 27) (Project OVIDE). In all cruises, high-quality measurements of standard tracers such as temperature, salinity (S), oxygen (O_2) and nutrients were performed. Additionally, in 2002 (19 June–11 July), 30 stations were sampled for DOC (around 340 samples), and measured using a Shimadzu TOC5000 analyzer with a measurement error of ±0.7 µmol·kg^{-1} (Figure 28) [*Álvarez-Salgado et al.,* 2013]. Samples for DOC (10 mL) were taken directly from the Niskin bottles without filtering process. The probability for particulate organic carbon inclusion in the samples is low, even lowering with increasing sampling depth, and below 1000 m there is no difference between filtered and unfiltered samples at the µmol·kg^{-1} resolution [*Hansell & Carlson,* 2001]. Therefore, we can assume that the total organic carbon (TOC) measured belongs to the DOC reservoir. The accuracy was tested with certified reference materials (CRM) provided by D.A. Hansell (University of Miami). Cruise data are available from the CCHDO (CLIVAR & Carbon Hydrographic Data Office) webpage.

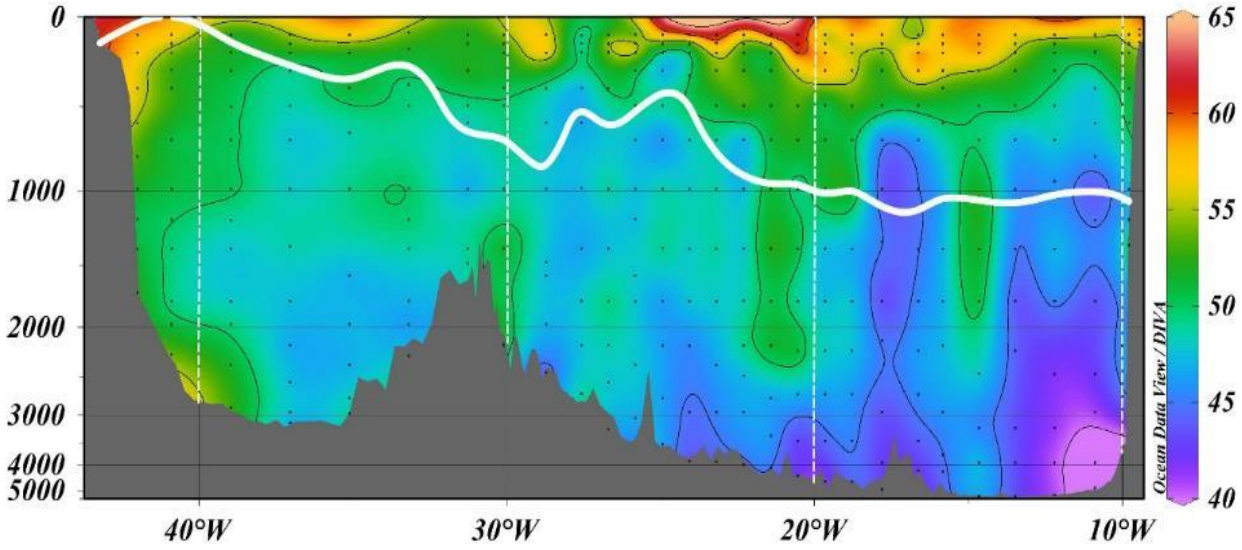

Figure 28. DOC distribution along OVIDE section. Dissolved organic carbon (DOC, in $\mu mol \cdot kg^{-1}$) vertical distribution along the OVIDE 2002 section from Greenland (left) to the Iberian Peninsula (right). Sampling points are indicated. Isopycnal σ_{AMOC}=32.14 (potential density referred to 1000 dbar, solid white line) separating the upper and lower limbs of AMOC is also shown. Note that the depth scale is not linear.

5.2.2. DOC water mass definitions by eOMP analysis

Here we use the eOMP analysis to infer the [DOC] along the OVIDE section for cruises when it was not measured. The eOMP has been successfully used in previous studies with similar needs for solving water mass mixing [*Vázquez-Rodríguez et al.,* 2012*; Pardo et al.,* 2012*; García-Ibañez et al.,* 2015]. The main difference between classical (cOMP) [*Tomczak,* 1981] and eOMP analyses is that the latter includes both conservative and non-conservative variables. We first define the [DOC] of the water masses of the region. To do so, we used DOC data from the 2002 cruise – $\left[DOC\right]^{2002}$ – (Figure 28) and the water mass structure of the 2002 cruise resulting from the eOMP analysis conducted by *García-Ibáñez et al.* [2015] where the distribution of 12 source water types (SWTs) are described. OMP analyses are based on the premise that the water mass fractions that constitute a sample can be reproduced by an appropriate mixture of some well-known end-member water types. The eOMP analysis quantifies the proportions of the mixtures of the SWTs that contribute to a given water sample [*Karstensen & Tomczak,* 1998*; Tomczak & Large,* 1989]. The SWTs were characterized by potential temperature (Θ), S, preformed O_2 and nutrients. The water mass fractions (X_i) were solved by minimizing the residuals of the linear mixing equations in a non-negative least-square sense, where mass is stringently conserved and the contributions of the SWTs must be positive. Each equation of the system is weighted in relation to the accuracy of the measured property. The eOMP analysis was restricted to pressure ≥100 dbar to avoid the non-

conservative behavior of Θ and S above the seasonal thermocline due to air-sea interactions after the last maximum of winter convection [*García-Ibañez et al.,* 2015].

The system of equations in the first step, the cOMP based on conservative variables, remains as follows:

$$\sum_{i=1}^{n} X_i * \theta_i^{SWT} = \theta^{sample} + R_\theta$$

$$\sum_{i=1}^{n} X_i * S_i^{SWT} = S^{sample} + R_S$$

$$\sum_{i=1}^{n} X_i * SiO_{4i}^{SWT} = SiO_4^{sample} + R_{SiO_4}$$

$$\sum_{i=1}^{n} X_i * NO_i^{SWT} = NO^{sample} + R_{NO}$$

$$\sum_{i=1}^{n} X_i * PO_i^{SWT} = PO^{sample} + R_{PO}$$

$$\sum_{i=1}^{n} X_i = 1 + R_{mass}$$

where *Rp* is the residual of each property *p* (Θ, S, SiO_4, NO=10.5*NO_3+O_2 and PO=175*PO_4+O_2 [*Broecker,* 1974*; Takahashi et al.,* 1985*; Anderson & Sarmiento,* 1994]) measured (p^{sample}) that the OMP tries to minimize and P_i^{SWT} is the property of each SWT_i. The last equation accounts for the mass conservation.

The cOMP analysis is solved for each mixing figure. The mixing figures are groups of SWTs that are susceptible to mix together, and are set considering the vertical characteristics and/or dynamics of the SWTs in the region of study. The analysis is applied to assign the mixing figure where the water sample presents the lowest residuals.

Using the same set-up as the cOMP, an eOMP analysis is solved also considering non-conservative variables (SiO_4, NO_3^-, PO_4^- and O_2). A new unknown has to be considered, ΔO, in order to account for the biogeochemical process of remineralization of the organic matter.

$$\sum_{i=1}^{n} X_i * \theta_i^{SWT} = \theta^{sample} + R_\theta$$

$$\sum_{i=1}^{n} X_i * S_i^{SWT} = S^{sample} + R_S$$

$$\sum_{i=1}^{n} X_i * SiO_{4i}^{SWT} + \Delta O / r_{Si} = SiO_4^{sample} + R_{SiO_4}$$

$$\sum_{i=1}^{n} X_i * O_{2i}^{0SWT} - \Delta O = O_2^{sample} + R_{O_2}$$

$$\sum_{i=1}^{n} X_i * NO_{3i}^{0SWT} + \Delta O / r_N = NO_3^{sample} + R_{NO_3}$$

$$\sum_{i=1}^{n} X_i * PO_{4i}^{0SWT} + \Delta O / r_P = PO_4^{sample} + R_{PO_4}$$

$$\sum_{i=1}^{n} X_i = 1 + R_{mass}$$

where R_{SiO4} is 12, R_{NO3} is 10.5 and R_{PO4} is 175 [*Takahashi et al.,* 1985*; Anderson & Sarmiento,* 1994]. The cOMP analysis selects the mixing figure based on conservative water mass tracers; once the mixing figures are selected, the estimates of the X_i are given by the eOMP analysis, which takes into account the effect of the biology in the measured variables.

The [DOC] of each SWT ($[DOC]_i$) was solved by an inversion of the eOMP equations. We performed an inversion of a system of 340 equations (the number of samples below 100 dbar) and 12 unknowns ([DOC]i; Table 1):

$$\left[DOC\right]^{2002} = \sum_{i=1}^{12} SWT_i^{2002} \times \left[DOC\right]_i \qquad \text{(Equation 2)}$$

where SWT_i^{2002} represents the proportion of each SWT for each sample of the OVIDE 2002 cruise with $\left[DOC\right]^{2002}$. Surface seasonal variability is avoided by excluding samples from <100 dbar. The standard deviation of the residuals of Equation 2 is 2.6 µmol·kg^{-1}, about 4 times the DOC measurement error, which is of the same order of fitting as that obtained for nutrients and O_2 in the eOMP [*Garcia-Ibañez et al.,* 2015].

Table 1. Potential temperature (Θ), salinity (S) and dissolved organic carbon (DOC) of each source water type* considered here with their corresponding standard deviations. Correlation coefficient (r2) between observed and estimated DOC is given together with the standard deviation of the residuals (SDR) and the SDR/ε ratios, with ε being the DOC measurement error.

	Θ (^{0}C)	**S**	**DOC (μmol·kg^{-1})**
$ENACW_{16}$	16.00±0.13	36.20±0.02	59.0±2.1
$ENACW_{12}$	12.30±0.18	35.66±0.03	55.4±0.5
MW	11.7±0.2	36.500±0.011	45.1±1.1
SAIW	6.0±0.2	34.70±0.03	51.7±1.0
$SPMW_8$	8.00±0.11	35.230±0.016	47.2±1.1
$SPMW_7$	7.07±0.07	35.160±0.006	50.2±1.1
IrSPMW	5.00±0.02	35.014±0.013	55.3±1.1
LSW	3.00±0.19	34.87±0.02	48.1±0.4
ISOW	2.60±0.08	34.980±0.003	48.4±1.2
DSOW	1.30±0.06	34.905±0.006	51.8±1.9
PIW	0.0±0.2	34.65±0.03	48.4±5.4
$NEADW_L$	1.98±0.03	34.895±0.003	42.1±0.6
r^2			0.68
SDR			2.6
SDR/ε			3.7

*$ENACW_{16}$ and $ENACW_{12}$: East North Atlantic Central Waters; MW: Mediterranean Water; SAIW: Subarctic Intermediate Water; $SPMW_8$ and $SPMW_7$: Subpolar Mode Waters of the Iceland Basin and IrSPMW of the Irminger Basin; LSW: Labrador Sea Water; ISOW: Iceland-Scotland Overflow Water; DSOW: Denmark Strait Overflow Water; PIW: Polar Intermediate Water; and $NEADW_L$: lower North East Atlantic Deep Water.

5.2.3. DOC transports

Absolute transports across the OVIDE section were estimated using a linear box inverse model constrained by direct acoustic Doppler current profiler velocity measurements and by a net mass transport of 1±3 Sv to the north [*Lherminier et al.,* 2007*, Gourcuff et al.,* 2011*, Mercier et al.,* 2015]. Transport across OVIDE estimated by the inverse model has been previously evaluated [*Gourcuff et al.,* 2011*; Mercier et al.,* 2015*; Daniault et al.,* 2011]. The integration of AMOC transport in density levels, rather than in depth levels, better separates the upper and lower limbs of the overturning cell [*Lherminier et al.,* 2010] and avoids the partial cancellation that supposes the existence of opposed flows at overlapping depths when integrating AMOC transports in depth coordinates [*Mercier et al.,* 2015]. The boundary between the upper and lower limbs of the AMOC is the density level (σ_{AMOC}) that corresponds to the maximum of the overturning streamfunction.

The water mass volume transports and structure for the upper and lower limbs of the AMOC have already been published by *García-Ibáñez et al.* [2015] for the period 2002–2010. Applying the same methodology, we solved the water mass volume transports for the 2012 cruise. Transports of DOC (T_{DOC}^{j-dl}) were integrated in density layers of 0.1 kg·m^{-3} (*j-dl*) and computed as the product of the volume transport (T_{SWT}^{j-dl}), the [*DOC*]$_i$, and the density (ρ) for each SWT:

$$T_{DOC}^{j-dl} = \sum_{i=1}^{12} T_{SWT_i}^{j-dl} \cdot [DOC]_i \cdot \rho \quad \text{(Equation 3)}$$

Since Equation 3 is restricted to ≥100 dbar, the contribution of the surface layer (<100 dbar) is accounted separately as:

$$T_{DOC}^{0-100} = T^{0-100} \cdot \overline{[DOC]}^{0-100} \cdot \overline{\rho}^{0-100} \quad \text{(Equation 4)}$$

where $T^{0\text{-}100}$ is the volume transport of the first 100 dbar, and $\overline{[DOC]}^{0-100}$ and $\overline{[\rho]}^{0-100}$ are the average [DOC]^{2002} and the average density in the upper 100 dbar, respectively.

For the error calculation, assuming that the OVIDE cruises are repetitions, i.e. they had been performed equally and represent a similar oceanographic behavior, the error in the estimate of the DOC transport can be calculated as follows:

$$errorT_{DOC_{OVIDE}} = \sqrt{\frac{std}{n}}$$

where *std* is the standard deviation of the computed transports and *n* is the number of cruises between 2002 and 2012 (*n*=6).

Analytical computations of errors were performed at the G-I-S sills (*error*$T_{DOC_{sills}}$) by means of a perturbation method. Independent normally-distributed perturbations (*n*=100 for each input variable) were generated using as the standard deviation the published uncertainties in the [DOC] data. Budget error quantities in the OVIDE box were also computed through:

$$BUDGETerror = \sqrt{errorT_{DOC_{OV}}{}^2 + errorT_{DOC_{sills}}{}^2 + errorDOC_{storage}{}^2}$$

where *error*$DOC_{storage}$ is evaluate from the variability of the inventory of DOC in the OVIDE box from 2002 to 2012 using the stoichiometric relationship between AOU and carbon (AOU-C_{eq}) and the proportion of carbon respired from the DOC pool.

Estimating transports in density levels allowed us to separate the DOC transport contributions of the upper and lower limbs of the AMOC. DOC transported by the lower limb of the AMOC was

computed by integrating the DOC transports between σ_{AMOC}=32.14 and the bottom. Similarly, DOC transported by the upper limb of the AMOC was computed as the sum of the surface layer contribution and the density-integrated DOC transport between 100 dbar and σ_{AMOC}=32.14.

5.2.4. DOC budget in the eSPNA

We define the eSPNA as the region bounded by the OVIDE section (southern boundary) and the Greenland-Iceland-Scotland (G-I-S) sills (northern boundary) (see section 2.1.4 and Figure 27). The DOC budget in the eSPNA is the net balance between DOC production/consumption due to biological activity and lateral advection due to ocean circulation through the OVIDE section and the G-I-S sills. Exchanges of water masses and DOC over the G-I-S sills, largely restricted by bottom topography and with a tight range of temporal variability, are available in the literature [*Hansen & Østerhus*, 2000*; Hansen & Østerhus*, 2007*; Jeansson et al.,* 2011; *Jochumsen et al.,* 2012]. Using data from the Table 2 we computed the T_{DOC} at the G-I-S sills as $T_{DOC}^{sills} = \sum_{i=1}^{6} T_{SWT_i}^{sills} \cdot [DOC]_i \cdot \overline{\rho}^{SWT_i}$.

Regarding the linear interannual trend of the DOC content in the box, we evaluate the apparent oxygen utilization (AOU, difference between the measured O_2 and its saturation concentration) as an indicator of DOC changes by cumulative respiration. The linear relationship between DOC and AOU [*Carlson et al.,* 2010] can be as high as 0.88 in the northeastern North Atlantic [*Álvarez-Salgado et al.,* 2013]. To evaluate if the time derivative of DOC storage in the OVIDE box is negligible, we evaluated the inventory of apparent oxygen utilization (AOU) in the eSPNA from 2002 to 2012 as a proxy of the DOC content (Figure 29). The range of interannual variation in AOU is tightly constrained around ~124 μmol·kg^{-1} between 2002 and 2012, with a standard deviation as low as ±1.2 μmol·kg^{-1}. Therefore, the assumption of no considerable differences in the interannual variability of DOC transport is also supported by the oxygen that have been respired.

Organic carbon inflows from rivers and rainwater could affect DOC budgets [*Hansell et al.,* 2004]. The amount of DOC discharged by the main rivers in the eSPNA is 0.26 Tg-C·yr^{-1} [*Dai et al* 2012]. The global mean rate of atmospheric deposition of organic carbon because of rainwater flux has been estimated at 0.26 g-C·m^{-2}·yr^{-1} [*Willey et al.,* 2000] resulting in a net input of 1.0 Tg-C·yr^{-1} for the eSPNA. Therefore, we neglected riverine and rainfall DOC inputs due to their small relevance compared to the lateral advection (~0.4%).

Table 2. Water mass characterization at the Greenland-Iceland-Scotland (G-I-S) sills.

Water mass	Volume transport (Sv)	Density ($kg \cdot m^{-3}$)	[DOC] ($\mu mol \cdot kg^{-1}$)
ENACW	3.85±1	1027.3	58±4
MNACW	3.85±1	1027.4	58±4
NIIW	0.8±0.2	1027.6	59±4
PIW	-1.8±0.5	1027.4	70±10
DSOW	-3±0.3	1027.9	58±6
ISOW	-3±0.6	1028	53±5

Volume transport (in Sv; 1 Sv=10^6 $m^3 \cdot s^{-1}$) from *Pérez et al.,* [2013] (ENACW, East North Atlantic Central Water; MNACW, Modified North Atlantic Central Water; and NIIW, North-Iceland Irminger Water), *Nillson et al.,* [2008] (PIW, Polar Intermediate Water), *Macrander et al.* [2005] (DSOW, Denmark Strait Overflow Water), *Hansen & Østerhus,* [2000], [2007] (ISOW, Iceland-Scotland Overflow Water). Positive transports are northward. [DOC] (in $\mu mol \cdot kg^{-1}$) and density (in $kg \cdot m^{-3}$) are taken from *Jeansson et al.,* [2011]. The exchanges with the Nordic Seas are restricted by the G-I-S sill topography. The mean depth of the sill, around 500 m, limits the exchange of deep water with the North Atlantic (Figure 12). The only regions that allow relatively deep overflows are the Denmark Strait and the Faroe Bank Channel. Shallower overflows also occur across the Iceland-Faroe Ridge, a broad ridge with minimum depths of 300–500 m (deepening at the Faroese end), and the Wyville-Thomson Ridge between the Faroes and the Scotland shelf (depth ~600 m) [*Hansen & Østerhus,* [2000]. This bathymetric restriction narrows the variability in annual circulation, so available literature data are well constrained.

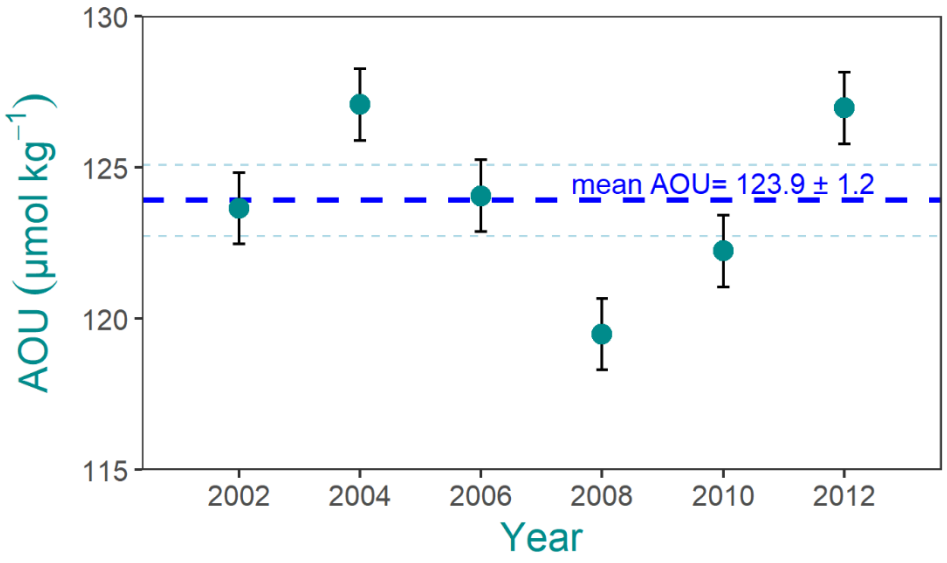

Figure 29. Apparent Oxygen Utilization (AOU, in $\mu mol \cdot kg^{-1}$) at OVIDE line for each one of the six cruises (2002–2012). The length of the vertical bar corresponds to the standard deviation. The horizontal dashed line (dark blue) represents the mean value of AOU along its uncertainty.

5.3. Results and Discussion

5.3.1. Water mass DOC characterization

Averaged [DOC] in the upper 100 dbar ($\overline{[DOC]}^{0-100}$) is 56.7±0.6 µmol·kg^{-1}, with values that range from 52.7±0.2 µmol·kg^{-1} in the northernmost latitudes to 56.4±0.6 µmol·kg^{-1} closer to the Iberian Peninsula, reaching >60 µmol·kg^{-1} in surface waters near 25ºW (Figure 28). The high [DOC] of the surface waters of the OVIDE section (40ºN–60ºN) present no meridional trend (p-level=0.91), which contrasts with the latitudinal gradient previously reported for a zonal section in the North Atlantic [*Carlson et al.,* 2010]. Since the OVIDE section crosses North Atlantic Current (NAC) branches with waters of different ages, the DOC features observed in surface correspond to the variability of the mode waters due to their formation processes instead of a latitudinal gradient (Figure 28). [DOC] decreases with depth to values <50 µmol·kg^{-1} in the deep waters, which are higher than those found in the deep waters of the South Atlantic and Pacific Oceans [*Hansell et al.,* 2009]. The lowest [DOC] is found in the Iberian Abyssal Plain (37.8 µmol·kg^{-1}) due to the Antarctic Bottom Water influence [*Hansell et al.,* 2009]. North of 45ºN (west of 18°W in Figure 28), [DOC] is >45 µmol·kg^{-1} at 2000 m depth, resembling the distribution shown in [*Hansell et al.,* 2013].

By SWTs (Table 1), the highest [DOC] is found in the ENACW$_{16}$ (East North Atlantic Central Water of 16ºC; 59.0±2.1 µmol·kg^{-1}), in agreement with the high [DOC] of the subtropical systems [*Hansell et al.,* 2004].

The DOC content of the Subpolar Mode Waters (SPMWs) is the result of the progressive renewal of the NAC waters during their cyclonic circulation in the Iceland and Irminger basins, which is evidenced by the [DOC] of SPMWs: the relatively old SPMW$_8$ presents lower [DOC] (47.2±1.1 µmol·kg^{-1}) than the youngest IrSPMW (55.3±1.1 µmol·kg^{-1}), with the [DOC] of the intermediate stage, SPMW$_7$, in between them (50.1±1.1 µmol·kg^{-1}). Thick layers with high [DOC] (52–54 µmol·kg^{-1}) were also observed in the Irminger Basin [*Amon et al.,* 2003]. At intermediate depths (1000–2500 m), Labrador Sea Water (LSW) is the dominant water mass of the section [*García-Ibañez et al.,* 2015], with a [DOC] of 48.1±0.4 µmol·kg^{-1}.

Both overflow waters, Iceland-Scotland Overflow Water (ISOW) and Denmark Strait Overflow Water (DSOW), contain relatively high [DOC] (Table 1). The [DOC] of ISOW is consistent with the mean [DOC] for the bathypelagic zone (1000–3000 m) at ~61ºN [*Carlson et al.,* 2010; its Figure 2c], typically dominated by ISOW [*García-Ibañez et al.,* 2015]. The [DOC] of DSOW has been related to the high load of organic matter transported by the Arctic rivers [*Amon et al.,* 2003*, Benner et al.,* 2005*, Jørgensen et al.,* 2011]. This terrestrial influence should also affect the [DOC] of the Polar Intermediate Water, but its magnitude is conditioned by its reduced presence in the section due to its geographical constraint in the East Greenland slope [*García-Ibañez et al.,* 2015],

which explains the high standard deviation of its [DOC] (48.4±5.4 µmol·kg^{-1}). The [DOC] of DSOW is responsible for the relative maximum located at the bottom of the west Irminger Basin (>50 µmol·kg^{-1}), flowing along the East Greenland slope (west of 40ºW) (Figure 28). The [DOC] for the overflows are ~5 µmol·kg^{-1} lower than those found at the G-I-S sills [*Jeansson et al.,* 2011], consistent with the expected decrease of their [DOC] due to the entrainment processes occurring between the G-I-S sills and the OVIDE section. Conversely, North Atlantic waters flowing northward through the G-I-S sills carry similar or slightly higher [DOC] than observed in the OVIDE section, suggesting a balance between DOC production and respiration. The [DOC] of the lower North East Atlantic Deep Water is the lowest of the water masses (42.1±0.6 µmol·kg^{-1}, Table 1), in agreement with the values found in deep and bottom layers at 24.5ºN where this water mass dominates [*Hansell et al.,* 2004].

Our results from the SWT-DOC characterization are comparable with those of *Álvarez-Salgado et al.* [2013], who also used an OMP-based methodology but with a different water mass setting. The SWTs proposed by *García-Ibáñez et al.* [2015] allowed us to reach a better [*DOC*]$_i$ adjustment (r^2=0.68 vs 0.62) with a lower standard deviation of the residuals (SDR=2.6 vs 3.1). The spatial distributions of modeled [DOC] resulting from the eOMP analysis (Figure 30) reflects the expected DOC distribution in the North Atlantic, and present interannual variability due to the interannual variability in the observed water mass properties that are modeled as varying proportions of the SWTs. The model is able to reproduce DOC changes in the sections between years based on the variability of the water mass contributions. In this way the model does not need the assumption of the time derivative of [DOC] being zero at OVIDE section.

Furthermore, the [*DOC*]$_i$ reached through our methodology agree with [DOC] previously reported. For example, *Amon et al.* [2003] reported a mean [DOC] of around 53 µmol·kg^{-1} for the Irminger Basin for samples taken in September–October 1998, in agreement with the values reported here. Besides, the robustness of the modeled [DOC] was also evaluated using measured data for a meridional section along 20ºW held in 2013 (Leg 1 of A16N) that included the eSPNA. Comparing the measured [DOC] in the section A16N inside the eSPNA (487 samples) with the reconstructed [DOC] result of the combination of the water mass proportions of the A16N section ($X_i^{A16N\_2013}$) with the source water types [*DOC*]$_i$ of Table 1 through the equation $\left[DOC\right]^{\mathrm{A16N\_2013}} = \sum_{i=1}^{12} SWT_i^{\mathrm{A16N\_2013}} \times \left[DOC\right]_i$. The correlation coefficient (r^2) between the measured and reconstructed [DOC] is 0.75, with a mean difference of 2.3±1.9 µmol·kg^{-1}, which is inside the uncertainty of the measurements. The good agreement between observed and modelled DOC supports the assumption of little interannual variability in the DOC content of each SWT ([*DOC*]$_i$).

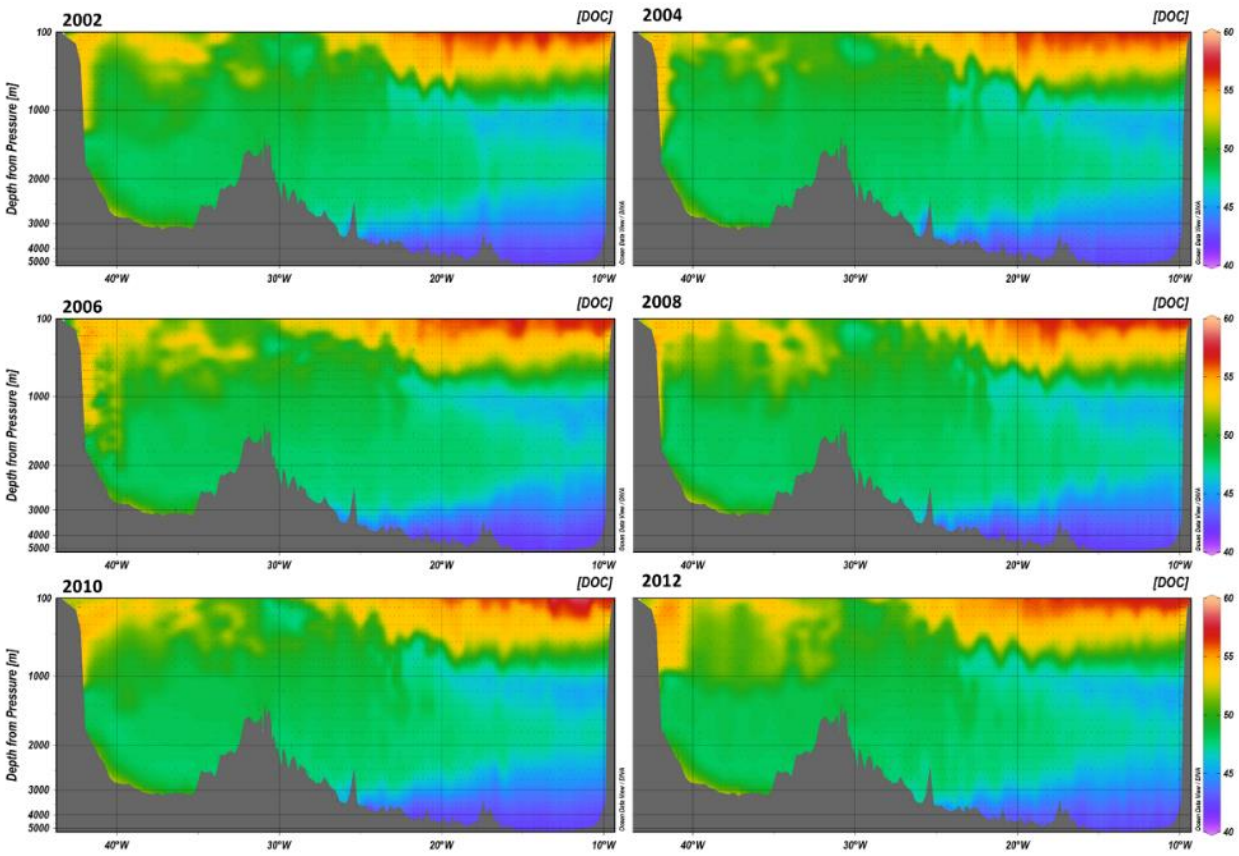

Figure 30. Dissolved organic carbon (DOC, in µmol·kg^{-1}) vertical distribution modeled along the OVIDE section from Greenland (left) to the Iberian Peninsula (right) for each one of the six cruises (2002–2012) by combining water mass distributions with the source water types [*DOC*]$_i$ (Table 1) through the equation $[DOC]^{year} = \sum_{i=1}^{12} SWT_i^{year} * [DOC]_i$. Note that the depth scale is not linear and the first hundred meters are excluded.

5.3.2. DOC transport across the OVIDE section

Following *Lherminier et al.* [2007], DOC transports were integrated in density levels to better represent the circulation and the AMOC in the eastern-SPNA. Figure 31 shows the averaged profile of DOC transport for the six cruises (2002–2012) integrated from Greenland to Portugal and plotted by density layers. Integrated DOC transport resembles the vertical profile of the overturning circulation, with the classical two layers of transports in opposite directions. This profile resembles other tracer profiles such as heat and C_{ant} [*Pérez et al.,* 2013*; Zunino et al.,* 2014], with a northward flowing upper layer and a southward flowing lower layer. The similarity is driven by the circulation, but C_{ant} and heat exhibit surface-intensified profiles while DOC is more balanced. The relative strength of the lower versus upper limb property transport is determined by the mean vertical gradient of the property; in terms of heat the lower limb's role is relatively small, but for DOC, with a

small vertical gradient, there is greater similarity between the upper and lower limb transports. A similar DOC transport profile was found in 24.5ºN with northward volume transports in upper layers and southward volume transport in deeper layers [*Hansell et al.,* 2004].

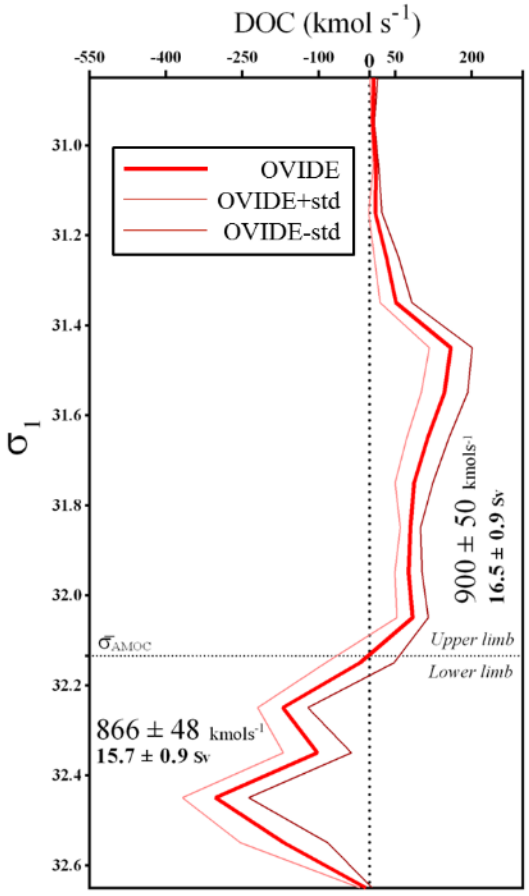

Figure 31. Average DOC transports (kmol·s^{-1}) for period 2002–2012 (± standard deviation) integrated in density (σ_1) layers with a 0.1 kg·m^{-3} resolution across the OVIDE section. Positive (negative) transports correspond to northward (southward) flow. The dashed horizontal line represents σ_{AMOC}=32.14, the mean density boundary between the upper and lower limbs of the AMOC for the period 2002–2012. Net DOC transports in kmol·s^{-1} and volume transports in Sv (1 Sv=10^6·m^3·s^{-1}) are also presented.

Volume and DOC transports at OVIDE section separated by layers are in Table 3. Southward transport of DOC across the section in the lower limb of the AMOC is 866±48 kmol·s^{-1}, consisting of two peaks: a lighter one (σ_1=32.25) related to IrSPMW and a denser and stronger one related to LSW and the overflows (DSOW and ISOW). DOC transported by the upper limb of the AMOC, 900±50 kmol·s^{-1}, is dominated by the North Atlantic Central Waters. The mean velocity-weighted [DOC] advected northward in the upper limb of the AMOC across the OVIDE section ([DOC]$_{upper}$) is

52.9±1.6 µmol·kg^{-1}, while the mean velocity-weighted [DOC] advected southward in the lower limb ([DOC]$_{lower}$) is 53.1±1.6 µmol·kg^{-1} (Figure 32).

Table 3. Volume (Sv) and DOC transports (kmol·s^{-1}) at OVIDE section separated as surface layer (<100 dbar), the upper limb of the AMOC without the first 100 dbar, and the lower limb of the AMOC. The sum of the three components results in the net transport represented in the row labeled "Total". Northward transports are positive.

	2002		2004		2006	
	T_{Sv}	T_{DOC}	T_{Sv}	T_{DOC}	T_{Sv}	T_{DOC}
Surface layer	0.89	84	1.18	119	1.31	41
Upper limb >100 dbar	15.85	855	15.11	818	11.34	619
Lower limb	-16.5	-913	-16.35	-927	-11.25	-631
Total	0.24	26	-0.06	10	1.4	29

	2008		2010		2012		Mean	
	T_{Sv}	T_{DOC}	T_{Sv}	T_{DOC}	T_{Sv}	T_{DOC}	T_{Sv}	T_{DOC}
Surface layer	1.69	92	1.43	58	1.15	59	1.26	76
Upper limb >100 dbar	16.6	901	17.04	916	15.5	836	15.28	824
Lower limb	-17.37	-933	-17.23	-915	-15.71	-874	-15.73	-866
Total	0.92	60	1.24	59	0.94	21	0.8	34.2

5.3.3. DOC circulation in the eastern Subpolar North Atlantic

DOC transports across the eSPNA are summarized in Figure 32. We find a net northward DOC transport of 34±8 kmol·s^{-1} (13 Tg-C·yr^{-1}), which is associated with the net northward transport of 0.8 Sv across the section [*Zunino et al.,* 2015]. Through the G-I-S sills, 384±29 kmol·s^{-1} of DOC are transported northward in the upper limb of the AMOC, while 342±19 kmol·s^{-1} are flowing southward as overflow waters, resulting in a net northward DOC transport of 42±33 kmol·s^{-1} (16 Tg-C·yr^{-1}) across the sills. The high overturning circulation inside the eSPNA (9.7±1.3 Sv), with an average [DOC] of 52.1±9 µmol·kg^{-1}, results in a downward DOC transport of 520±52 kmol·s^{-1} (197 Tg-C·y^{-1}). In the eSPNA, the sum of the advection terms is close to zero (8±77 kmol·s^{-1}). When DOC advection in the eSPNA is considered, the DOC is balanced, suggesting that DOC production is balanced by its removal. This balance contrasts with the DIC fixation of ~107 kmol·s^{-1} determined in the eSPNA via an inorganic nutrient budget [*Maze et al.,* 2012], suggesting that the fate of DIC fixation should be vertical export of biogenic particles instead of an accumulation of

DOC. DIC imbalance is also supported by large particulate organic carbon fluxes to the ocean interior occurring at 2000 m horizon in the Irminger and Iceland Basins [*Honjo et al.,* 2008].

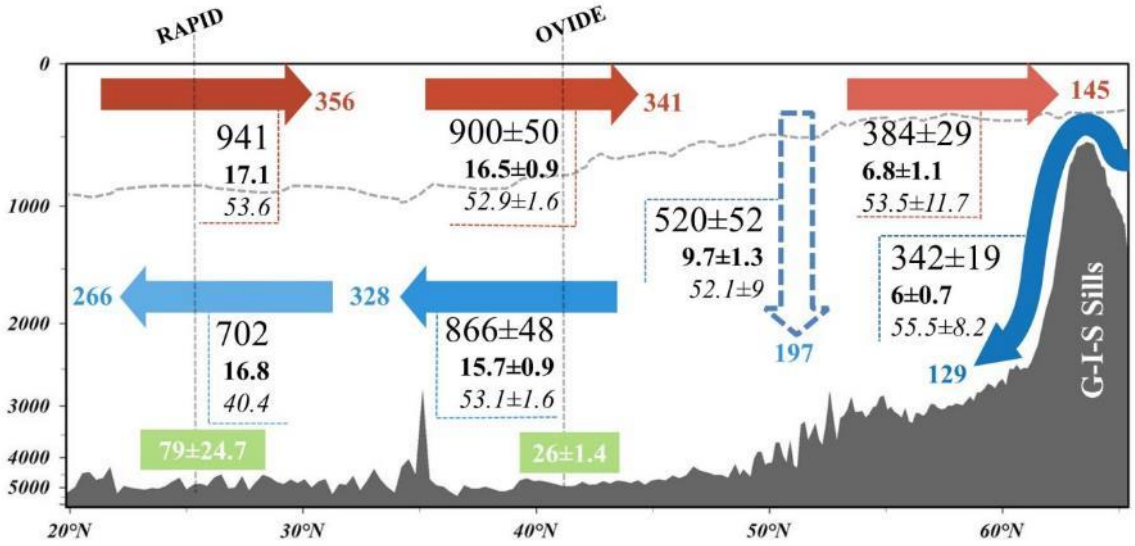

Figure 32. Mean DOC budget in the North Atlantic (from 24.5ºN to 65ºN) for the period 2002–2012. Schematic representation of the DOC transport (kmol·s^{-1}, large font; and in Tg-C·yr^{-1} in color at the arrows tips), volume transport (Sv, bold numbers below DOC transport) and mean [DOC] (µmol·kg^{-1}, italicized numbers below volume transport) between the RAPID section (left), the OVIDE section (middle) and the G-I-S sills (right). Values inside the green boxes represent the mean apparent oxygen utilization (in µmol·kg^{-1}) in the lower limb. Dashed blue arrow represents the downward export inferred from the observed values (solid arrows). Associated uncertainties (±) are depicted when available. The dashed line represents the separation between upper and lower AMOC limbs.

Despite modification of the thermohaline properties of the water masses due to air-sea interaction, the average [DOC] along the AMOC pathways between the G-I-S sills and the OVIDE section show no substantial differences (Figure 32), suggesting a relatively conservative DOC circulation. The relatively high velocity-weighted [DOC] of the lower limb of the AMOC is due to three factors: (i) the important contribution of DSOW, (ii) the arrival of IrSPMW transported by the strong EGIC [*Daniault et al.,* 2011,*Sarafanov et al.,* 2012], and (iii) the fact that the deep waters with low [DOC] appear mainly southeast of the NAC (Figure 28), where their net volume transport is close to zero, which greatly attenuates their contribution to the velocity-weighted [DOC] of the lower limb of the AMOC.

5.3.4. DOC exchanges between subtropical and subpolar gyres

Full-depth DOC data for the 24.5ºN section have been published [*Hansell et al.,* 2004] with volume transport data for the WOCE-A05 cruise in January/February 1998. We reconstruct the DOC transports using the RAPID-MOC time series [*McCarthy et al.,* 2015] for the period 2004–2014 to

get a robust DOC transport for the 24.5ºN section. Combining velocity-weighted [DOC] along the latitude 24.5ºN [*Hansell et al.,* 2004] with volume transport data from RAPID-MOC time series (www.rapid.ac.uk/rapidmoc), DOC transports have been reconstructed to allow comparison between subtropical latitudes (24.5ºN–26.5ºN, from now on, RAPID) and the OVIDE section.

Velocity-weighted mean [DOC] for each layer ($[DOC]_{mean}$'98, in $\mu mol \cdot kg^{-1}$) was computed using the volume transports (T_{1998}, in Sv) and the DOC transports ($T_{1998}DOC$, in $kmol \cdot s^{-1}$) of the 24.5ºN cruise in January/February 1998 reported by *Hansell et al.* [2004] (their Table 1). To obtain the same water column separation used for the RAPID-MOC time series [*McCarthy et al.,* 2015], we restructured *Hansell et al.* [2004]'s data for the upper limb of the AMOC into three layers: Ekman, upper mid-ocean and Gulf Stream. Volume transports and DOC transports for the Ekman layer were taken from *Hansell et al.* [2004]'s Figure 4(c and d). Volume transports and DOC transports for the upper mid-ocean layer were obtained by adding the surface and intermediate layers in *Hansell et al.* [2004]'s Table 1 and then removing the transports associated to the Ekman layer. Finally, $[DOC]_{mean}$'98 was combined with the average volume transport in RAPID-MOC time series [*McCarthy et al.,* 2015] (T_{RAPID}, in Sv) for the period between 1 April 2004 and 22 March 2014, thus obtaining the reconstructed DOC transports at subtropical latitudes (24.5–26.5ºN) ($T_{RAPID}DOC$, in $kmol \cdot s^{-1}$). All data required for these computations are given in the Table 4.

Table 4. Reconstruction of DOC transports at 24.5ºN during the RAPID period

	T_{1998} (Sv)	$T_{1998}DOC$ ($kmol \cdot s^{-1}$)	$[DOC]_{mean}$'98 ($\mu mol \cdot kg^{-1}$)	T_{RAPID}* (Sv)	$T_{RAPID}DOC$ ($kmol \cdot s^{-1}$)	
Ekman	2.72	190.2	67.9	3.57	250	941
Upper mid-ocean	-21.65	-1239.6	55.6	-17.90	-1025	
Gulf Stream	30.49	1661.3	53.1	31.40	1716.4	
Deep ocean	-15.86	-659.4	40.6	-17.80	-746.4	-702
Deeper than 5000m	4.26	187.1	42.5	1.02	44.7	

* The RAPID/MOCHA/WBTS array is a collaborative effort supported through the UK Natural Environment Research Council (NERC) RAPID-WATCH program, the US National Science Foundation (NSF) Meridional Overturning Circulation Heat-flux Array project, and the US National Oceanographic and Atmospheric Administration (NOAA) Western Boundary Time Series project; and transports including error estimates are freely available at www.rapid.ac.uk/rapidmoc

At RAPID, the DOC circulation is characterized by an upper-limb northward transport of 941 kmol·s^{-1} (17.1 Sv) and a lower-limb southward transport of 702 kmol·s^{-1} (16.8 Sv), resulting in a net northward DOC transport of 239 kmol·s^{-1} (~90 Tg-C·yr^{-1}). This net DOC transport is quite similar to the 81 Tg-C·yr^{-1} previously reported by *Carlson et al.* [2010] for the North Atlantic, computed as the product of the [DOC] gradient along the ocean ventilation path and the ventilation rate (AMOC term).

The velocity-weighted [DOC] of the upper limb of the AMOC at RAPID (53.6 µmol·kg^{-1}) is very similar to that found at the OVIDE section. However, a decrease in the velocity-weighted [DOC] of the lower-limb of the AMOC of 12.7±1.2 µmol·kg^{-1} is observed between OVIDE and RAPID (40.4 µmol·kg^{-1}) (Figure 32). This DOC consumption results in a decrease in the DOC transport of the lower limb of the AMOC of 164 kmol·s^{-1} (~62 Tg-C·yr^{-1}) between OVIDE and RAPID. Therefore, we found that most of the DOC remineralization occurs in the lower limb of the AMOC in contrast with results from *Carlson et al.* [2010], who located the DOC remineralization almost equally among the upper and lower limbs of the AMOC. The differences between estimates may be explained by the criteria used to distinguish the upper and lower limbs of the AMOC. The separation based on the density levels that maximizes AMOC transport [*Lherminier et al.,* 2007] applied in our study is quite different to the separation between the main thermocline versus North Atlantic Deep Water (NADW) ventilation rate applied by *Carlson et al.* [2010]. By applying the density separation criteria, the important contribution of IrSPMW to the DOC transport is assigned to the lower limb of the AMOC and not shared between both limbs. In addition, the contribution of DSOW in the lower limb is not accounted for in *Carlson et al.* [2010] because it was not sampled. Assuming a level of ~40 µmol·kg^{-1} for the deep-water background [DOC], we interpret the strong DOC decrease in the North Atlantic deep waters as a sign of the bioavailability of the DOC exported from the eSPNA to the subtropical latitudes. This downstream DOC consumption at decadal time-scale is contributing to the CO_2 production in deep waters [*Hansell et al.,* 2004*; Carlson et al.,* 2010].

The relationship between DOC and AOU gradients could give insights about the origin of the differences found between OVIDE and RAPID. In our data, the ratio of $\Delta DOC/\Delta AOU\text{-}C_{eq}$ (converted to carbon equivalents with the molar ratio $\Delta C/\Delta O2$=-0.72 [*Anderson et al.,* 1995]) is 33±6%. This ratio is slightly above the 5–29% found by *Carlson et al.* [2010] for the same region. The enhanced contribution of DOC oxidation to oxygen consumption could be due to the proportion of non-refractory DOC and the relatively young age of the water masses [*Hansell & Carlson, 2013*].

We are aware that the assumption of no seasonal variability deserves a close justification, even more so in the surface layer where biological activity could result in a seasonal variation of the [DOC] between winter lows of 42 µmol·kg^{-1} to summer highs of 65–70 µmol·kg^{-1} [*Hansell et al.,* 2015]. However, the seasonal [DOC] range in the surface layer of the eastern North Atlantic is only ±5 µmol·kg^{-1} [*Körtzinger et al.,* 2001]. The DOC transported northward by the surface layer (0–100

dbar) at OVIDE section (76 kmol·s^{-1}) represents ~9% of the DOC transported by the upper limb of the AMOC (Table 3). The surface layer (0–100 dbar) is where the seasonal [DOC] variability is most relevant. Based on our methodology, a 1 µmol·kg^{-1} perturbation of the [DOC] in the first 100 dbar results in a perturbation of 1.4 kmol·s^{-1} of the DOC transport. So the seasonal variability of the northward DOC transport would be ±7 kmol·s^{-1}. This would be a minor correction to the DOC transport at OVIDE. In addition, the seasonal [DOC] variability at OVIDE is expected to co-vary with that in the G-I-S sills, so that both lateral boundaries of the eSPNA would be affected in the same way by the DOC seasonal changes of the surface layer. Therefore, neglecting seasonal variability in the surface layer does not generate any seasonal bias in the net DOC budget.

We then conclude that a central characteristic of the DOC cycle in the eastern-SPNA is its export from the upper to the lower limbs of the AMOC. The relatively fast vertical transport of DOC contributes to carbon sequestration, analogous to the vertical transport of DIC. DOC injected to the deep layers is more labile than the majority of the deep DOC observed in the South Atlantic and Pacific Oceans, so it is more susceptible to remineralization. In the North Atlantic, DOC consumption of 62 Tg-C·yr^{-1} taking place in the lower limb of the AMOC (bathypelagic and mesopelagic layers) between subpolar and subtropical latitudes consumes 72% of the DOC exported by the whole Atlantic Ocean.

This outcome implies that much of the net DOC exported with the overturning circulation in the eSPNA, the major source of new DOC in the deep global ocean, is remineralized within decades, thus impacting deep microbial and dissolved organic matter compositional dynamics. DOC downward export due to overturning circulation acts as a carbon sink and represents a considerable contribution to CO_2 sequestration. Given the atmospheric CO_2 uptake of 0.20 Pg-C·yr^{-1} in the area [*Takahashi et al.,* 2009], the carbon sequestration mediated by DOC would represent ~30% of the total North Atlantic CO_2 sink.

The methodology applied here, coupling well-solved water mass transport along transoceanic sections with high-quality [DOC] measurements, could solve the problem of too few DOC data throughout the world oceans, and the North Atlantic in particular. However, more direct observations to test this assessment are required.

PART III. Biogeochemical budget

Chapter 6: Long-term integrated budget of biogeochemical elements driven by circulation in the eastern subpolar North Atlantic

6.1. Introduction

The North Atlantic is the most sampled ocean in the history of oceanography. Knowledge on its mean circulation state has been greatly improved during XXIst century, with repeated ship-based measurements, moorings, drifters –ARGO- and satellite altimetry [*Hansen & Østerhus*, 2000; *Willis*, 2010; *Sarafanov et al.,* 2012; *Roessler et al.,* 2015; *Daniault et al.,* 2016]. Budgets of mass, heat and salt have been constructed [*Lumpkin & Speer,* 2007*; Lozier et al.,* 2008]*,* but biogeochemical basin-scale approaches are still scarce [*Álvarez et al.,* 2002; *Maze et al.,* 2012].

Carbon (C) plays a central role in ocean biogeochemical cycles not only by its relevance in climate system (CO_2), but also because is the central element of organic chemistry, therefore of life on Earth. The fixation of carbon into biogenic material and its subsequent transfer to the deep ocean through sinking or subduction is termed the biological carbon pump (BCP) [*Broecker & Peng*, 1982]. Marine primary producers convert dissolved inorganic carbon (DIC) in particulate organic carbon (POC). The vertical transport of POC decreases with depth as organic matter is respired (remineralized) once again to DIC or transformed into dissolved organic carbon (DOC). The quantification of atmospheric CO_2 sequestered by the BCP is a key knowledge to evaluate the ocean's carbon budget [*Falkowski et al.,* 1998; *Sabine et al.,* 2004; *Körtzinger et al.,* 2001].

The drivers of the BCP are primary production and export. There are several production and export terms usually used in the literature, illustrating somewhat different fluxes. Marine net primary production (NPP), the photosynthetically fixed carbon available for export, is ~50 Pg-C yr^{-1} at global scale [*Longhurst et al.,* 1995; *Behrenfeld & Falkowski,* 1997; *Falkowski et al.,* 1998], near ~13 Pg-C yr^{-1} for the Atlantic Ocean [*Carr et al.,* 2006]. Only a fraction of that organic carbon is exported out of the euphotic zone, with current estimates from different measurement techniques ranging from ~5 to 16 Pg-C yr^{-1}, around an increasing consensus of a global mean of 10-12 Pg-C yr^{-1} in the world ocean [*Falkowski et al.,* 1998; *Henson et al.,* 2015; *Laws et al.,* 2000; *Sambrotto et al.,* 1993] and a magnitude close to 1.5 Pg-C yr^{-1} occurring in the North Atlantic [*Dunne et al.,* 2007; *Laws et al.,* 2000; *Sanders et al.,* 2014]. A very high fraction it is going to be respired in the dark ocean [*del Giorgio and Duarte,* 2002;

Arístegui et al., 2003], so at 2000 m depth the global vertical flux is only between 0.3-0.7 Pg-C yr^{-1} [*Guidi et al.,* 2016; *Henson et al.,* 2012a; *Honjo et al.,* 2008; *Lutz et al.,* 2007]. With an area of 41.5 x 10^6 km^2 [*Eakins & Sharman,* 2010], and a mean vertical flux at 2000 m of ~1.5-2 g-C·m^2·yr^1 [*Honjo et al.,* 2008, *Henson et al.,* 2012a], a first estimation of the magnitude for the North Atlantic would be between ~62-83 Tg-C·yr^{-1}. The net export flux depends on multiple factors like primary production, plankton community structure [*Guidi et al.,* 2009], temperature of the water column and mesopelagic remineralization [*Marsay et al.,* 2015], physical processes like convection or advection [*Neuer et al.,* 1997; *Dall'Olmo et al.,* 2016], or even the nature of the sinking particles, if they are rich in biominerals [*Armstrong et al.,* 2002; *Francois et al.,* 2002] or there are present fecal pellets [*Turner,* 2015]. As a practical rule, can be said that <1% of the CO_2 fixed by photosynthesis in the upper ocean reaches the deeper ocean and constitutes a long-term sink for atmospheric CO_2 [*Ducklow et al.,* 2001; *Lampitt et al.,* 2010; *Legendre et al.,* 2015; *Martin et al.,* 1987; *Poulton et al.,* 2006].

To quantify that sink, we are going to evaluate the net balance between the carbon fixation, limited to the euphotic zone, and the respiration that occurs throughout the whole water column. For a top-to-bottom ocean budget like the one proposed here, if all the inputs and outputs are assessed, the only possible exportation it is via sedimentation at the sea floor.

Production and consumption of organic matter in the ocean plays a role not only in the cycling of carbon, but also in nitrogen (N), phosphorus (P), and silicate (Si), along with micronutrients and oxygen (O). The seminal papers of *Redfield,* [1934, 1963] proposed that on a global annual mean the organic matter is produced in constant molar element ratios of 106 C:16 N:1 P:-138 O. The Redfield relationships are a useful tool to evaluate the BCP because allow the conversion of budgets based on nutrients or oxygen into carbon units by applying a stoichiometric ratio [*Körtzinger et al.,* 2001; *Álvarez et al.,* 2002; *Waniek et al.,* 2005; *Álvarez & Álvarez-Salgado,* 2007; *Hartman et al.,* 2010; *Maze et al.,* 2012]. Despite that variability at basin-scale [*Brea et al.,* 2004] and preferential remineralization of elements versus carbon with increasing depth [*Boyd & Trull,* 2007] are common processes, posterior studies have evaluated the classical Redfield ratios proposing only some minor modifications [*Takahashi et al.,* 1985; *Anderson & Sarmiento,* 1994].

The North Atlantic is a well-known sink area for atmospheric CO_2 that is becoming stronger since the 2000 [*Landschützer et al.,* 2016]. The ocean actually accumulates ~30% of anthropogenic carbon [*Sabine et al.,* 2004; *Le Quéré et al.,* 2016], altering the chemistry of seawater (Ocean Acidification). While the chemical changes are well understood, the uncertain impact on biogeochemical cycles needs to revisit the budget status of the organic component of the carbon cycle. The area of analysis, the eastern subpolar North Atlantic (eSPNA) (Figure 33), is located at the confluence of the northward-flowing upper limb and the southward-flowing lower limb of the Atlantic Meridional Overturning Circulation (AMOC) (Figure 33). First studies reported a southward export of dissolved inorganic carbon (DIC), nutrients and oxygen (O_2) toward subtropical Atlantic [*Álvarez et al.,* 2002, 2003] for section WOCE A25, a section

comparable to OVIDE [*García-Ibañez et al.,* 2015]. But more recently, with data from OVIDE section and an improved circulation model [*Lherminier et al.,* 2007; 2010], the transport of DIC [*Zunino et al.,* 2015] and nitrate (NO_3^-) is reported northwards, phosphate (PO_4^-) transport is negligible and O_2 still shows a significant southward export [*Maze et al.,* 2012].

Either under the nutrient-O_2 biogeochemical budget [*Maze et al.,* 2012], or the inorganic carbon budget approach [*Zunino et al.,* 2015], the zone has been identified like a sink region where around 40 Tg-C·yr^{-1} (107 kmol·s^{-1}) are exported to sediments. Global synthesis of export fluxes appoints that in our region the vertical export of organic carbon particles collected at 2000 m depth with sediment traps is more than twice the global average and until five times bigger (~90 kmol·s^{-1}) than the export of inorganic carbon [*Honjo et al.*, 2008]. The organic carbon export in the area of analysis has been modeled from satellite-derived data as ~2 g-C·m^{-2}·yr^{-1} (20 kmol·s^{-1}) [*Henson et al.,* 2012a]. In fact, the North Atlantic represents an extremely strong and efficient biological pump, where about half of the net primary production is exported out of the euphotic zone, together with a low particulate organic carbon (POC) flux attenuation in the first 1000 m (Figure 7) [*Buesseler & Boyd,* 2009].

Concerning our region of study, how much carbon is exported to the deep ocean? How much is the contribution of organic carbon/$CaCO_3$ in this exportation? It is relevant the role of the DOC in the exportation? and what about the oxygen, can a long-term evaluation quantify properly the air-sea O_2 flux? And the projected climate change-driven deoxygenation, it is detected in the subpolar gyre with a fourteen-year time series? To hand some insight into these questions, supported by data at basin-scale, is the objective of this biogeochemical analysis centered on carbon. The approach of this study is to provide an integrated top-to-bottom biogeochemical budget constrained by decadal mass-balanced transports of carbon variables, dissolved inorganic nutrients and oxygen within an interrelated inverse box model consistent with stoichiometric relationships. The objective is to give a well-reasoned estimate for the export of organic carbon (E_{Corg}) and $CaCO_3$ (E_{CaCO3}) to sediment and evaluate the budget status of the biological component of the carbon and the oxygen cycle in our study area.

The text is organized as follows. Area of study, data ensemble, and model framework with its uncertainties are described in the subchapter 6.2. In subchapter 6.3 we present the mass and biogeochemical results. The suitability of the approach is validated in subchapter 6.4, along with a discussion of the biogeochemical cycles and a summary of the main conclusions.

6.2. Material and methods

6.2.1 Region of study

For our basin-scale biogeochemical budget, we will analyze the region bounded at the south by the OVIDE section (from 40ºN Portugal to 60ºN Greenland, biennial periodicity since 2002) and by the north for the Greenland-Iceland-Scotland (G-I-S) sills (Figure 33). In addition to the sills, the Mid-Atlantic Ridge northern than 50ºN, the Reykjanes Ridge (RR), is a major topographic feature in the study area. The RR affects the circulation and separates the Irminger Basin (IB) from the Iceland and West European Basins (Eastern North Atlantic from now on, ENA). So we can define an operational geographical area, that we are going to call eastern Subpolar North Atlantic (eSPNA, 3.78 x 10^{12} m^2), that is the sum of IB (6.12 x 10^{11} m^2) and ENA (3.18 x 10^{12} m^2), separated by the RR. Similar geographical box-model configurations have been used previously in studies of the same region [*Lherminier et al.,* 2010; *Maze et al.,* 2012; *García-Ibáñez et al.,* 2015].

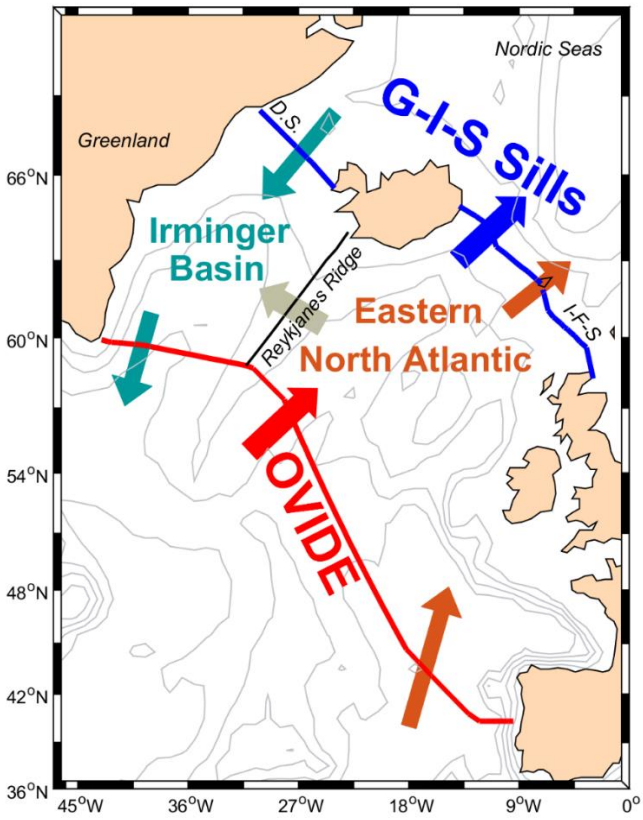

Figure 33. Map of the study region within the eastern subpolar North Atlantic. Section track of OVIDE (red thick line), main axe of Reykjanes Ridge (black line) and Greenland-Iceland-Scotland (G-I-S) sills (blue line) are indicated. The domain of the model lies between them, and defines three boxes: Irminger Basin (IB), Eastern North Atlantic (ENA), and its sum, the eastern Subpolar North Atlantic (eSPNA). Arrows indicate net volume direction exclusively. D.S.: Denmark Strait. I-F-S: Iceland-Faroe-Shetland Channel.

6.2.2 Data ensemble

6.2.2.1 Velocity and tracer data

OVIDE section were repeated biennially since 2002 to 2016 (Table 5). Salinity, oxygen, nutrients and carbon variables have been routinely sampled and measured. More info about the analytical procedures can be found in [*García-Ibañez et al.,* 2015*;* 2016] and in the previous Chapter 5. Absolute geostrophic velocity field orthogonal to OVIDE section is estimated using a linear box inverse model constrained by direct acoustic Doppler current profiler velocity measurements and by a net mass transport of 1±3 Sv to the north [see references in Table 5 for more info about the inversion and each cruise peculiarities]. All OVIDE data, except the last cruise, are available from CLIVAR, Carbon Hydrographic Data Office (CCHDO) and Seanoe (Sea scientific open data edition) webpage. Data at the G-I-S Sills and cross-RR are based mainly in literature, public available datasets or own sources (Table 6 and Table 8), but without velocity fields associated.

Table 5. OVIDE cruises 2002-2016

Date	Project	Expocode	Research Vessel	Chief scientist	Velocity field reference
Jun 10–Jul 12, **2002**	OVIDE	35TH20020610	Thalassa	H. Mercier	[*Lherminier et al.,* 2007]
Jun 4–Jul 7, **2004**	OVIDE	35TH20040604	Thalassa	T. Huck	[*Lherminier et al.,* 2007]
May 21–Jun 28, **2006**	OVIDE	06MM20060523	M.S. Merian	P. Lherminier	[*Lherminier et al.,* 2010]
Jun 10–Jul 10, **2008**	OVIDE	35TH20080610	Thalassa	B. Ferron	[*Gourcuff et al.,* 2011]
Jun 8–Jul 7, **2010**	OVIDE	35TH20100610	Thalassa	V. Thierry	[*Mercier et al.,* 2015]
Jun 23–Aug 12, **2012**	CATARINA	29AH20120622	Sarmiento de Gamboa	A. F. Ríos	[*Daniault et al.,* 2016]
May 20–Jun 26, **2014**	GEOVIDE	35PK20140515	Pourquoi Pas?	P. Lherminier	[*Zunino et al.,* 2017]
Jun 17–Jul 31, **2016**	BOCATS	29AH20160617	Sarmiento de Gamboa	F. F. Pérez	[*Pérez et al.,* 2018]

Table 6. Sills and Reykjanes Ridge data

Area	Water Mass	Density [1] (Kg·m^{-3})	Salinity[1]	DIC[1+] (µm·kg^{-1})	Alkalinity[1] (µm·kg^{-1})	DOC[1+] (µm·kg^{-1})	Oxygen[2] (µm·kg^{-1})	Nitrate[2] (µm·kg^{-1})	Phosphate[2] (µm·kg^{-1})	Silicate[2] (µm·kg^{-1})
G-I-S SILLS	**ENACW**	1.0273	35.27±0.11	2127.2±20	2325±7	58±4	267.5±3	11.9±0.4[3]	0.8±0.05[3]	4.5±0.5
	MNACW	1.0274	35.18±0.6	2132.9±22	2323±6	58±4	272±3[3]	13.7±0.4[3]	0.9±0.05[3]	5.85±0.5[3]
	ISOW1	1.0280	34.89±0.06	2160.1±5	2304±8	53±5	277.5±3	16±0.4	1.2±0.05	12.5±0.5
	ISOW2	1.0280	34.91±0.02	2166.4±3	2303±3	53±5	277.5±3	16±0.4	1.2±0.05	12.5±0.5
	NIIW	1.0276	35.06±0.03	2144±3	2309±2	59±4	277.5±3	14.8±0.4	1.05±0.05	7.5±0.5
	PW	1.0274	34.07±0.27	2118.7±8	2266±3	70±10	328±3	12.1±0.4	0.95±0.05	7±0.5
	DSOW	1.0279	34.86±0.09	2152.6±6	2294±5	58±6	305±3	13.8±0.4	1.05±0.05	9±0.5
Reykjanes Ridge[4]		1.0299	35.05±0.01	2153.5±4[*]	2310.3±2.8	51.7±2.7[5]	271.3±1	15.3±0.2	1.06±0.02	8.63±0.1

1 [*Jeansson et al.,* 2011]

[+] DIC concentration in Table 2 of *Jeansson et al*. [2011] is for the year 2002-2003. Here we show the representative concentration for the central year of the budget, 2009, increased with the anthropogenic carbon rate of increase of *Steinfeld et al* [2009] (+0.0169 yr^{-1}).

2 [*Fogelqvist et al.,* 2003] (except when indicate with the superscript 3)

3 modified from real measured data from GLODAPv2 [*Olsen et al.,* 2016] at Faroe-Shetland Channel according to the T_{pot} water mass definition and the physical properties T>3ºC and density <1027.8 Kg·m^{-3}

4 Mean full-depth section over the main axe of Reykjanes Ridge between OVIDE and Iceland realized during the 2016 BOCATS cruise

[*] DIC concentration decreased to central year 2009 with *Steinfeld et al* [2009] anthropogenic carbon rate.

5 Water mass transports across the Reykjanes Ridge [*García-Ibañez et al.,* 2015] combined with the concentration of DOC for each source water type described in Part II. Dissolved organic carbon (Table 1)

6.2.2.2. Additional input and terms

Lateral advection is the main term for an oceanic budget, but for some tracers additional inputs are required. For example, air-sea exchanges or inputs related with freshwater supplies are relevant in some biogeochemical cycles. A clear example is the atmospheric CO_2 uptake: our region of study has long been recognized like an important sink of CO_2 area [*Takahashi et al.,* 2002, 2009], so the model also requires the flux of CO_2 at the air-sea interface ($F^{CO2\ air\text{-}sea}$). In fact, the magnitude is as important as to deserve the closest approximation possible in order to obtain the best estimate of CO_2 uptake. Best resolved air-sea CO_2 fluxes are acquired when the difference in real measurements of the atmospheric and oceanic partial pressures of CO_2 (pCO_2) are multiplied by the CO_2 gas transfer coefficient [*Takahashi et al.,* 2009]. Despite the growing database of SOCATv2, with more than 10 million surface ocean pCO_2 measurements [*Bakker et al.,* 2014], the dataset is still sparse in time and space. To obtain continuous sea-air CO_2 flux fields, interpolation methods are needed to estimate values in all the periods and areas not directly observed [*Rödenbeck et al.,* 2015]. The Surface Ocean pCO_2 Mapping intercomparison initiative (SOCOM), published in the year 2015 a intercomparison dataset for fourteen different mapping methods at global scale. The methods span a wide range of approaches: statistical interpolation [*Jones et al.,* 2015*; Shutler et al.,* 2015*; Rödenbeck et al.,*

2014*; Jacobson et al.,* unpublished], model-based regression [*Valsala & Maksyutov,* 2010*; Majkut et al.,* 2014], multilinear regression [*Park et al.,* 2010*; Schuster et al.,* 2013*; Iida et al.,* 2015] and non-linear regression [*Sasse et al.,* 2013*; Landschützer et al.,* 2014*; Nakaoka et al.,* 2013*; Zeng et al.,* 2014].

The SOCOM initiative, in order to make its results comparable, used the time-independent "mean biomes" of [*Fay & McKinley,* 2014]. The utilization of biomes allows the partition of the surface ocean into large regions with biogeochemical similarities, rather than artificial geographical criteria [*Fay & McKinley,* 2014]. Global ocean biomes were downloaded from PANGAEA [last time accessed: 28/06/2017]. Our region belongs mostly to the biome "North Atlantic Subpolar Seasonally Stratified" (NASPSS), with an area being "North Atlantic Subtropical Seasonally Stratified" (NASTSS) and a very little region close to Greenland as "North Atlantic Ice" (NAICE). The environmental criteria that characterize the biomes and the area extension is shown in Table 7.

Table 7. Biome definition following [*Fay & McKinley*, 2014] and the extension (in km^2) that represents in the eSPNA. NASPSS: North Atlantic Subpolar Seasonally Stratified, NASTSS: North Atlantic Subtropical Seasonally Stratified, NAICE: North Atlantic Ice. *Chl* a: chlorophyll *a* concentrations.

Biome	**Area in eSPNA ($10^6 \cdot km^2$)**	**Area Mean Biome ($10^6 \cdot km^2$)**	**SST (ºC)**	**Chl *a* ($mg \cdot m^{-3}$)**	**Notes**
NASPSS	2.71	10.10	T^a <14ºC	*Chl* a ≥ 0.4	
NASTSS	0.96	5.97	11≤T^a <29ºC	0.16 ≤ *Chl* a < 0.4	Latitude ≥ 25ºN
NAICE	0.097	5.48			Sea ice fraction > 0.5

In the eSPNA, the biome NASPSS supposes the 72% of the area, occupying almost all the Irminger Basin and the Iceland Basin (Figure 34). A part of the Eastern North Atlantic, the West European Basin and the Bay of Biscay, is characterized as NASTSS, in agreement with its position to the east of the Subarctic Front [*Daniault et al.,* 2016].

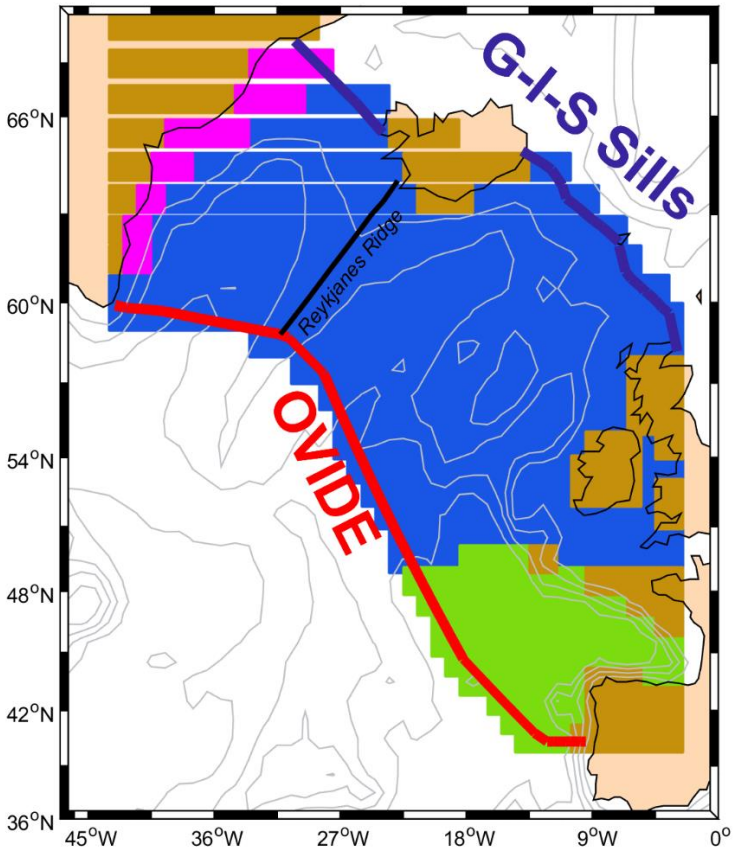

Figure 34. Biome characterization [*Fay & McKinley,* 2014] in the eastern Subpolar North Atlantic (eSPNA). In magenta "North Atlantic Ice" (NAICE), in blue "North Atlantic Subpolar Seasonally Stratified" (NASPSS) and in green "North Atlantic Subtropical Seasonally Stratified" (NASTSS). In brown, not marine areas, or ocean areas that do not fit the criteria for any biome.

The time-series for the period 1992-2009 for each one of the methods and the mean biomes can be downloaded from the SOCOM webpage [last time accessed: 28/06/2017]. There is no data available for NAICE biome in the SOCOM intercomparison dataset. The area contribution of NAICE to our study region is only around 2.5% of the total eSPNA, so it was treated as if it were NASPSS. The inclusion of NAICE area as NASPSS, supposes an increase in the uptake of around 5-7.5 kmol·s^{-1} only depending on the method. The trend of sea-surface pCO_2 follow the atmospheric increase (Figure 4).

The biome-mean sea-air CO_2 flux at each time ($SOCOM_{biome}^{fluxf}$) is then multiplied by the relative contribution of that biome inside eSPNA with respect to the total biome mean area:

$$F^{CO_2\ air-sea} = SOCOM_{biome}^{fluxf} * \frac{Area_{eSPNA}^{biome}}{Area\_biome}$$

In Figure 35 is show the estimated CO_2 uptake for the 1986-2012 period, in Figure 35a) all the mapping models are included; and in Figure 35b) it is represented the mean estimate of uptake when all models are considered together.

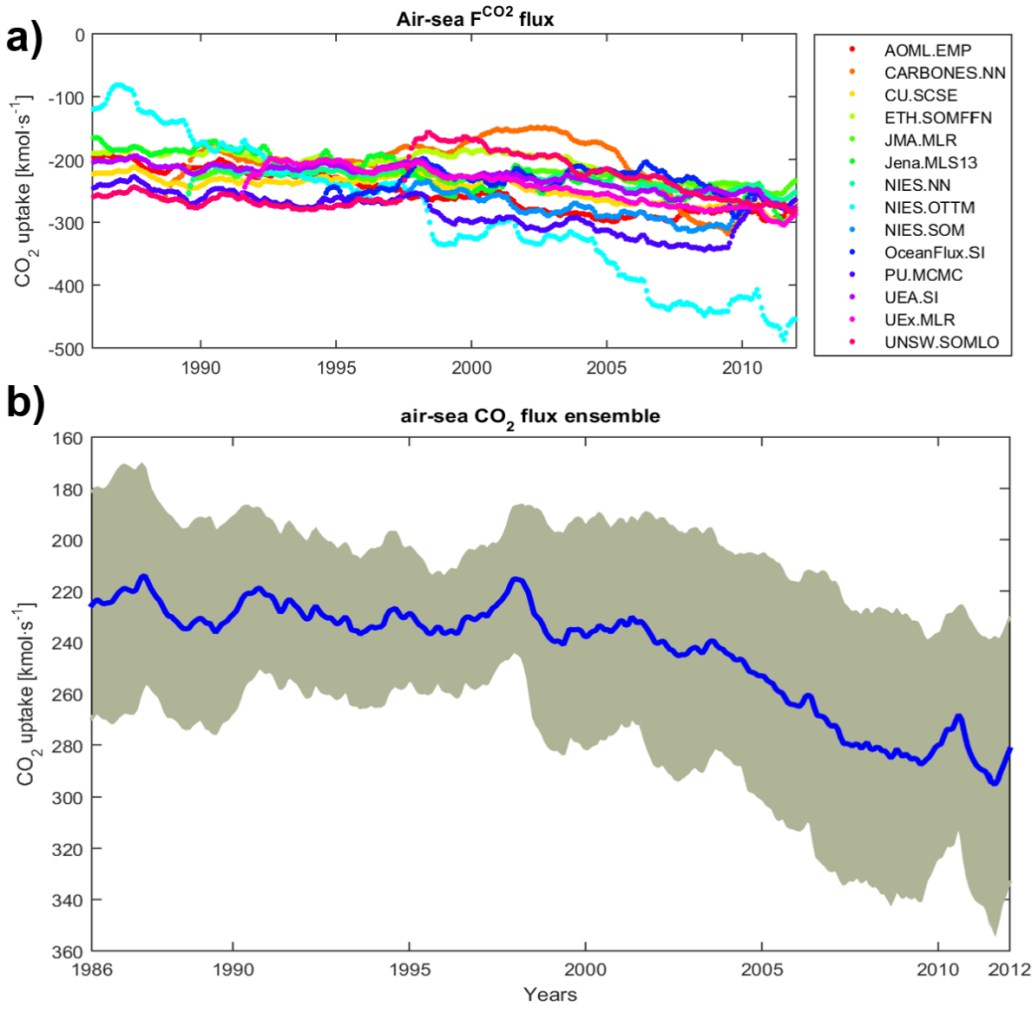

Figure 35. a) averaged air-sea flux of CO_2 (kmol·s^{-1}) over the study region estimated by all mapping methods available at SOCOM. b) averaged air-sea flux of CO_2 (blue line) and standard deviation (gray area) when all models are considered together. For model acronyms, see *Rödenbeck et al.,* [2015]. Carbon units for air-sea fluxes, originally in Pg-C·yr^{-1} in SOCOM, have been transformed at kmol·s^{-1}.

The $F^{CO2\ air-sea}$ used in the study for each one of the boxes comes from the mean uptake flux of 2002-2012 referred to year 2009 using an annual rate of increase of 1.69% [*Steinfeldt et al.,* 2009] and its standard error. Input model values for $F^{CO2\ air-sea}$ with its standard error are showed in Table 8.

The oxygen cycle it is also affected by uptake/release processes in the air-sea interface. Currently, the estimates of oxygen fluxes across oceanic areas show inconsistencies or they are available within a mapping resolution hard to extrapolate to specific locations. The

relevance of the air-sea oxygen exchange in the eSPNA is such that instead of being added as an additional input, it is optimized inside the model as an unknown [*Maze et al.,* 2012].

Input of freshwater from river discharge or meltwater was also considered. The relevance of biogeochemical nutrients reaching the open ocean from riverine sources has gained attention recently [*Sharples et al.,* 2017], so the inclusion of freshwater tracer supplies in the model is more realistic than the assumption that there is no input of nutrients due riverine discharge or meltwater in our area. Besides, the key nutrient nitrate is also affected by inputs coming from atmospheric nitrogen deposition (AND) [*Yang & Gruber,* 2016] and biological nitrogen fixation (BNF) processes [*Jickells et al.,* 2017], that are integrated in the model.

For the carbon variables, DIC, alkalinity and DOC, the external inputs are considered as follows. DIC and alkalinity input from freshwater supply it is calculated from the concentration at the discharge, the flux of freshwater and an assumed density of 1 $kg \cdot m^{-3}$. For the alkalinity concentration in freshwater, we used the regression relationship between alkalinity and sea surface salinity for Atlantic-influenced water, as well as ice melt water for the northern North Atlantic [Eq. 6 in *Nondal et al.,* 2009]. The election of the same concentration for the DIC amount in freshwater it is supported by the fact that in the Nordic Seas carbon budget of *Jeansson et al.,* [2011] both concentrations (DIC and alkalinity) are also similar. For the external inputs of DOC, we considered that DOC inputs from rivers and rainwater affects DOC budgets [*Hansell et al.,* 2004]. The riverine discharge of DOC is estimated combining the mean concentration of DOC in rivers that flow into the eSPNA with the freshwater fluxes used in the model. There are four rivers that flows into the eSPNA whose mean DOC concentration ($mg \cdot L^{-1}$) is available in a global database of riverine DOC inputs to the ocean [*Dai et al.,* 2012]: Severn (UK), Douro (Portugal) and Loire and Garonne (France). The gross mean concentration is 3.3 $mg \cdot L^{-1}$ [*Dai et al.,* 2012]. With the consideration that approximately half of the river DOC flux is mineralized in the estuaries and shelves [*Ludwig et al.,* 1996*; Smith & Hollibaugh,* 1993], the combination of the concentration of DOC in rivers with the flux of water considered in the model results in 4 $kmol \cdot s^{-1}$ in the eSPNA distributed as 0.4 $kmol \cdot s^{-1}$ in the IB and 3.6 $kmol \cdot s^{-1}$ in the ENA. Another external input is the flux of DOC from rainwater. With the global mean rate of atmospheric deposition of 0.26 $g\text{-}C \cdot m^{-2} \cdot yr^{-1}$ [*Wiley et al.,* 2010] the net input in the eSPNA is 2.6 $kmol \cdot s^{-1}$ in the eSPNA distributed as 0.4 $kmol \cdot s^{-1}$ in the IB and 2.2 $kmol \cdot s^{-1}$ in the ENA. The total external input of DOC for the eSPNA, considering both riverine discharge and rainwater flux, is 6.6 $kmol \cdot s^{-1}$ in the eSPNA, distributed as 0.8 $kmol \cdot s^{-1}$ in the IB and 5.8 $kmol \cdot s^{-1}$ in the ENA. These magnitudes are included in the model and affects the DOC budget estimate.

All additional sources are listed in Table 8 and they are fully integrated in the model.

Table 8. Additional inputs and terms in kmol·s^{-1} except for freshwater runoff (Sv)

		eSPNA	Irminger Basin	ENA	Source
	Freshwater runoff (Sv)	0.030	0.003[1]	0.027[2]	[1] [*Hawkings et al.,* 2017] [2] Global Runoff Data Center
Flux from rivers	DIC	17.26	1.61	15.65	[*Nondal et al.,* 2009]*
	Alkalinity	17.26	1.61	15.65	
	Nitrate	1.118	0.036	1.082	[*Sharples et al.,* 2017]
	Phosphate	0.095	0.002	0.094	
	Silicate	4.69	0.44	4.25	[*Dürr et al.,* 2011]*
	DOC	4	0.4	3.6	[*Dai et al.,* 2012]
Atmospheric DOC deposition		2.6	0.4	2.2	[*Willey et al.,* 2000]
Atmospheric Nitrate deposition		1.36	0.22	1.14	[*Yang & Gruber,* 2016]
Nitrogen fixation		5.42	0.39	5.03	[*Jickells et al.,* 2017]
$F^{CO2\ air\text{-}sea}$		274±14	56±3	218±11	[*Rödenbeck et al.,* 2015]¥

* Flux from rivers calculated with the tracer concentration (µm·kg^{-1}) from the source along the freshwater runoff considered here
¥ Mean flux of 2002-2012 referred to year 2009 using an annual rate of increase of 1.69% [*Steinfeldt et al.,* 2009].

6.2.2.3. Storage terms

The storages of all tracers are estimated using OVIDE data and the total inventory time series [*Pérez et al.,* 2010; *Zunino et al.,* 2015]. For each cruise and basin, an integrated tracer inventory for all the water masses and layers was achieved. The storage rate for the period 2002-2016 is the slope of a linear regression over the total inventories with time. The error of each storage rate is the standard error of coefficient estimates. The time-evolution of DIC inventory (mol-C·m^{-2}·yr^{-1}) in each basin is represented in Figure 36, along with the storage of DIC. The relevance of anthropogenic carbon (C_{ant}) in the progressive increase in DIC inventory is such that the temporal variation of DIC is mainly a representation of the C_{ant} uptake.

Estimates of storage rate for each tracer and his associated error for the period 2002 to 2016 are available in the Table 9. The storage rate for the carbon variables DIC and alkalinity –the excess of proton acceptors over proton donors [*Wolf-Gladrow et al.,* 2007]-, can be affected by changes in the salt inventory. In order to evaluate this effect, the storage rate of salinity was also evaluated under the same method. The strong linear relationship between DIC (alkalinity) transports and salinity transports of 62.7±0.5 (66.8±0.2), permit to remove the salt influence in the DIC (alkalinity) storage rate (Figure 37). The difference between the storage rate magnitude represented in the Figure 37 and the magnitude in the Table 9, represents the change mediated by salt effects.

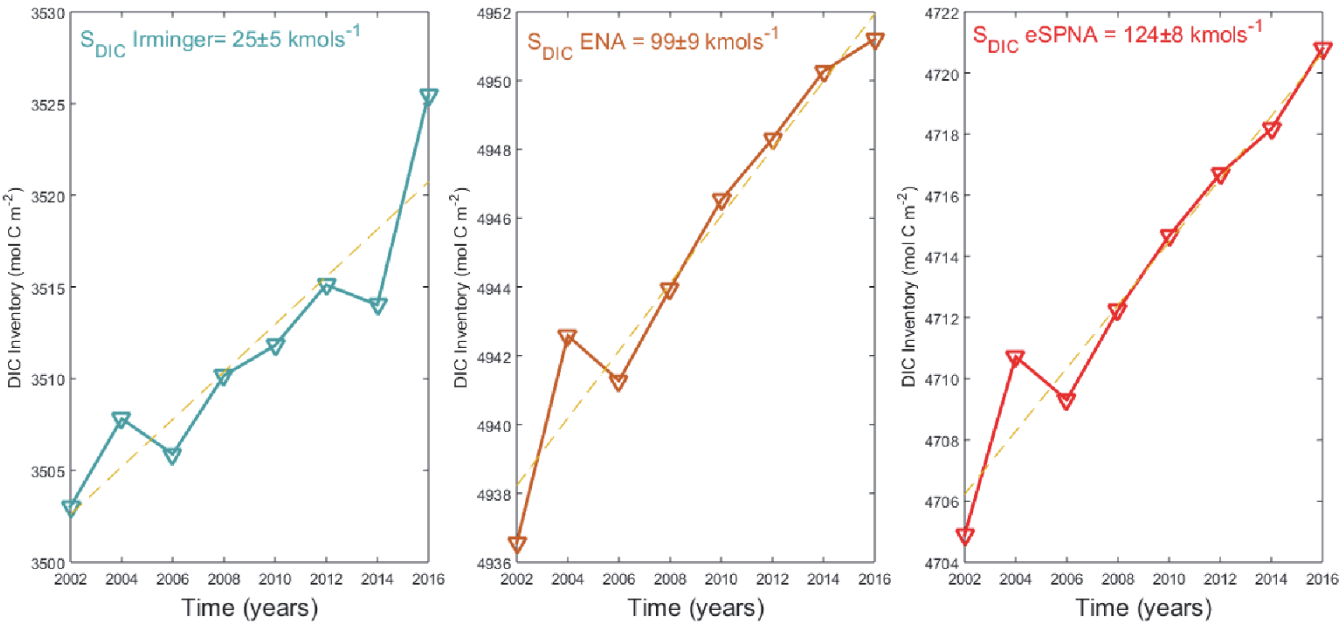

Figure 36. Time evolution of DIC inventory (mol-C·m^{-2}·yr^{-1}) in the Irminger Basin (left plot), ENA (middle plot) and the total eSPNA (right plot) over 2002-2016. The storage rate of DIC in each basin (in kmol·s^{-1} in the upper part of the plot) is the slope of the linear fit (dashed yellow line).

Table 9. Basin tracer storages

Storage rate (kmol·s^{-1})	eSPNA	Irminger Basin	ENA
DIC^{s}	155±7.6^{p}	26.1±4.6 ^{p}	128.9±8.9 ^{p}
Alkalinity^{s}	26.6±20.5	7±3.2	19.6±20.8
Nitrate	-5.5±3.5	-0.71±0.8	-4.8±3.6
Phosphate	-0.32±0.6	0.003±0.07	-0.3±0.6
Silicate	1.6±5.2	0.6±0.2	1±5.2
Oxygen	55.7±27.5	11±5.3	44.7±28
Salt (10^{6} kg·s^{-1})	-0.5±0.2	-0.015±0.06	-0.48±0.2

^{s} The magnitude showed in the table it is corrected with salinity (DIC^{s}=DIC-Salt*62.7; Alk^{s}=Alk-Salt*66.8)

^{p} The magnitude it is statistically significant (p-value<0.005)

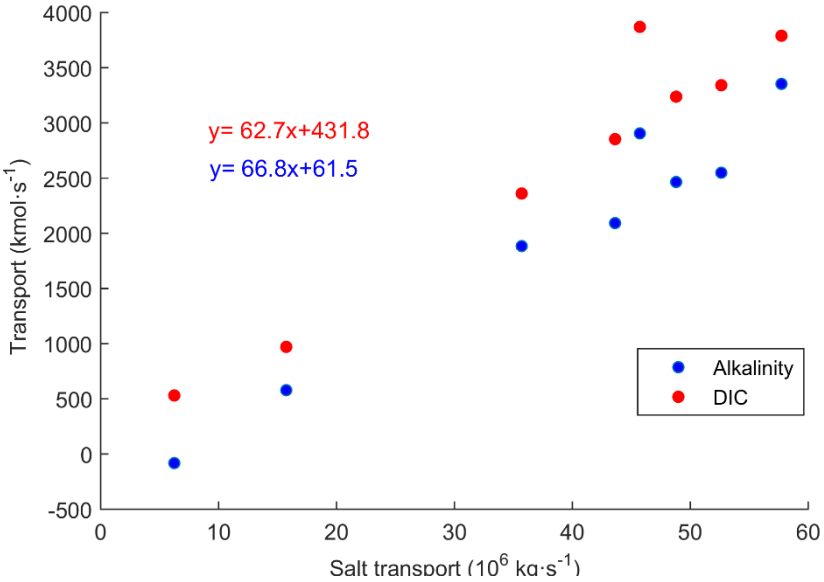

Figure 37. Scatter plot showing the linear relationship between the transport of total dissolved inorganic carbon (DIC, in red) and total alkalinity (blue) in kmol·s^{-1}, with the salinity transport in 10^6 kg·s^{-1}. Equations for the linear fit of DIC (red) and alkalinity (blue) versus salt are also represented.

6.2.2.4. Stoichiometric ratios

The central element in our biogeochemical approach it is the carbon. Following the Redfield ratios of *Anderson & Sarmiento,* [1994], the formation or the mineralization of organic matter can be represented by a chemical equation (Eq.5) with stoichiometric relationship between nutrients (N and P) and oxygen with carbon:

$$(C_{117}H_{110}ON_{16}P)+170\ O_2 \rightarrow 117CO_2+16NO_3^-+PO_4^{3-}+55H_2O \qquad \text{(Equation 5)}$$

The stoichiometric relationships between nutrients, oxygen and carbon of Eq.5 allows the conversion of tracer consumptions to carbon units and vice versa. Remineralization ratios for carbon conversion between biogeochemical elements are included in the model. Taking into account that we are focusing in the net exportation from the whole water column, the election of the ratios needs to reflect the biogeochemical fluxes to the sediment, integrating the processes occurring all along the water column, and not only in the surface. Data and references are listed in Table 10.

The ratios of Si:C are estimated with the depth-dependent parameterization of *Ragueneau et al.,* [2002]. The Si:C molar ratio increases with depth [*Ragueneau et al., 2002*] due slower remineralization of Si compared to C [*Nelson et al.,* 1996]. A global ocean parameterization based on production, export, vertical transport and sedimentation of biogenic silica and organic carbon establish a general equation (Eq. 6) to model the downward increase in Si:C flux ratios [*Ragueneau et al.,* 2002].

$$(Si:C)_z = (Si:C)_0 * z^{0.41} \qquad \text{(Equation 6)}$$

The stoichiometric ratio used inside the model it is the Si:C flux ratio at depth z ($(Si{:}C)_z$), estimated with the Si:C flux ratio during production in surface waters $(Si{:}C)_0$), and the real bottom depth (z). The $(Si{:}C)_0$ value in our area of study it is 0.02, among the lowest values found in the global ocean [*Pondaven,* 1999]. In the North Atlantic, the low silicate concentrations in the upper ocean limits the contribution of diatoms to total production [*Brzezinski & Nelson,* 1996] and the production of diatoms that are not heavily silicified is common [*Nelson & Brzezinski,* 1997]. The downward increase of Si:C flux ratios has been estimated at each geographical point within a grid 6'x6' resolution using a gridded bathymetric data of the General Bathymetric Chart of the Oceans (GEBCO) 2014. The mean values for the Si:C molar ratio are 0.39, 0.34, 0.40 for the whole eSPNA, the Irminger and the ENA respectively.

Table 10. Redfield ratios

$r_{N:C}$	16:117	[*Anderson & Sarmiento,* 1994]
$r_{P:C}$	1:117	[*Anderson & Sarmiento,* 1994]
$r_{Si:C}^{eSPNA}$	0.39	[*Ragueneau et al.,* 2002]
$r_{Si:C}^{Irminger}$	0.34	[*Ragueneau et al.,* 2002]
$r_{Si:C}^{ENA}$	0.40	[*Ragueneau et al.,* 2002]
$r_{O:C}$	170:117	[*Anderson & Sarmiento,* 1994]
$r_{At:N}$	1.36	[*Wolf-Gladrow et al.,* 2007]

6.2.3. Inverse model

A budget of a biogeochemical tracer in any oceanic region is the interplay between its net gains and losses. A generic conservation equation (Eq. 7) must account for lateral advection (mainly oceanic, but also freshwater supplies (Fw_{tracer})), air-sea fluxes of gas exchange ($F_{tracer}^{air-sea}$), atmospheric tracer deposition (ATD) and/or biological tracer fixation (BTF) when exists, and changes in the tracer inventory of the ocean over time (i.e. storage rates) (S_{tracer}). All these magnitudes must be balanced by a sink/source term due biological activity (B_{tracer}):

$$B_{tracer} = -\nabla tracerT + Fw_{tracer} + F_{tracer}^{air-sea} + ATD + BTF - S_{tracer} \quad \text{(Equation 7)}$$

First term of the right side of the equation is the tracer transport divergence ($\nabla_{tracer}T$), the difference between the outputs and the inputs exclusively dependent of oceanic advection. Note that along this document the net uptake of gas by the ocean ($F_{tracer}^{air-sea}$) has positive sign,

since it is an input term for the system. In the general conservation equation, diffusive flux processes due to eddy influence are neglected.

The approach of this study is to combine in a single model a set of interrelated biogeochemical conservation equations to solve, simultaneously, different budgets in such a way that all constraints are satisfied. The model includes conservation equations for six tracers with key roles in biogeochemical cycles: DIC, alkalinity, nitrate, phosphate, silicate and oxygen. Generic conservation equation terms that can be neglected, like for example the atmospheric deposition of silicate, or that simply doesn't exist, like the air-sea flux of alkalinity, are excluded from equations 8-13.

$$B_{DIC} = -\nabla DIC \cdot T + Fw_{DIC} + F^{CO2\ air-sea} - S_{DIC} \quad \text{(Equation 8)}$$

$$B_{Alk} = -\nabla Alk \cdot T + Fw_{Alk} - S_{Alk} \quad \text{(Equation 9)}$$

$$B_{NO3} = -\nabla N \cdot T + Fw_{NO3} + AND + BNF - S_{NO3} \quad \text{(Equation 10)}$$

$$B_{PO4} = -\nabla P \cdot T + Fw_{PO4} - S_{PO4} \quad \text{(Equation 11)}$$

$$B_{SiO4} = -\nabla Si \cdot T + Fw_{SiO4} - S_{SiO4} \quad \text{(Equation 12)}$$

$$B_{O2} = \nabla O_2 \cdot T + F^{O2\ air-sea} - S_{O2} \quad \text{(Equation 13)}$$

The B terms are rates, changes in the pool by unit of time. B_{DIC} represents the sink term for DIC transformations, both related with organic matter (B_{DICorg}) or with the production/dissolution of CaCO3 (B_{CaCO_3}) (Eq. 14).

$$B_{DIC_{org}} + B_{CaCO3} = -\nabla DIC \cdot T + Fw_{DIC} + F^{CO2\ air-sea} - S_{DIC} \quad \text{(Equation 14)}$$

The central carbon term in the model it is B_{DICorg}. With B_{DICorg} we are evaluating the changes in carbon mediated by changes in the pool of nutrients, oxygen and DIC during the net synthesis (or remineralization) of organic matter that follows the classic stoichiometric relationship [*Takahashi et al.,* 1985; *Anderson & Sarmiento,* 1994]. Some biological processes as nitrogen fixation, with a minor contribution, follows a different stoichiometry, so they are taken as an external source, and not considered under the same organic production bulk that follows the Redfield ratios. It is important to note the no inclusion of dissolved organic matter (DOM), especially carbon (DOC), inside the model. There are several reasons: (i) DOM remineralization doesn't follow Redfieldian ratios [*Hansell & Carlson,* 2015] (ii) the budget of DOC in the eSPNA it is practically balanced (see Chapter 5) and (iii) its inclusion would not add more information to the system of equations because its biogeochemical rate of change, B_{DOC}, it is not linked with B_{DICorg} through the synthesis of new organic matter from nutrients –i.e., its inclusion does not constrain any of the equations 8-13.

The biological term of carbonate it is also essential in the alkalinity equation (Eq. 9), because the main sink (source) of alkalinity is the calcification (dissolution) of $CaCO_3$. The sink of alkalinity is also affected by organic matter oxidation, because NO_3, PO_4 and sulfate are produced during remineralization [*Wolf-Gladrow et al.,* 2007]. So, B_{Alk} integrates the interplay between B_{CaCO_3} and B_{Alkorg} (Eq. 15),

$$B_{Alk_{org}} + 2B_{CaCO3} = -\nabla Alk \cdot T + Fw_{Alk} - S_{Alk} \qquad \text{(Equation 15)}$$

with its respective stoichiometric relationship: one-unit decrease in B_{Alk} corresponds to two units decrease in B_{CaCO_3} [*Wolf-Gladrow et al.,* 2007].

With the known stoichiometric relationships, the biological term (B_{Tracer}) for each tracer in the model can be related with the biological drawdown of organic carbon (B_{DICorg}): following the stoichiometric relationships between elements (Table 10). The consumption of N, P, and O_2 (B_{NO3}, B_{PO4}, B_{O2}) can be converted to organic carbon units (B_{DICorg}) with the stoichiometric ratios [*Anderson & Sarmiento,* 1994]. In a similar way, the silicate (B_{SiO4}) to DIC conversion can be obtained with the depth-dependent Si:C ratio parameterization [*Ragueneau et al.,* 2002]. For the change in alkalinity mediated by organic matter (B_{Alkom}), it is necessary to take into account that during the mineralization of the organic matter there is a small decrease of alkalinity, thus it is a negative term, equivalent to 1.36 units in B_N [*Wolf-Gladrow et al.,* 2007]. B_N can then be converted to B_{DICorg} same as before [*Anderson & Sarmiento,* 1994].

The definitive set of conservation equations adapted to each tracer is:

$$0 = -(\nabla DIC \cdot T)^S - B_{DIC_{org}} - B_{CaCO3} + Fw_{DIC} + F^{CO2\ air-sea} - S^S_{DIC} \qquad \text{(Equation 16)}$$

$$0 = -(\nabla Alk \cdot T)^S + r_{AT:N} r_{N:C} B_{DIC_{org}} - 2 \cdot B_{CaCO3} + Fw_{Alk} - S^S_{Alk} \qquad \text{(Equation 17)}$$

$$0 = -\nabla N \cdot T - r_{N:C} B_{DIC_{org}} + Fw_{NO3} + AND + BNF - S_{NO3} \qquad \text{(Equation 18)}$$

$$0 = -\nabla P \cdot T - r_{P:C} B_{DIC_{org}} + Fw_{PO4} - S_{PO4} \qquad \text{(Equation 19)}$$

$$0 = -\nabla Si \cdot T - r_{Si:C} B_{DIC_{org}} + Fw_{SiO4} - S_{SiO4} \qquad \text{(Equation 20)}$$

$$0 = -\nabla O_2 \cdot T - r_{O:C} B_{DIC_{org}} + F^{O2\ air-sea} - S_{O2} \qquad \text{(Equation 21)}$$

Note that nitrate is the only tracer equation affected by inputs from atmospheric nitrate deposition and biological N_2 fixation processes (AND and BNF in Eq. 18), and that oxygen is not affected by freshwater supply (Eq. 21).

Note also that salinity transport is also relevant even if it is not included as a constraint in the model. Same as happened with the storages, salt divergence transports also DIC and alkalinity within, so that effect should be removed in order to get only DIC and alkalinity sinks due to biological processes. In the equations 16 and 17, the tracer divergence corrected by salinity it is expressed as $-(\nabla tracer \cdot T)^S$ and the storages as S^S_{Tracer}. The salinity effect is discounted from

the divergence following the same equation that with the storages and using the tracer transport divergence for salinity, that is 1.27, 0.12 and 1.15 x10^6 kg·s^{-1} for the eSPNA, IB and ENA respectively.

Besides tracer relationships, mass conservation is a mandatory constraint since volume needs to be balanced to avoid biogeochemical biases. With respect to the box-model configuration previously defined (Figure 33), the net transport across OVIDE section (T^{OVIDE}) and the G-I-S Sills (T^{Sills}), its components ($T^{Irminger}$, T^{ENA}, $T^{WestSills}$, $T^{EastSills}$) and the volume transport cross-RR (T^{RR}) are interrelated in the mass conservation equations (Eq. 22-24), along with the freshwater input via rivers and/or melting (T^{fw}).

$$0 = T^{OVIDE} - T^{Sills} + T^{fw} \quad \text{(Equation 22)}$$

$$0 = T^{Irminger} - T^{WestSills} + T^{Irminger_{fw}} \quad \text{(Equation 23)}$$

$$0 = T^{ENA} - T^{EastSills} + T^{ENA_{fw}} \quad \text{(Equation 24)}$$

In order to improve the conservation of mass, the fluxes of the different water masses crossing the sills are going to be also optimized (Table 11), i.e, the model treated them as unknowns. In the linear set of constraints are represented biogeochemical equations: carbon variables (DIC and alkalinity), nutrients (nitrate, phosphate and silicate) and oxygen, along with mass conservation equations. The aim of the model is to evaluate in a single procedure the following unknowns: the sinks/sources of DIC and $CaCO_3$ (B_{DICorg}, B_{CaCO_3} respectively) and the ingass/outgass of oxygen flux ($F^{O2\ air\text{-}sea}$) keeping the coherence between them and the tracer constraints. Defining the tracer conservation equations independently for the three boxes results in a final inverse model configuration made of 21 equations (18 biogeochemical and 3 mass conservation equations) and 16 unknowns (9 biogeochemical – three unknowns B_{DICorg}, B_{CaCO_3}, $F^{O2\ air\text{-}sea}$ for three boxes- and 7 water mass fluxes unknowns).

Due the box-model configuration, any biogeochemical variable in the eSPNA has to be necessarily the sum of the estimates of IB and ENA:

$$X^{eSPNA} = X^{IB} + X^{ENA} \quad \text{(Equation 25)}$$

With this association, the number of biogeochemical unknowns in the system is reduced from nine to six, because it is only needed to know the same variable in two boxes to infer the third. This relationship contributes to enhance the robustness of the model and its biogeochemical coherence, so the model it is finally solved with 21 constraint equations and 13 unknowns. Here, we solved the unknowns for the whole eSPNA and the Irminger, and infer the ENA magnitudes as the difference. Besides, with independence of the two boxes chosen to solve the model, the results are similar (see Appendix 6.5.A. Robustness assesment and sensitivities testing).

The formulation of the inverse model is as follow: Given an a priori state of information for the unknowns (X0) and its associated error covariance matrix (C0), we can define a set of constraints for the unknowns (X) and its error covariance matrix (C_t). The set of formal constraints used in this work are a combination of biogeochemical (Equations 16-21), and mass conservation equations (Equations 22-24). The system is solved using a least-squares method which assumes that unknowns and errors have Gaussian probability distributions. The procedure minimizes a cost function (Eq. 26) using the error covariance matrices as weighting factors in the optimization function and creates an estimate of the unknown that is consistent with both the a priori observation (X0) and the formal constraints f(X)=0.

$$(X - X_0)' \cdot C_0^{-1} \cdot (X - X_0) + \left(f(X)' \cdot C_t^{-1} \cdot f(X)\right) \qquad \text{(Equation 26)}$$

The reader interested in more details regarding the mathematical aspects is referred to *Mercier,* [1986].

Once presented the inverse model setup, the following sub-sections will present 1) how the a priori values of the unknowns were selected; 2) how were computed the known tracer transports terms of the constraints, and 3) how the uncertainties on the constraints were estimated.

6.2.3.1 Velocity and tracer data

The objective of the inversion is to give a value for the biogeochemical unknowns by minimizing –in a least squares sense- the set of constraints (tracers and G-I-S sills water masses volumes) and the distance to the a priori solution. A priori information is by definition implicitly used in the inverse model, therefore a priori choices have to be checked carefully [*Mercier,* 1986]. The source of the a priori state of the model with their error bars is detailed in Table 11.

In our approach there are three principal biogeochemical magnitudes that are going to be optimized by the procedure: B_{DICorg}, B_{CaCO_3} and $F^{O2\ air\text{-}sea}$. B_{DICorg} and $F^{O2\ air\text{-}sea}$ where estimated previously for the same area in [*Maze et al.,* 2012], and its values are going to be our a priori state estimate. During model development and sensitivity testing more possibilities were proved: for B_{DICorg} [*Lee,* 2001; *Zunino et al.,* 2015] and $F^{O2\ air\text{-}sea}$ [*Najjar & Keeling*, 2000], but the election of *Maze et al.,* [2012] as starting point allows to contrast the validity of its findings. Furthermore, this a priori are already defined for each basin of study because *Maze et al.,* [2012] used the same box-model configuration.

To our knowledge, there are no current estimates for B_{CaCO_3} from top-to-bottom $CaCO_3$ exportation adjusted to our area. The closest approach is a synthesis of carbon fluxes to the ocean interior based in sediment traps [*Honjo et al.,* 2008]. In the global parameterization of C in $CaCO_3$ flux at 2000m depth (Fig.10 in *Honjo et al., 2008*), our region of study lies in the range of ~100-200 $mmolC \cdot m^{-2}yr^{-1}$, being around 18 $kmol \cdot s^{-1}$ for the whole eSPNA. With no

more info about how that sink is distributed between the basins, was split at 50% between IB and ENA.

A common characteristic of inverse modelling is that if the errors of the a priori are too narrow, the model loses operability and the optimization procedure it's not able to improve the knowledge of the system. In order to allow a wider range of options, the relative error amplitude of the biogeochemical a priori magnitudes have been settled at 100% for the B_{DICorg} and the $F^{O2}_{air\text{-}sea}$ and 200% for the B_{CaCO_3}. It is a common practice in optimization procedures, and the range of error amplitude applied it's not larger than in *Maze et al.,* [2012]. In the Appendix 6.5.A. Robustness assesment and sensitivities testing of the model, there is also an evaluation of the changes when a priori values and/or the range of errors are modified.

Along with the biogeochemical unknowns, volume fluxes of the water masses crossing the sills are going to be also optimized. The sources of info are also in Table 11 and in the a priori status of the model neither the volume or the error were modified from the original ones.

Table 11. Input and output data

		Input a priori	Source a priori	Output optimized
$B_{DIC_{org}}$ (kmol·s^{-1})	eSPNA	107±107	[*Maze et al.,* 2012]	86±26
	Irminger	51±51		8.5±15
	ENA			78±30
B_{CaCO_3} (kmol·s^{-1})	eSPNA	18±36	[*Honjo et al.,* 2008]	20±27
	Irminger	9±18		9±18
	ENA			11±33
$F^{O2\ air\text{-}sea}$ (kmol·s^{-1})	eSPNA	707±354	[*Maze et al.,* 2012]	856±74
	Irminger	264±528		339±46
	ENA			517±87
Volume Transport^{Sills} (Sv)	SV_{ENACW}^{Sills}	3.9±0.5	[*Østerhus et al.,* 2005]	3.97±0.41
	SV_{MNACW}^{Sills}	3.9±0.5	[*Østerhus et al.,* 2005]	3.93±0.42
	SV_{ISOW1}^{Sills}	-1±0.5	[*Hansen & Østerhus et al.,* 2000]	-1.07±0.41
	SV_{ISOW2}^{Sills}	-2±0.3	[*Hansen & Østerhus et al.,* 2000]	-2.02±0.28
	SV_{NIIW}^{Sills}	0.88±0.13	[*Jónsson & Valdimarsson,* 2012]	0.88_5±0.13
	SV_{PW}^{Sills}	-1.8±0.5	[*Zunino et al.,* 2015]	-1.79±0.32
	SV_{DSOW}^{Sills}	-3±0.4	[*Macrander et al.,* 2005]	-3.00±0.31

6.2.3.2 Tracer transport computation

The importance of the known terms in an inversion is such that inverse-model estimates are as good as the data used to constrain them. Here, the known terms in the constraints are mainly transports of tracers along the limits of the domain. Tracer transport is defined as the product of the net volume flux by density and tracer concentration. At OVIDE, transports (T_{tracer}^{OVIDE}) for each cruise and tracer were computed as in equation 27,

$$T_{tracer}^{OVIDE} = \int_{60^oN}^{40^oN} \int_{bottom}^{surface} v \cdot \rho_{i.s.} \cdot [tracer] dx dz \qquad \text{(Equation 27)}$$

combining the absolute velocity fields orthogonal to the section (*v*) with interpolated tracer data from discrete bottle samples ([tracer]) and in situ densities ($\rho_{i.s.}$) (see Appendix 6.5.B for the vertical distribution of tracers along OVIDE section 2002-2016). The horizontal coordinate goes through the beginning of OVIDE section at 40ºN in Portugal until 60ºN in Greenland. The vertical coordinate is the full-depth water column.

The transport cross-RR and at the G-I-S sills does not have an associated velocity field orthogonal to the boundary. At the G-I-S sills the transports are computed as the product of the volume transport (T_{wm}^{sills}), and the mean tracer concentration ($\overline{[tracer]_{wm}}$) and density ($\overline{\rho_{wm}}$) for each water mass (Eq. 23). The transports crossing the RR are computed as the product of the net volume transport (T^{RR}), the mean tracer concentration ($\overline{[tracer]_{RR}}$), and mean density ($\overline{\rho_{RR}}$) for the whole section (Eq. 29):

$$T_{tracer}^{sills} = \sum_{wm=1}^{7} T_{wm}^{sills} * \overline{[tracer]_{wm}} * \overline{\rho_{wm}} \qquad \text{(Equation 28)}$$

$$T_{tracer}^{RR} = T^{RR} * \overline{[tracer]_{RR}} * \overline{\rho_{RR}} \qquad \text{(Equation 29)}$$

The RR and Iceland allows a physical separation of the T_{tracer}^{OVIDE} and T_{tracer}^{sills} transports in $T_{tracer}^{Irminger}$ /T_{tracer}^{ENA} and $T_{tracer}^{WestSill}$ /$T_{tracer}^{EastSill}$ respectively.The error of the transports across OVIDE section were calculated as the standard error of the mean of the eight cruises during 2002–2016 (s.e. = std/√8). At the G-I-S Sills and cross-RR, analytical computations of errors were performed by means of a perturbation method. Independent normally-distributed perturbations (n=10^6 for each input variable) were generated using as the standard deviation the uncertainties in the Table 6 data. The uncertainties at the G-I-S Sills and cross-RR include both error in the concentrations of the tracer and in the volume transport, assuming that errors in density (ρ) are negligible.

Transports for OVIDE section are in Table 13. All terms required for the estimates of transports cross-RR and at the G-I-S sills are available in Table 8. Along the document, positive (negative) numbers indicates northward (southward) transports.

Transport estimates are the basis of the first term in the general conservation equation (Eq. 5), the tracer transport divergence, which equations are:

$$\nabla tracer \cdot T^{SPNA} = T_{tracer}^{OVIDE} - T_{tracer}^{sills} \qquad \text{(Equation 30)}$$

$$\nabla tracer \cdot T^{Irminger} = T_{tracer}^{Irminger} - T_{tracer}^{WestSills} + T_{tracer}^{RR} \quad \text{(Equation 31)}$$

$$\nabla tracer \cdot T^{ENA} = T_{tracer}^{ENA} - T_{tracer}^{EastSills} - T_{tracer}^{RR} \quad \text{(Equation 32)}$$

Uncertainties calculated without volume conservation framework give results unrealistically large in similar budgets [*Jeansson et al.,* 2011], so the error of the tracer transport divergence were estimated taking into account volume conservation as in [*Zunino et al.,* 2015].

6.2.3.3 Uncertainties on the constraints

The uncertainty on a constraint weights the influence of that constraint in the solution. The weight of each constraint is inversely proportional to its uncertainty. If the uncertainty is too small, the constraint will dominate the solution; and if it is too large, it will have no influence at all. Each term in the constraints (either biogeochemical or volume constraint) have its own associated error integrated in the model. The error of the additional input terms (Table 8), when not available, is settled at 100% relative error amplitude, i.e., as high as the magnitude of the term. Uncertainties on the constraint are computed as the square root of the sum of all squared errors for each equation term. Uncertainties are used as weighting factors in the resolution step (Table 12). In order to achieve volume conservation, the uncertainty on volume conservation at the eSPNA is imposed as a requisite (Table 12, italic number).

Table 12. Uncertainties on the constraints

Uncertainty on the constraint (kmol·s^{-1})	eSPNA	Irminger Basin	ENA
DIC	95	170	101
Alkalinity	127	133	81
Nitrate	9.8	5.6	11.1
Phosphate	0.78	0.69	0.77
Silicate	16.9	6.2	19.7
Oxygen	102	40	68.
Volume (Sv)	*0.00*	5.2	5.2

6.3. Results

6.3.1. Tracer transport data and divergences

The mean transport of the eight cruises with his associated standard error are in Table 13. Net tracer transports at OVIDE section are associated with a northward volume transport of 0.88±0.18 Sv. Taking the section as a whole, the transport of all tracers except oxygen, are

northeastwards or almost zero (NO_3^-, PO_4^-). The 1968±413 kmol·s^{-1} of DIC are advected into the eSPNA while -909±132 kmol·s^{-1} of O_2 are exported from OVIDE to southern latitudes. DOC advection is also considerably, with a mean value of 57±15 kmol·s^{-1}. Net transports at OVIDE section at each side of the RR has opposite signs: is negative (southwards) for the IB, and positive (northwards) at the ENA for volume and all tracers. When combined with the transport data calculated from G-I-S Sills and cross-RR, tracer transports divergences can be obtained.

Table 13. OVIDE transports in kmol·s^{-1}, except for Volume (Sv) and Salinity (10^6 kg·s^{-1})

		Volume	Salinity	DIC	Alkalinity	DOC	O_2	NO_3^-	PO_4^-	SiO_4
OVIDE	**Net section**	0.88±0.18	38.3±6.4	1968±413	2619±444	56.8±15.4	-909±132	-0.04±6.2	-0.8±0.7	4.2±15
	Irminger	-16.2±3.7	-583±134	-35882±8331	-38365±8902	-871±185	-5074±1058	-246±62	-16.4±3.7	-145±38
	ENA	17.1±3.7	621±133	37850±8221	40984±8789	928±185	4164±1018	245±63	15.5±4.1	149±49

6.3.2. Budgets

The output of the model is presented in Table 11 and in Figure 38 and Figure 39. Transports and divergences shown in the budget figures are computed with the optimized volume flux at the Sills (Table 11, Output optimized). Description of the mass budget, the carbon related variables, oxygen and nutrients are described below:

6.3.2.1 Mass budget

Volume transport is conserved in the whole domain (Figure 38A), with a net northward transport at OVIDE section of 0.88±0.18 Sv plus a freshwater input of 0.03 Sv that is balanced by the same amount going through the G-I-S Sills. Western transport across RR is 12.3±3.7 Sv, i.e. around a ~70% of water that enter the eSPNA trough the ENA is recirculated westward to the IB and a ~30% is exported to the Nordic Seas. The magnitude of the volume flux crossing RR is three times the exchanges with the Denmark Strait/Iceland-Faroe-Shetland.

6.3.2.2. Dissolved inorganic carbon budget

The 1968±413 kmol·s^{-1} of DIC are advected into the eSPNA, while 1843±122 kmol·s^{-1} goes northward through the G-I-S sills (Figure 38B). Including the salt correction there is a low divergence of -45±92 kmol·s^{-1} for the whole eSPNA. With that magnitude for the divergence, B_{DICorg} sinks in (Eq. 14) must be conditioned mainly by the opposite sign terms: uptake of CO_2 and storage rate. Air-sea exchange of CO_2 represents an important source of DIC (274±14 kmol·s^{-1}), being accumulated in the region at a storage rate of 155±8 kmols^{-1}. Mainly related

with the surface area, these magnitudes are larger in the ENA (218±11 kmol·s^{-1} for CO_2 ingassing and 129±9 kmols^{-1} for storage rate) than in the IB (56±3 kmol·s^{-1} and 26±5 kmol·s^{-1} respectively). The transport of DIC crossing the RR is controlled by the large net volume transport (27325±7974 kmol·s^{-1}).

6.3.2.3. Alkalinity budget

Being pretty similar as the previous DIC budget, 2619±444 kmol·s^{-1} of total alkalinity are transported northward into the eSPNA, while 2420±45 kmol·s^{-1} are exported through the Nordic Seas (Figure 38C). After salt adjustment, there are an even more larger divergence of -113±125 kmol·s^{-1} for the whole eSPNA, unequally divided between ENA (-43±77 kmol·s^{-1}) and IB (-70±133 kmol·s^{-1}). The amount of alkalinity crossing the RR is 29314±8545 kmol·s^{-1}.

6.3.2.4. Dissolved organic carbon budget

A northward transport of 928±185 kmol·s^{-1} of DOC are advected from subtropical latitudes into the ENA. Of those, 656±195 kmol·s^{-1} cross the RR in westward direction and 303±25 kmol·s^{-1} are exported to the Nordic Seas (Figure 38D). In the IB, the input of -254±26 kmol·s^{-1} through the Denmark Strait and the output of -871±185 kmol·s^{-1} through the OVIDE section are both southwards. The net northward transport into the eSPNA is 57±15 kmol·s^{-1}, while 49±36 kmol·s^{-1} are exported to the Nordic Seas.

The DOC budget can be evaluated following the general conservation equation (Eq. 5):

$$B_{DOC} = -\nabla DOC \cdot T + Fw_{DOC} + ADD - S_{DOC} \qquad \text{(Equation 33)}$$

where S_{DOC}, the storage rate of DOC, has been evaluated with OVIDE data for all basins and layers. Same as in the Chapter 5 for the period 2002-2012, there are no variation in the total inventory of the DOC content when the temporal period is extended until 2016, so $S_{DOC} \cong 0$. The budget of DOC is defined by the tracer transport divergence of DOC and the organic input from freshwater discharge (Fw_{DOC}) and rainwater deposition (*ADD*). DOC transport divergence at the eSPNA is practically balanced (-7.8±7.7 kmol·s^{-1}), but there is a notable difference between IB (-38±14 kmol·s^{-1}) and ENA (30±11 kmol·s^{-1}).

6.3.2.5 Oxygen budget

The 4164±1018 kmol·s^{-1} of oxygen are advected into the ENA via OVIDE section, while -5074±1058 kmol·s^{-1} goes out at the IB, so a total amount of -909±132 kmol·s^{-1} are exported toward southern latitudes from OVIDE section (Figure 39A). This export contrast with the almost balanced situation in the G-I-S Sills. The net transport of oxygen at the sills is even northward, but taking into account the order of magnitude of both sides of the sill fluxes (-1290±14 and 1309±19 kmol·s^{-1} for Denmark Strait and Iceland-Faroe-Shetland respectively) and the error of the net flux (18±28 kmol·s^{-1}) we can say that is indistinguishable from zero.

In the eSPNA there are an important oxygen divergence of 928±102 kmol·s^{-1}, being the divergence at IB (342±40 kmol·s^{-1}), similar in magnitude to ENA (586±68 kmol·s^{-1}) regardless the area difference. Considering that storage rates for O_2 (Table 9) are most than ten times smaller than divergences, the uptake of atmospheric O_2 according with the conservation equation is considerable: 856±74 kmol·s^{-1} for the whole eSPNA, distributed in 339±46 kmol·s^{-1} in the IB and 517±87 kmol·s^{-1} for the ENA. How much of this uptake is mediated by biological processes would be discussed in the discussion section.

6.3.2.6. Nutrient budgets

Nitrate, phosphate and silicate constraints also have a role in the integrated inverse model. Net nitrate advection is virtually zero at OVIDE section (-0.04±6.2 kmol·s^{-1}), and slightly positive at the Sills (1.7±3.2 kmol·s^{-1}) (Figure 39B). Total amount of nitrate is conditioned by the external inputs: river advection, atmospheric deposition and nitrogen fixation; but with a different magnitude between ENA (total input by external sources: 7.25 kmol·s^{-1}) and IB (0.64 kmol·s^{-1}). For the phosphate (Figure 39C), both net transports of -0.8±0.7 kmol·s^{-1} at OVIDE section and -0.9±0.4 kmol·s^{-1} at the G-I-S Sills are southwards, creating a divergence of almost zero in the whole eSPNA (-0.11±0.71 kmol·s^{-1}). Besides that, ENA and IB has small but significant divergences of opposing sign (0.95±0.7 and -1.1±0.7 kmol·s^{-1}, respectively). Magnitudes of silicate transports are larger than for the other nutrients (Figure 39D). At OVIDE section there are a net transport of 4.2±15 kmol·s^{-1}. This northward advection, even with an important error, contrasts with the southward transport of -31.5±4.6 kmol·s^{-1} of silicate at the G-I-S Sills. These advections to the eSPNA, generates a transport divergence for silicate of -35.7±15.2 kmol·s^{-1}. For the silicate budget, this divergence is strongly dissimilar for the IB (2±6.2 kmol·s^{-1}) and the ENA (-37.7±19.2 kmol·s^{-1}).

6.3.3. Biogeochemical estimates optimized by the model

The output of the model is showed in the Table 11. Variables for the eSPNA and the Irminger are optimized inside the model, and the magnitude for the ENA is the difference between them (Eq. 25). The model confirms the net biological production of organic carbon (86±26 kmol·s^{-1}) and $CaCO_3$ (20±27 kmol·s^{-1}), and the ingass of oxygen flux (856±74 kmol·s^{-1}) for the whole area. Biogeochemical estimates of B_{DICorg}, B_{CaCO_3} and $F^{O2\ air\text{-}sea}$ for ENA are larger than for IB, but the contribution of the IB to the total magnitude is larger than it would be based only in its area proportion.

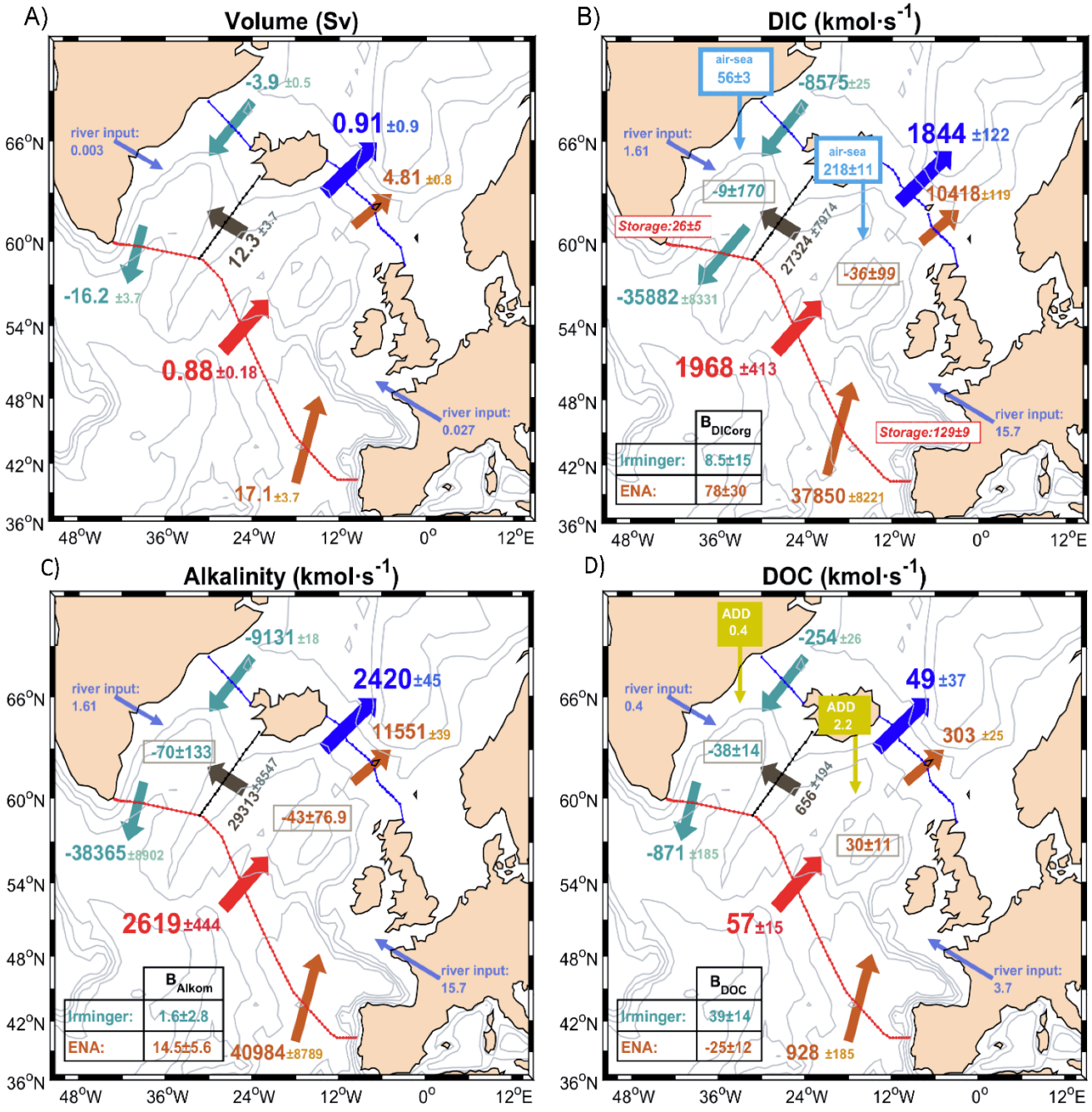

Figure 38. A) volume budget B) Dissolved inorganic carbon budget C) Alkalinity budget D) Dissolved organic carbon budget. Arrows indicate net direction exclusively. The magnitude framed in the center of each box is the tracer transport divergence. The biological term for each tracer along with its uncertainty it is in the left-down corner table. In the DIC budget, due its relevance, air-sea CO_2 uptake is represented with the blue and white square and the storage rate with the red and white square. In the DOC budget, atmospheric DOC deposition (ADD) from rainwater fluxes is represented with the yellow square.

6.3.4. Exportation of organic and inorganic carbon

The central element in our biogeochemical approach it is the carbon. A general exportation equation for total carbon (E_{C_T}) will account the net exportations mediated by the organic and inorganic fractions:

$$E_{C_T} = E_{C_{org}} + E_{C_{inorg}} \quad \text{(Equation 34)}$$

Each one of the export terms needs to be equal to the sum of the net rate of change in the pools that constitute them: the organic pools B_{DICorg}, B_{POC} and B_{DOC} and the inorganic pools, B_{CaCO_3} and B_{PIC}.

$$E_{C_T} = E_{C_{org}} + E_{C_{inorg}} = B_{DIC_{org}} + B_{POC} + B_{DOC} + B_{PIC} + B_{CaCO3} \quad \text{(Equation 35)}$$

Under the assumption that the inventory of POC and PIC are in steady state (B_{POC} and $B_{PIC} \cong 0$), and that the exportation of inorganic carbon corresponds exclusively to calcium carbonate ($E_{Cinorg} = E_{CaCO3}$) all pools of carbon relevant to production and export in the whole water column have been evaluated.

Here, we are going to evaluate the contribution to the exportation of organic and inorganic matter separately: the total net export of organic carbon combining the estimates for B_{DICorg} and B_{DOC} (Figure 38B & D) and the inorganic carbon with B_{CaCO_3}.

$$E_{C_{org}} = B_{DIC_{org}} + B_{DOC} \quad \text{(Equation 36)}$$

$$E_{CaCO3} = B_{CaCO3} \quad \text{(Equation 37)}$$

According to Eq.36, the final exportation of organic carbon is 101±27 kmol·s^{-1} in the whole eSPNA, distributed as 48±21 kmol·s^{-1} in the IB and 53±32 kmol·s^{-1} in the ENA. The IB, with a 16% of the total area in the eSPNA, is the place where almost 48% of organic carbon export occurs. According to Eq. 37, exportation of calcium carbonate equals the B_{CaCO_3} value, so we found a net export of carbonate of 20±27 kmol·s^{-1} for the eSPNA. This net exportation is distributed as 9±18 kmol·s^{-1} taking place in the IB, and 11±33 kmol·s^{-1} in the ENA.

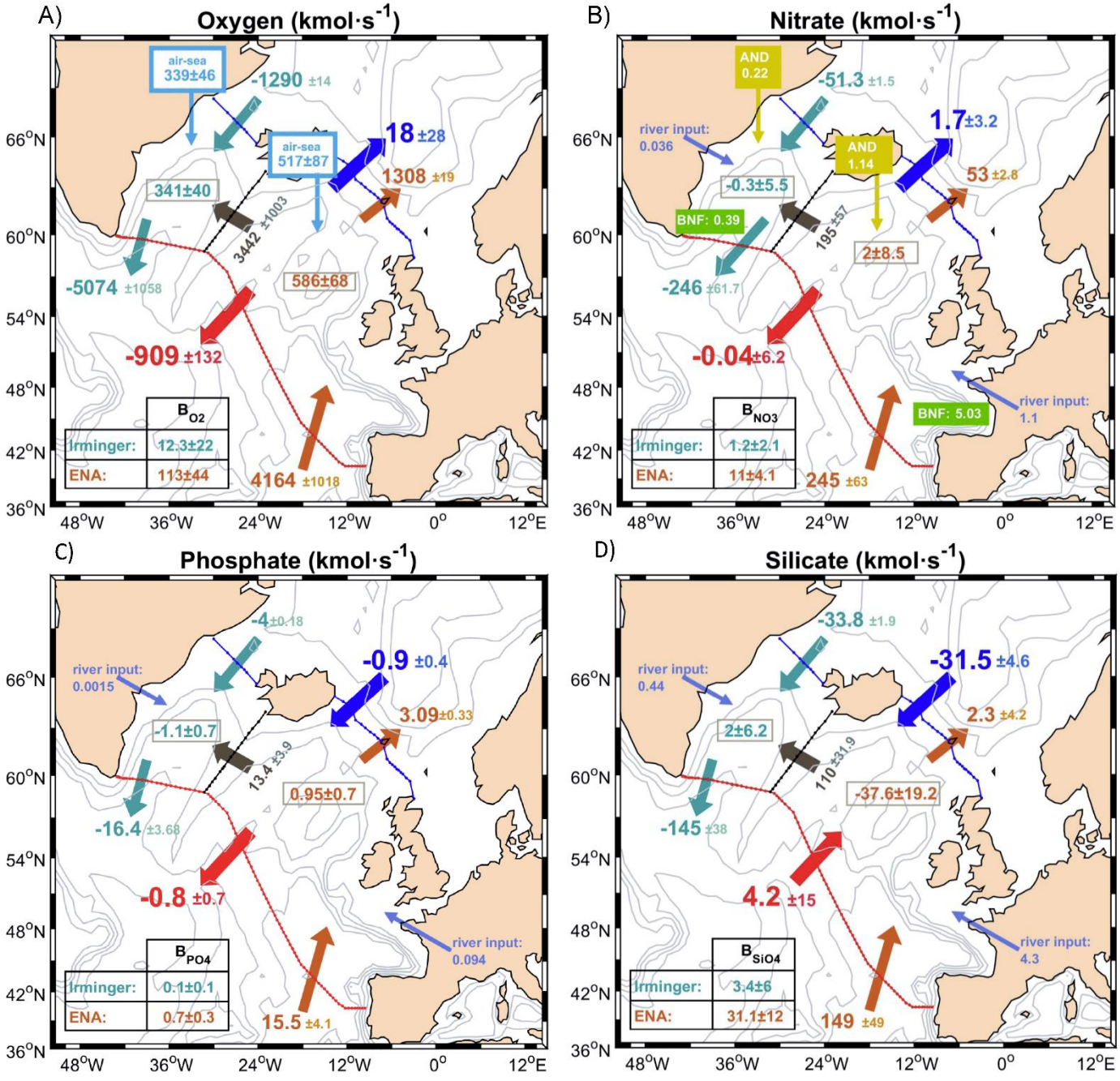

Figure 39. A) oxygen budget B) nitrate budget C) phosphate budget D) silicate budget. The magnitude framed in the center of each box is the tracer transport divergence. The biological term for each tracer along with its uncertainty it is in the left-down corner table. In the nitrate budget, due its relevance, atmospheric nitrogen deposition (AND) and the biological nitrate fixation (BNF) are represented with the yellow and the green square respectively.

6.4. Discussion

This is not the first attempt to close a carbon related budget for the identical area: in *Maze et al.,* [2012] is done for mass, nitrate, phosphate and oxygen and in *Zunino et al.,* [2015] is done for DIC. This new study has some differences/improvements with both of them:

1) It is the first time that carbon, nutrients and oxygen are valued together as a whole, keeping its biogeochemical interrelationships. In *Maze et al.,* [2012] there were no carbon variables and in *Zunino et al.,* [2015] neither nutrients or oxygen.

2) The carbon variable alkalinity and the macronutrient silicate are included for first time.

3) The temporal range is longer (2002-20016) than in *Maze et al.,* [2012] (2002-2006) and *Zunino et al.,* [2015] (2002-2010).

4) Precisely, the number of cruises (8) allows the evaluation of changes in the inventory over time, i.e., storage rates. Storages rates for each tracer in each basin are estimated instead of been assumed constant, and included in the model.

5) Tracer concentrations at the RR are from cruise data (29AH20160617) instead of World Ocean Atlas [*Maze et al.,* 2012]. The separation between basins mediated by the RR was not present in the DIC budget [*Zunino et al.,* 2015].

6) Sills tracer data are validated and/or modified from real measured data from GLODAPv2 [*Olsen et al.,* 2016].

7) Other inputs/outputs with potential to alter biogeochemical cycles in the system were included in the model: freshwater inputs, atmospheric deposition and biological fixation.

8) It is the first time that the carbonate exportation (E_{CaCO3}) is evaluated and that the budget of organic carbon takes also into account DOC.

6.4.1. Robustness of the model

In this section we address the strengths and limitations of our model resolution. First of all, the oceanic transports and divergences can be considerably improved through the averaging of repeated sections [*Ganachaud & Wunsch,* 2002]. Here we show total transports supported by eight repetitions of OVIDE section, a number quite considerable for a basin-scale section.

Our approach has a number of limitations that must be kept in mind, being the most important the influence of the seasonal variability. With regard to the transports, the MOC circulation at the timing of OVIDE section (June-July) is close to the mean circulation state [*Mercier et al.,* 2015]. With regard to the changes in tracer concentration due seasonality, they might affect both lateral boundaries (OVIDE section and G-I-S sills) in the same way. Then, seasonal variability can be neglected in the surface layer without generate any important seasonal bias in

the tracer transport divergence. Seasonal variability does not affect the storage rate term because all cruises were made in the same season.

Several criteria were required for the output of the model to be considered acceptable: It was required a decrease in the residuals of the constraints with respect to the input; it was required that unchanged results were obtained when a section is removed; and also independent final results with regard of the initial box-model configuration election. Sensitivities testing modifying the stoichiometric ratios or the a priori values and/or its range of errors were also done. In order to evaluate the robustness of our results, a set of tests have been performed, and their results are in Appendix 7.A: Robustness assessment and sensitivities testing.

The main finding it was that the unknowns B_{DICorg} and $F^{O_2\ air\text{-}sea}$ were quite insensitive to initial guesses of the a priori and its relative error amplitude, while B_{CaCO_3} was more conditioned by the initial input. This information points to the fact that B_{DICorg} and $F^{O2\ air\text{-}sea}$ are constrained enough and its results can be taken with confidence. On the other hand, the inclusion of B_{CaCO_3} in the model helps to constrain and better define B_{DICorg}, but its individual results must be taken with caution.

6.4.2. Mass

The mean circulation for the North Atlantic has been recently reviewed using altimetry and OVIDE data until 2012 [*Daniault et al.,* 2016]. The temporal extension of this study does not alter the mean circulation pathways or the transport estimates, regardless the change of the North Atlantic in the regimen of heat status from warm to cold since then [*Yashayaev & Loder*, 2016; *Zunino et al.,* 2017]. About ~40% of Atlantic water crossing 59.5ºN is exported to the Nordic Seas, and the rest recirculates cyclonically inside the Subpolar Gyre [*Sarafanov et al.,* 2012]. Here, our distribution is ~30% export versus ~70% recirculation, coincident with *Maze et al.,* [2012]. The difference with *Sarafanov et al.,* [2012] can be explained for the southern latitude in the intersection of RR with OVIDE section. Light-to-dense water conversion inside the subpolar gyre leads that almost 80% of volume crossing the RR overturns to compose, together with the overflows, the southward flowing lower limb of the AMOC [*Sarafanov et al.,* 2012].

In *Maze et al.,* [2012] it was assumed that tracer concentrations were better known than mass transports, so the volume fluxes were optimized inside the model for all the faces. In our approach, we are assuming that mass transports at OVIDE section are strong enough after eight repetitions to take it as a constraint, i.e. only the volume fluxes at the G-I-S Sills are optimized. This is a crucial difference between model set-ups because it is implicit in our assumption that the system would improve the biogeochemical knowledge on the basis of a well-known circulation.

The results of the inclusion as unknown of the volume flux of each water mass crossing the G-I-S Sills supports the notion of small interannual and seasonal variability in its transports [*Hansen & Østerhus,* 2000, 2007; *Jochumsen et al.,* 2012]. At the sills, transports are restricted by bathymetry and well constrained by current estimates available in literature, so optimized mean changes suppose less than 0.03 Sv, and have never been greater than 0.07 Sv for the water masses at the G-I-S Sills. The volume flux crossing the RR in western direction (12.3±3.7 Sv) is in close agreement with [*Daniault et al.,* 2016] (11.3±4.3 Sv) and it is between the range of 9.1-15.6 Sv proposed by other methods [*Bower et al.,* 2002*; Sarafanov et al.,* 2012*; García-Ibáñez et al.,* 2015].

As a general depiction of the circulation, the non-exported flux is recirculated in the subpolar gyre, cross the RR in westward direction and arrives the IB. The IB is a well-recognized deep water formation area [*Lherminier et al.,* 2010*; Sarafanov et al.,* 2012], where surface waters sink, joins the overflows and becomes the southward lower limb of the AMOC. Deep water formation due AMOC combined with regular deep convection events [*de Jong & de Steur,* 2016; *Piron et al.,* 2016] makes the IB a hotspot for tracers to be long-time sequestered in the deep ocean. This general circulation pattern is applicable to all the tracers.

6.4.3. Dissolved inorganic carbon

As was appointed in *Zunino et al.,* [2015], biological activity is not properly considered in the majority of DIC budgets. DOC source and sinks were included in a Nordic Seas carbon budget [*Jeansson et al.,* 2011], but also without establishing a link with primary production. One noticeable exception is [*Álvarez et al.,* 2003], who considered the production/consumption of DIC due respiration/photosynthesis. Under our approach, the combination of macronutrient drawdown relates primary production with B_{DICorg} sink and then with exportation of organic carbon.

For the eSPNA, transports and budget of DIC for the period 2002-2016 are consistent with *Pérez et al.,* [2013] and *Zunino et al.,* [2015]. The DIC transports are intrinsically related with volume transports, and the variability in DIC transport depends on the variability of volume transport [*Zunino et al.,* 2015]. Carbon-laden waters from subtropical latitudes reaches the eSPNA already saturated in anthropogenic carbon [*Pérez et al.,* 2013]. Around a third of the DIC that enters the eSPNA via ENA cross the G-I-S Sills, becoming the principal input of DIC to the Nordic Seas [*Jeansson et al.,* 2011]. Besides the DIC budgets of *Zunino et al.,* [2015] and *Pérez et al.,* [2013] already discussed, there was a previous attempt for an inorganic carbon budget in the North Atlantic [*Álvarez et al.,* 2003]. The direct comparison with our results is not valid since the area of *Álvarez et al.,* [2003], includes the Arctic, but some insights can be contrasted. They found a notably southward transport of DIC for section WOCE A25 (-1015±490 $kmol \cdot s^{-1}$), a section with transports comparable with OVIDE [*García-Ibañez et al.,* 2015]. The possibility of a mean net southward transport for DIC is discarded within the eight

repetitions of OVIDE section used in this study (p-value<0.002), so we can conclude that inorganic carbon is unequivocally transported northward in the North Atlantic. The difference between our results and those of *Álvarez et al.,* [2003] are related with a better characterization of the East Greenland Current (EGC) in the IB in the velocity field [*Lherminier et al.,* 2007]. A northward transport across the G-I-S Sills minor than 800 kmol·s^{-1} was previously estimated [*Jeansson et al.,* 2011], whereas here we show that the amount is more than 1800 kmol·s^{-1}. Discrepancies in the net volume crossing the G-I-S sills in northward direction (~0.4 Sv in *Jeansson et al.,* [2011], ~0.88 Sv here) can explain the difference.

The storage rate for the period 2002-2016 is practically identical with the one found by the period 2002-2010 [*Zunino et al.,* 2015], and statistically large than the 113±34 kmol·s^{-1} estimate of *Tanhua & Keeling,* [2012]. Our basin-scale approach to the total inventories included the whole water column, not only the first two thousand meters [*Tanhua & Keeling,* 2012], and the eight repetitions of OVIDE section used here give more confidence in the accumulation trend (p-value<0.001).

The air-sea flux of CO_2, $F^{CO2\ air\text{-}sea}$, has been revisited (section 6.2.2). Using the ensemble of data from SOCOM [*Rödenbeck et al.,* 2015], the uptake was estimated at 274±14 kmol·s^{-1}. The robustness in the uptake of $F^{CO2\ air\text{-}sea}$ for the 2002-2012 period is such that the standard error considering all models is less than 14kmol·s^{-1} for the whole eSPNA. The magnitude of the uptake is clearly higher than the magnitude used in *Zunino et al.,* [2015] (164±53 kmol·s^{-1}) based in *Takahashi et al.,* [2009] even when rescaled to year 2009 (not shown). In the Nordic Seas carbon budget of *Jeansson et al.,* [2011], the residual term that closes the budget it was the net uptake of atmospheric CO_2, with an estimate as high as 502±158 kmol·s^{-1}. Then, it is reasonable our magnitude for $F^{CO2\ air\text{-}sea}$, reflecting that the eSPNA acts as a CO_2 sink but with a smaller uptake than in the Nordic Seas.

There is a positive trend for CO_2 uptake in our region since 2000's (Figure 35), so in the eSPNA the sink is currently reinvigorated as in global scale [*Landschützer et al.,* 2016]. Noting that the S_{DIC} magnitude is similar here and in *Zunino et al.,* [2015], and that $F^{CO2\ air\text{-}sea}$ is increased, one would expect following the general conservation equation that given approximately the same transport divergence between *Zunino et al.,* [2015] and this study, the B_{DICorg} term would be much higher for the eSPNA. Here it is where the optimization model makes sense. A resolution exclusively dependent of the DIC budget, would close the balance with greater exportation terms, in order to fulfill the conservation equation. The integrated approach with the optimization method solves the budgets together, constrained by the biogeochemical relationships, increasing the coherence of the system and the consistency of the results. With an optimized output for B_{DICorg} of 85±26 kmol·s^{-1}, the eSPNA it is confirmed like an important sink of inorganic carbon.

In the election of a priori estimate to initialize the model, we could had chosen *Zunino et al.,* [2015] result instead of *Maze et al.,* [2012]. If we use -113±103kmol·s^{-1} ([*Zunino et al.,* 2015], Table1) as a priori for B_{DICorg}, the final result is pretty identical. This is due the similarity

between *Zunino et al.,* [2015] and *Maze et al.,* [2012] results, and also because the system is robust enough and well-determined.

6.4.4. Alkalinity

To our knowledge, this is the first alkalinity budget in the North Atlantic. It is interesting to add the alkalinity budget for two reasons: from a biogeochemical point of view because the production of $CaCO_3$, a structural element widely used in marine life, supposes an increase of two moles in alkalinity for each mole of $CaCO_3$ that precipitates (Eq. 17); on the other hand, from a methodological point of view because the B_{CaCO_3} term becomes constrained by two tracer conservation equations instead of one, allowing a large adjustment proficiency to the model. Alkalinity transports and divergences are pretty similar in magnitude and behavior than the DIC previously described, in fact their horizontal transports through the eSPNA are approximately two orders of magnitude larger than any other tracer implied in the carbon balance. Salty waters with high alkalinities are advected by the North Atlantic Current (NAC) inside the ENA. In their path along the subpolar gyre, water is progressively freshened, and alkalinity charge diminished. Alkalinity is a conservative tracer that is diluted (concentrated) by precipitation (evaporation) [*Carter et al.,* 2014]. The saltier a water mass is, the higher will be its alkalinity concentration. The unique previous published estimates for North Atlantic alkalinity transport concluded that it is not significantly different from zero at WOCE A25 section [*Álvarez et al.,* 2003] while it is as high as -71.280 $kmol \cdot s^{-1}$ going southward at subtropical latitudes (24.5ºN) [*Rosón et al.,* 2003]. As was appointed in the previous DIC discussion, a posterior reevaluation of the velocity field for that same cruise by *Lherminier et al.,* [2007] found notably differences in the EGC in the IB. Here, the balance in alkalinity transport between the flux southward at the IB and the flux northward at the ENA face of OVIDE section is 2619±444 $kmol \cdot s^{-1}$, but the net transport is strongly conditioned by the net volume transport, same as DIC. The range of alkalinity concentration for the water masses crossing the G-I-S Sills is 59 $\mu mol \cdot kg^{-1}$. The highest values are in the surface of the Iceland-Faroe-Shetland Channel (both Eastern/Modified North Atlantic Central Water) and the smallest in the surface of Denmark Strait (Polar Water). This fact creates a notably difference in the mean velocity-weighted alkalinity between the eastern channel flowing northward (2314 $\mu mol \cdot kg^{-1}$) and the southward flowing western strait (2290 $\mu mol \cdot kg^{-1}$). Iceland acts as a topographic barrier separating relatively salty waters at the east going northward from relatively fresh waters at the west going southwards.

Even after the salt-influence correction to the divergence and the storage rate is applied, the alkalinity budget it is imbalanced in the eSPNA. Currently, a convergence of 113±125 $kmol \cdot s^{-1}$ of alkalinity is taking place. Despite the important uncertainty associated, what are the reasons for such increase? With the effect of the salinity changes removed, and the fact that total alkalinity does not change with the ingassing or outgassing of CO_2 from the ocean [*Carter et al.,*

2014]; biogeochemical processes such as calcium carbonate precipitation or organic matter production must take a role [*Wolf-Gladrow et al.,* 2007]. In the alkalinity conservation equation (Eq. 17) there are two biological terms with opposing signs: B_{CaCO_3} and B_{Alkorg}. We found an exportation of $CaCO_3$ of 20±27 kmol·s^{-1} for the eSPNA distributed almost equally between basins. The output is consistent with the previous knowledge, with an export that varies little geographically [*Honjo et al.,* 2008]. A revised global carbonate budget established a flux into deep sediment traps of 0.4 mmol-$CaCO_3$·m^{-2}d^{-1} [*Berelson et al.,* 2007], that when scaled to the eSPNA would be close to the value found here (17 kmol·s^{-1}). Here, the annual export in the ENA (11 kmol·s^{-1}) is ~100 mmol-C·m^{-2}yr^{-1}, in agreement with annual fluxes of carbonate at 2000 m depth of 136±67 mmol-C·m^{-2}yr^{-1} for the biogeochemical region North Atlantic Drift [*Honjo et al.,* 2008] and 120±50 mmol-C·m^{-2}yr^{-1} for the Porcupine Abyssal Plain [*Lampitt et al.,* 2010].

Carbonate dissolution from sediments to water column could alter the budget value found here because we are assuming that changes in the carbonate pool are only related with processes of organic matter production/remineralization occurring in the water column. Carbonate dissolution from sediments to the water column can occur at any depth, but is significantly greater than 0 in zones below ~3000 m depth [*Berelson et al.,* 2007]. The area deeper than 3000 m depth in the IB is almost inexistent, with the exception of the main channel in the central Irminger (~3100 m). In the ENA there are a large proportion of zones below that depth (36%). If dissolution processes occurring in the sediment affect the budget estimates, it is reasonable to think that the ENA region will show the larger biases. Diffusive fluxes of carbonate from sediments would be another input in our top-to-bottom water column budget, but has not been evaluated, so the magnitudes for the B_{CaCO_3} export could be underestimations, especially for the ENA.

6.4.5. Dissolved organic carbon

For the period 2002-2016, the DOC divergence for the eSPNA (7.8±7.7 kmol·s^{-1}) is equal to the budget for the period 2002-2012 (8±77 kmol·s^{-1}) discussed in the previous Chapter 6. The diminished error in the actual result (7.7 vs 77 kmol·s^{-1}) is due the volume conservation error calculation, the inclusion of more cruises, and the no separation between upper and lower limb of the MOC.

Although the balance is close to zero, the contrast between the IB and the ENA is remarkable. While the ENA has a deficit of -30.3±11 kmol·s^{-1}, in the IB 38.1±14 kmol·s^{-1} of DOC have influence in the total exportation of organic carbon. It is the first time that this basin-separation is examined, and its biogeochemical relevance must be discussed. Oceanic DOC produced in the euphotic zone is horizontally redistributed by wind-driven circulation [*Hansell et al.,* 2009], and the western advection of DOC relatively enriched layers mediated by the NAC branches and subpolar mode waters recently formed over the RR contribute to the deficit of DOC

observed in the ENA. In the eSPNA, the fast export of DOC mediated by the AMOC, results in the sink observed at the IB, a basin where almost the whole column belongs to the lower limb of the AMOC.

An evaluation of the dissolved organic nutrient budgets for the Arctic Ocean give an estimate of -3.79±0.77 kmol·s^{-1} for dissolved organic nitrogen (DON) when considering a volume transport of -0.87±0.17 Sv flowing south in the EGC [*Torres-Valdés et al.,* 2016]. The EGC polar outflow current considered in *Torres-Valdés et al.,* [2016] is analogous to our PW flux, but the magnitude considered here for PW transport is greater (-1.76±0.32 Sv). The DON samples analyzed in *Torres-Valdés et al.,* [2016] are located in the Denmark Strait, so using our current flow for PW and taking into account that the stoichiometry of DOC:DON deviates substantially from Redfield ratios (199:20) [*Hopkinson & Vallino,* 2005], the amount of DOC flowing southwards will be around -77 kmol·s^{-1}. This value for PW transport of DOC is lower than the one used here, -129±40 kmol·s^{-1}. An important contribution in the southern flow, not considered in *Torres-Valdés et al.,* [2016] and suggested by us as the reason of the difference, is the high load of dissolved organic nutrients existent in the overflows [*Benner et al.,* 2005]. As we show in the Chapter 6, both DSOW and ISOW are important sources of DOC to the eSPNA, where they are components of the North Atlantic Deep Water.

6.4.6. Nutrients

There are a few studies about nutrient transports across North Atlantic sections [*Álvarez et al.,* 2002; *Ganachaud & Wunsch,* 2002; *Lavín et al.,* 2003; *Maze et al.,* 2012; *Torres-Valdés et al.,* 2013]. Using data from WOCE, -130±50 kmol·s^{-1}, 10±35 kmol·s^{-1} and 1.1±2.5 kmol·s^{-1} of silicate, nitrate and phosphate are respectively transported at 47ºN [*Ganachaud & Wunsch,* 2002]. A section near OVIDE reported a southward export of -26±15 kmol·s^{-1}, -50±19 kmol·s^{-1} and -6±2 kmol·s^{-1} for silicate, nitrate and phosphate respectively [*Álvarez et al.,* 2002]. Even when the nutrients transports for OVIDE section in 2002-2006 [*Maze et al.,* 2012] are extended to 2002-2016, there are differences: the published northward transport of 11±16 kmol·s^{-1} for nitrate are now negligible -0.04±6.2 kmol·s^{-1}, while phosphate transport it is still similar (0.2±1 kmol·s^{-1} in *Maze et al.,* [2012], -0.8±2 kmol·s^{-1} here).

At the northern limit of the eSPNA, the closest published fluxes for nutrients are from the Arctic gateways [*Torres-Valdés et al.,* 2013]. Taking into account the fluxes across the Fram Strait and the Barents Sea Opening, the fluxes of silicate, nitrate and phosphate in northward direction would be 6.2±6 kmol·s^{-1}, 23.3±9 kmol·s^{-1} and 1.5±0.9 kmol·s^{-1}, respectively. There are important discrepancies between these magnitudes and the fluxes showed here for the G-I-S sills. Attending at the nitrate, the difference between the amount of nitrate crossing the sills and this estimate is more than 20 kmol·s^{-1}. For the silicate the difference is even greater between the northern input to the Arctic reported in *Torres-Valdés et al.,* [2013] and the southward flux reported here, there are a difference of almost 40 kmol·s^{-1}. Phosphate is not controversial,

mainly because all fluxes are so small that they are always around zero. If this estimates are certain, the Nordic Sea – the region comprehended between the eSPNA and the Arctic gateways- would be a source for nitrate and silicate. The unique physically based mass-balanced export of nutrients from the Arctic Ocean was evaluated within a single summer cruise (year 2005) [*Torres-Valdés et al.,* 2013]. The range of values for the eight physically based mass-balanced transports repetitions of the OVIDE section showed here, spans ~6.5 kmol·s^{-1} for phosphate, ~49 kmol·s^{-1} for nitrate and ~114 kmol·s^{-1} for silicate with a range of volume of 1.47 Sv. This is where the strength of the utilization of multiple section repetitions arises. Even under the reasonable assumption that the variability in volume is smaller in the Arctic gateways influenced by Atlantic water, a unique repetition may not represent the mean status.

There are substantial differences in the nitrate budget shown here (Figure 39B) and the budget published for the period 2002-2006 (Fig. 2A in *Maze et al.,* [2012]). The strong organic matter production in *Maze et al.,* [2012] was supported by a nitrate divergence as high as 3.7±17.5 kmol·s^{-1} and 5.2±17 kmol·s^{-1}, for the ENA and the IB respectively. The higher concentration of nitrate in the ENA face of the OVIDE section was pointed as the cause for the divergence in the ENA box; whereas the amount of nitrate crossing the RR was the main agent in the divergence of the Irminger box. Here we show that the nitrate divergence due oceanic advection is -2±8 kmol·s^{-1} and 0.4±5 kmol·s^{-1}, for the ENA and the IB respectively, then -1.6±5.7 kmol·s^{-1} for the whole eSPNA. Besides a non-existent northward transport of nitrate, the reason pointed in *Maze et al.,* [2012] as the causative of the horizontal convergence in the ENA box is no longer sustained: the top-to-bottom eastern side of the OVIDE section (ENA-OVIDE face) is not richer in nitrate than the cross-RR face. There are two complementary explanations for this fact. First, upper water nutrient concentrations decrease from the subpolar to the subtropical gyre, and the ENA-OVIDE face cross a intergyre section to the east of the Subarctic Front (SAF) between the subpolar and the subtropical gyre [*Pollard et al.,* 1996]. Second, the amount of subtropical poor-nutrient waters reaching the ENA has become more important since the beginning of the 2000's due weakening of the subpolar gyre [*Johnson et al.,* 2013].

It is under this balanced oceanic advection of nitrate when external inputs show its influence. Inputs of nitrogen to the ocean have potential to increase productivity [*Jickells et al.,* 2017]. At the eSPNA, the total external input is 7.9±5.7 kmol·s^{-1}. The decision to include external inputs of river origin for all the tracers it is sustained by the projected increase in freshwater discharge at high latitudes with global warming [*Peterson et al.,* 2002], and for the high proportions of riverine nutrients that could reach the open ocean unmodified by shelf biogeochemistry [*Sharples et al.,* 2017]. Furthermore, the influence of Greenland ice sheet melting in biogeochemical cycles is higher than previously considered [*Hawkings et al.,* 2016; 2017]. BNF, the main external source of nitrogen to the open ocean, is taken from the biogeochemical model PlankTOM [Figure 2 in *Jickells et al.,* 2017]. The inclusion of the BNF magnitude is supported with the fact that *Trichodesmium* cyanobacteria, the most representative of marine N_2 fixers, is present at North Atlantic high latitudes [*Rivero-Calle et al.,* 2016] and that

measurable BNF is detected throughout the year in the ENA [*Moreira-Coello et al.,* 2017]. The AND magnitude is taken from an evaluation that captures the increase in the anthropogenic perturbation since preindustrial times (Fig. 2c in *Yang & Gruber,* [2016]). Combining the nitrate transport divergence with the total external nitrogen input, the whole eSPNA would present a net uptake of 6.2 kmol·s^{-1} if no nitrate accumulation were taking place in the eSPNA as was hypothesized in *Maze et al.,* [2012]. This magnitude is still far from the more than 16 kmol·s^{-1} of nitrate that they transformed into carbon units [*Anderson,* 1995] to obtain 107 kmol·s^{-1} of whole water column exportation. Furthermore, the assumption that the temporal accumulation of nitrate can be neglected was evaluated here. When the storage rate of NO_3^- (Table 9) is considered, the net uptake of nitrate in the whole eSPNA is even smaller, around 1 kmol·s^{-1}. Here we show that a budget exclusively dependent of nitrate would conclude that, under the same stoichiometric ratios applied in *Maze et al.,* [2012] [*Anderson,* 1995], the B_{DICorg} term would be smaller than 5 kmol·s^{-1}. This is clearly not the case, and it is another prove for the relevance of evaluate interrelated budgets as a whole.

The silicate budget (Figure 39D) is strongly conditioned by the dissimilar divergence existent between IB and ENA. Whereas the silicate in IB it is in balance inside the uncertainty, here we show that the ENA is a considerable sink for this macronutrient. The amount of silicate crossing the RR in westward direction is not enough to approximate the divergences. The vertical distribution of silicate in the ocean shows a typical profile of lower concentrations in the upper layers increasing with depth, so deep-sea basins shows the higher concentrations in silicate. The advection of silicate cross-RR it is conditioned by the mean depth of the ridge, less than 1500 m in the deepest point considered here, so the mean concentration advected for silicate (8.63±0.01 µm·kg^{-1}, Table 6) is representative of intermediate layers. The ISOW is the responsible water mass for the largest amount of silicate advected into the ENA, and it is the water mass present at the bottom of the eastern flank of the RR [*García-Ibañez et al.,* 2015; 2017]. ISOW enriched-silicate transport could cross the RR out of the ENA through the deepest gaps, but the main pathways for the cross transport of ISOW –Charlie Gibbs Fracture Zone and Bight Fracture Zone- are located farther south than our limit [*Kanzow & Zenk,* 2014; *Bower & Furey,* 2017].

6.4.7. Oxygen cycle

Southward exportation of oxygen from high latitudes has long been recognized [*Gruber et al.,* 2001; *Bopp et al.,* 2002]. Published North Atlantic oxygen transports agree in the southward direction but span a considerable range of values: -924±314 kmol·s^{-1} at OVIDE section [*Maze et al.,* 2012], -1992±440 kmol·s^{-1} at WOCE A25 [*Álvarez et al.,* 2002], -1750±500 kmol·s^{-1} at 47ºN [*Ganachaud & Wunsch,* 2002]. Apparently, there is an increasing trend in Equator direction, with even larger oxygen southward transports observed at 24ºN: -2070±600 kmol·s^{-1} [*Ganachaud & Wunsch,* 2002] and -2621±705 kmol·s^{-1} [*Lavín et al.,* 2003]. The NAC advects

subtropical waters poor in oxygen inside the eSPNA. In the eastern part of the ENA there is even an input of low oxygen Mediterranean Water (MW) [*García-Ibañez et al.,* 2015]. The inputs of highly oxygenated water masses from the Nordic Sea: overflows (ISOW, DSOW) and PW; counteracts the outflow of waters advected by the NAC and there is no net flux of oxygen at the G-I-S sills. During the cyclonic recirculation in the eSPNA and its returning south as a Deep Western Boundary Current (DWBC) in the IB, the waters are cooled and affected by convection processes. Both cooling (thermal effect) and convection (dynamical effect) imply oxygenation [*Bopp et al.,* 2002], so the final balance is the exportation of well-oxygenated waters southward, here reported as high as -909±132 kmol·s^{-1} of oxygen. The magnitude is comparable with the published for the period 2002-2006 [*Maze et al.,* 2012], and it is considerably constant among cruises. The formation of North Atlantic Deep Water (NADW) is the principal mechanism for the southward flux of oxygen.

The oxygen cycle accounts in the biogeochemical model, and the interrelationships between oxygen, nutrients and carbon allows to evaluate the net biological production of oxygen through photosynthesis (Eq. 21): a total of 12.3±22 kmol·s^{-1} and 112±58 kmol·s^{-1} for the IB and the ENA respectively sets the eSPNA as a net autotrophic region. The ingass/outgass of oxygen flux ($F^{O2\ air\text{-}sea}$) it is an optimized variable. The model resolves an uptake of oxygen as high as 856±74 kmol·s^{-1} for the whole eSPNA, even greater than the a priori selected as starting point, the air-sea oxygen flux estimated by *Maze et al.,* [2012] (707±96 kmol·s^{-1}). The optimized estimate is relatively insensitive to the a priori testing, and the uptake magnitude for O_2 is maintained when other starting points like for example the ~240 kmol·s^{-1} of uptake found in *Najjar & Keeling,* [2000] were selected. It is an evidence of a system well constrained by observations. The distribution of the net uptake, with an ingassing of 339±46 kmol·s^{-1} in the IB and 517±87 kmol·s^{-1} in the ENA implies that in the IB occurs almost the 40% of the uptake despite being only the 16% in area. In the IB, the uptake is dominated by the intense southward flow of the waters carried by the EGC that leads to an important heat lose [*Lherminier et al.,* 2007] and the regular deep convection events that occurs in the Irminger Sea [*de Jong & de Steur,* 2016; *Pickart et al., 2003*; *Piron et al.,* 2017]. Mixing events can lead to air-sea oxygen fluxes if water masses undersaturated/oversaturated in oxygen reaches the air–sea interface. In the ENA, the role of vertical mixing in the uptake of oxygen is considerable because the oxygen vertical distribution [*Maze et al.,* 2012]. The existence in the ENA of a layer poor in oxygen due remineralization processes can be seen in the vertical distribution of apparent oxygen utilization (AOU, difference between measured O_2 and its saturation concentration) (Figure 40). Convective events upwells undersaturated water masses located just below the thermocline depth, resulting in a large mixing flux uptake of oxygen [*Maze et al.,* 2012].

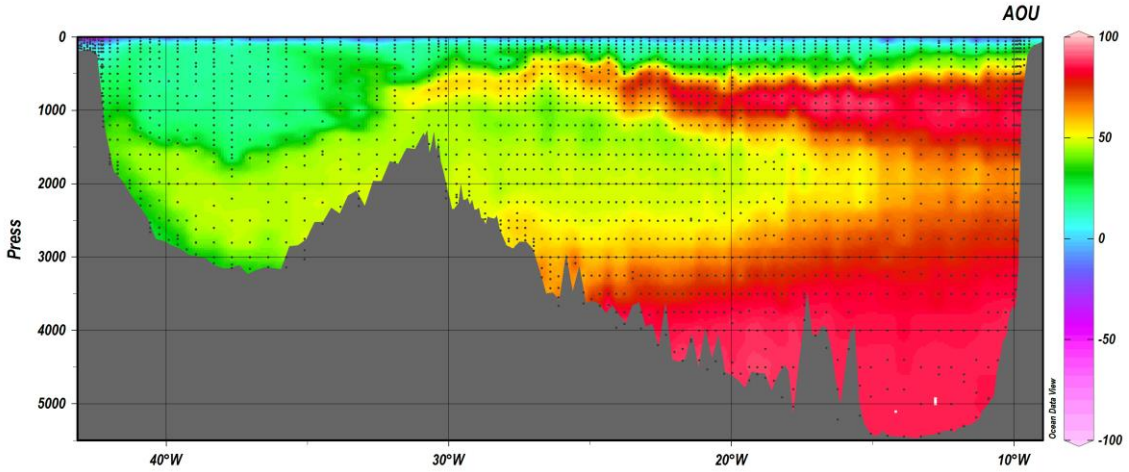

Figure 40. Apparent oxygen utilization (AOU) vertical distribution along the OVIDE 2016 section from Greenland (left) to the Iberian Peninsula (right). Sampling points are indicated as black dots.

The increase of temperatures by global warming will lead to ocean deoxygenation by a decrease of O_2 solubility in warmer waters (thermal effect) along with changes in ocean circulation (dynamical effect) [*Bopp et al.,* 2002; *Keeling et al.,* 2010]. Dissolved O_2 in seawater equilibrates so fast with the atmosphere that a heat uptake will be shown as an oxygen release and vice versa [*Sarmiento & Gruber,* 2006]. Assigning a maximum air-sea O_2 flux of ~1500 kmol·s^{-1}·for each PW (10^{15} W) of heat released [*Holfort et al.,* 1998], the uptake of O_2 found here, 840±79 kmol·s^{-1}, would represent a heat loss of 0.56±0.05 PW. It is in agreement with the mean northward heat transport observed in OVIDE in the period 2002-2010, 0.47±0.05 PW [*Mercier et al.,* 2015], and with the 2014 cruise (0.56±0.06 PW), whose transport was due mainly by the overturning circulation [*Zunino et al.,* 2017]. The main agent for heat and oxygen redistribution in the eSPNA it is the circulation mediated by the AMOC. At global scale, dynamical effects like surface stratification and the consequent decrease in the formation of intermediate and deep water masses are the main contributors to ocean deoxygenation [*Bopp et al.,* 2002]. Paradoxically, the fast overturning inherent to the AMOC role in the eSPNA it is also a dynamical effect but with the opposite effect: the downward export of waters saturated in O_2 due recent ventilation imply an oxygenation of the deep ocean. Earth system models predict a very likely slow-down of the AMOC by 2100 [*Ciais et al.,* 2013] that would lead to a reduction in the deep eSPNA ventilation and a consequent deoxygenation [*Tagklis et al.,* 2017]. Here, at interannual scale and during the temporal framework of our analysis, neither AMOC slow-down or O_2 decrease are appreciable. The no detection of deoxygenation within a fourteen-year time series agrees with the late time of emergence over natural variability necessary to detect a decrease in oxygen content in the subpolar gyre (predicted by 2060-2080) [*Henson et al.,* 2017].

In the whole Atlantic Ocean there is a significant deoxygenation trend for the period 1980-2005, dominated by the subpolar North Atlantic with a mean negative trend around -105±58 kmol·s^{-1}

[*Tanhua & Keeling,* 2012]. This results contrasts with the found here: a relatively constant export of oxygen from the eSPNA to southward latitudes, an important uptake of oxygen and a positive storage rate for the whole domain (55.7±27.5 kmol·s^{-1}, Table 9). In the latest years of our time span, a succession of winters with positive phase of the North Atlantic Oscillation (NAO) and strong heat loss by atmospheric forcing, has led to deep convection events in the Labrador and Irminger Seas [*de Jong & de Steur,* 2016; *Yashayaev & Loder,* 2016; *Piron et al.,* 2017]. For example, the deepening of convection during winter 2014-2015 reached 1700 m and 1400 m of winter mixed layer at the south of Greenland and the IB respectively [*Piron et al.,* 2017]. As a result, it was developed a very thick LSW vintage ($LSW_{2012-2016}$) [*Yashayaev & Loder,* 2016], and oxygen concentrations are high in the entire winter mixed layer due recent ventilation [*Fröb et al.,* 2016; *García-Ibáñez et al., 2017*]. The supply of oxygen is directly enhanced after deep convection events in the IB. In the ENA, the expected spreading of the newly formed LSW will bring oxygenated waters in the incoming years, so by the moment, there are no any deoxygenation signal in the eSPNA despite the existence of oxygen minima related with the MW spreading. Furthermore, with regard to the storage rate contrast, as was also appointed in the DIC discussion, *Tanhua & Keeling,* [2012] included only the first two thousand meters. Our inventories accounts for the whole-depth water column, then including the high-oxygen overflows waters. Even so, the North Atlantic is one of the regions where the natural variability of oxygen is largest [*Frölicher et al.,* 2009]. The seasonal variability of oxygen fluxes (uptake in fall-winter and release in spring-summer) is maximum between 50º-60º latitude [*Bopp et al.,* 2002]. The cruises take place during summer, so under a theoretical phase of oxygen release due warming and/or biological processes. Nevertheless, the results show an unequivocal uptake of oxygen, so probably the $F^{O2\ air\text{-}sea}$ estimate found here could be a lower limit in the annual cycle of the eSPNA.

6.4.8. Organic carbon sinks

We are going to discuss in this section the total export of organic carbon (E_{Corg}), represented by the sum of the net drawdown of carbon transformed in organic matter (B_{DICorg}) and the net change in the DOC pool (B_{DOC}). We concluded that 101±27 kmol·s^{-1} of organic carbon are exported in the eSPNA, distributed practically at 50% between the IB (48±21 kmol·s^{-1}) and ENA (53±32 kmol·s^{-1}). This result is in agreement with the magnitude (107 kmol·s^{-1}) and the relative contribution to the exportation of each box found by nutrients consumption [*Maze et al.,* 2012].

A global parameterization for the exportation of POC based in sediment traps set a mean global value of 120 mmol·m^{-2}·yr^{-1} at 2000 m depth [*Honjo et al.,* 2008]. In that parameterization, the eSPNA shows values notably larger for an open ocean site, ranging between 200-1000 mmol·m^{-2}·yr^{-1} (Figure 9 in *Honjo et al.,* [2008]). If this magnitude is scaled to the extension of the eSPNA the total exportation of POC would be between 24-120 kmol·s^{-1}. The magnitudes of *Honjo et al.,* [2008] are defined for zones with depths below 2000 m. In the eSPNA there are

large areas with important primary production that are above this limit: east Greenland shelf, the RR or the Rockall Bank (NW of Ireland). Then, the organic carbon export found here is in the upper range of *Honjo et al.,* [2008]'s values.

The contribution to E_{Corg} is similar at the two sides of the RR, but what can be the reasons behind the dichotomy IB/ENA observed in B_{DICorg} and B_{DOC}? While the export in the ENA is sustained by biological drawdown of DIC, in the IB the recycling of DOC contributes to the carbon fixation and the dominant processes of export are related with changes in the B_{DOC}. Net primary production (NPP) is similar in the IB and the northern part of the ENA [*Falkowski et al.,* 1998]. In the northeastern North Atlantic, only a 0.6-1.2% of the annual organic carbon PP reaches depths greater than 3000 m [*Lampitt et al.,* 2010], so the possible differences in PP are not enough to explain the contrast in B_{DICorg}. The abundance and composition of plankton community it is correlated with the magnitude of the export [*Guidi et al.,* 2016]. The plankton community structure at the IB is dominated by diatoms (microplankton) and affected by spring blooms events [*Sanders et al.,* 2005; *Henson et al.,* 2006]. In the ENA the calcifying nanoplankton have a larger relative relevance, with its occurrence increasing since 1965 [*Rivero-Calle et al.,* 2016] and with common blooms of coccolitophores (haptophytes) [*Iglesias-Rodríguez et al.,* 2002; *Harlay et al.,* 2010]. The "ballast hypothesis" holds the idea that biogenic carbonate act as effective ballast increasing organic carbon export [*Klaas & Archer,* 2002]. If the different contribution to B_{DICorg} export were based in a higher relevance of the biogenic carbonate production and consequent exportation, this will lead also to a dichotomy in the inorganic carbon exportation that could be seen in the E_{CaCO3}, i.e., we would expect a much higher carbonate sink in the ENA than in the IB. That is not the case, so a community structure with greater presence of calcifying phytoplankton can't explain the difference between boxes existent in B_{DICorg}. The traditional view for organic carbon export assumes that diatom-dominated phytoplankton communities, with its bigger size and with the ability to form aggregates are efficient POC-exporters out of the upper ocean [*Guidi et al.,* 2009]. Opposed to that vision, and supported by the longest time series of sediment trap in our region of study, carbon export to the deep ocean can be greater when diatoms are outcompeted by other phytoplankton-dominated communities (mostly dinoflagellates) [*Henson et al.,* 2012b]. The unexpected evidence that some plankton functional types as prokaryotes, radiolarian and viruses can potentially contribute to carbon exportation in oligotrophic regions [*Guidi et al.,* 2016], needs to be contrasted in eutrophic regions like the eSPNA as an alternative way to find why the IB with a diatom-dominated community structure doesn't have a larger B_{DICorg} export than ENA.

The remineralization length, the depth by which 63% of POC flux has been remineralized [*Baker et al.,* 2017], is deeper in warmer than in cold waters [*Marsay et al.,* 2015]. In the eSPNA, the ENA has higher temperatures, so the remineralization by heterotrophic bacteria should be favored with respect to the IB that is a colder basin. If the temperature-dependent remineralization of the organic matter were the prevalent process, one would expect higher remineralization of sinking particles in the ENA than in the IB. Surprisingly, the IB belongs to a

biogeochemical province who shows one of the highest mesopelagic remineralization flux in the world (34 mmol-C $m^{-2}·d^{-1}$, *Honjo et al.,* [2008]). That magnitude would suppose a mesopelagic respiration in the IB of 240 $kmol·s^{-1}$. Under a similar production and a similar ecological community status, maybe the difference can be related with our finding of the important remineralization of DOC that occurs in the IB.

The representability of sediment traps it is being discussed in recent times due the increasing relevance of slow-sinking particles in the total flux [*Alonso-Gonzalez et al.,* 2010*; Riley et al.,* 2012*; Villa-Alfageme et al.,* 2014, 2016*; Baker et al.,* 2017]. The potential contribution of this particles, usually smalls and with sinking speeds <$100m·d^{-1}$ [*Villa-Alfageme et al.,* 2016], are probably not accounted for in models of export based in deep sediment traps like *Honjo et al.,* [2008] especially because they are mostly remineralized in the mesopelagic zone [*Riley et al.,* 2012]. Under our approach, we integrate the whole-water column transports with independence of assumptions about the biogeochemical behavior of sinking particles, so the export mediated by slow-sinking particles it is included in our estimates. We suggest that this contribution to the export it is the main reason behind the large values found here.

The relevant role of the eSPNA in the DOC cycling influences the organic carbon exportation (E_{Corg}). The disequilibria in the DOC exportation, with the ENA acting as a source and the IB as a sink, equilibrate the relation of export between the two boxes of the eSPNA. In the IB, the advected DOC-enriched and the in-situ formed water masses, suffer downwelling processes and fill the deep ocean with non-refractory DOC. The result is that near 50 $kmol·s^{-1}$ (~18 Pg-C yr^{-1}) of organic carbon are exported in each box of the eSPNA, regardless the area extension.

The ratios of E_{Corg}/E_{CaCO3} found here are 4.4, 5.2 and 3.7 for the whole eSPNA, IB and ENA respectively. They agree with the relationship between E_{Corg}/E_{CaCO3} in the model parameterization of *Honjo et al.*, [2008] for our region of study. With annually averaged sediment trap data the ratio has been found as 1.4 in the northeast Atlantic [*Lampitt et al.*, 2010], close to the global scale ratio of 1.1 [*Honjo et al.*, 2008], but showing temporal periods of ratios larger than 5 [*Lampitt et al.*, 2010]. Higher ratios imply an enhanced sequestration for each unit of organic carbon produced [*Antia et al.*, 2001; *Lampitt et al.*, 2010] along with a reduced loss of alkalinity from the surface ocean [*Honjo et al.*, 2008]. The smaller ratios in the ENA that in the IB can be related with a greater relevance of calcifying phytoplankton in that basin, as was appointed previously.

Table 14. Summary of the biogeochemical estimates solved by the model expressed in different units.

		kmol·s^{-1}	Tg·yr^{-1}	mol·m^2·yr^{-1}
$E_{C_{org}}$	eSPNA	101±27	38±10	0.8±0.2
	Irminger	48±21	18±8	2.5±1
	ENA	53±32	20±12	0.5±0.3
$B_{DIC_{org}}$	eSPNA	86±26	32±10	0.72±0.2
	Irminger	8.5±15	3±6	0.44±0.8
	ENA	78±30	29±11	0.77±0.3
B_{CaCO_3}	eSPNA	20±27	7.5±10	0.16±0.2
	Irminger	9±18	3±7	0.46±0.9
	ENA	11±33	4±12	0.11±0.3
$F^{O2\ air\text{-}sea}$	eSPNA	856±74	432±37	7.1±0.6
	Irminger	339±46	171±23	17.5±2
	ENA	517±87	261±44	5.1±0.9

Summarizing, using a linear inverse box model constrained by biogeochemical relationships, sources and sinks of carbon, nitrate, phosphate, silicate and oxygen were estimated in the eSPNA. The combination of several repetitions of the high-quality hydrographic section OVIDE with public available data sources allows the assessment of biogeochemical cycles in an integrated budget model. This approach based in transports allows a quantitative evaluation with independence of assumptions about biogeochemical behavior and with an output consistent between tracers.

On decadal time scale, this biogeochemical budget confirms that the region acts as an important atmospheric carbon sink. The eSPNA is a net autotrophic region where biological primary production exceeds respiration with an organic (inorganic) carbon export to bottom/sediment layer of 101±27 kmol·s^{-1} (20±27 kmol·s^{-1}). The connection of the northward upper limb with the southward lower limb of the AMOC mediated by deep water formation processes lead to tracer export. The Irminger Sea, located at the confluence of the two limbs of the AMOC is a hotspot for tracers to be long-time sequestered in the deep ocean: represents the 48% of the organic and 46% of the $CaCO_3$ sediment flux being less than 20% in area. The contribution of DOC to total carbon exportation is especially relevant in the eSPNA, particularly in the Irminger.

We suggest that light-to-dense water formation processes occurring in the eSPNA are the reason for the oxygen uptake (856±74 kmol·s^{-1}) and the heat release, and that the transport of high-oxygen waters in the lower limb of the AMOC is the principal mechanism for the southward flux of oxygen.

With increasing atmospheric CO_2 levels, the assumption that the biological carbon cycle it is in steady state would require further evaluation. Within the variability observed in the time period

2002-2016, there are not important changes in the surface-to-bottom biological carbon cycle in the eSPNA. The combination of observations coming from different methodologies and the utilization of open access databases along with modelling efforts, allowed to analyze carbon fluxes in a dynamical complex region within an integrated approach. These results have to be accounted to constrain global ocean carbon models and can be taken as a baseline in future evaluations of carbon cycle in the North Atlantic.

6.5. Appendix

Appendix 6.5.A: Robustness assessment and sensitivities testing

In order to evaluate the robustness of our results, a series of tests have been performed:

Residuals of the constraints after inversion

If the mathematical optimization worked, it is expectable a decrease in the majority of the residuals of the constraints with respect to the input. In order to visualize the optimization provided by the inverse model in the final resolution, and taking into account that the residuals in the equations between different tracers have different orders of magnitude, in the Figure 41 the values represented are typified, i.e., the residual of each equation has been divided by the uncertainty on the constraint equation (Table 12).

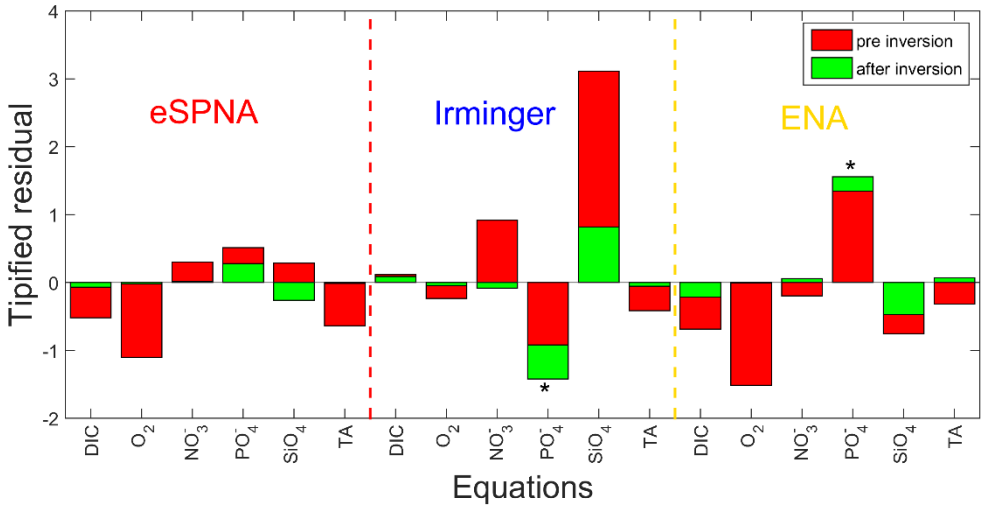

Figure 41. Bar plot representation of the typified residuals of the constraint equations pre-inversion (red bar) and after inversion (green bar) for the biogeochemical equations. Note that when the green bar is not visible it is because is very close to zero. X-label inform of the tracer equation. The red (yellow) dash line separates IB from eSPNA (ENA).

As can be seen in Figure 41, the improvement in the residuals is a generalized feature of the model, the typified residual pre-inversion is usually greater than the typified residual after-inversion. This means that the final output enhances the knowledge of the system without compromise its internal consistency. There are only two equations that do not meet the residual improvement criteria: the phosphate equations in the Irminger and ENA. The inverse model gives us an output that is the best estimate among the information possibilities, and included in that possibilities is the existence of contradictory constraints inside the model, so it is normal if

the residual of some constraints with minor importance it is not reduced. The magnitudes involved in the transports and budgets of the phosphate equations are with difference the smaller among all the tracers considered, so the range of improvement was also the lesser. Nevertheless, the influence of phosphate in the final output is minor and can be said that the inverse model output accomplishes the optimization and improves the knowledge of the biogeochemical system proposed.

Unknown errors after inversion

If the mathematical optimization worked, the error of the unknowns after inversion should be inferior than the a priori errors. After the inversion, error bars for the unknowns are always smaller than before (Figure 42).

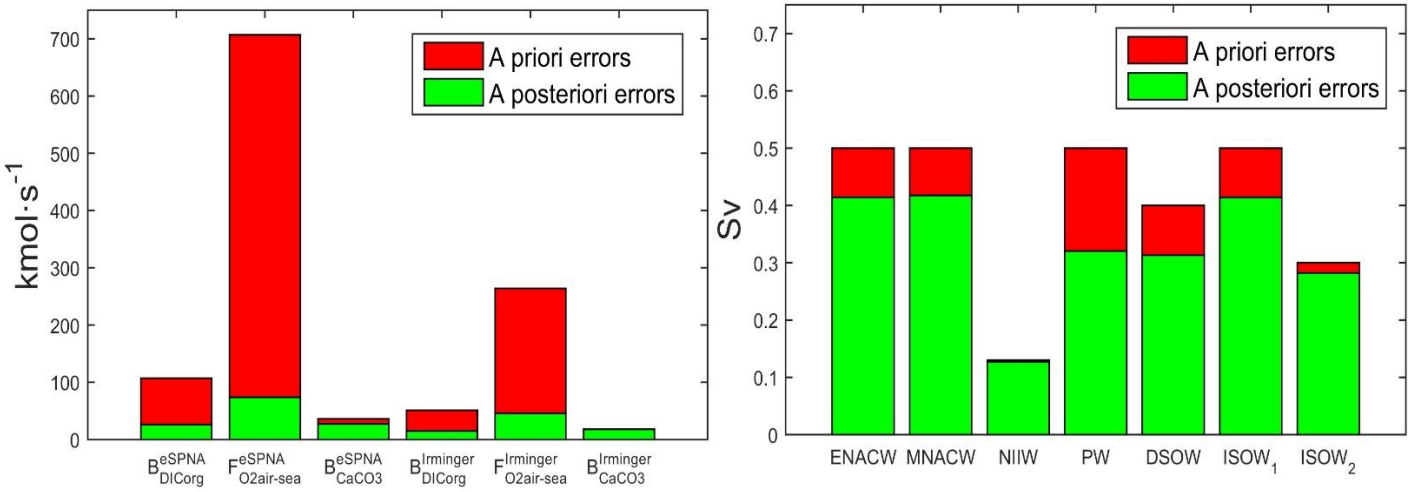

Figure 42. Bar plot representation of the error of the unknowns a priori (red bar) and after inversion (green bar) for the biogeochemical unknowns (left) and for the water masses at the G-I-S sills (right).

Box-model configuration

In a three box-model configuration, the linear relationship between the boxes (represented by the Equation 25 in the main text) allows to determine the unknowns in the three regions resolving only two inside the model. The hypothesis tested in this point is that with independence of the selected boxes to solve the model, the results would be similar. If in the main text we give the output for the combination of whole eSPNA plus Irminger Basin (Table 11, main text), the following alternative outputs explore the rest of box-model configurations: resolving the whole eSPNA and the ENA or resolving the Irminger plus the ENA. The results are given in the Table 15.

Table 15. Inverse box-model solution for all the possible box-model configurations. The column "eSPNA & Irminger" is the configuration developed in the main text, that solves the ENA outside the model; "eSPNA & ENA" is the configuration that solves the Irminger outside the model; and "Irminger & ENA" solves the whole eSPNA outside the model, as the sum of its parts.

		eSPNA & Irminger	eSPNA & ENA	Irminger & ENA
$B_{DIC_{org}}$ (kmol·s^{-1})	eSPNA	86±26	75±24	87±30
	Irminger	8.5±15	-6±37	9±14
	ENA	78±30	82±28	77±27
B_{CaCO_3} (kmol·s^{-1})	eSPNA	20±27	20±28	19±24
	Irminger	9±18	10±33	9.5±17
	ENA	11±33	10±18	9.6±17
$F^{O2\ air\text{-}sea}$ (kmol·s^{-1})	eSPNA	856±74	872±73	856±85
	Irminger	339±46	361±103	337±45
	ENA	517±87	511±73	519±72
Volume Transport^{Sills} (Sv)	SV_{ENACW}^{Sills}	3.97±0.41	3.95±0.41	3.96±0.41
	SV_{MNACW}^{Sills}	3.93±0.42	3.91±0.42	3.92±0.42
	SV_{ISOW1}^{Sills}	-1.07±0.41	-1.04±0.41	-1.05±0.41
	SV_{ISOW2}^{Sills}	-2.02±0.28	-2.01±0.28	-2.02±0.28
	SV_{NIIW}^{Sills}	0.88_5±0.13	0.89±0.13	0.88±0.13
	SV_{PW}^{Sills}	-1.79±0.32	-1.82±0.32	-1.79±0.32
	SV_{DSOW}^{Sills}	-3.00±0.31	-2.97±0.31	-2.99±0.31

As expected, there is variability in the outputs with the change of the information used to constraint, but it is always inside the range of uncertainties. The error calculation of the unknowns solved outside the model as a linear combination of the outputs used an error propagation technique. This creates that the unknown estimate of the biogeochemical tracer not solved by the model shows always the greater error. The consistency of the water mass fluxes at the G-I-S sills give us confidence in that the election of one box-model configuration or another does not have a substantial impact in the biogeochemical budgets.

Interannual variability

Interannual variability is represented by the large variation observed in the tracer transport at the OVIDE section. It is the final result conditioned by a single cruise? Are there any variability in the outputs bigger than expected when a cruise is deleted? If the model is not robust enough, the change associated with the inclusion/not inclusion of a specific cruise would be significantly large in the output. In order to evaluate the robustness of our results, a series of tests have been performed. The Figure 43 shows the output of the unknowns optimized by the model with respect to the cruise election.

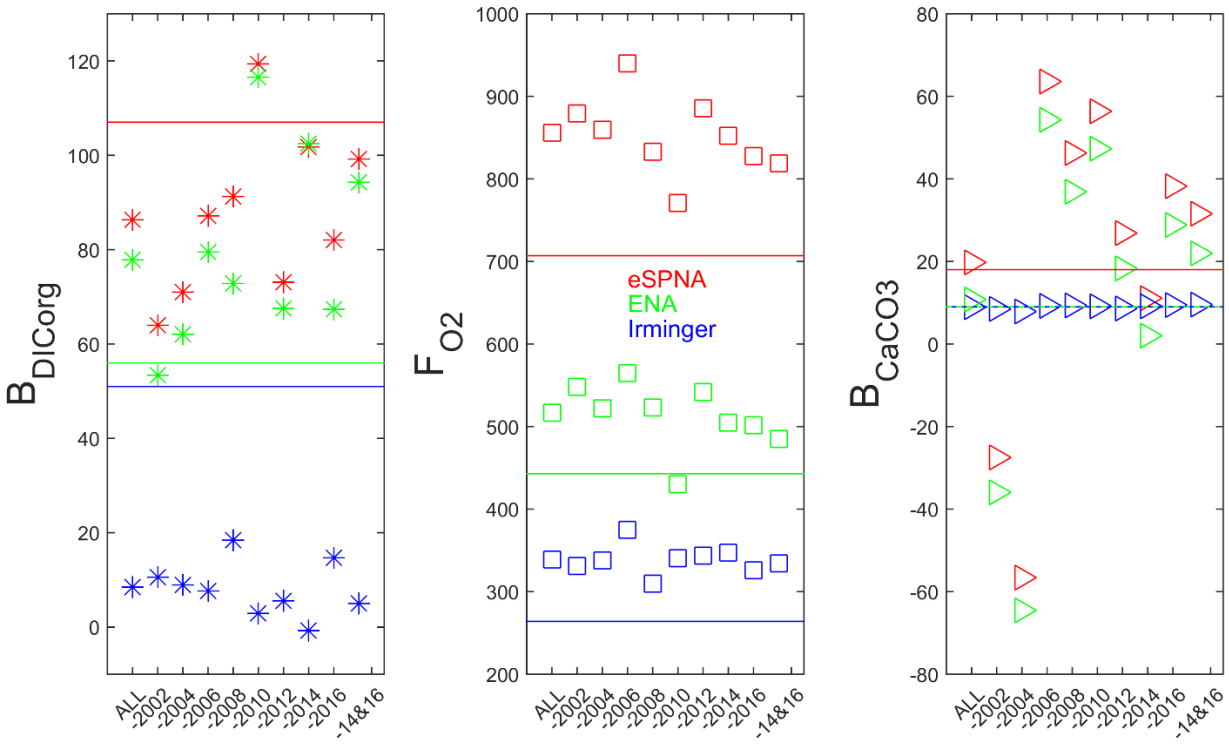

Figure 43. Interannual variability assessment. Output values for different combinations are coded as: eSPNA values in red, IB in blue, and ENA in green. The situation "ALL" (first value at the left in each subplot) is the one described in the main text, with the inclusion of all the repetitions of OVIDE section. In order to compare with the "ALL" situation, the model was re-run deleting a cruise (situation "-2002" not includes the 2002 cruise, "-2004" not includes the 2004 cruise and so on…) or even the two last cruises (situation "-14&16", the value at the rightest location in each subplot). Horizontal lines represent the a priori values.

The output is consistent with the expected. The existence of response against the inclusion of a set or another of cruises shows that the model is sensitive enough to a change in the constraints. There are interannual variability but even the extreme values are usually inside the range of the uncertainties with respect to the standard output: ~±30 kmol·s^{-1} for B_{DICorg}, ~±85 kmol·s^{-1} for $F^{O_2\ air\text{-}sea}$ and ~±60 kmol·s^{-1} for B_{CaCO_3}. The greater range of dispersion of the results for the B_{CaCO_3} output agrees with its condition of the least constrained unknown.

Recently, a cooling trend in the heat status of the North Atlantic has been proposed [*Robson et al., 2016*], sharply affected by the short-term cooling event of years 2013-2014 [*Zunino et al., 2017*]. The no inclusion of both 2014 and 2016 cruise allows to test the alteration of the model when two cruises are deleted, at the same time that the potential effect of a cold eSPNA has over the biogeochemical status of the system. As can be seen in Figure 43, the outputs are not

anomalous. The no inclusion of two cruises alters the output, as expected, but it is too soon to infer any change in the biogeochemical status with respect to a colder status of the eSPNA.

Modifying the a priori values and/or its range of errors

By definition, inverse modelling needs the election of a priori values that represents the assumed state of knowledge about the magnitude to be modelled. Same as happens with the a priori elections, the procedure is initialized with an error for each variable to be optimized. The model solves the budget within the error bars imposed by the modelled variables. In order to evaluate the robustness of our outputs with regard to the initial a priori value and its error amplitude associated, we perform tests to determine the sensitivity of the unknown variables in response to fluctuations in the a priori variables.

In the Figure 44 is represented the change in each biogeochemical unknown when a single a priori is modified between the range of 0 to 250 kmol·s^{-1} for B_{DICorg} and B_{CaCO_3}, and for the range of 0 to 2500 kmol·s^{-1} for the $F^{O_2\ air\text{-}sea}$. In this testing, the error is also changed keeping the same proportion that in the original model. The change of the a priori unknown for the organic carbon export, shows that the model output is affected by underestimations of the a priori, but that is quite consistent from ~80 kmol·s^{-1} thenceforth. The output is mainly an interplay between B_{DICorg} and $F^{O_2\ air\text{-}sea}$, when one of them is underestimated, the other gains relevance. The change in B_{CaCO_3} (last row of Figure 44), does not affect neither B_{DICorg} or $F^{O_2\ air\text{-}sea}$, but show linear response with itself. This is a clear indicator of the minor weight that B_{CaCO_3} has in the final output. As a general rule, we can say that the a priori election is adequate and reflects fine the balance between the two main biogeochemical unknowns that rules the model: B_{DICorg} and $F^{O_2\ air\text{-}sea}$.

In summary, even though our output unknowns show some dependence on the a priori values and/or its range of errors, we do not find any systematic deviation. This gives us confidence that our biogeochemical estimates are a robust feature of the data.

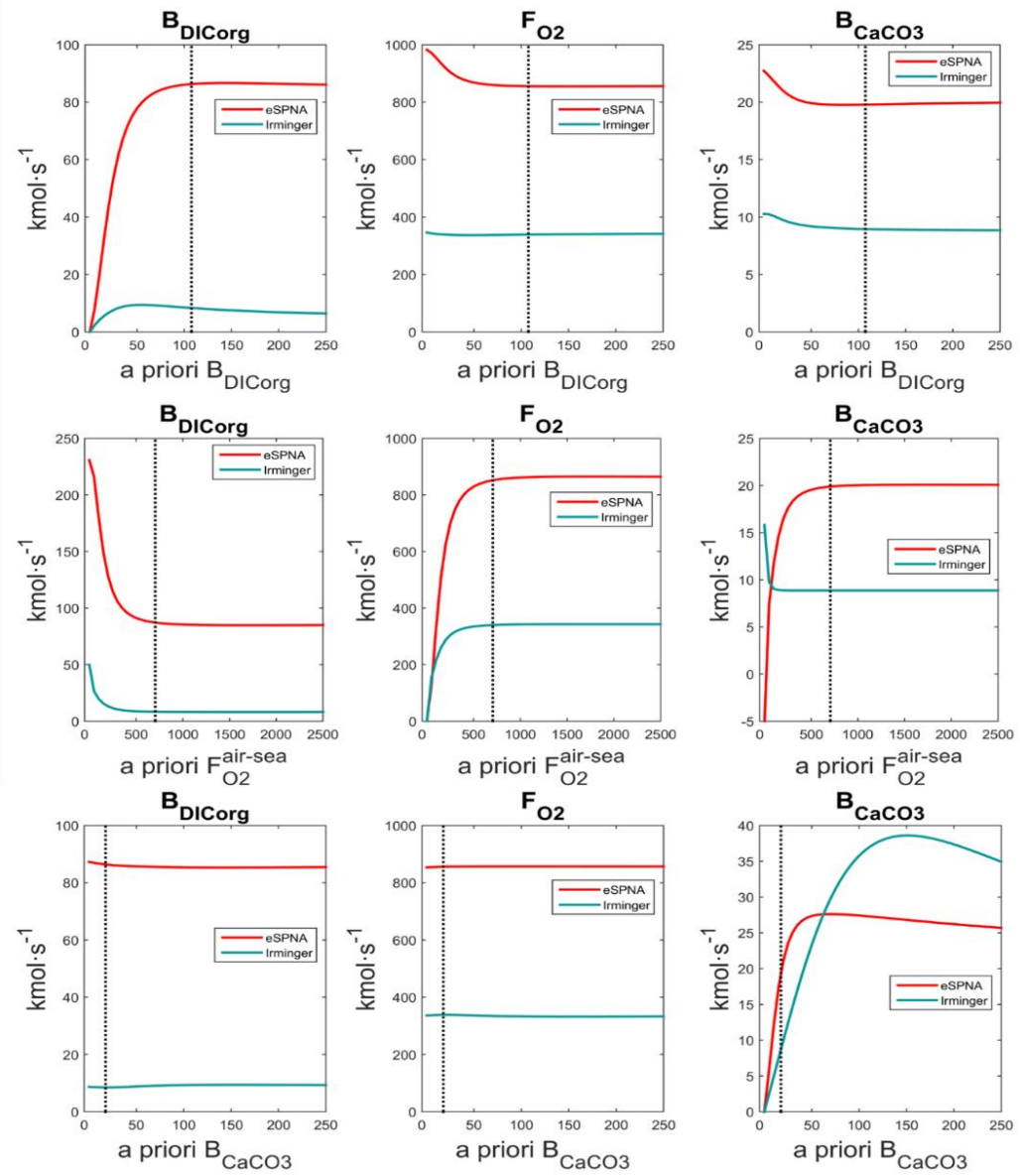

Figure 44. Plots of change in the output of the eSPNA (red) and IB (blue) (y-axis, kmol·s^{-1}) with respect to the initial a priori value (x-axis, kmol·s^{-1}) when is changed the B_{DICorg} value (upper), $F^{O_2\ air\text{-}sea}$ (middle) and B_{CaCO_3} (lower). Vertical black dashed line is at the a priori magnitude used in the main output.

Another possibility to test it is if the change in the error associated with each a priori has significant impact in the final output. In this testing, keeping constant the usual a priori magnitude for the unknowns, we change the errors. As can be seen in Figure 45, greater deviations from the standard output are found when narrow errors are provided than when the error is large. It makes sense, since smaller errors in the a priori constrains more the possibilities of the solution. The biogeochemical unknown more sensitive to this kind of variation is the B_{DICorg}, output when the B_{DICorg} a priori error is modified (left corner upper row of Figure 45). It is logical because the B_{DICorg} is the central element of the model and the one with more number of constraining equations.

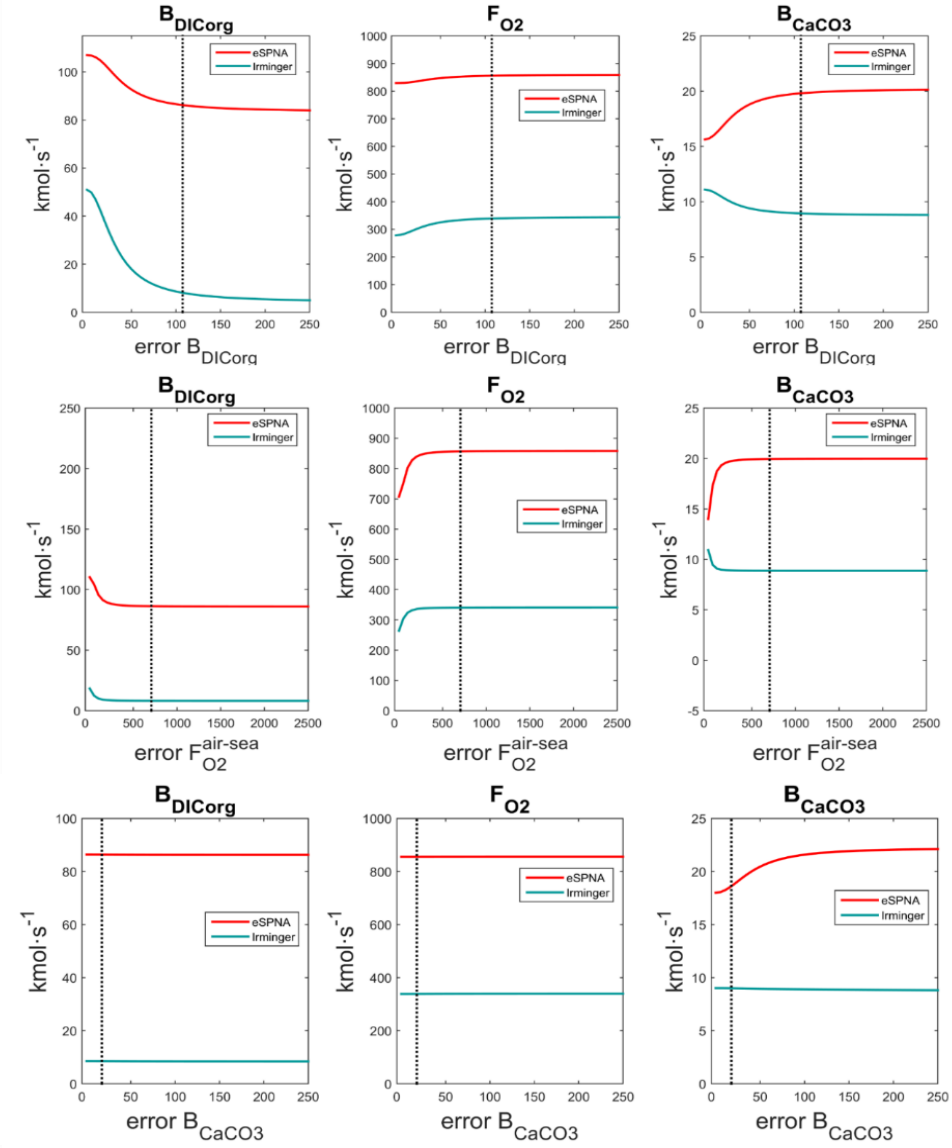

Figure 45. Plots of change in the output of the eSPNA (red) and IB (blue) (y-axis, kmol·s^{-1}) with respect to the initial a priori error (x-axis, kmol·s^{-1}) when is changed the B_{DICorg} value (upper), $F^{O_2\ air\text{-}sea}$ (middle) and B_{CaCO_3} (lower). Vertical black dashed line is at the a priori magnitude used in the main output.

Modifying the stoichiometric ratios

There are five stoichiometric ratios relating the biogeochemical constraining equations (Table 10). Elemental biogeochemical composition can change within limits [*Fraga et al.,* 1998], so the combination of possibilities is then considerable. We conducted a sensitivity study modifying the stoichiometric ratios between the main components of organic matter, the nitrogen:carbon ratio ($r_{N:C}$), the phosphorus:carbon ($r_{P:C}$) and the oxygen:carbon ($r_{O:C}$) used inside the model to relate the biological budgets. We keep constant during the testing the ratio Si:C, that is depth-dependent and is integrated inside the model with different values for each region, and the ratio between the change in total alkalinity and nitrogen ($r_{AT:N}$). The tested ranges are inside the

theoretical limits of marine organic matter composition [*Fraga et al., 1998*]. Although the model does show sensitivity to the ratios (Figure 46), especially to $r_{N:C}$ and $r_{P:C}$, it is smaller than the errors and can be neglected.

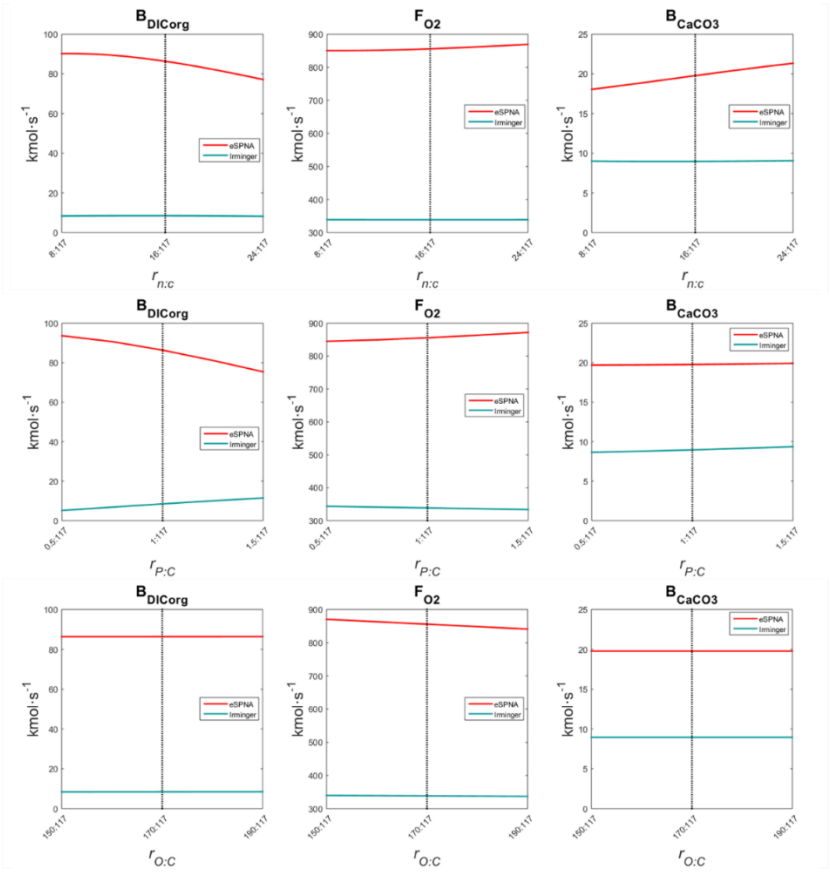

Figure 46. Plots of change in the output of the eSPNA (red) and IB (blue) (y-axis, kmol·s^{-1}) with the change in the stoichiometric ratios (x-axis) when is changed the $r_{N:C}$ ratio (upper), the $r_{P:C}$ (middle) and the $r_{O:C}$ (lower). Central vertical black dashed line is the stoichiometric ratio used by default in the main output.

Appendix 6.5.B: vertical tracer distribution along OVIDE section 2002-2016

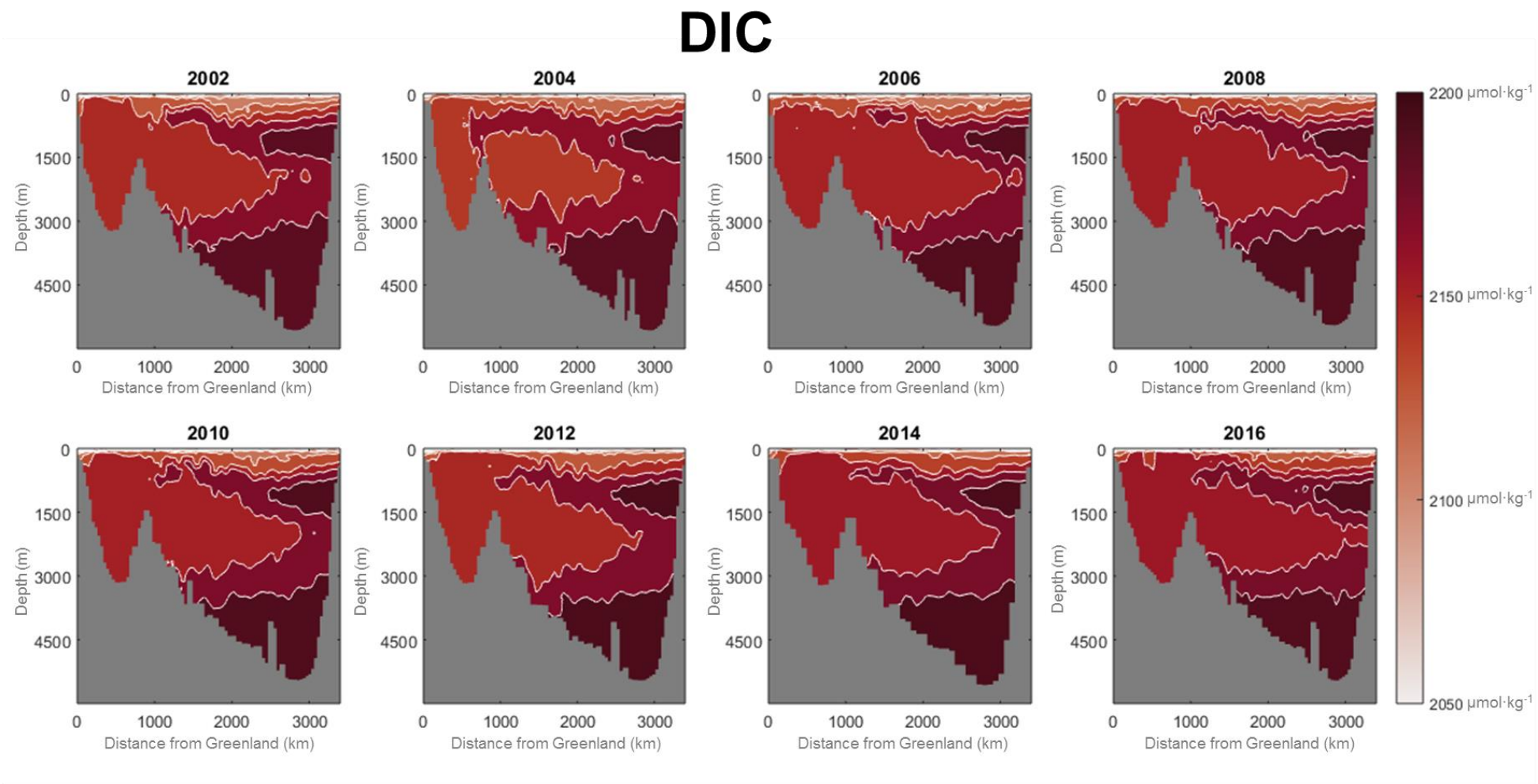

Figure 47. Dissolved inorganic carbon (DIC, in µmol·kg^{-1}) vertical distribution along the OVIDE section from Greenland (left) to the Iberian Peninsula (right). Represented is the density interpolated bottle data from each one of the eight repetitions of the OVIDE section, from 2002 to 2016.

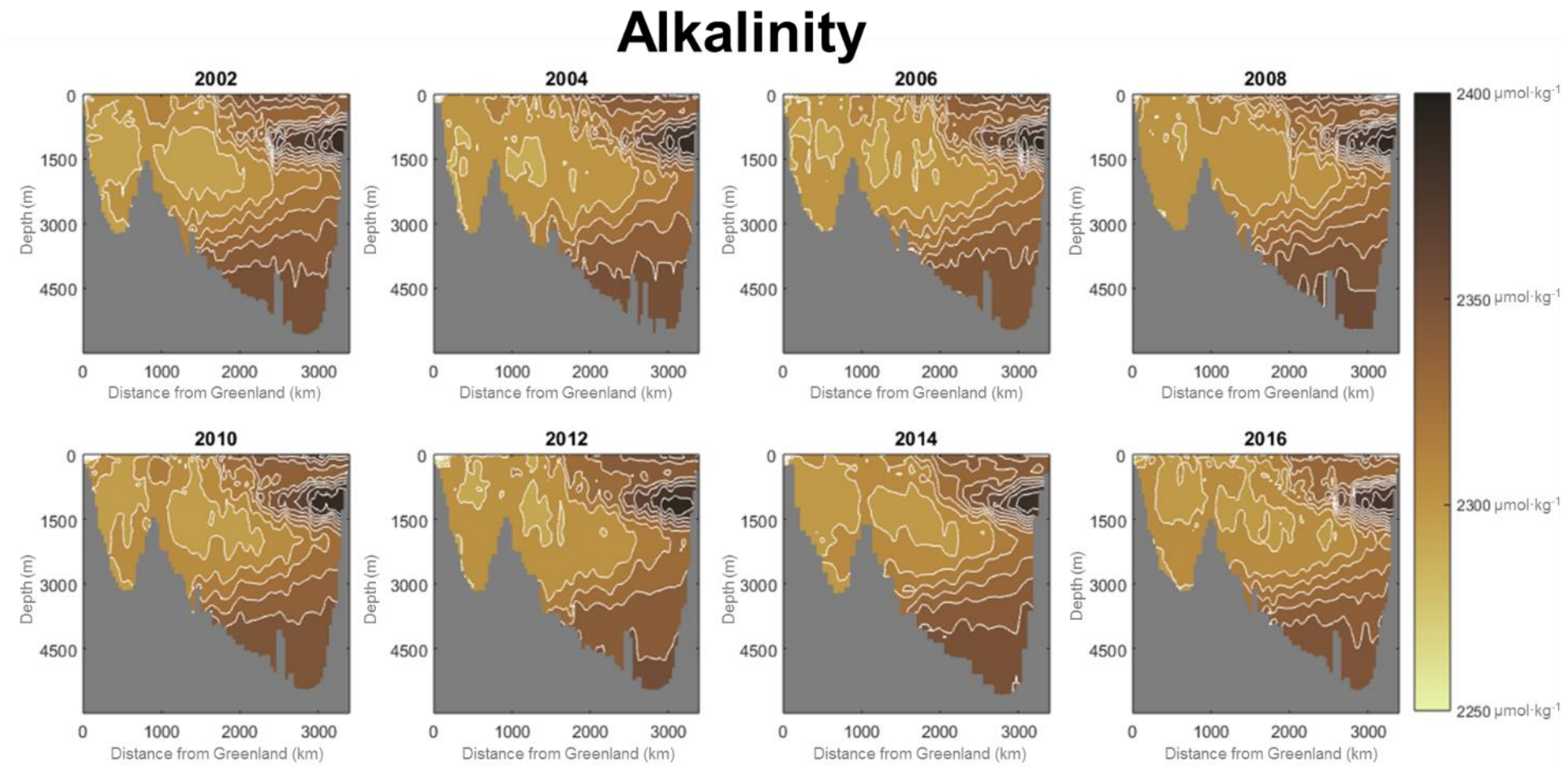

Figure 48. Total alkalinity (µmol·kg^{-1}) vertical distribution along the OVIDE section from Greenland (left) to the Iberian Peninsula (right). Represented is the density interpolated bottle data from each one of the eight repetitions of the OVIDE section, from 2002 to 2016.

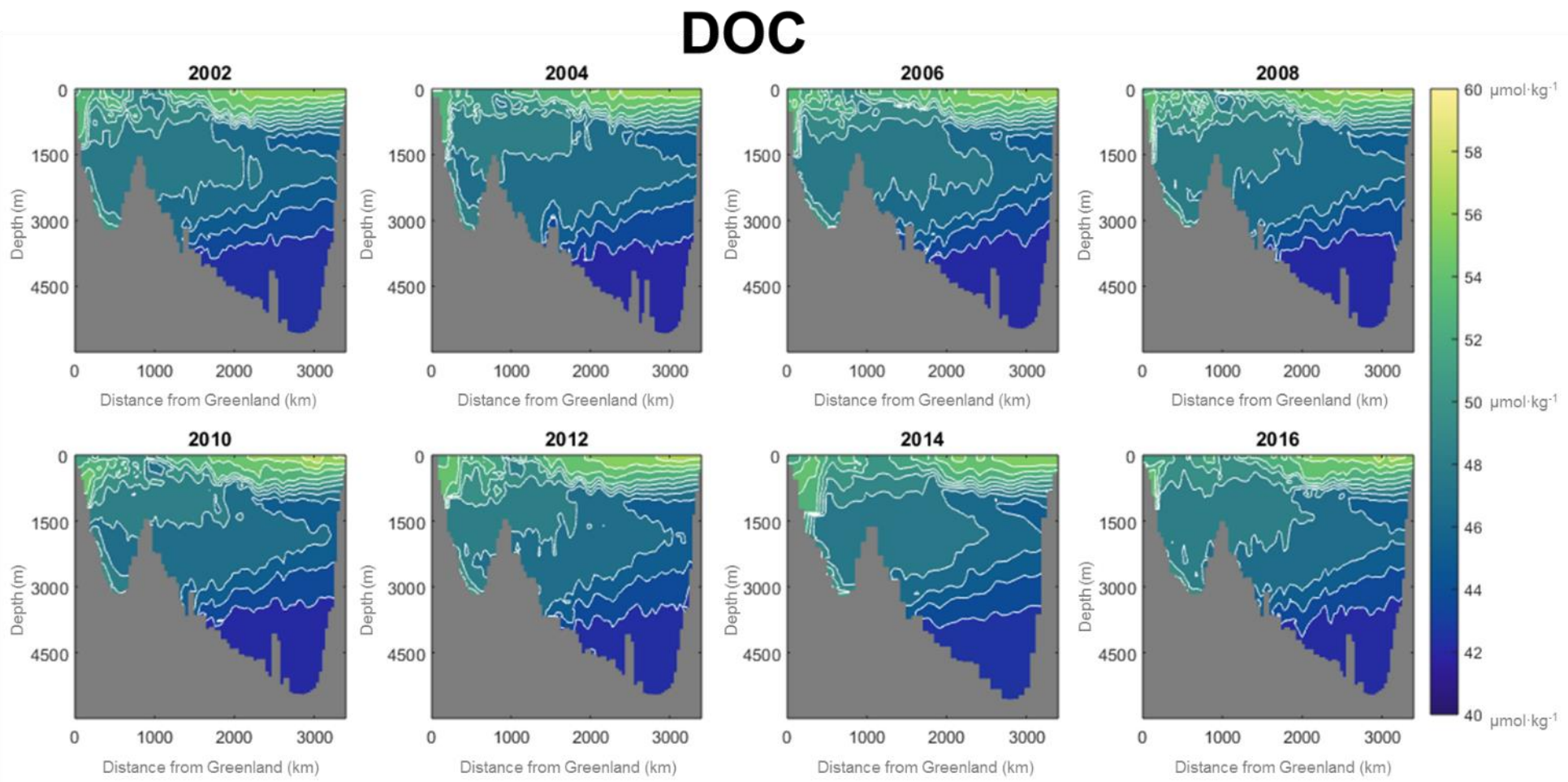

Figure 49. Dissolved organic carbon (DOC, in µmol·kg^{-1}) vertical distribution along the OVIDE section from Greenland (left) to the Iberian Peninsula (right). Represented is the density interpolated data reconstructed with the eOMP [*García-Ibañez et al.*, 2015] and the source water type DOC (Table 1) for each one of the eight repetitions of the OVIDE section, from 2002 to 2016.

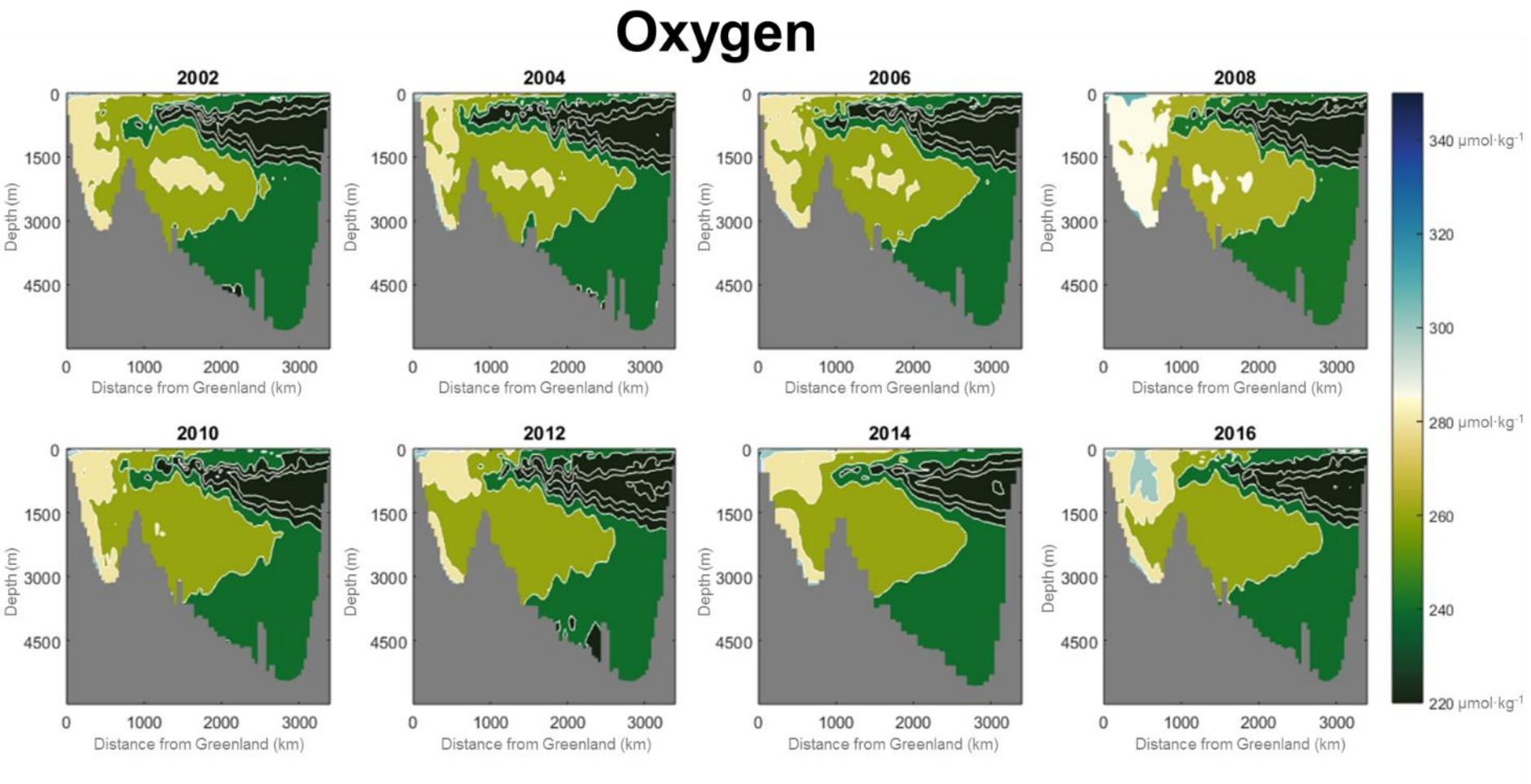

Figure 50. Dissolved oxygen (µmol·kg^{-1}) vertical distribution along the OVIDE section from Greenland (left) to the Iberian Peninsula (right). Represented is the density interpolated bottle data from each one of the eight repetitions of the OVIDE section, from 2002 to 2016.

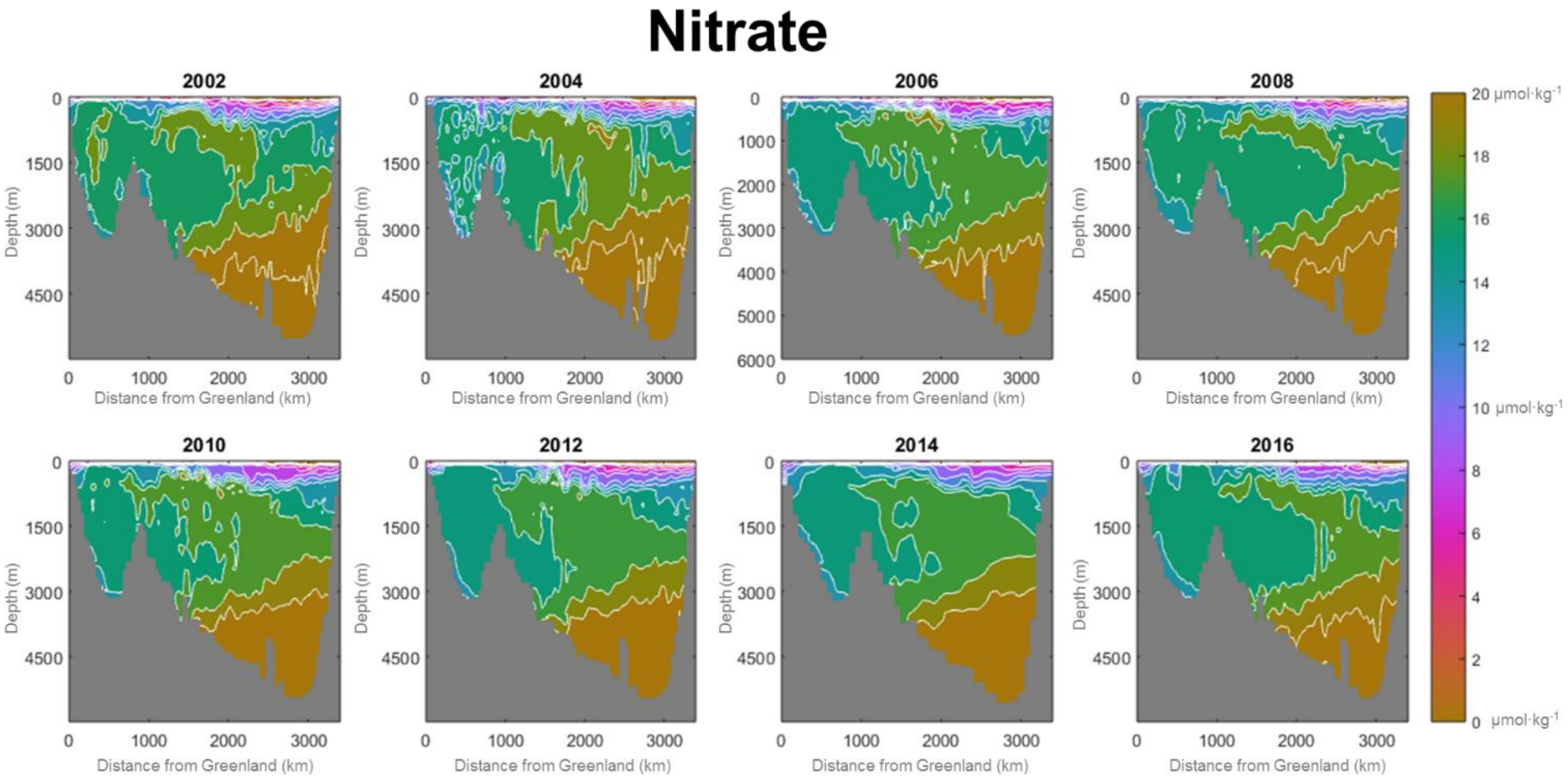

Figure 51. Nitrate (NO_3^-, in µmol·kg^{-1}) vertical distribution along the OVIDE section from Greenland (left) to the Iberian Peninsula (right). Represented is the density interpolated bottle data from each one of the eight repetitions of the OVIDE section, from 2002 to 2016.

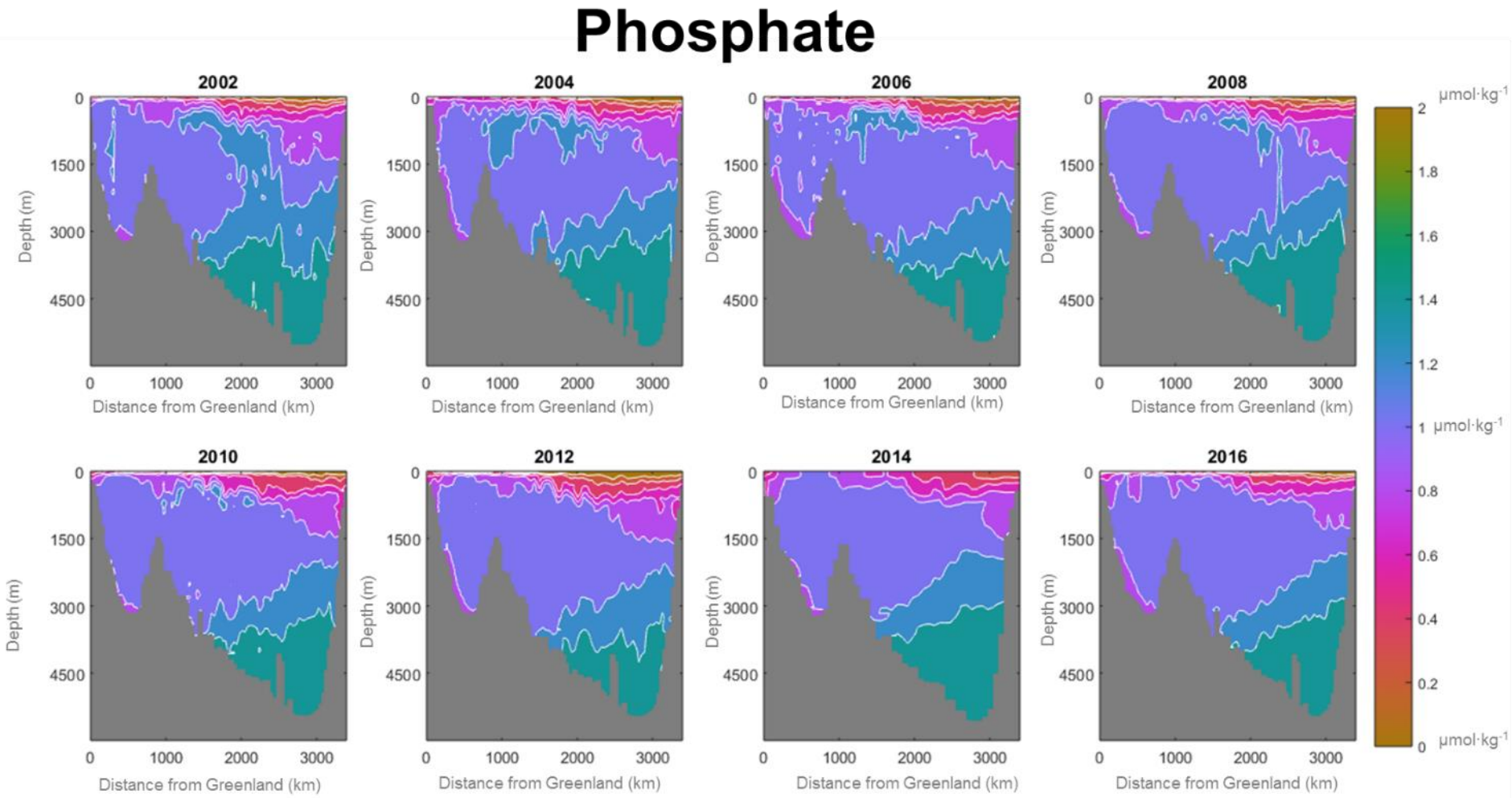

Figure 52. Phosphate (PO_4^-, in µmol·kg^{-1}) vertical distribution along the OVIDE section from Greenland (left) to the Iberian Peninsula (right). Represented is the density interpolated bottle data from each one of the eight repetitions of the OVIDE section, from 2002 to 2016.

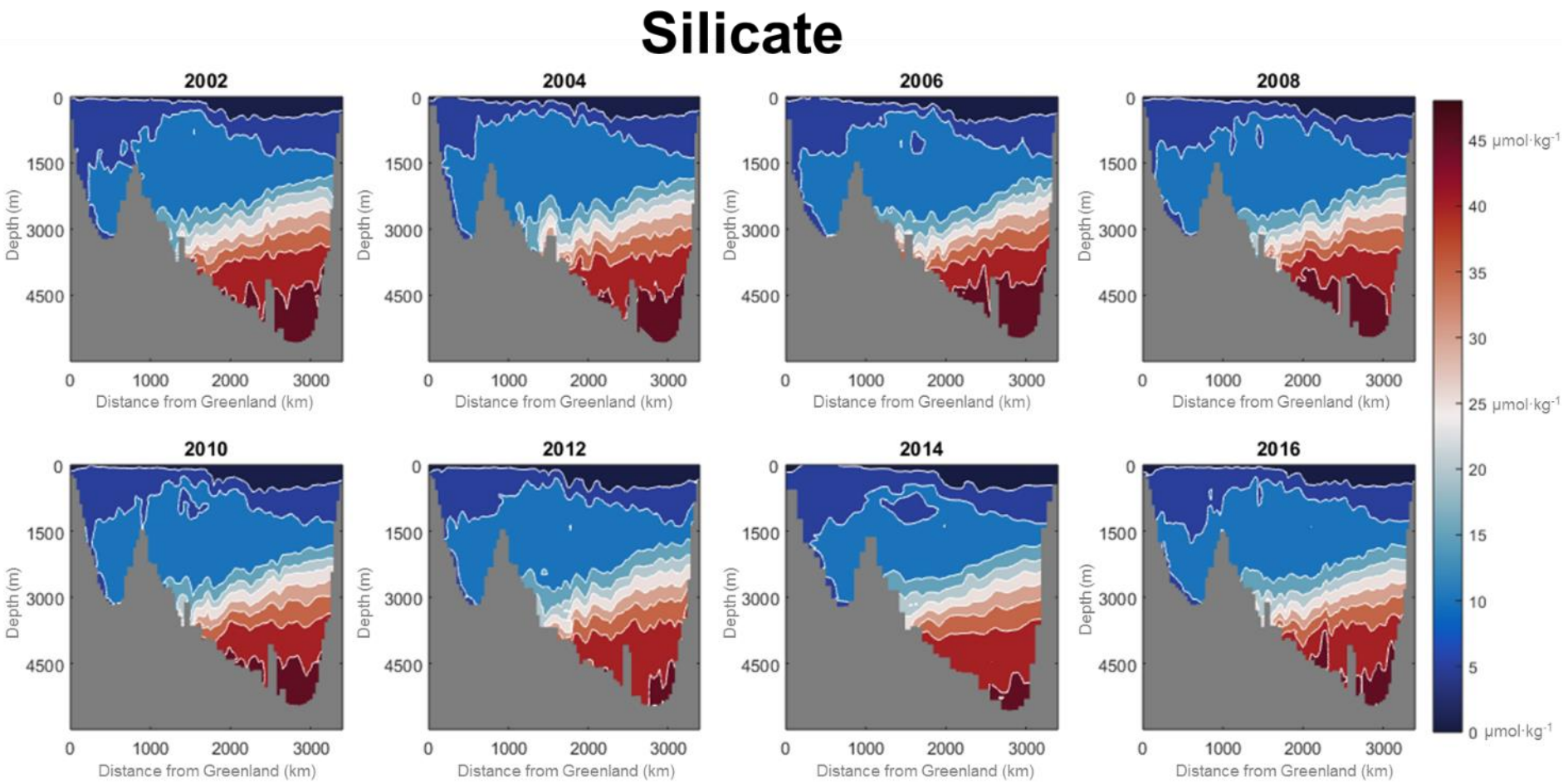

Figure 53. Silicate (SiO_4, in µmol·kg^{-1}) vertical distribution along the OVIDE section from Greenland (left) to the Iberian Peninsula (right). Represented is the density interpolated bottle data from each one of the eight repetitions of the OVIDE section, from 2002 to 2016.

PART IV. Sedimentation rates and carbon fluxes

Chapter 7: Radiometric dating with the short-lived isotope ^{210}Pb

7.1. The natural radionuclide ^{210}Pb as an environmental tracer

Lead (Pb) is a chemical element belonging to the heavy metal group. It has an atomic number of 82, i.e. the number of protons in the atomic nucleus; and there are four natural stable isotopes: ^{206}Pb, ^{207}Pb, ^{208}Pb and ^{204}Pb [*Mabit et al.,* 2014]. ^{210}Pb is a natural geogenic radioisotope occurring as one of the decay products of the ^{238}U series, the most common uranium isotope found in the nature (Figure 54) [*Loveland et al., 2005*]. In a decay chain, the intermediate radionuclides that are formed during the course of decay are both the daughters of previous nuclear transformations and the parents in subsequent radioactive decay [*Walker,* 2005]. ^{210}Pb is produced as a result of the decay of so-called short-lived progeny of ^{222}Rn, which comes from the decay of ^{214}Po (99.98%) and ^{214}Bi by ^{219}Tl (0.02%). ^{210}Pb is subject to beta decay into ^{210}Bi. The radioactive decay of ^{210}Pb is accompanied by the emission of a gamma radiation of energy 46.5 keV.

The most up-to-date ^{210}Pb half-life reported in the Data Decay Evaluation Project (DDEP) webpage is 22.23±0.12 yr [*DDEP*, 2017]. It is precisely that ^{210}Pb half-life which converts it in a valuable radioactive isotope of ecological and biogeochemical significance for environmental investigations [*Soetaert et al.,* 1996]. It has been widely used in natural sciences for dating, tracing, and modelling biogeochemical cycling and ^{210}Pb measurements are part of environmental radioactivity monitoring programs of analytical laboratories world-wide. Since ^{210}Pb was first used to date ice cores [*Goldberg,* 1963], ^{210}Pb measurements have been used for dating sediments and to attain sedimentation rates in multiple environments: lakes [*Krishnaswami et al.* 1971*; Kamula et al.,* 2017], estuaries [*Alongi et al;* 2005*; Álvarez-Iglesias et al.,* 2007*; Álvarez-Vazquez et al.,* 2016*; Mazarrasa et al.,* 2017], coasts [*Koide et al.,* 1972*; Oguri et al.,* 2003*; Kuzik et al.,* 2013*; Szmytkiewicz et al.,* 2014*; Puig et al.,* 2015*; Oberle et al.,* 2016*; Ribeiro et al.*, 2016] and open ocean [*Thomson et al.,* 1993*; Masqué et al.,* 2002*,* 2003*; Miralles et al.,* 2005*; Boessenkool et al.,* 2007 *Zaborska* 2007*,* 2008*; Nieto-Moreno et al.,* 2013*; Moffa-Sánchez et al.,* 2014*; Jonkers et al.,* 2010a*; Garcia-Orellana et al.,* 2009*; Zalewska* 2015*; Chong et al.,* 2016]. The radioactive decay of ^{210}Pb limits its detection to the last 100–150 years, so that is the maximum temporal framework that allows to evaluate.

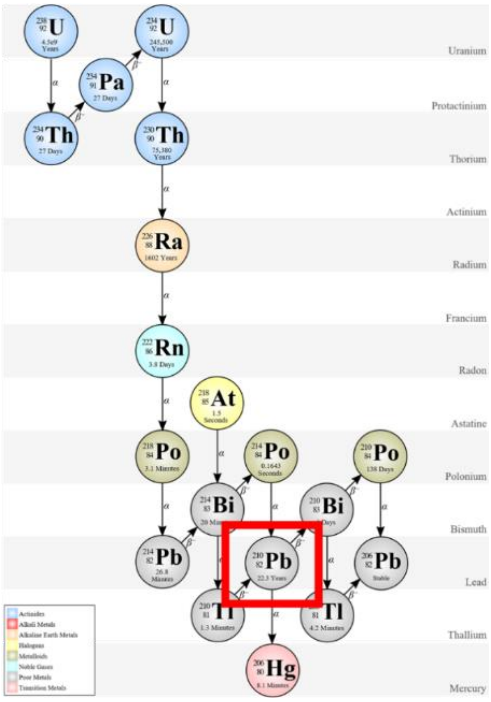

Figure 54. Decay chain of ^{238}U. The series decays over the chemical elements: protactinium (Pa), thorium (Th), actinium, (Ac), radium (Ra), radon (Rn), astatine (At), polonium (Po) bismuth (Bi), lead (Pb), thallium (Tl), and mercury (Hg). The relative situation of the isotope ^{210}Pb is framed in red square. The stable isotope in which the series ends is the ^{206}Pb. Source: www.berkeley.edu

There is another useful characteristic of ^{210}Pb with regard of their particle reactivity, and it is its potential to be preferentially attached in the water column to sinking organic carbon [*Cochran,* 1990]. Then, on the basis of the sediment accumulation rates, it is possible to infer the flux of sinking particles onto the sea floor [*Masque et al.,* 2003].

The method of ^{210}Pb dating is based on the escape of radon gas (^{222}Rn) from the earth into the atmosphere (Figure 55) [*Walker,* 2005]. ^{210}Pb identified in sediments originates from two sources: a fraction is the result of radium (^{226}Ra) radioactive decay in the inner sediment, and this is called supported ^{210}Pb ($^{210}Pb_{supported}$) [*Kuzyk et al.,* 2013]. The other fraction in marine sediments comes mainly from atmospheric deposition at the surface ocean of ^{210}Pb previously generated from ^{222}Rn that has emanated from terrestrial rocks and soils. Dissolved ^{210}Pb in the water column attaches to suspended matter and deposits to bottom sediments [*Sanchez-Cabeza & Ruiz-Fernández*, 2012]. The higher affinity of ^{210}Pb for fine-grained particles and organic matter compared to that of ^{226}Ra causes an excess of ^{210}Pb with respect to ^{226}Ra in the settling particles that are subsequently deposited on the sea floor. Sediments will contain an excess of ^{210}Pb with respect to that produced in situ by ^{226}Ra disintegration, that is called excess ^{210}Pb ($^{210}Pb_{excess}$) [*Mabit et al.,* 2014]. The excess fraction is useful for dating because it diminishes with depth according to the time elapsed between the sediment formation and its measurement following the radioactive decay. The activity of $^{210}Pb_{excess}$ is the basis for the

determination of ages and sediment accumulation rates, with independence of the dating model applied.

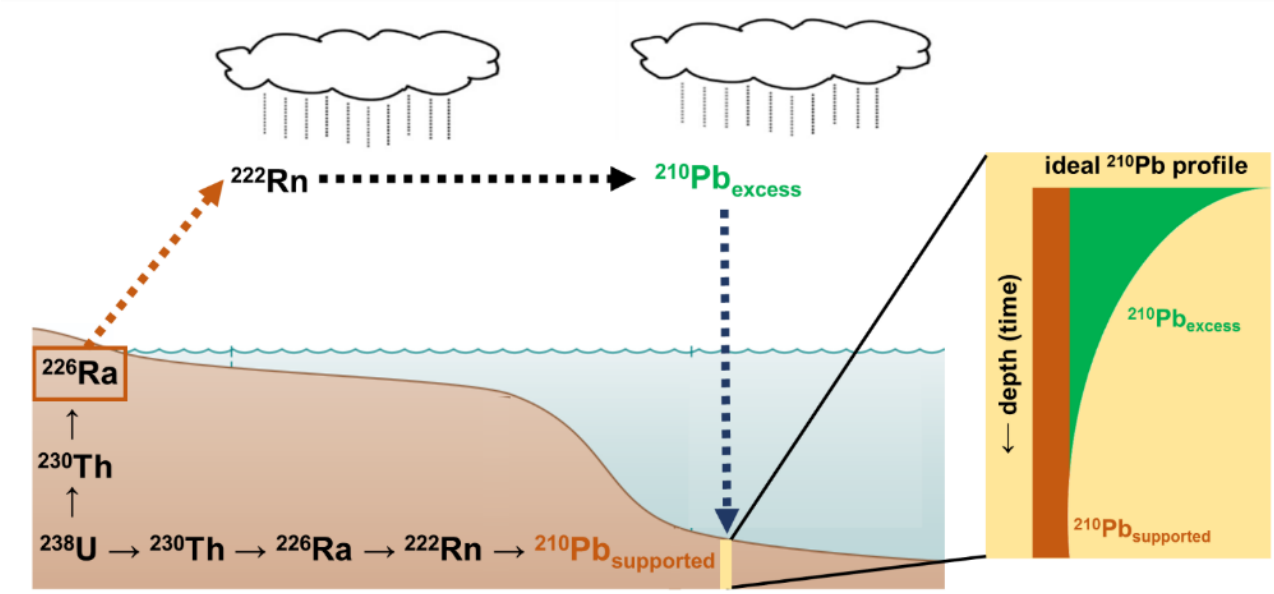

Figure 55. Schematic representation of the origin of geogenic ^{210}Pb and the differentiation between the supported and the excess fraction. Source: author elaboration based on *Mabit et al.,* [2014].

There are two major mechanisms by which the scavenging of tropospheric ^{210}Pb takes place, large-scale precipitation or dry deposition [*Baskaran et al., 2011*]. Depositional flux of ^{210}Pb at any given site depends on the ^{222}Rn concentration in the air and the scavenging efficiency by rain [*Baskaran et al.,* 2011]. The amount and frequency of precipitation could be a key factor in atmospheric scavenging because the depositional flux is strongly correlated with the amounts of precipitation [*Garcia-Orellana et al.,* 2006*; Baskaran et al.,* 2011]. The rate of atmospheric ^{210}Pb fallout reported by a 100-year integrated fallout record measured in the Greenland ice sheet is 10 Bq·m^{-2}·yr^{-1} [*Nijampurkar and Clausen,* 1990].

From an analytical point of view there are four alternative methods of analyzing the total activity of ^{210}Pb in a sediment sample: (i) alpha spectrometry, it is an indirect measurement through the assessment of its daughter radionuclide 210-Polonium (^{210}Po) when secular equilibrium is guaranteed [*Sánchez-Cabeza et al.,* 1998]; (ii) gamma spectrometry; with the direct measurement of ^{210}Pb [*Schelske et al.,* 1994]; and the less commons (iii) liquid scintillation [*Vajda et al.,* 1997] and (iv) beta counting [*Godoy et al.,* 1998].

The use of ^{210}Pb as geochronometer for sediment accumulation has becoming the habitual technique for determining accumulation rates in coastal sediments [*Cochran & Masqué* 2004], but its implementation in pelagic environments it is still in its infancy due the higher resolution requirements. In the following sections, we are going to explain the full methodology to date deep-sea sediments with the ^{210}Pb method under a high resolution gamma spectrometric

approach. A more reduced version, centered in an applied study case, can be found in the Chapter 9.

7.2. Material and methods: from corer to sources

7.2.1. Fieldwork: sediment sampling

The first step is the retrieving of the deep-sea sediments. Sediment recovery took place during BOCATS/OVIDE 2016 cruise (Expocode: 29AH20160617) at the R/V Sarmiento de Gamboa. The surface sedimentary samples were retrieved using a box-corer (Figure 56) that should ensure nearly intact sampling of the surface sediments. Recovered box core was sub-sampled aboard using four PVC tubes in order to get samples, not only from chronology determination but also for a complete characterization of micropaleontological, sedimentological and geochemistry features. In every recovery a preliminary description of the material and all the relevant data referent to the status of the sample at arrival on deck has been filled out. The top of the core, the interphase between sediment and water, it was not methodologically separable in situ and it was sliced as a whole centimeter (0-1 cm). The rest was sliced aboard every 0.5 cm up to 10 cm and every 1 cm from 10 cm to bottom. Subsamples are identified by their basal centimeter, with increasing numbers from the top to the bottom. Plastic material was used for all the steps of slicing and storing. Samples were stored in a refrigerator at 4ºC.

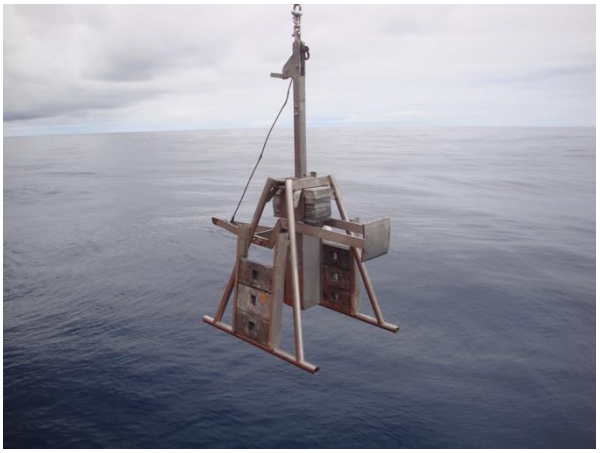

Figure 56. Box-corer dredge used during the BOCATS/OVIDE 2016 cruise to retrieve surface sediments

7.2.2. Lab work: sample preparation

Water content was determined in each of the subsamples from the difference between wet and dry weights. Oven dried subsamples (45±2ºC) were individually powdered in an agate ball-mill and packed into plastic gas-tight containers of a special geometry (Figure 57) with a known weight of around ~15 g per sample. Samples were sealed at least three weeks before being measured to ensure that secular equilibrium between parent isotope ^{226}Ra and its short-lived daughters isotopes was reached.

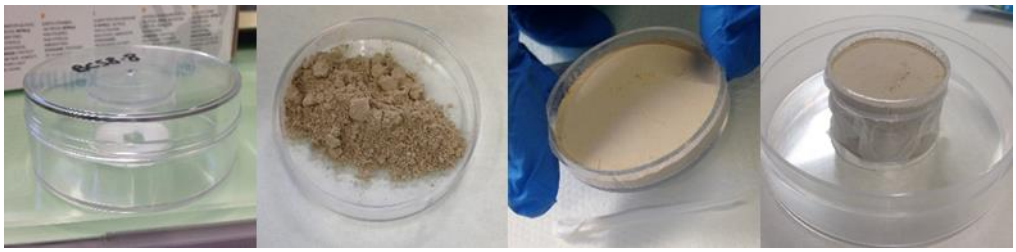

Figure 57. Photographs that illustrate the process of package for each individual subsample into the gas-tight plastic container used in the measure chamber of the spectrometer.

The plastic container introduced in the measure chamber of the spectrometer is standardized and have a characteristic very low gamma absorption. The inner geometry was a polystyrene cylindrical box with a diameter of 42 mm and a height of 24 mm, and it is the geometry that is filled with the powder sample. It has been implemented to enhance the area of the sample in proximity with the germanium detectors of the equipment. The outward container was a polystyrene cylindrical box with a diameter of 94 mm and a height of 32 mm. During all the steps of the sample processing, the use of non-metallic material was selected and potentially crossed contamination were avoided.

7.3. Gamma spectrometry measurements

The emission of high-energy electromagnetic radiation by the gamma-decay of radionuclides can be measured with a gamma spectrometer. Gamma spectrometry with hyper-pure germanium (HPGe) detectors is an effective tool in the study of marine radioactivity [*Cochran & Masqué,* 2004] and can constitute a very useful technique in sediment dating because performs a simultaneous measurement of the full content in gamma-emitters of the sample [*Quintana et al.,* 2006]. It is a non-destructive technique that does not require a previous chemical treatment or digestion of the samples, like occurs in the alpha spectrometry [*Sánchez-Cabeza et al.,* 1998].

Gamma ray spectrometry has been criticized due to the strong dependence of counting efficiency on matrix composition [*Kaminski et al.,* 2014] and because the cosmic rays from deep space that constantly bombard the earth's upper atmosphere are largely composed of gamma radiation [*Walker,* 2005]. Then, the application range of the technique is determined by the effects of the high background, which has repercussions, first, on the detection limit and, afterwards, on the technique accuracy. These handicaps can be resolved with two improvements: selecting suitable detectors and shielding configurations; and optimizing the spectral analysis to reduce uncertainties [*Álvarez-Iglesias et al.,* 2007].

Another additional advantage of the gamma spectrometry technique is that the measurement gives us also additional info on more radionuclides, including all the gamma emitters present in the three naturally occurring decay series ^{238}U, ^{232}Th and ^{235}U along with anthropogenic radionuclides (^{137}Cs, ^{241}Am). The detection of anthropogenic radionuclides can be used as independent time-stratigraphic markers, allowing the validation of the dating model [*García-Orellana et al.,* 2006].

Currently, the number of environmental studies in which the ^{210}Pb measurements were done with alpha spectrometry is larger than those did with gamma spectrometry. Both methods show some inherent disadvantages. The alpha method requires a time consuming chemical separation procedure, while the gamma method not. On the other hand, gamma method depends on high-quality detectors that are not as common as alpha radioactivity detectors [*Zaborska et al.,* 2007*; Schelske et al.,* 1994]. Since the probability for gamma-decay and the sensitivity of the instrument are generally less than those for alpha-decay, larger samples and longer times of measurement are needed for the gamma approach.

Regardless of which method is chosen, intercomparison studies have concluded that both alpha and gamma methods are equally suitable for use in sedimentation investigations and the activities can be compared with confidence [*Zaborka et al.,* 2007].

7.3.1. Mazinger: a gamma spectrometer with two HPGe detectors

Samples were counted in a low level background gamma-ray spectrometer with two hyper-pure germanium (HPGe) planar detectors (BEGe Model, Canberra) located at LRI of University of Salamanca. To our knowledge, this equipment named *Mazinger* (Figure 58), that have two opposed planar HPGe detectors, is unique in the world and for sure, it was the first time that was used to measure the radionuclide content in marine sediments.

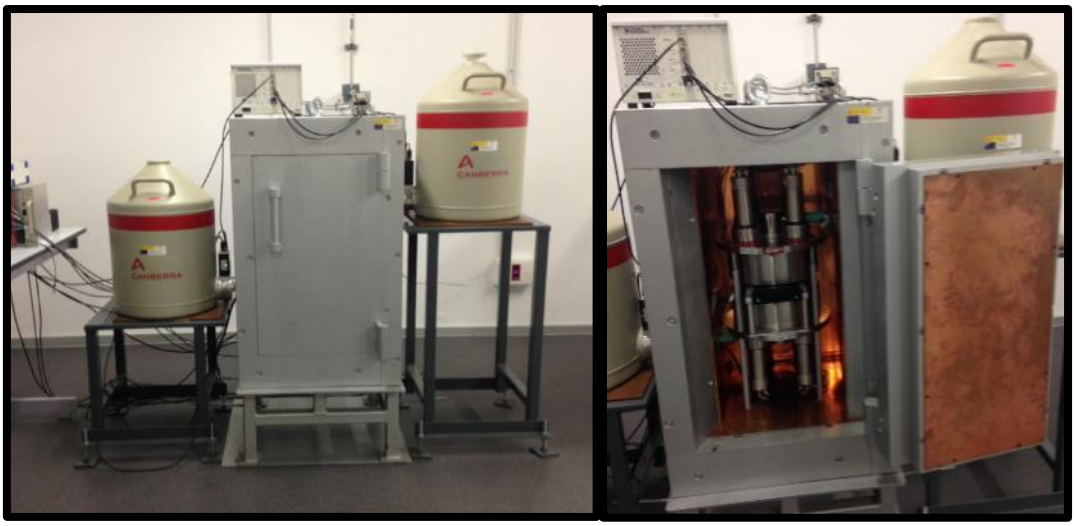

Figure 58. Photograph of *Mazinger*, the gamma spectrometer with two opposed planar HPGe detectors used in this work. It is installed in the third basement of the Edificio i+D+I of University of Salamanca.

In order to reduce the background level as much as possible a series of active and passive shieldings were developed: (i) each one of the detectors is mounted in an impurity-free cryostat (Canberra) (ii) and surrounded by anti-Compton rings (NaI(Tl), Scionix), (iii) the chamber of detection is shielded with iron (10 cm thick) and very old lead (5 cm thick), (iv) and is continuously ventilated with nitrogen gas in order to avoid inferences due radon accumulation. Furthermore (v), all the equipment is installed in the third basement of the Edificio i+D+I of University of Salamanca, then reducing the cosmogenic radiation. Detectors are coupled with a multichannel analyzer. Time of measurements was long enough to achieve statistical significance in the emissions. For the first centimeters a duration of 200.000 s (~2.5 days) was sufficient, while for the deepest ones longer measurements, near 350.000 s (~4 days), were necessary.

The equipment was calibrated in energy and efficiency. The energy calibration is done during the emission spectra analysis (see next section 7.3.2. Galea, a software for natural radionuclide gamma emission spectra analysis). For an accurate quantification of the activities determined via gamma spectrometry, an efficiency calibration needs to be done that allows the connection between the measured signal and the real activity in the sample. Efficiency in gamma-ray spectrometry depends on the measurement system, the density and composition of the sample, the sample-detector geometrical arrangement and the photon energy [*Kaminski et al.,* 2014]. For the efficiency calibration, the results were contrasted with the measurement of standard certified material (IAEA-300). Spiked sources of three certified standard solutions were added to the same sediment matrix containing ^{210}Pb and measured in *Mazinger* under the same configuration. The relationship between the activities measured with and without the certified tracer allows the acquisition of absolute peak efficiencies.

7.3.2. Galea, a software for natural radionuclide gamma emission spectra analysis

The spectrum analysis was made with the software GAmma Line Expert Analyser (*Galea*) [*Quintana and Fernández,* 1998*; Quintana et al.,* 2017], developed for the optimization of gamma emission spectra from natural radionuclides. *Galea* provides reliable results of the radionuclide activity present in the measured material, even with low counting statistics in the full-energy peaks. As it was said previously, it is an important phase in the energy calibration of the measures. The raw output of the measurement is a spectrum of emission where the peak heights are proportional to the activity of the radionuclide and the horizontal axis increases with energy (Figure 59A).

The gamma-ray emission spectrum program allows the identification of the radionuclide emissions and the calculation of the activities corresponding to the emitters. It includes two steps: starting with the raw spectra, the analysis tool locates full-energy peaks and determines the intervals between them; and also the continuum background following the COSPAJ algorithm (Figure 59A) [*Quintana and Fernández,* 1998]. In the second step, a genetic algorithm for peak analysis fits the characteristics of the spectra analyzed by using a specific library (LNHB, 2017) that contains the more likely emissions occurring within the spectra (Figure 59B) The peak function selected to fit the peaks measured by the HPGe detectors is given by an exponential convoluted with a Gaussian function [*Siegert and Janssen,* 1990]. The statistical relevance of each fitted peak is determined by the decision limit or critical level (*Lc*) [*Currie,* 1968], calculated for 95% probability. The last step of the algorithm identifies the emissions present in the spectrum.

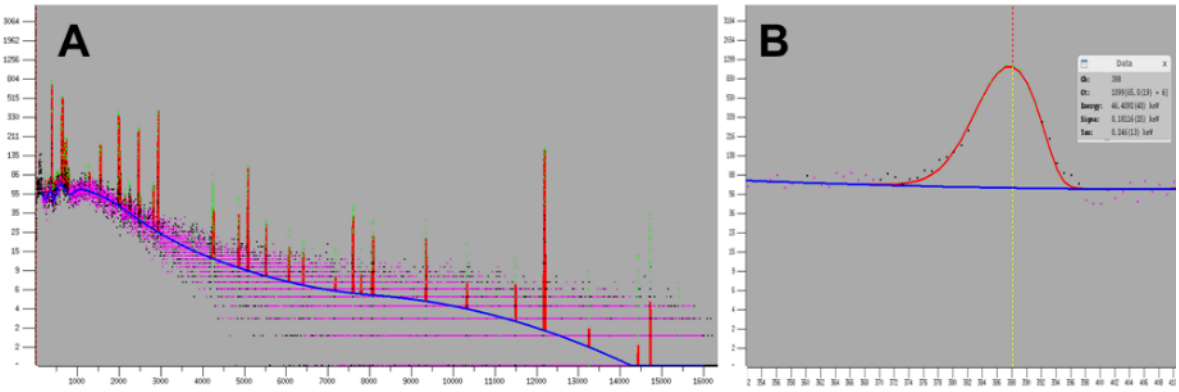

Figure 59. A-Gamma-ray emission spectra analysis for a single sample. B- An individual peak of emission for a specific radionuclide after the fitting and the identifying procedure. Represented in red are the peaks of emission of each radionuclide and in the blue the continuum background.

Total activity of ^{210}Pb was determined from its isolated gamma ray at 46.54 keV (keV=kiloelectronvolt; 1 keV≈1.6x10^{-16} J). Apart from ^{210}Pb, there are other radionuclides whose activities are necessary to known in order to apply the different dating models, as for example ^{226}Ra and ^{214}Pb, that were determined by gamma emission at 185.72 keV and 351.93 keV, respectively. A list of some of the radionuclides detected in the marine samples measured along with the energy gamma-ray of its emission is available in Table 16. The detection is conditioned

by the presence/absence of the radionuclide and the detection limit of the measure, so not all the radionuclides exists in all the samples.

The detection and quantification of artificial radionuclides who have its origin in military nuclear weapons or in discharges from the nuclear energy industry (^{137}Cs, ^{241}Am) are useful to contrast the age model because the timing of its appearance is well known.

Table 16. List of gamma-emitters radionuclides detected in the measured marine samples and the energy gamma-rays of its emission.

Radionuclide	Energy (keV)
^{210}Pb	46.539
^{241}Am	59.54
^{238}U	63.1
^{234}Th	63.3
^{230}Th	67.6
^{235}U	185.72
^{226}Ra	186.211
^{214}Pb	351.93
^{214}Bi	609.312
^{137}Cs	661.65
^{228}Ac	911
^{40}K	1460.82

7.4. Dating models

The first step is common among all the existent dating models: the determination of the $^{210}Pb_{excess}$. The $^{210}Pb_{excess}$ is defined as the difference between the total ^{210}Pb measured and the $^{210}Pb_{supported}$. The $^{210}Pb_{supported}$ represents the fraction coming from ^{226}Ra. The activity of ^{226}Ra can be measured at each section (typical of gamma spectrometry approach) or assumed constant along the core by average or extrapolation from the total ^{210}Pb content of the bottom sections of the profile (the alpha spectrometry approach usually do this procedure). This is another advantage of the gamma-methodology, because the value of $^{210}Pb_{supported}$ can be estimated at each section and not necessarily assumed that the $^{210}Pb_{supported}$ activity does not vary with depth. The study of $^{210}Pb_{excess}$ decay is the basis of ^{210}Pb dating of sediment cores [*Sánchez-Cabeza & Ruiz-Fernández*, 2012].

In the literature of ^{210}Pb dating models, there are different conceptual models that act under different assumptions. The model names reflect the underlying assumption of each model, and they are generally named by its acronyms, as for example the Constant Initial Concentration or Constant Activity (CIC/CA) [*Robbins & Edgington,* 1975*; Pennington* 1976*, Appleby & Oldfield,* 1978*,* 1983*; Binford,* 1990*, Carroll & Lerche,* 2003], Constant Sedimentation (CS) [*Robbins,* 1978], Constant Flux Constant Sedimentation (CFCS) [*Krishnaswamy et al.,* 1971*, Koide,* 1972; *Appleby & Oldfield,* 1983] or Constant rate of Supply (CRS) [*Goldberg,* 1963*; Appleby & Oldfield,* 1978] among others. There is not a single model that will give a reliable ^{210}Pb chronology under all the situations, so each core consistency must be individually evaluated with one or other of the dating models [*Appleby & Oldfield,* 1983].

With independence of the dating model applied, the development of the equations shared common generic expressions. For the equation development along this text, we are going to follow the integrated formulation proposed by [*Sanchez-Cabeza & Ruiz-Fernández*, 2012]. All conceptual ^{210}Pb models used to date undisturbed sediment cores can be derived from a single fundamental equation (Eq. 38) [*Krishnaswamy et al.,* 1971],

$$C(i, t=0) = \frac{f(i)}{r(i)} \qquad \text{(Equation 38)}$$

that relates the concentration of ^{210}Pb$_{excess}$ in interval *(i)* at the time of formation $C(i, t=0)$ as the ratio between the ^{210}Pb$_{excess}$ flux to the sediment surface ($f(i)$) and the mass accumulation rate ($r(i)$).

Once a section *(i)* is formed, ^{210}Pb$_{excess}$ concentration (C) decays exponentially following the radioactive decay law (Eq. 39):

$$C_i = C(i, t=0) \cdot e^{-\lambda t} \qquad \text{(Equation 39)}$$

, and the ^{210}Pb$_{excess}$ concentration measured in interval *(i)*, (C_i), is dependent of the ^{210}Pb$_{excess}$ concentration in interval *(i)* when formed ($C(i, t=0)$), the time elapsed ($t_{(i)}$) and the disintegration constant of ^{210}Pb isotope (λ=0.03118±0.00017 yr^{-1}, *DDEP*,[2017]).

Combining the two previous equations:

$$C_i = \frac{f(i)}{r(i)} \cdot e^{-\lambda t} \qquad \text{(Equation 40)}$$

As the values of $f(i)$ and $r(i)$, the ^{210}Pb$_{excess}$ flux and the mass accumulation rate, are unknowns, the age *t* cannot be determined from Equation 40. In order to solve this problem, each one of the dating models stablishes some assumptions to simplify the equations and get the age *t*.

In the next sections we are going to focus on the dating models more used for marine sediments: the CRS and the CF:CS.

7.4.1. Constant rate of supply (CRS)

The CRS is the most widely used and validated dating model. The model was proposed as an alternative to the constant initial concentration model to date sediments when there were changes in the accumulation rate [*Appleby & Oldfield,* 1978]. The fundamental assumption of the model is that the flux of $^{210}Pb_{excess}$ to the sediment surface is constant $(f(i) = k)$.

Under this assumption, and by integration of the whole core inventory of $^{210}Pb_{excess}$ (A), a simple dating equation can be reach. Once section *(i)* is formed, $^{210}Pb_{excess}$ inventory decays exponentially following the radioactive decay law (Eq. 41):

$$A_i = A_0 \cdot e^{-\lambda t_{(i)}} \qquad \text{(Equation 41)}$$

, and the $^{210}Pb_{excess}$ inventory measured in interval *(i)*, (A_i) can be related with the $^{210}Pb_{excess}$ inventory at actual time "zero" (A_0, i.e., the total inventory of the core) taking into account the time elapsed $(t_{(i)})$ and the disintegration constant of ^{210}Pb isotope (λ=0.03118±0.00017 yr^{-1}). Following Equation 41 can be calculated the age of section *(i)* as in Equation 42:

$$t_{(i)} = \frac{1}{\lambda} \ln\left(\frac{A_0}{A_{(i)}}\right) \text{(Equation 42)}$$

Besides the fundamental assumption of constant $^{210}Pb_{excess}$ flux from the atmosphere to the ocean and from the water column to the sediment surface it is that no redistribution processes occur in the sediment [*Mabit et al.,* 2014], while the sedimentation rate might vary [*Appleby and Oldfield,* 1983; *Sánchez-Cabeza et al.,* 2000].

The CRS model allows to take sediment compaction into account, a feature especially important in the dating of deep-sea sediments. The model is able to get a date and a sediment rate for each section considered, so variability in sedimentation rate can be detected. A requirement for this model is that it is mandatory to know the total inventory (A_0) in order to date. If the total ^{210}Pb profile does not reach the supported value at the bottom it will have an underestimated inventory and although there are some strategies to estimate the missing inventory [*Sánchez-Cabeza & Ruiz-Fernández*, 2012], dating capabilities would be compromised.

7.4.2. Constant flux constant sedimentation (CF:CS)

The CF:CS model combines the CRS model assumption of constant flux to the sediment surface $(f(i) = k)$ and the assumption of constant mass accumulation rate $(r(i) = k')$, i.e. both fluxes of ^{210}Pb and sediments are considered constant.

The sediment rate is estimated from a least-squares fit between the logarithm of $^{210}Pb_{excess}$ and the mass depth, considering measurement uncertainties. As a result of the constant sedimentation assumption, the model resolves a unique value of sedimentation rate for all the core, in contrast with the CRS model that is able to show temporal changes in sedimentation

rates. In this model the compaction effect is not considered [*Miralles et al.,* 2005], and the apparent sedimentation rates correspond to maximum values [*Álvarez-Iglesias et al.,* 2007].

It is a useful dating model when the $^{210}Pb_{excess}$ profile shows abrupt changes originated, for example, by a rapid mass accumulation event. If the analysis of the profile suggests that a change in the sedimentation did occur, invalidating the constant sedimentation assumption, the CF:CS model can be applied independently to the separate sectors of the profile, allowing the consideration of different sedimentation rates in each sector.

7.4.3. Sedimentation rates

Defining sedimentation as the settling of material onto the seabed, the sedimentation rate will be the net balance between sedimentation and removal/erosion processes. With the age resolved by the dating model, the time between samples is known and sediment accumulation rates (s, cm·yr^{-1}) can be calculated as simply as the ratio of the same intervals for depth ($z_{i+1} - z_i$) and time ($t_i - t_{i+1}$) (Eq. 43):

$$s_i = \frac{(z_{i+1} - z_i)}{(t_i - t_{i+1})} \qquad \text{(Equation 43)}$$

Sedimentation rate is the magnitude that quantifies the flux of material to be long-term accumulated in sediments. Higher rates of sedimentation will lead to higher preservation, and carbon preservation in marine sediments is the primary mechanism that moves carbon into the geologic carbon cycle [*Keil et al.,* 2017].

Chapter 8: Dating the Anthropocene in deep-sea sediments: how much carbon sequester the Irminger and Iceland Basins?

8.1. Introduction

Recently, a new geological epoch has been proposed: the Anthropocene [*Crutzen & Stoermer,* 2000]. It is based in the scientific community consensus that humankind has already alters the Earth-system and has become a global geological force by its own [*Steffen et al.,* 2011; *Waters et al.,* 2016]. Anthropocene detection is relatively easier in coastal and estuarine areas with greater anthropogenic pressure [*Álvarez-Iglesias et al.,* 2007*; Leorri et al.,* 2014; *Irabien et al.,* 2015, *Álvarez-Vázquez et al.,* 2016], than in remote deep-sea basins, where the relatively low sedimentation rates require precise dating techniques to identify the onset. Deep-sea sediments integrate signals from the environment, being one of the most reliable paleoclimate archives. The combination of an accurate Anthropocene detection with sedimentological analysis and elemental composition allows the evaluation of fluxes to the sediment [*Álvarez-Vázquez et al.,* 2016], and can give an insight to comprehend recent biogeochemical processes. In the current status of knowledge of biogeochemical cycles, included the carbon cycle, the amount of material exported from the water column to deep-sea sediments remains poorly constrained [*Honjo et al.,* 2008; *Burd et al.,* 2010; *Heinze et al.,* 2015].

Here we show the results of a radiocronologic approach via gamma spectrometry for two sites in the subpolar North Atlantic: the Irminger Basin (IRM) and the Iceland Basin (ICE). To our knowledge, it is the first time that high resolution low level background gamma-ray spectrometry with two hyper-pure germanium (HPGe) detectors is used for marine sediment dating. The dating is based in ^{210}Pb, a natural geogenic radionuclide that enters the ocean mainly via atmospheric deposition and is one of the decay products of the ^{238}U series ($T_{1/2}$ = 22.23±0.12 yr) [*Mabit et al.,* 2014, *DDEP*, 2017]. The method can be applied to date sediments from the last 100-150 years, it is a non-destructive technique and gives information on all gamma emitters present in the sample (^{226}Ra, ^{234}Th, ^{137}Cs, ^{241}Am…). The detection of anthropogenic radionuclides ^{137}Cs and ^{241}Am, with known dates of input can be used to validate the age model [*Sánchez-Cabeza & Ruiz-Fernández*, 2012].

The fundamentals of the dating model are based on two facts: the enrichment of ^{210}Pb with respect to ^{226}Ra in aerosols and suspended particles in the atmosphere, which fall onto the ocean; and the higher affinity of ^{210}Pb for organic matter and suspended particles. The particles enriched in ^{210}Pb are scavenged from water column and deposited in the sediment, creating an excess of ^{210}Pb with respect to ^{226}Ra within the sediment. The total concentration of ^{210}Pb in

sediments is unequally distributed in two fractions: a constant supported fraction which originates in situ from the ^{222}Rn decay; and the excess fraction ($^{210}Pb_{excess}$), that is related with the sedimentation rate. The decline of $^{210}Pb_{excess}$ with sediment depth is proportional to the time elapsed since sediment formation, allowing the chronological reconstruction. The source of particulate matter to the pelagic sediments is the upper ocean, where production of biogenic particles takes place. The relationship of ^{210}Pb and organic carbon (C_{org}) is such that the inventory of $^{210}Pb_{excess}$ in sediments can be used as a proxy for the flux of C_{org} to the sediments [*Moore & Dymondt,* 1988].

The study sites are located at the subpolar gyre of the North Atlantic. The subpolar North Atlantic is a well-recognized carbon sink area [*Takahashi et al.,* 2009; *Landschützer et al.,* 2016], with primary production dynamics characterized by the North Atlantic spring bloom [*Henson et al.,* 2006]. Both basins are important water mass transformation areas [*Brambilla & Talley,* 2008] and in the IRM winter deep convection events occur regularly [*de Jong & de Steur,* 2016; *Piron et al.,* 2017]. The Irminger Sea is a semi-enclosed basin with a characteristic V-shaped (Figure 60), limited by the Denmark Strait, the coast of Greenland and the Reykjanes Ridge. The ICE is located at the south of Iceland, between the Reykjanes Ridge and the Rockall Plateau. The study site at the IRM is located in the central deepest part of the basin, where continental influence is very scarce, while the study site at the ICE it is in the east flank of the Reykjanes Ridge, northwestward to the deepest part of the basin, the Maury Channel (Figure 16). Both sites are heavily influenced by strong bottom currents from the Nordic overflows. Bottom circulation at the ICE is dominated by the Iceland-Scotland Overflow Water (ISOW), while IRM is dominated by Denmark Strait Overflow Water (DSOW). Both water masses are precursors of North Atlantic Deep Water (NADW) and important components of the southward flowing lower limb of the Atlantic Meridional Overturning Circulation (AMOC) [*Våge et al.,* 2011]. At intermediate depths Labrador Sea Water (LSW) is the dominant water mass along with ISOW, while in the shallower layers young Subpolar Mode Water appears (Irminger Subpolar Mode Water –IrSPMW- in the IRM and Subpolar Mode Water of 7ºC –$SPMW_7$- in the ICE) [*García-Ibáñez et al.,* 2015].

The question is, the anthropogenic perturbation of the marine carbon cycle has reached the sediments? It is already quantifiable? This chapter is addressed to quantify the fluxes of organic and inorganic carbon reaching the bottom of the Irminger and Iceland Basins in order to evaluate its role as a carbon sink during the Anthropocene combining a chronology based in the natural radionuclide ^{210}Pb with sedimentological analysis and elemental composition.

The chapter is organized as follows. A general sedimentological core description along with geochemical sediment analysis and spectrometry measures are described in Section 8.2, while their results are presented in Section 8.3 In section 8.4 the chronology framework and sedimentation variability during the Anthropocene are corroborated and discussed, and a quantitative estimate of actual long-term carbon sequestration is given.

8.2. Materials and methods

The IRM core, BOC16-BC77, consists on 21 cm of ochre calcareous oozes (sandy silt in texture). Despite quite homogenous at glance, a detailed description and grain-size analyses permits distinguishing three intervals. Bottom interval (21-14 cm) is the siltiest interval (61-68%). Sand fraction, mainly very fine and fine sand, represents less than 25% and the mean grain-size is around 16-18 µm. Percentage of silt (56-63%) slightly decreases in the middle interval (14-6 cm), where the amount of sand increases upwards from 22% at the base up to 31% at the top. Mean grain-size oscillates due to bioturbation observed in this interval. The youngest interval is coarser (mean grain-size is 24-28 µm) due to higher abundance of fine and very fine sand fractions (34-38% of sand). Most of the grains of sand correspond to foraminifera tests, because of that the amount of calcium carbonate increases upwards. As a whole, the box-core shows a clear coarsening upwards trend, caused by the progressively increase of fine sand and the decreasing percentages of very coarse silt.

The ICE core, BOC16-BC58, is constituted by 35 cm of yellowish-to-dark ochre hemipelagic sediments ranging from sandy silt (mainly in the lower half) to silty sand in the upper half. As it occurs in Irminger core, BOC16-BC58 shows also three intervals. Bottom interval (35-23 cm) is profusely bioturbated, displaying grain-size heterogeneity because of that. Most levels of this interval consist on sandy silt (30-40% of sand, mainly fine sand), but interlayered levels of silty sand also appear (up to 60% of sand). Middle interval (23-7 cm) show a clear increasing trend of mean grain-size upwards (from 15 to 45 µm) and sand content (from 35% to 53%). Percentages of silt (45-35%) and clay (18-10%) decrease in parallel to the increase of sand. Upper interval (7-0 cm) is the coarsest interval, constituted by silty sand (53-60% of sand). The observed coarsening upward trend in the previous interval keep going in the youngest part of the core (mean grain-size goes from 46 µm to 57 µm). Considering the whole core, fine and medium sand (12-26% and 6-22%, respectively) are the most abundant in the sand fraction, while fine and very fine silts (8-18% and 7-14%, respectively) dominates the silt fraction. The sand fraction is dominated by foraminifera test, but volcanic and quartz grains also appear. Biogenic grains are concentrated in the medium sand and coarser fractions, because this fractions practically disappear in grain-size analyses of free-carbonate samples. Terrigenous and volcanic particles are thus most abundant in the fine sand and finer sizes. A significant part of silt is also from biological origin (very likely, coccoliths). Fine and very fine silt are the most frequent fractions in the bulk samples, but medium silt is the most abundant fraction in free-carbonate samples. Besides, mean size of sand and silt from the free-carbonate samples increases upwards, as it occurs in the bulk samples, revealing a clear coarsening upwards sequence.

8.2.1. Sediment analysis: radionuclide and geochemistry

We present data obtained from two sediment cores recovered in summer 2016. The IRM core named BOC16-BC77 (59º 29.46' N, 37º 41.15' W, at 3118 m water depth, Figure 60) is 21 cm long. The ICE, named BOC16-BC58 (56º 37.52'N, 27º 35.18' W, at 2749 m water depth, Figure 60) is 35 cm long. The sediment was retrieved using a box-corer that should ensure nearly intact sampling of the superficial sediment. Selected well-preserved core were sliced aboard every 0.5 cm up to 10 cm and every 1 cm from 10 cm to bottom. Samples were stored in a refrigerator at 4ºC. Plastic material was used for all the steps of slicing and storing. Water content was determined from the difference between wet and dry weights. Oven dried samples (45±2ºC) were powdered in an agate ball-mill and vacuum-packed into plastic containers of a standard geometry with a known weight of around ~15 g per sample. Samples were sealed at least three weeks before being measured to ensure that secular equilibrium between parent isotope ^{226}Ra and its short-lived daughters isotopes was reached.

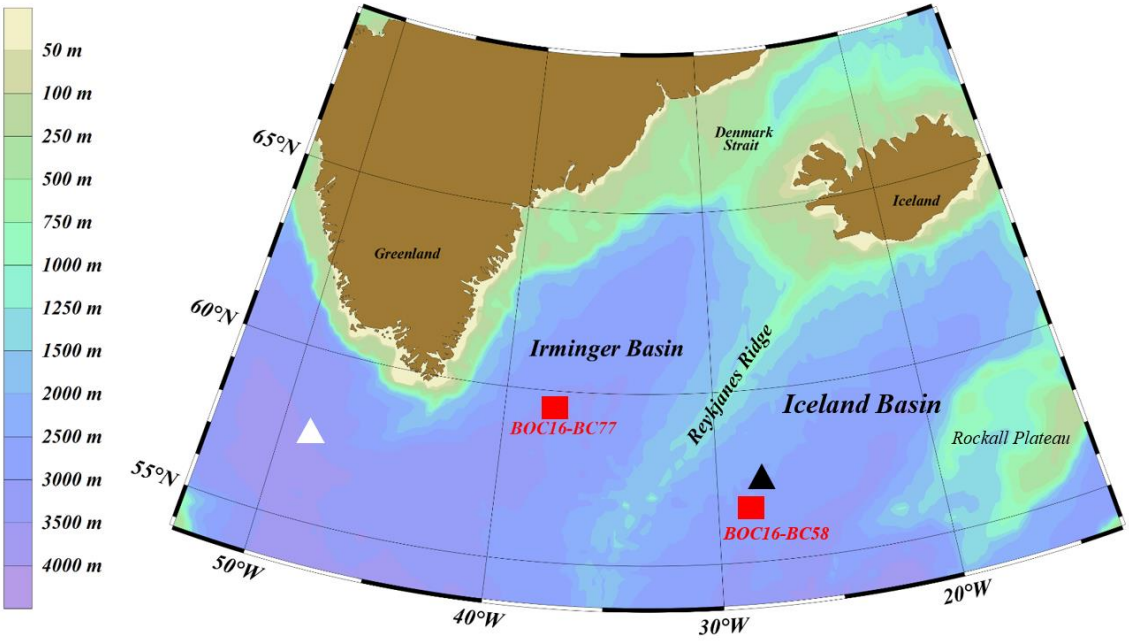

Figure 60. a) Map of the study sites: the sample BOC16-BC77 (59º 29.46' N, -37º 41.15' W at 3118 m water depth) located at the Irminger Basin, and the sample BOC16-BC58 (56º 37.52'N, 27º 35.18' W, at 2749 m water depth) in the Iceland Basin. Location of samples is represented by a red square. The site location of other studies discussed along the text are represented with a black triangle [*Boessenkool et al.,* 2007; *Jonkers et al.,* 2010a] and a white triangle [*Moffa-Sánchez et al.,* 2014].

Samples were counted in a low level background gamma-ray spectrometer with two hyper-pure germanium (HPGe) planar detectors (BEGe Model, Canberra). A series of active and passive shieldings were developed to reduce the background level as much as possible: (i) each detector is mounted in an impurity-free cryostat (7915-30-ULB model, Canberra) (ii) and surrounded by anti-Compton rings (NaI(Tl), Scionix), (iii) the chamber of detection is shielded with iron (10 cm thick) and very old lead (5 cm thick), (iv) and is continuously ventilated with nitrogen gas in order to avoid inferences due radon accumulation. Furthermore (v), all the equipment is installed in the third basement of the Edificio i+D+I of University of Salamanca, reducing the background effect of cosmogenic radiation. Detectors are coupled with a multichannel analyzer (ACCUSPEC/B model, Canberra).

Individual samples were counted between 48-96 hours until statistically significant emission's spectra were achieved. Total activity of ^{210}Pb, ^{226}Ra and ^{214}Pb was determined by gamma emission at 46.54 keV, 185.72keV and 351.93 keV, respectively. Assuming secular equilibrium between ^{226}Ra and its daughter nuclide ^{214}Pb, the specific activity of $^{210}Pb_{excess}$ is the difference between the activities of ^{210}Pb and ^{214}Pb. The equipment was adequately calibrated in energy and efficiency. Energy calibration is done together with an optimum spectrum analysis using the software *Galea* [*Quintana and Fernández*, 1998], developed for the optimization of gamma emission spectra from natural radionuclides. For the efficiency calibration, the results were contrasted with the measurement of standard certified material (IAEA-300). In total, 30 and 20 sources were analyzed for specific activities determined by gamma spectrometry for the IRM and the ICE core, respectively.

Quantitative analysis of the carbon composition has been done on dried sub-samples with a LECO CN system analyzer. After a first determination of total carbon (TC), the aliquot is heated under 400ºC during 3h in order to remove the organic fraction prior to a second analysis. The second determination represents the total inorganic carbon fraction (TIC). Total organic carbon (TOC) is the difference between TC and TIC. Accuracy and precision in carbon element content is σ=0.08. Carbon elemental composition across all the core was obtained at centimetric resolution from top to 20 cm depth. Semiquantitative elemental composition has been measured in continuous every 2 mm by means of a high-resolution XRF core scanner (ITRAX).

8.2.2. Dating model

The Constant Rate of Supply (CRS) was selected as the main model for core dating [*Krishnaswamy et al.,* 1971]. Conceptual ^{210}Pb models used to date undisturbed sediment cores can be derived from a single fundamental equation (Eq. 44) [*Sánchez-Cabeza and Ruiz-Fernández,* 2012],

$$C(i, t = 0) = \frac{f(i)}{r(i)} \qquad \text{(Equation 44)}$$

that relates the concentration of $^{210}Pb_{excess}$ in interval *(i)* at the time of formation $C(i, t = 0)$ as the ratio between the $^{210}Pb_{excess}$ flux to the sediment surface ($f(i)$) and the mass accumulation rate ($r(i)$). Once section *(i)* is formed, $^{210}Pb_{excess}$ inventory (A) decays exponentially following the radioactive decay law (Eq. 45):

$$A_i = A_0 \cdot e^{-\lambda t_{(i)}} \qquad \text{(Equation 45)}$$

, and the $^{210}Pb_{excess}$ inventory measured in interval *(i)*, (A_i) can be related with the $^{210}Pb_{excess}$ inventory at actual time "zero" (A_0, i.e., the total inventory of the core) taking into account the time elapsed ($t_{(i)}$) and the disintegration constant of ^{210}Pb isotope (λ=0.03118±0.00017 yr^{-1}). Following Eq.2 can be calculated the age of section *(i)* as in Eq. 46:

$$t_{(i)} = \frac{1}{\lambda}\ln(\frac{A_0}{A_{(i)}}) \qquad \text{(Equation 46)}$$

The fundamental assumptions of the CRS model are that the supply of $^{210}Pb_{excess}$ flux from the atmosphere to the ocean and from the water column to the sediment surface are both constant, while the sedimentation rate might vary [*Appleby and Oldfield,* 1983; *Sánchez-Cabeza et al.,* 2000], and no redistribution processes occur in the sediment [*Mabit et al.,* 2014]. To take into account sediment compaction, the dating was performed as a function of mass depth ($kg \cdot m^{-2}$) and not only depth.

A requirement of CRS model is that it is mandatory to know the total inventory (A_0) in order to date. If the total ^{210}Pb profile does not reach the supported value at the bottom it will have an underestimated inventory and dating capabilities would be compromised. In that cases, an estimation of the missing inventory ($A_{missing}$) can be done under different approaches. Following [*Appleby,* 1998] and selecting a fixed reference date (t_j), the missing inventory can be estimated with the Eq. 47:

$$A_{missing} = \frac{A_j}{e^{\lambda t_j} - 1} \qquad \text{(Equation 47)}$$

,where A_j is the $^{210}Pb_{excess}$ inventory from the top of the core until the layer that represents the age selected as reference *(j)* [*Sánchez-Cabeza and Ruiz-Fernández,* 2012]. In the inevitably arbitrary election of a reference date, the existence of good correspondence with the known-age of appearance of anthropogenic radionuclides can be used as guide. The second approach to the estimation of the missing inventory relies in a polinomial fit of the decay of the $^{210}Pb_{excess}$. The exponential nature of the decay supposes that the $^{210}Pb_{excess}$ value declines asymptotically in the proximity of the supported value. Another estimate for the missing inventory can be get with the coefficients of a linear fit of that section for the $^{210}Pb_{excess}$ profile.

Once time between samples is known, sediment accumulation rates (s, $cm \cdot yr^{-1}$) can be calculated as simply as the ratio of the same intervals for depth ($z_{i+1} - z_i$) and time ($t_i - t_{i+1}$) (Eq. 48):

$$s_i = \frac{(z_{i+1} - z_i)}{(t_i - t_{i+1})} \qquad \text{(Equation 48)}$$

The total mass can be obtained with the slope of the log-linear relationship between $^{210}Pb_{excess}$ activity and mass depth at each interval, combined with the known decay in time of the ^{210}Pb isotope.

The Constant Flux Constant Sedimentation (CF:CS) model [*Koide,* 1973] was also applied as a way to evaluate the consistency of the dating results [*Appleby & Oldfield,* 1983]. The assumption of the model is that both fluxes of $^{210}Pb_{excess}$ and sediments are constant. The sedimentation rate calculated with the CF:CS model is estimated from a weighted least-squares fit between the logarithm of $^{210}Pb_{excess}$ and the mass depth [*Oldfield & Appleby*, 1984].

8.2.3. Carbon fluxes

We determined the organic and inorganic carbon fluxes combining the elemental composition of the sediments with the sediment accumulation rate obtained by $^{210}Pb_{excess}$ profiles. For each layer *(i)*, maximum carbon flux rates ($C_{f(i)}$, mg-C·cm^{-2}·yr^{-1}) were calculated (Eq. 49) as the product of sediment accumulation rates derived from the dating model (*s*, cm·yr^{-1}), carbon concentrations (C_c, mg·g^{-1}) and the dry bulk density (ρ, g·cm^{-3}).

$$C_{f(i)} = C_{c(i)} * s_{(i)} * \rho_{(i)} \qquad \text{(Equation 49)}$$

Evaluation of biogeochemical processes in Anthropocene deep-sea sediments require accurate dating techniques. Here we show the results of a novel approach using high resolution low level background gamma spectrometry with two simultaneous hyper-pure germanium (HPGe) detectors. The quantitative role of the Irminger and Iceland Basins (Subpolar North Atlantic Ocean) as a carbon sink during the Anthropocene are evaluated combining a chronology based in the natural radionuclide ^{210}Pb with sedimentological analysis and elemental composition.

8.3. Results

8.3.1 Core dating

All sediment radionuclide concentrations are given in Bq·kg^{-1} dry weight (Table 17). Minimum detectable activities (MDA) depend on radionuclide gamma energy, count time and sample mass, but were typically below 0.60 Bq·kg^{-1} for ^{210}Pb, 0.56 Bq·kg^{-1} for ^{214}Pb and 2.26 Bq·kg^{-1} for ^{226}Ra. Efficiencies obtained are 0.3073(90), 0.2544(92), and 0.1612(44) at 46.54 keV (^{210}Pb), 186.21 keV (^{226}Ra) and 351.93 keV (^{214}Pb) respectively.

The vertical distributions of ^{210}Pb, ^{214}Pb and ^{226}Ra specific activities and its uncertainties are given in Figure 61a for the IRM and in Figure 61d for the ICE. In the IRM, the specific activities for radionuclide ^{210}Pb are detected along the whole core, with maxima at surface and a clearly

diminishing exponential profile towards deeper sediments. The shape of the profile is similar in the ICE core, but in this case the measurements stopped at centimeter 11. The $^{210}Pb_{excess}$ value in the last two points measured (Figure 61d), and the general shape of the profile give us confidence in that the supported value was reach. Furthermore, the similar specific activities for the radionuclides at the supported value in the IRM reinforce that idea. Total ^{210}Pb specific activities range from 29.28(1.34) $Bq \cdot kg^{-1}$ to 188.71(6.28) $Bq \cdot kg^{-1}$ in the IRM and 44.46(1.66) $Bq \cdot kg^{-1}$ to 126.70(4.29) $Bq \cdot kg^{-1}$ in the ICE. Total ^{226}Ra specific activities ranged from 21.27(10.95) $Bq \cdot kg^{-1}$ to 34.78(6.2) $Bq \cdot kg^{-1}$ and from 25.13(7.99) $Bq \cdot kg^{-1}$ to 40.51(3.29) $Bq \cdot kg^{-1}$ in the IRM and ICE respectively. The specific activity of ^{214}Pb is relatively constant around 30 $Bq \cdot kg^{-1}$, ranging between 23.05(1.19) $Bq \cdot kg^{-1}$ to 33.86(0.97) $Bq \cdot kg^{-1}$ for the IRM and 29.49(1.03) $Bq \cdot kg^{-1}$ to 40.46(1.20) $Bq \cdot kg^{-1}$ for the ICE. In both cores, the specific activity of ^{214}Pb have the smallest uncertainties, around 1 $Bq \cdot kg^{-1}$ usually. The relative vertical distribution of ^{214}Pb and ^{226}Ra gives confidence to the assumption of secular equilibrium between them. The excess of ^{210}Pb with respect to ^{214}Pb, therefore the $^{210}Pb_{excess}$ fraction, can be clearly observed in the first 10 cm for the two cores and $^{210}Pb_{excess}$ specific activity is maximum at surface (IRM: 162.10(6.98) $Bq \cdot kg^{-1}$; ICE: 89.55(4.44) $Bq \cdot kg^{-1}$), and decays following an exponential profile towards the bottom.

The IRM core was deep enough to reach the supported value before the bottom, and a complete total $^{210}Pb_{excess}$ inventory was determined at 4.16(0.07) $kBq \cdot m^{-2}$. The measurements at the ICE core were interrupted at the 11 cm, and despite that we have relatively high confidence in the arrival at the supported value, a missing inventory estimation were done by two different methods. Applying the equation 47, and using as fixed date the first appearance of the anthropogenic radionuclide ^{241}Am in 1952 in the 8 cm (Figure 61e), the missing inventory would be 23.22 $Bq \cdot m^{-2}$. When the missing inventory is estimated with the fitting approach of $^{210}Pb_{excess}$ the result is 24.81 $Bq \cdot m^{-2}$. These magnitudes are almost two order of magnitude lower than the summation of the $^{210}Pb_{excess}$ inventory for the layers measured, 2184.3 $Bq \cdot m^{-2}$, once more supporting the assumption that at the last measurement the base value was practically reached. Nevertheless, the total inventory of $^{210}Pb_{excess}$ for the ICE core includes the missing inventory for the sake of consistency, and it is 2.21(0.01) $kBq \cdot m^{-2}$. The flux of ^{210}Pb is 23.3(201) $Bq \cdot m^{-2} \cdot yr^{-1}$ and 18.8(28.6) $Bq \cdot m^{-2} \cdot yr^{-1}$ for the IRM and the ICE respectively. In mass, the total flux is 788(96) $g \cdot m^{-2} \cdot yr^{-1}$.for the IRM and 941(272) $g \cdot m^{-2} \cdot yr^{-1}$.for the ICE.

Table 17. Specific activities for the radionuclides ^{210}Pb, ^{214}Pb, ^{226}Ra and for the $^{210}Pb_{excess}$ term, along with age and sedimentation rate obtained for each depth.

	Depth (cm)	^{210}Pb (Bq·kg^{-1})	^{214}Pb (Bq·kg^{-1})	^{226}Ra (Bq·kg^{-1})	$^{210}Pb_{excess}$ (Bq·kg^{-1})	Year (CE)	Sedimentation rate (mm yr^{-1})	Organic carbon flux (g-C_{org}·m^{-2}·yr^{-1})	Inorganic carbon flux (g-C_{inorg}·m^{-2}·yr^{-1})
Irminger Basin	1	189±6.3	26.6±0.85	27.5±18	162±6.3	2016.5±0	0.84±0.12	4.09±0.67	23.6±3.9
	1.5	161±5.6	27.9±0.93	24.8±8.5	133±5.7	2010.6±0.85	1.03±0.17	5.92±1.1	39.9±7.5
	2	157±5.7	26.9±0.94	29.9±7.9	130±5.8	2005.7±0.96	0.90±0.1	4.53±0.63	36.5±5.1
	2.5	149±5.2	25.2±0.9	28.8±3.2	124±5.3	2000.2±1.13	0.83±0.08	3.99±0.49	30.9±3.8
	3	93.4±3.5	29.6±0.97	26.9±6.9	63.8±3.6	1994.1±1.35	1.15±0.10	6.93±0.8	51.4±6
	3.5	85.1±3.1	29.4±0.94	27.3±18	55.7±3.3	1989.8±1.54	1.31±0.11	6.27±0.72	47.5±5.4
	4	93.7±3.5	27.1±0.93	26.4±10	66.6±3.6	1986±1.73	0.95±0.08	3.97±0.45	30.7±3.5
	4.5	76.8±2.9	30.7±0.97	31.3±3.9	46.1±3.1	1980.7±2.03	1.04±0.09	5.88±0.68	36.1±4.1
	5	76.9±3	29.9±0.99	32.5±12	47±3.2	1975.9±2.37	0.89±0.08	6.43±0.75	32.1±3.8
	5.5	60.3±2.2	32.2±1	33.5±18	28.1±2.4	1970.3±2.83	1.21±0.11	7.79±0.94	40.5±4.9
	6	56.7±2.1	31.9±0.94	26.4±14	24.8±2.3	1966.1±3.23	1.12±0.10	7.13±0.88	38.7±4.8
	6.5	57.4±2.1	32±0.99	33.1±8.1	25.4±2.4	1961.7±3.73	0.86±0.09	4.9±0.63	33.9±4.4
	7	49.6±1.8	32.4±0.99	34.8±6.2	17.3±2.1	1955.9±4.49	1.16±0.13	5.07±0.69	46.1±6.2
	7.5	41.4±1.6	32.3±0.97	25.6±5.7	9.1±1.9	1951.6±5.15	1.81±0.21	5.85±0.82	78.6±11
	8	43.3±1.7	32.7±0.97	31.3±12	10.6±2	1948.8±5.64	1.33±0.16	2.33±0.34	59.8±8.8
	8.5	50.5±1.8	29.6±0.86	28±6.9	20.8±2	1945.1±6.38	0.60±0.08	1.78±0.28	26.6±4.2
	9	47±1.7	30.9±0.91	29.4±7.5	16±1.9	1936.7±8.34	0.55±0.09	2.52±0.46	27.1±4.9
	9.5	42.6±1.6	33.8±1	26.9±9.7	8.77±1.9	1927.6±11.1	0.80±0.15	3.9±0.81	35.9±7.4
	10	31.8±1.5	23.1±1.2	22.4±1.5	8.74±1.9	1921.3±13.6	1.24±0.28	6.55±1.6	51±12
	11	37±1.4	33.4±0.94	34.3±15	3.65±1.7	1913.2±17.6	2.61±0.66	15.8±4.2	89.3±24
	12	38.1±1.4	33.5±0.96	29.8±5.6	4.56±1.7	1909.4±19.9	1.84±0.52	11.7±3.4	52.1±15
	13	36.6±1.4	33.9±0.97	30.9±7.4	2.75±1.7	1904±23.7	2.69±0.84	18.6±6	79.8±26
	14	34.7±1.3	26.5±0.77	25.3±6.6	8.18±1.5	1900.3±26.7	0.65±0.26	3.76±1.5	19.8±8.1
	15	35.2±1.5	31.8±0.95	30.9±8.2	3.41±1.8	1884.9±43.4	1.23±0.64	6.1±3.2	40.2±21
	16	33.1±1.4	29.2±0.9	21.3±11	3.87±1.6	1876.8±56	0.81±0.55	3.46±2.4	19.2±13
	17	32.1±1.4	30.3±0.92	24.6±18	1.83±1.7	1864.4±82.5	1.37±1.2	6.72±5.7	26.3±22
	18	32.7±1.4	29.9±0.9	27.3±6.6	2.84±1.7	1857.2±104	0.61±0.72	2.44±2.9	10.4±12
	19	29.3±1.3	28.9±0.92	24.7±12	0.35±1.6	1840.7±174	3.65±5.3	14.5±21	57.4±84
	20	30.4±1.5	30.1±0.9	27±11	0.35±1.7	1837.9±190	3.33±5.2	11.2±18	61.6±97
Iceland Basin	1	127±4.3	37.2±1.1	27.6±12	89.6±4.4	2016.5±0	0.96±0.08	3.18±0.37	26.4±3.1
	1.5	95.9±3.5	31.4±0.96	26.5±8.8	64.5±3.6	2011.3±0.411	1.53±0.15	7.91±1.0	63.4±8.1
	2	80.8±3.1	32.3±1	30.7±11	48.5±3.2	2008±0.487	1.47±0.11	9.62±1.1	74.4±8.3
	2.5	96.5±3.9	35.7±1.2	27.6±16	60.8±4	2004.6±0.584	1.19±0.08	6.77±0.71	55.3±5.8
	3	87.6±3.6	29.5±1	31.8±12	58.1±3.7	2000.4±0.722	1.1±0.07	6.07±0.62	52.2±5.4
	3.5	67.1±2.8	40.1±1.3	39.2±5	27±3.1	1995.9±0.881	1.91±0.12	10.2±1.0	100±10
	4	63.7±2.4	38.4±1.1	31.8±11	25.3±2.7	1993.3±1	2.09±0.13	8.65±0.88	99.7±10
	4.5	60.9±2.4	39.2±1.2	32.3±11	21.7±2.7	1990.9±1.11	2.3±0.14	8.9±0.91	111±11
	5	64.5±2.4	37.3±1.1	40.5±3.3	27.2±2.7	1988.7±1.21	1.68±0.1	6.12±0.63	82.3±8.5
	5.5	59.9±2.4	32.7±1	33.6±20	27.2±2.6	1985.7±1.36	1.47±0.10	7.13±0.74	73.3±7.6
	6	55.6±2.3	34.3±1	25.1±8	21.4±2.5	1982.3±1.55	1.62±0.11	9.73±1.0	80±8.4
	6.5	66.6±2.4	37.4±1.1	31.8±24	29.2±2.6	1979.2±1.75	0.93±0.06	6.53±0.69	50±5.3
	7	74.9±2.7	33.8±1.1	28.3±5.8	41.1±2.9	1973.9±2.13	0.56±0.04	4±0.44	28.7±3.2
	7.5	70.4±2.6	38±1.1	30.1±7.9	32.4±2.8	1965±2.9	0.51±0.04	4.34±0.52	26.4±3.1
	8	55.9±2.2	39.6±1.2	30.5±8.7	16.3±2.5	1955.2±4.05	0.72±0.07	7.44±0.96	39.1±5.0
	8.5	56.5±2	34.8±1	27.9±8.1	21.7±2.2	1948.2±5.17	0.41±0.05	3.4±0.5	21.8±3.2
	9	52±1.9	36±1.1	30.6±5.2	16±2.2	1935.9±7.75	0.35±0.06	2.48±0.45	20.2±3.7
	9.5	53.2±1.9	38.5±1.2	31±19	14.7±2.3	1921.7±12.3	0.22±0.06	1.45±0.38	12.4±3.3
	10	45.1±1.7	40.5±1.2	30.8±8.3	4.65±2.1	1899.2±25.3	0.85±0.3	5.33±2	47.7±18
	11	44.5±1.7	40.3±1.1	33.3±17	4.12±2	1887.4±37.2			

Dates and sedimentation rates with its correspondent uncertainties have been obtained for each layer by applying the CRS model (Figure 61c and f). The difference in years between the top of the core (time zero, summer 2016) and the last centimeter dated are 182 years for the IRM with 20 cm dated and 129 for the ICE in only 11 cm. As we move backward in time the uncertainties in age and sedimentation rate become larger. This is a common feature in all dating models based in short-lived radionuclides with propagation errors. Taking into account the half-life of the ^{210}Pb radionuclide (22.23 yr), the maximum period of time datable using this technique with relative confidence is 150 years [*Mabit et al.,* 2014]. From now on, the results and discussion related with age and sedimentation rate are going to be limited to that temporal range.

In both cores the time-evolution of the artificial radionuclides ^{137}Cs and ^{241}Am shows maximum values at present times (Figure 61b and e) In the IRM, the maximum specific activity detected for ^{137}Cs is 2.014(0.144) Bq·kg^{-1} and 1.184(0.124) Bq·kg^{-1} for ^{241}Am. In the ICE, the presence of anthropogenic radionuclides coincides, but the amount detected is lower, with a superficial maximum of 1.11(0.11) Bq·kg^{-1} for ^{137}Cs and a sub-superficial maximum of 0.485(0.091) Bq·kg^{-1} for ^{241}Am. According with the dating model, in the ICE core the first presence of anthropogenic radionuclides is near 1950. Same happened in the ICE for the ^{241}Am, while the ^{137}Cs is detected until the depth correspondent with the year 1921.

Analyzing the chronological framework, the mean weighted sedimentation rate is as high as 1.0 ±0.13 mm·yr^{-1} in the IRM and 0.96±0.08 mm·yr^{-1} in the ICE. The time-evolution of sedimentation rates in the IRM (Figure 61c) shows that since the end of the XIXth century the sedimentation rates were similar to those from the most recent period, with values around 1 mm·yr^{-1}. Then, at the first decades of the XXth century there was an important increase in the sedimentation rate (2.7±0.84 mm·yr^{-1}, almost three-fold the mean value). This peak is supported by three samples close in time and space (11-13 cm, 1913-1904 AD). After that short-lived maximum event, from ~1940 to now there is a period characterized by an almost constant sedimentation rate, with a slightly decreasing trend with age.

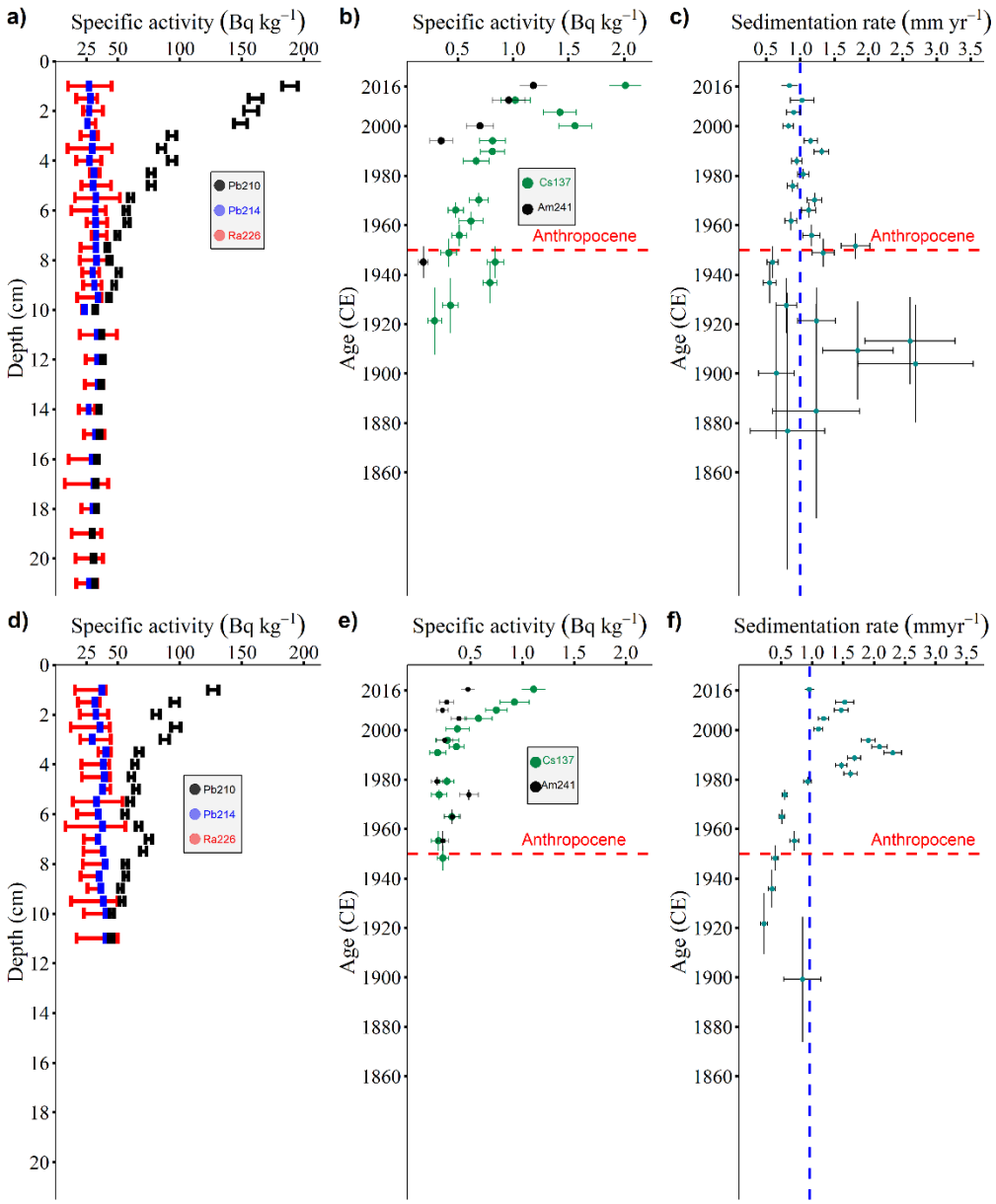

Figure 61. In the upper row, for the IRM core: a) Vertical distributions (cm) of specific activities (Bq·kg^{-1}) and its uncertainties for the radionuclides: ^{210}Pb (black), ^{214}Pb (blue) and ^{226}Ra (red). b) Time evolution of specific activities (Bq·kg^{-1}) for the anthropogenic radionuclides ^{137}Cs (green) and ^{241}Am (black) The length of the vertical (horizontal) line correspond to the uncertainty in the specific activity (age). c) Time evolution of sedimentation rate obtained with the CRS mode. The length of the vertical (horizontal) line correspond to the uncertainty in the sedimentation rate (age). Depicted in blue is the mean value for the sedimentation rate: 1.0(0.13) mm·yr^{-1}. Dashed red line in b) and c) represent the limit of the Anthropocene at 1950 AD considered in the text. In the lower row, for the ICE core, d) analogous to a), e) analogous to b) and f) analogous to c) with the exception that the vertical dashed blue line is the mean value for the sedimentation rate: 0.96(0.08) mm·yr^{-1}.

For the ICE (Figure 61f), the temporal evolution of sedimentation rates shows a XXth century characterized by constant values that were altered at 1980 CE approx. From mid-1980 until the beginning of the XXIth century the sedimentation rate was close to 2 mm·yr^{-1}. After that two decades of maximum sedimentation, since ~2000 to now a decreasing trend appears to be occurring.

With the CF:CS dating model, the result is a single value for the sedimentation rate across all the core, being 0.81±0.02 mm·yr^{-1} for the IRM and 0.94±0.14 mm·yr^{-1} for the ICE.

8.3.2 Geochemical evolution

Time evolution profiles of TC and its components TOC and TIC are plotted in Figure 63a-b. The content of TC for the IRM ranged between 3% and 5.6% with an increasing trend from 1910 to 1940 CE. The last 70 yr records higher values that previous decades. The content of TC in the ICE is constant, and represents the 8% in mass. In both cores, around 90% of the carbon present was TIC. TOC content ranged between 0.16% and 0.86% in the IRM and was higher at the ICE, ranging between 0.56% and 1.28%. The maximum content in TOC occurs in surface for the IRM and there is a minimum in 1949 CE. It is precisely at the same age when the maximum content in TOC in the ICE appears. The minimum content of TOC at the ICE also coincides in time with a subsuperficial second maximum in TOC at the IRM. The TOC burial efficiency, or the percentage of deposited organic carbon preserved in the sediment, can be estimated by comparing the concentration at the top of the core and the constant concentration at depth where it has undergone some diagenesis [*Masqué et al.,* 2002]. For the IRM, the organic carbon burial efficiency was about ~58%. In the ICE, despite the observed variability in TOC content (Figure 63e), there are no difference in concentration between the TOC content at surface and at the bottom of the sediment sequence dated, because they are around 0.8% so the burial efficiency would be 100%. The situation does not change when all the core is analyzed (data not shown), and the mean content of TOC it is still around 0.8%.

X-ray fluorescence (XRF) measurements data for the biogenic proxy element Ca and the terrigenous proxy Fe are represented normalized by Ti (Figure 63c-d and g-h). In the IRM the Ca/Ti profile, as it occurs with previous proxies, shows a clearly increasing trend in recent time, with enhanced biogenic input during the latest 50 years. The Ca/Ti trend is not so obvious in the ICE, where the variability is greater, nevertheless an increasing trend is observed since 1980 CE. The Fe/Ti profile it is similar in both cores, showing short-time and low amplitude variability around a constant mean value without any visible trend.

8.3.3 Carbon fluxes

Following equation 49, fluxes can be estimated for each layer and each element. The most determinant factor in the time evolution profile of mass flux is the sediment accumulation rate (SAR), periods with greater sedimentation rates have higher fluxes (Figure 62). Actually, there is not a global consensus to mark the onset of the Anthropocene, but the option to set as lower boundary the mid-20th century is gaining strength [*Steffen et al., 2016; Waters et al., 2016*]. Taking into account that the aim of the study is to quantify sedimentary carbon fluxes in the

Anthropocene, from now on results and discussion related with fluxes are going to be limited to the temporal range from 1950 to the present. During the Anthropocene, mean weighted flux to the sediment of inorganic and organic carbon are 3.76±0.5 mg C_{inorg}·cm^{-2}·yr^{-1} and 0.54±0.07 mg C_{org}·cm^{-2}·yr^{-1} respectively in the IRM and 5.29±0.6 mg C_{inorg}·cm^{-2}·yr^{-1} and 0.64±0.07 mg C_{org}·cm^{-2}·yr^{-1} respectively in the ICE. With an extension for the Irminger Basin of 6.12 x 10^5 km^2 [*Pérez et al.,* 2010], annual fluxes at basin-scale with the IRM carbon flux are 23±3 Tg C_{inorg}·yr^{-1}, 3.3±0.4 Tg C_{org}·yr^{-1}, and 26.5±3.4 Tg C_T·yr^{-1}. Following also *Pérez et al.,* [2010] for the definition of the Iceland Basin extension as the region between the Reykjanes Ridge axis and the line joining the Eriador Seamount and the Faroe Islands (9.61 x 10^5 km^2), annual fluxes at basin-scale with the ICE carbon flux results are 50.8±5.5 Tg C_{inorg}·yr^{-1}, 6.2±0.7 Tg C_{org}·yr^{-1}, and 57.3±6.2 Tg C_T·yr^{-1}.

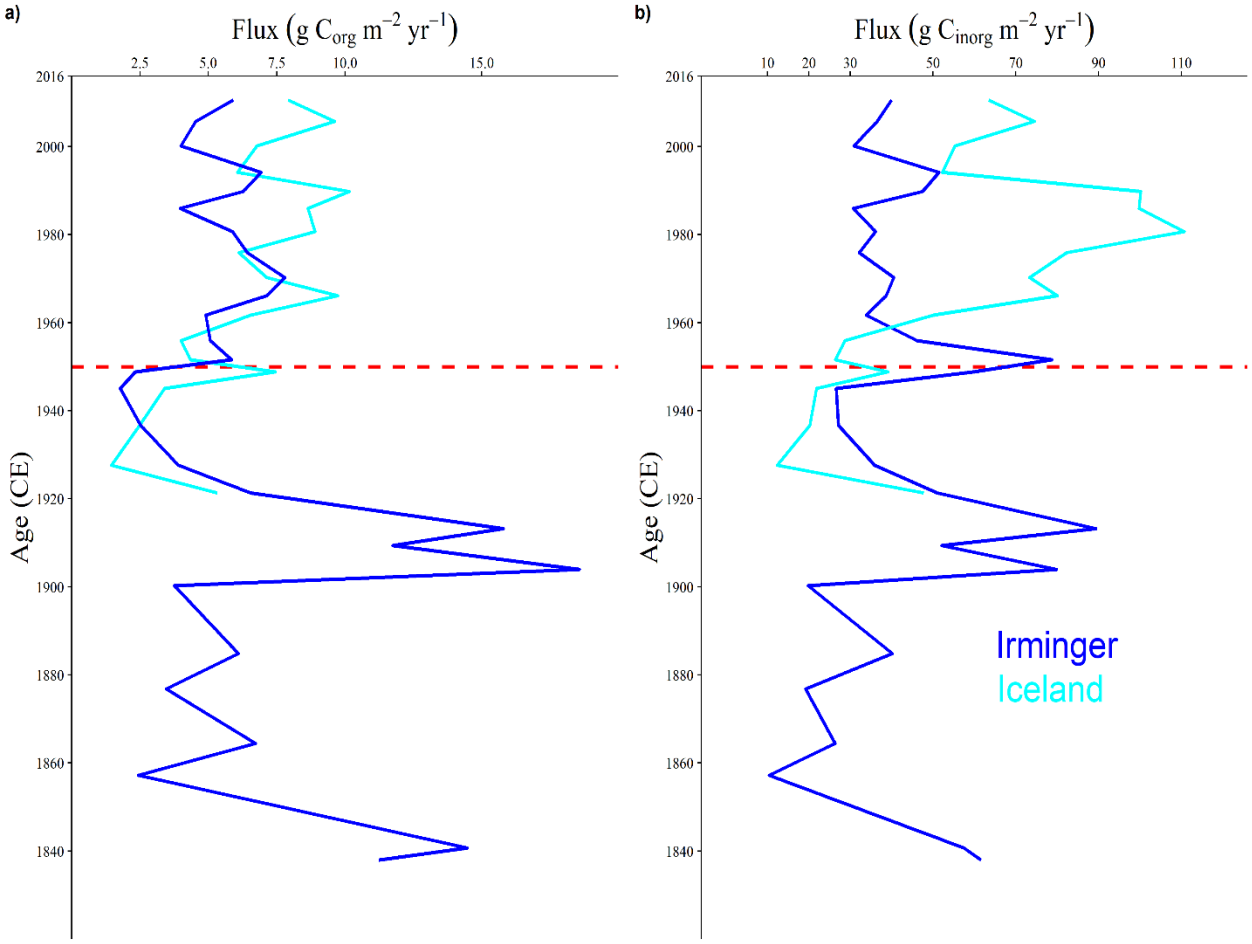

Figure 62. Time evolution of mass flux in the IRM (dark blue) and the ICE (light blue) for a) organic and b) inorganic carbon. Dashed red line represents the limit of the Anthropocene, considered in the text at 1950 CE

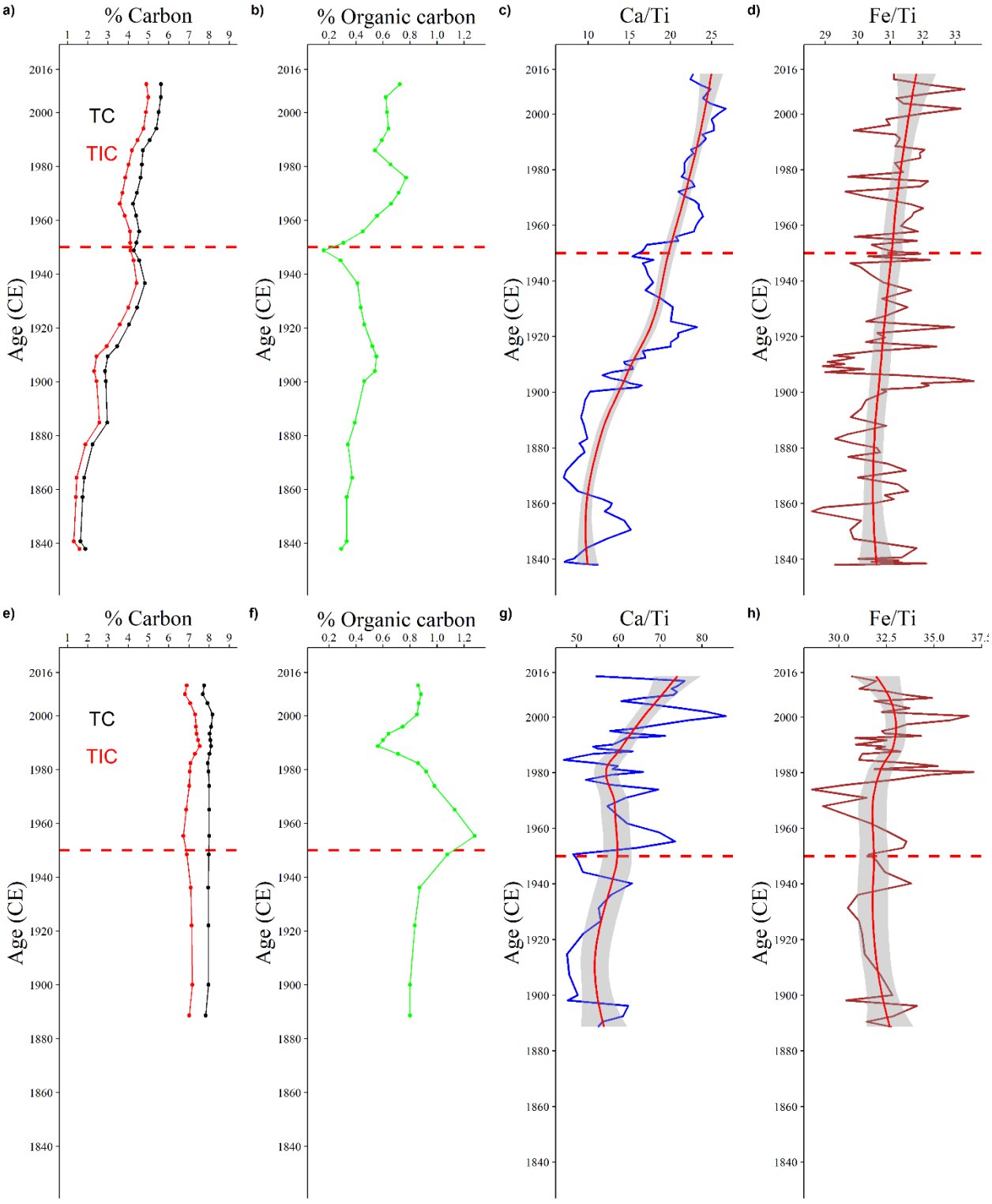

Figure 63. In the upper row, for the IRM core: time evolution of quantitative a) total (TC, black) and inorganic carbon (TIC, red) elemental composition b) total organic carbon. Time evolution of semiquantitative elemental composition for c) the ratio Ca/Ti; and d) the ratio Fe/Ti. In c) and d) a locally weighted least squares regression for the elemental composition with a 95% confidence interval is also represented (red line and grey confidence interval). Horizontal dashed red line represents the limit of the Anthropocene, considered in the text at 1950 CE. In the lower row, for the ICE core, e) analogous to a), f) analogous to b), g) analogous to c) and h) analogous to d).

8.4 Discussion

The hypothetical profile of the $^{210}Pb_{excess}$ concentration under the assumptions of the CRS model would be a pure exponential curve [*Mabit et al.,* 2014]. $^{210}Pb_{excess}$ specific activity profiles (Figure 61a/d) follows the radioactive decay law and in both cases shows a near-perfect exponential signal. This shape of the profile suggests that no significant sediment mixing occurs [*Oberle et al.,* 2016]. The chronology of Irminger deep-sea corer spans 182 years in 20 cm. In that time, annual atmospheric CO_2 global concentrations raised almost 120 ppm, from 283 [*Meinshausen et al.,* 2017] to 402.8 ppm (NOAA/ESRL), altering marine chemistry [*Orr et al.,* 2005] and potentially altering the flux of carbon to marine sediments.

The superficial activity of $^{210}Pb_{excess}$ is 162.1±6.3 Bq·kg^{-1}in the IRM and 89.6±4.4 Bq·kg^{-1} in the ICE. Some studies have reported $^{210}Pb_{excess}$ specific activities in surface sediments of deep water zones of the subpolar North Atlantic. Very near to the ICE site in the eastern flank of the Reykjanes Ridge, *Boessenkool et al.,* [2007] measured surface concentrations of $^{210}Pb_{excess}$ of 290 Bq·kg^{-1} by gamma spectrometry in sediments collected at 2630 m water depth (black triangle in Figure 60). At a similar depth in the same location, *Jonkers et al.,* [2010] reported activities from sediment and particles intercepted as high as 1028 Bq·kg^{-1} and around 1500 Bq·kg^{-1} respectively. Another deep sample, located near the IRM at the south of Greenland at almost 3500 m water depth (white triangle in Figure 60), gives a superficial activity for $^{210}Pb_{excess}$ of around 360 Bq·kg^{-1} [*Moffa-Sánchez et al.,* 2014]. The range of values is quite large even at the same location, and our data is clearly at the lower end. On one hand the $^{210}Pb_{excess}$ activities at the sediment interface tend to increase with water depth due continuous scavenging by settling particles [*Miralles et al.,* 2005]. On the other hand the activity of ^{210}Pb in the sediment provides a measure of the freshness of the material, with fresh particles having higher activity [*Jonkers et al.,* 2010a]. Neither depth distribution of the samples or freshness of the material can't explain the observed differences. In our zone, the depth distribution of the samples doesn't support the criteria; and the organic carbon contribution in our cores, is not as much different as organic matter contribution in *Jonkers et al.,* [2010] (around 2%). If there is no reason to think that our sediment is not as fresh as theirs, fresh argument won't support the large difference in surface concentrations. While some measures were done with gamma-spectrometry [*Boessenkool et al.,* 2007; *Moffa-Sánchez et al.,* 2014, the data showed here], others were acquired with alpha-spectrometry [*Jonkers et al.,* 2010a]. The $^{210}Pb_{excess}$ activities derived by alpha or gamma methods can be compared with confidence [*Zaborska et al.,* 2007], so this dichotomy can't either explain the differences between the superficial activities observed. A magnitude more interesting to compare than the superficial activity of $^{210}Pb_{excess}$ is the flux to the sediment surface (Bq·m^{-2}·yr^{-1}). This flux should be similar between cores and atmospheric fluxes in the same region [*Masqué et al.,* 2002]. Unfortunately, this magnitude is given only once for near sediments and with a value as high as 661 Bq·m^{-2}·yr^{-1} [*Jonkers et al.,* 2010a]. Our flux estimates (23.3/18.8 Bq·m^{-2}·yr^{-1} for IRM/ICE) are notably minor, but they are in consonance with the atmospheric fallout values for sites remote from major land masses (30-40 Bq·m^{-2}·yr^{-1})

[*Appleby*, 1998] and for the fluxes in the northeast Atlantic (50 $Bq \cdot m^{-2} \cdot yr^{-1}$) [*Cochran,* 1990; *Thomson et al.,* 1993]. The correspondence of flux values, dependent on total $^{210}Pb_{excess}$ inventory and the span of the chronology, give us confidence in the magnitude found for the surface activity.

Artificial radionuclides ^{137}Cs and ^{241}Am are detectable in the environment after 1952 [*Povinec et al.,* 2003]. Since the decline of nuclear-bomb testing, nuclear accidents (Chernobyl 1986, Fukushima 2011) and intentional discharges from nuclear treatment plants (Sellafield, UK; Cape de la Hague, France) are the events of maximum inputs to the environment [*Povinec et al.,* 2003; *Buesseler et al.,* 2011]. The detection of this radionuclides in deep-sea sediments is strongly dependent of a high resolution measurement, because their concentration levels are close to counter detection limits [*Harden et al.,* 1992]. Furthermore, ^{137}Cs have post-depositional diagenetic mobility, limiting the resolution of specific dates [*Sholkovitz & Mann,* 1984]. A downward migration process is proposed here as the cause for the detection of ^{137}Cs at 1921 in the IRM core (Figure 61b). For this reasons, the capabilities of a quantitative approach that shows clear correspondences between maximum peaks and CE dates are compromised. Nevertheless, here we show that both age model can be validated with anthropogenic radionuclides under a presence/absence criteria because in the two study sites they appear approximately since the onset of the Anthropocene.

According with the CRS model, the sediment accumulation rates are relatively high by pelagic deep-sea environments. This imply that there is a sufficient supply of organic-rich suspended particles, that are scavenging $^{210}Pb_{excess}$ from the water column to be later deposited as fine-grained sediments at the bottom. The value found in the central Irminger Basin for sediment accumulation rate (1.0±0.13 $mm \cdot yr^{-1}$) is in good agreement with the estimate given at the south tip of Greenland in the Labrador Sea (~0.4 $mm \cdot yr^{-1}$), [*Moffa-Sánchez et al.,* 2014]. The minor magnitude for the *Moffa-Sánchez et al.,* [2014] core can be related with its deeper situation, near 3500 m water depth. When all the dated sequence of ICE is analyzed, the mean weighted value found in the Iceland Basin for sediment accumulation rate is similar, 0.96±0.08 $mm \cdot yr^{-1}$. Despite of that, there are two decades (1980-2000 CE) in the temporal sequence showing a tightly cluster of coherent sedimentation rates around 2 $mm \cdot yr^{-1}$ (Figure 61f). Published rates of sedimentation in the eastern flank of the Reykjanes Ridge are around ~2 $mm \cdot yr^{-1}$ [*Boessenkool et al.,* 2007; *Jonkers et al.,* 2010a]. This higher magnitude is expected, because they are located in the Gardar Drift, a contourite deposit well-known by its high sediment accumulation rates [*Bianchi and McCave,* 2000].

One of the studies in the Gardar Drift gives the comparative between the accumulation flux determined with the ^{210}Pb sediment dating and the flux intercepted with sediment traps [*Jonkers et al.,* 2010a]. Despite the uncertainties associated with its use [*Buesseler et al.,* 2006], deep tethered sediment traps are the only way to provide direct estimates of the magnitude of the sedimentation flux into the deep ocean [*Lampitt et al.,* 2008]. *Jonkers et al.,* [2010] gives values of 363 $g \cdot m^{-2} \cdot yr^{-1}$ and 600 $g \cdot m^{-2} \cdot yr^{-1}$ for the fluxes with sediment traps and from the sediment

respectively. They are quite different, but in the same order of magnitude that our estimate of 941±272 $g \cdot m^{-2} \cdot yr^{-1}$.for the ICE. Sediment focusing for high turbidity between the bottom and the depth of sediment trap (4 m above bottom), was suggested as a reason for the disparity [*Jonkers et al.,* 2010a].

In the Irminger Basin, there is only one location with public available sediment trap data currently [*Torres-Valdés et al.,* 2014]. The mean total mass flux reported for all the episodic periods between 2003-2007 is 11.6 $g \cdot m^{-2} \cdot yr^{-1}$ [*Jonkers et al.,* 2010b], really far from our estimate of 788 $g \cdot m^{-2} \cdot yr^{-1}$, and clearly not in the same order of magnitude. Even the largest episode of export, like the one reported between May and June 2007 with almost 38 $g \cdot m^{-2} \cdot yr^{-1}$ [*Jonkers et al.,* 2010b], it is still short. In fact, this value is close to the flux reported here for total carbon (36.4 $g \cdot m^{-2} \cdot yr^{-1}$), without having into account the lithogenic mass flux. The distance between the bottom and the sediment trap in *Jonkers et al.,* [2010b] was ~250 meters, so deposition from nepheloid bottom layers can't be disregard as one of the causes of such discrepancies. Unfortunately, we have no info about turbidity, and moreover, it is a large difference so more factors are needed to explain it.

Input of terrigenous elements is similar for the two basins in terms of composition, origin and transport agent, presumably aeolian deposition (Figure 63d/h), and with a decreasing trend with time (Figure 64a-b/d-e). In contrast, the time-evolution of elemental composition shows that the biogenic component of the total mass flux in the IRM (Figure 63a-c and Figure 64c) has increased its relevance since the XX^{th} century, even when periods of carbon content drops in TOC are observed (1945-1952 and 1985 CE, Figure 63b). The general trend in biogenic component is not so obvious in the ICE (Figure 63e-g). If in the IRM the events of less carbon content accumulation were not sufficiently important as to avoid the increasing biogenic trend, it is possible that in the ICE the high sedimentation events of the period 1980-2000, combined with a decrease in the proportion of the biogenic fraction (Figure 63g and Figure 64f) had smooth the trend in the biogenic component. Short-time inputs of lithogenic material would explain both higher sedimentation rates in the 1980-2000 period and the disappearance of any trend in the ICE temporal sequence as a whole. In the IRM, despite relatively lower sedimentation rates during the last 25 years than during previous decades (Figure 61c), it is very likely that biogenic inputs are increasing in the most recent times. In the ICE, the proposed short-time accumulation events prevent the assessment of general trends, but it appears that in the latest years the regime of sedimentation is returning to the status it was at the beginning of the XX^{th} century. The alternance of low sedimentation rates dominated by pelagic biogenic particles with episodic high-accumulation events in which the terrigenous fraction gain relevance appears to be a common process.

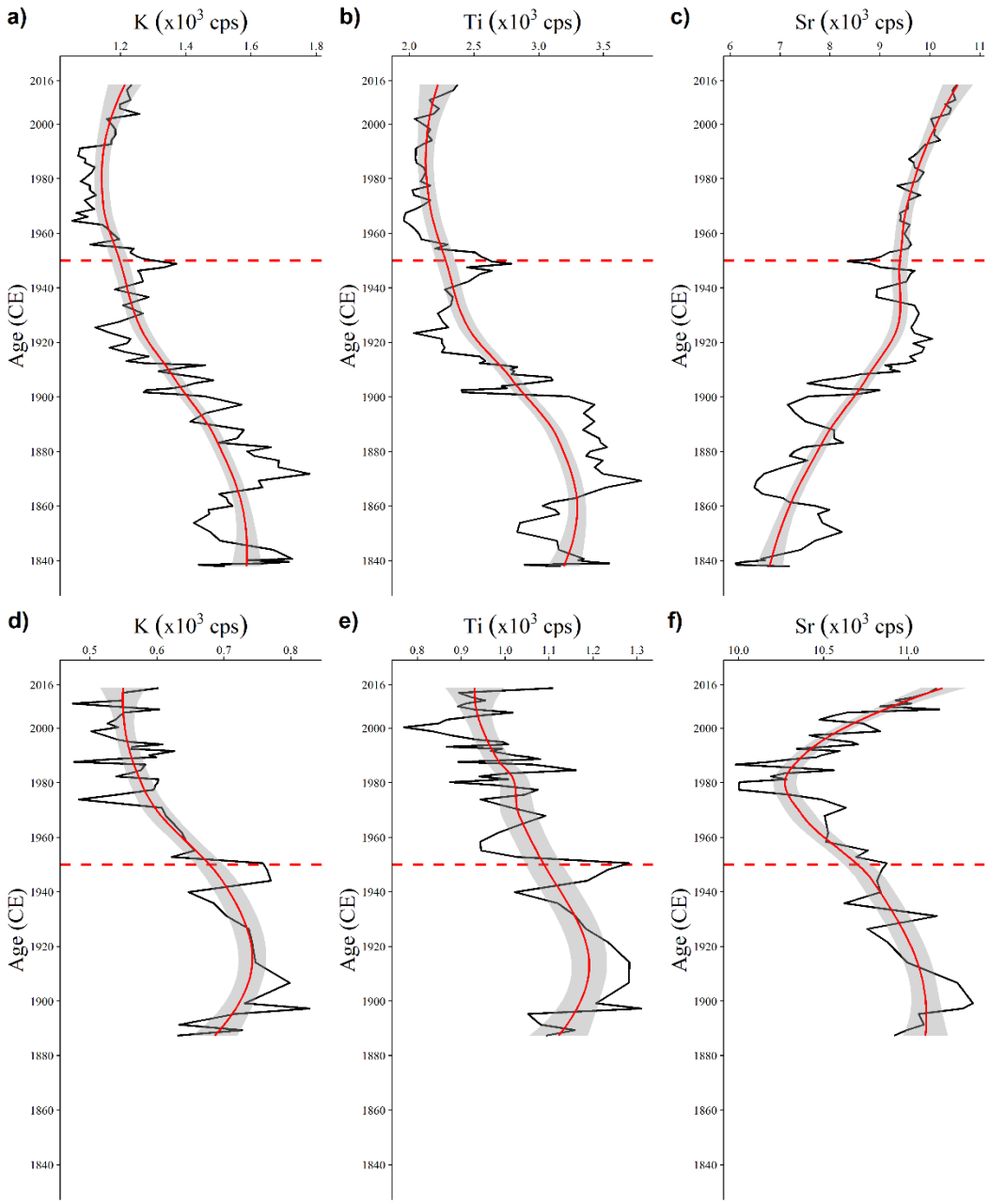

Figure 64. In the upper row, for the IRM core: time evolution of semiquantitative elemental composition for terrigenous elements a) K; b) Ti, and the marker for biogenic origin c) Sr. Locally weighted least squares regression for the elemental composition with a 95% confidence interval is also represented (red line and grey confidence interval). Horizontal dashed red line represents the limit of the Anthropocene, considered in the text at 1950 CE. In the lower row, for the ICE core, d) analogous to a), e) analogous to b), and f) analogous to c).

The flux of C_{inorg} modelled for the same zone in Fig.10 of *Honjo et al.,* [2008] is between 0.1-0.2 mol $C_{inorg} \cdot m^{-2} \cdot yr^{-1}$, five times smaller than the C_{org} fluxes. Despite that local peculiarity, they concluded that at large scale the molar ratio of C_{org}/C_{inorg} is one. Here, given the increasing prevalence of carbonates along the core (Figure 63c/g), the assumption that all the flux of C_{inorg} is because of carbonates is feasible, so the molar ratio of C_{org}/C_{inorg} since the Anthropocene is

0.15 for the IRM and 0.12 for the ICE. The molar ratio of C_{org}/C_{inorg} in particle flux for a time series sediment trap in the deep northeast Atlantic is 1.4 [*Lampitt et al.,* 2010]. That same value is found when the subpolar North Atlantic in a pan-Atlantic data compilation is analyzed [*Torres-Valdés et al.,* 2014]. The processes behind the observed differences can be multiple: important local variability in export production, the longer timescale integrated under our approach (mutidecadal timescale), or the high TIC content in the measured cores due biogenic carbonate sedimentation (Figure 63c/g) among others; but none of them by itself can explain a deviation as high as ~1 C_{org} : 7 C_{inorg}. Our C_{org}/C_{inorg} ratios were obtained under a different approach that *Honjo et al.* [2008] or *Lampitt et al.,* [2010], but the results suggest that an important biogeochemical process alters significantly the ratios preserved at the sediment. Organic carbon cycling in the uppermost centimeters of the seafloor can be the reason why the C_{org}/C_{inorg} molar ratio of settlement equal to one is displaced to molar ratios ~1:7 in the final configuration of the sediment.

In order to summarise, we can conclude that gamma-ray spectrometry using two simultaneous hyper-pure germanium (HPGe) detectors is an accurate technique and sensitive enough for dating deep-sea pelagic sediments. The chronological framework based in ^{210}Pb dating reveals that in the central and deeper areas of Irminger Basin, the Anthropocene represents the firsts 7.5 cm of sediment and the first 16 cm covers the last 150 years. Based on this chronology, the average sedimentation rate of the Irminger core is 1.0±0.13 $mm \cdot yr^{-1}$. In the Iceland Basin the Anthropocene represents the first 8 cm, and in the last 130 years the average sedimentation rate was 0.96±0.08 $mm \cdot yr^{-1}$. Both rates are quite high for deep-sea basins.

Inter-annual variability in the sedimentation rate and in the terrigenous and biogenic proxies suggests short time-scale changes of bottom currents and/or biological productivity at the subpolar North Atlantic during the Anthropocene. The latest 50 years show an enhanced biological productivity in both basins. During the Anthropocene, 37.6±4.8 $g\text{-}C_{inorg} \cdot m^{-2} \cdot yr^{-1}$ and 5.4±0.7 $g\text{-}C_{org} \cdot m^{-2} \cdot yr^{-1}$ are being deposited in the Irminger Sea, while 53±6 $g\text{-}C_{inorg} \cdot m^{-2} \cdot yr^{-1}$ and 6.4±0.7 $g\text{-}C_{org} \cdot m^{-2} \cdot yr^{-1}$ are deposited in the Iceland Basin. The sedimentation generates a substantial total carbon sink in the area of 26 Tg $C \cdot yr^{-1}$ for the Irminger and 48 Tg $C \cdot yr^{-1}$ for the Iceland basin. Taking together this two important basins of the subpolar North Atlantic, the annual quantity of organic carbon preserved in the sediments is 8 Tg $C \cdot yr^{-1}$. This outcome has to be accounted for in current ocean carbon models and budgets. It is too soon to infer any reliable trend in the flux of carbon since 1950, the onset of the Anthropocene, but the current status of knowledge would act as a baseline in future evaluations of carbon cycle in marine sediments of the North Atlantic

PART V. Conclusions

The current biogeochemical status of the eastern subpolar North Atlantic (eSPNA, Figure 33) was evaluated under an integrated approach based on quantifications of transports and budgets of carbon, nutrients and oxygen.

The first component of the carbon cycle analyzed was the organic component. In the ocean carbon cycle, the dissolved organic fraction (DOC) represents practically the whole amount in the total organic carbon (TOC) pool because the particulate fraction (POC) is minority and assumed in balance. The scarcity of DOC data throughout the oceans, and the North Atlantic in particular, hamper a correct evaluation of the relative importance of DOC in the total carbon cycle [*Hansell et al.,* 2004]. In order to solve this, here we show an assessment coupling well-solved water mass transports along transoceanic sections with high-quality [DOC] measurements.

With [DOC] samples measured in the OVIDE 2002 cruise and a recent water mass mixing model developed for the subpolar North Atlantic gyre [*García-Ibañez et al.,* 2015], a characterization of the [DOC] source water type for each water mass existent at the OVIDE section was resolved by an inversion system. With the [DOC] defined for each water mass, the combination of the water mass structure resolved by means of an extended optimum multiparameter (eOMP) analysis [*García-Ibañez et al.,* 2015] with absolute velocity fields for the OVIDE section [*Lherminier et al.,* 2007*,* 2010], the transport of DOC could be evaluated for cruises when it was not measured. Combining transports at OVIDE section with transports of water mass and DOC available in the literature at the northern limit of the eSPNA (G-I-S sills) [*Hansen & Ø*sterhus*,* 2000; 2007*; Jeansson et al.,* 2011*; Jochumsen et al.,* 2012], the carbon organic budget in the eSPNA was elaborated. The combination of own data at OVIDE section with public available estimates at the boundaries of the eSPNA is a common characteristic followed along this thesis for the budget assembly.

We separated the contribution of the upper and lower limb of the AMOC to the total transport of DOC, and concluded that when DOC advection in the eastern subpolar North Atlantic is considered, the DOC budget is in balance (8±77 kmol·s^{-1}), suggesting that DOC production in the eSPNA is balanced by its removal. With regard to the [DOC] water mass characterization, our results confirm that the Nordic overflows (DSOW and ISOW) are relatively rich in DOC content, adding important quantities of DOC to North Atlantic deep waters. We also found that a significant characteristic of the DOC cycle in the eSPNA is its export from the upper to the lower limbs of the AMOC. The relatively fast vertical transport of DOC contributes to carbon sequestration, analogous to the vertical transport of DIC. DOC injected to the deep layers is more labile than the majority of the deep DOC observed in the South Atlantic and Pacific Oceans, so it is more susceptible to remineralization.

Following a similar strategy, and inspired by the closely similar mean velocity-weighted [DOC] found in both limbs of the AMOC at the eSPNA, we also reconstructed the DOC transports at subtropical latitudes in the North Atlantic (24ºN). Here we show that in the North Atlantic, 62 Tg-C·yr^{-1} of DOC

are consumed in the lower limb of the AMOC between subpolar and subtropical latitudes, representing 72% of the DOC exported by the whole Atlantic Ocean. This outcome implies that much of the net DOC exported with the overturning circulation in the eastern-SPNA, the major source of new DOC in the deep global ocean, is remineralized within decades, thus impacting deep microbial and dissolved organic matter compositional dynamics. DOC downward export due to overturning circulation acts as a carbon sink and represents a considerable contribution to CO_2 sequestration. Given the atmospheric CO_2 uptake of 0.20 Pg-C·yr^{-1} in the area [*Takahashi et al.,* 2009], the carbon sequestration mediated by DOC would represent ~30% of the total North Atlantic CO_2 sink.

Once evaluated the organic component in a separate way, we focus on the main core of the thesis, the elaboration of an integrated biogeochemical budget balanced around carbon and analyzing the longest time-series available for the OVIDE section (2002-2016). This study-case is based in the combination of eight repetitions of the high-quality hydrographic section OVIDE with public available data sources. Using an optimization method, a linear inverse box model was developed. Stablishing relationships between biogeochemical tracers based in stoichiometric ratios, sources and sinks of carbon, nutrients and oxygen in the eSPNA are estimated. This approach allows the assessment of biogeochemical cycles in an integrated budget model using well-known elemental relations as conversion factors. The evaluation relies on a robust circulation scheme of the mean circulation in the northern North Atlantic [*Daniault et al.,* 2016] and quantitative tracer transports estimates, allowing an integrated evaluation that is independent of assumptions about biogeochemical behavior and with an output consistent between tracers.

On decadal time scale, the biogeochemical budget model confirms that the eSPNA is a significant atmospheric carbon sink. The eSPNA is a net autotrophic region where biological primary production exceeds respiration, and where an organic carbon export to sediment of 38±10 Tg-C_{org}·yr^{-1} (101±27 kmol·s^{-1}) occurs. The hydrographical conditions and the specific location of the Irminger Sea, located just at the confluence of the two limbs of the AMOC, where around 10 Sv of deep-water formation occurs, make it an ideal hotspot for tracers to be long-time sequestered in the deep ocean. The Irminger Sea, representing the 16% in area, is the place where the 48% of the organic and 46% of the $CaCO_3$ sediment flux in the eSPNA takes place.

We suggest that in a similar way, light-to-dense water formation processes are the reason for the oxygen uptake (856±74 kmol·s^{-1}) and the heat release that occurs in the eSPNA, and that the transport of recently ventilated waters, with high-oxygen concentration, in the southward flowing lower limb of the AMOC is the principal mechanism for the equatorward flux of oxygen observed in the North Atlantic. The predicted ocean deoxygenation due global warming is not detected with our dataset. There are two complementary explanations: in the heterogeneous ocean, deoxygenation at global scale can happen without alteration in the oxygen levels of the eSPNA; and/or a longer time

series is needed in this highly dynamic location with strong natural variability, in order to detect trends in oxygen deviations.

Finally, the sink detected by the water-column balance approach was contrasted against sediment fluxes. With newly retrieved superficial sediment cores attained at the OVIDE/BOCATS 2016 cruise and a novel technique to stablish absolute chronologies, a quantitative first-estimate of carbon fluxes into the deep-sea sediment of the subpolar basins Irminger and Iceland was reached. As a way to link the time-scale of biogeochemical processes potentially affected by anthropogenic climate change with geological processes that usually acts at longer time-scales, we focus in the contemporary times, in the recently proposed geological epoch called Anthropocene.

The geochronology based on high-resolution low background gamma-ray spectrometry with two simultaneous hyper-pure germanium (HPGe) detectors is shown as an accurate technique and sensitive enough for dating deep-sea pelagic sediments. The chronological framework based in the natural radionuclide ^{210}Pb reveals that the average sedimentation rate is 1.0±0.13 $mm \cdot yr^{-1}$ in the central Irminger Basin; and 0.96±0.08 $mm \cdot yr^{-1}$ in the east flank of the Reykjanes Ridge in the Iceland Basin. Both rates are quite high for deep-sea sediments. Applying the dating model Constant rate of Supply (CRS), the time-evolution of sedimentation rates could also be evaluated. With the exception of short-time deposition events, both cores show quite constant sedimentation rates, implying that the deposition framework was uniform during the Anthropocene.

Combining accurate chronologies with geochemical characterizations, allows the quantification of elemental fluxes into the sediment. Inter-annual variability in the sedimentation rate and in the terrigenous and biogenic proxies suggests short time-scale changes of bottom currents and/or biological productivity at the subpolar North Atlantic during the Anthropocene. The proxies support an enhanced biological productivity since the latest 50 years in both basins, but it is too soon to infer any reliable trend in the flux of carbon since the onset of the Anthropocene. The flux analysis concluded that during the Anthropocene 38±5 g $C_{inorg} \cdot m^{-2} \cdot yr^{-1}$ and 5.4±0.7 g $C_{org} \cdot m^{-2} \cdot yr^{-1}$ are deposited in the Irminger Sea, while 53±6 g $C_{inorg} \cdot m^{-2} \cdot yr^{-1}$ and 6.4±0.7 g $C_{org} \cdot m^{-2} \cdot yr^{-1}$ are deposited in the Iceland Basin. This burial sedimentation estimates supposes that a substantial carbon sink in the area exists, quantified in more than 26 $Tg\text{-}C \cdot yr^{-1}$ for the Irminger and almost 48 $Tg\text{-}C \cdot yr^{-1}$ for the Iceland basin. Taking together this two important basins of the subpolar North Atlantic, the annual quantity of organic carbon preserved in the sediments is 8 $Tg\text{-}C_{org} \cdot yr^{-1}$.

In summary, an integrated approach it is a requirement not only to comprehend the carbon cycle, but also to quantify it. The combination of observations coming from different methodologies and the utilization of open access databases along with modelling efforts, allowed to analyze carbon fluxes in a dynamical complex region. The relevance of the North Atlantic as a carbon sink area in the global carbon cycle was once again confirmed under a broad set of approaches. Following the order of the research chapters, we conclude that: (i) the DOC downward export mediated by the

AMOC supposes a significant fraction (~30%) of the total carbon sink and has to be accounted for in current ocean carbon models and in studies carried out by the biogeochemical and microbiological communities. (ii) Transports and budgets of carbon, nutrients and oxygen in the subpolar North Atlantic can be taken as a baseline in future evaluations of the Atlantic carbon cycle, and should be used to test and/or constrain global ocean models outputs. And (iii), it is possible to evaluate contemporary fluxes of carbon into deep-sea marine sediments with the combination of high-resolution dating techniques and geochemical analysis.

The unabated increase in atmospheric CO_2 levels, together with the whole set of anthropogenic perturbations in the natural cycle of elements, will require further evaluations on the assumption that the biological carbon cycle it is in steady state. The results of this memory can be seen as a try to integrate the organic/inorganic and natural/anthropogenic components of the carbon cycle in the North Atlantic on its fluxes between the pools of atmosphere-ocean-sediments. The combination of different sources of data along with a set of well stablished biogeochemical relationships in the elemental composition of organic matter, allows the assessment of marine biogeochemical budgets in an integrated way. This study case also suggests the possibility that benthic communities have a significant role in the carbon fluxes, still not appropriate accounted for.

Currently, the growing necessity of climate change simulations makes that the study of Earth Sciences is led by modelling efforts. The potential change in multiple stressors with biogeochemical impact in ocean ecosystems (oxygen, nutrients, primary production, pH…) are almost routinely modelled, but not always properly validated. We suggest that the kind of budgets shown here can be applied to evaluate data products from Earth System model outputs in order to test if the models keep the biogeochemical coherency.

References

Aarkrog, A. (2003), Input of anthropogenic radionuclides into the World Ocean, *Deep-Sea Research Part I: Oceanographic Research Papers*, *50*(17–21), 2597–2606, doi:10.1016/S0967-0645(03)00137-1.

Alongi, D. M., J. Pfitzner, L. A. Trott, F. Tirendi, P. Dixon, and D. W. Klumpp (2005), Rapid sediment accumulation and microbial mineralization in forests of the mangrove Kandelia candel in the Jiulongjiang Estuary, China, *Estuarine, Coastal and Shelf Science*, *63*(4), 605–618, doi:10.1016/j.ecss.2005.01.004.

Alonso-González, I. J., J. Arístegui, C. Lee, A. Sánchez-Vidal, A. Calafat, J. Fabres, P. Sangra, P. Masqué, A. Hernández-Guerra, and V. Benitez-Barrios (2010), Role of slowly settling particles in the ocean, *Geophysical Research Letters*, 37(13), doi:10.1029/2010GL043827.

Álvarez, M., H. L. Bryden, F. F. Pérez, A. F. Ríos, and G. Rosón (2002), Physical and biogeochemical fluxes and net budgets in the subpolar and temperate North Atlantic, *Journal of Marine Research*, *60*(1), 191–226, doi:10.1357/00222400260497462.

Álvarez, M., A. F. Ríos, F. F. Pérez, H. L. Bryden, and G. Rosón (2003), Transports and budgets of total inorganic carbon in the subpolar and temperate North Atlantic, *Global Biogeochemical Cycles*, *17*(1), 2-1-2–21, doi:10.1029/2002GB001881.

Álvarez, M., F. F. Pérez, H. Bryden, and A. F. Ríos (2004), Physical and biogeochemical transports structure in the North Atlantic subpolar gyre, *Journal of Geophysical Research: Ocean.*, *109*(C3), C03027, doi:10.1029/2003JC002015

Álvarez, M., and X. A. Álvarez-Salgado (2007), Biogeochemical budgets in the eastern boundary current system of the North Atlantic: Evidence of net heterotrophy and nitrogen fixation, *Limnology & Oceanography*, *52*(4), 1328–1335, doi:10.4319/lo.2007.52.4.1328.

Álvarez-Iglesias, P., B. Quintana, B. Rubio, and M. Pérez-Arlucea (2007), Sedimentation rates and trace metal input history in intertidal sediments from San Simón Bay (Ría de Vigo, NW Spain) derived from 210Pb and 137Cs chronology, *Journal of Environmental Radioactivity,* 98(3), 229–250, doi:10.1016/j.jenvrad.2007.05.001.

Álvarez-Salgado, X. A., M. Nieto-Cid, M. Álvarez, F. F. Pérez, P. Morin, and H. Mercier (2013), New insights on the mineralization of dissolved organic matter in central, intermediate, and deep water masses of the northeast North Atlantic, *Limnology & Oceanography*, *58*, 681–696, doi:10.4319/lo.2013.58.2.0681.

Álvarez-Vázquez, M. Á., M. Caetano, P. Álvarez-Iglesias, M. del C. Pedrosa-García, S. Calvo, E. De Uña-Álvarez, B. Quintana, C. Vale, and R. Prego (2016), Natural and Anthropocene fluxes of trace elements in estuarine sediments of Galician Rias*, Estuarine, Coastal and Shelf Science,* 198, 329–342, doi:10.1016/j.ecss.2016.08.022.

Amon, R. M. W., B. Gereon, and M. Benedikt (2003), Dissolved organic carbon distribution and origin in the Nordic Seas: Exchanges with the Arctic Ocean and the North Atlantic, *Journal of Geophysical Research*, *108*(C7), 3221, doi:10.1029/2002JC001594.

Amon, R. M. W., and R. Benner (2003), Combined neutral sugars as indicators of the diagenetic state of dissolved organic matter in the Arctic Ocean, *Deep-Sea Research Part I: Oceanographic Research Papers*, *50*(1), 151–169, doi:10.1016/S0967-0637(02)00130-9.

Anderson, L. a. (1995), On the hydrogen and oxygen content of marine phytoplankton, *Deep-Sea Research Part I: Oceanographic Research Papers, 42*(1), 1675–1680, doi:10.1016/0967-0637(95)00072-E.

Anderson, L. A., and J. L. Sarmiento (1994), Redfield ratios of remineralization determined by nutrient data analysis, *Global Biogeochemical Cycles*, *8*(1), 65–80, doi:10.1029/93GB03318.

Andersson, A. J., F. T. Mackenzie, and A. Lerman (2006), Coastal ocean CO_2 -carbonic acid-carbonate sediment system of the Anthropocene, *Global Biogeochemical Cycles*, *20*(1), doi:10.1029/2005GB00250

Antia, N., R. Peinert, D. Hebbeln, U. Bathmann, U. Fehner, and B. Zeitzschel (2001), Basin-wide particulate carbon flux in the Atlantic Ocean: Regional export patterns and potential for atmospheric CO_2 sequestration, *Global Biogeochemical Cycles,* 15(4), 845–862, doi:10.1029/2000GB001376.

Appleby, P. G., and F. Oldfield (1978), The calculation of lead-210 dates assuming a constant rate of supply of unsupported ^{210}Pb to the sediment, *Catena*, *5*(1), 1–8, doi:10.1016/S0341-8162(78)8

Appleby, P. G., and F. Oldfield (1983), The assessment of ^{210}Pb data from sites with varying sediment accumulation rates, *Hydrobiologia*, *103*(1), 29–35, doi:10.1007/BF00028424.

Appleby, P. G. (1998), Dating recent sediments by ^{210}Pb: problems and solutions, *Stuk a-145*, 7–24.

Arhan, M. (1990), The North Atlantic Current and Subarctic Intermediate Water, *Journal of Marine Research*, *48*(1), 109–144, doi:10.1357/002224090784984605.

Arístegui, J., S. Susana Agustí, and C. M. Duarte (2003), Respiration in the dark ocean, *Geophysical Research Letters*, *30*(2), 1–4, doi:10.1029/2002GL016227.

Armstrong, R. A., C. Lee, J. I. Hedges, S. Honjo, and S. G. Wakeham (2002), A new, mechanistic model for organic carbon fluxes in the ocean based on the quantitative association of POC with ballast minerals *Deep-Sea Research Part I: Oceanographic Research Papers*, *49*(1–3), 219–236, doi:10.1016/S0967-0645(01)00101-1.

Arrigo, K. R. (2005), Marine microorganisms and global nutrient cycles, *Nature*, *437*(7057), 349–355, doi:10.1038/nature04159.

Baker, C. A., S. A. Henson, E. L. Cavan, S. L. C. Giering, A. Yool, M. Gehlen, A. Belcher, J. S. Riley, H. E. K. Smith, and R. Sanders (2017), Slow Sinking Particulate Organic Carbon in the Atlantic Ocean: magnitude, flux and potential controls. *Global Biogeochemical Cycles,* doi: 10.1002/2017GB005638

Bakker, D. C. E. et al. (2014), An update to the surface ocean CO2 atlas (SOCAT version 2), *Earth System Science Data*, *6*(1), 69–90, doi:10.5194/essd-6-69-2014.

Baskaran, M. (2011), Po-210 and Pb-210 as atmospheric tracers and global atmospheric Pb-210 fallout: A Review, *Journal of Environmental Radioactivity*, *102*(5), 500–513, doi:10.1016/j.jenvrad.2010.10.007.

Bauer, J. E., P. M. Williams, and E. R. M. Druffel (1992), ^{14}C activity of dissolved organic carbon fractions in the north-central Pacific and Sargasso Sea, *Nature*, *357*(6380), 667–670, doi:10.1038/357667a0.

Beaird, N. L., P. B. Rhines, and C. C. Eriksen (2013), Overflow Waters at the Iceland–Faroe Ridge Observed in Multiyear Seaglider Surveys, *Journal of Physical Oceanography*, *43*(11), 2334–2351, doi:10.1175/JPO

Behrenfeld, M. J., and P. G. Falkowski (1997), Photosynthetic rates derived from satellite-based chlorophyll concentration, *Limnology & Oceanography*, *42*(1), 1–20, doi:10.4319/lo.1997.42.1.0001.

Belcher, A., M. Iversen, S. Giering, V. Riou, S. A. Henson, L. Berline, L. Guilloux, and R. Sanders (2016), Depth-resolved particle-associated microbial respiration in the northeast Atlantic, *Biogeosciencies.* 14, 1511–1525, doi:10.5194/bg-14-1511-2017

Benitez-Nelson, C. R. (2000), The biogeochemical cycling of phosphorus in marine systems, *Earth Science Review*, *51*(1–4), 109–135, doi:10.1016/S0012-8252(00)00018-0.

Benner, R., P. Louchouarn, and R. M. W. Amon (2005), Terrigenous dissolved organic matter in the Arctic Ocean and its transport to surface and deep waters of the North Atlantic, *Global Biogeochemical Cycles*, *19*(2), doi:10.1029/2004GB002398.

Benner, R., and R. M. W. Amon (2015), The Size-Reactivity Continuum of Major Bioelements in the Ocean, *Annual Review of Marine Science*, *7*(1), 185–205, doi:10.1146/annurev-marine-010213-135126.

Bercovici, S. K., and D. A. Hansell (2016), Dissolved organic carbon in the deep Southern Ocean: Local versus distant controls, *Global Biogeochemical Cycles*, *30*(2), 350–360, doi:10.1002/2015GB005252.

Berelson, W. M., W. M. Balch, R. Najjar, R. A. Feely, C. Sabine, and K. Lee (2007), Relating estimates of CaCO3 production, export, and dissolution in the water column to measurements of CaCO3 rain into sediment traps and dissolution on the sea floor:A revised global carbonate budget, *Global Biogeochemical Cycles*, *21*(1), 1–15, doi:10.1029/2006GB002803.

Bersch, M. (2002), North Atlantic Oscillation–induced changes of the upper layer circulation in the northern North Atlantic Ocean, *Journal of Geophysical Research*, *107*(C10), 3156, doi:10.1029/2001JC000901.

Bianchi, G. G., and I. N. McCave (2000), Hydrography and sedimentation under the deep western boundary current on Bjorn and Gardar Drifts, Iceland Basin, *Marine Geology*, *165*(1–4), 137–169, doi:10.1016/S0025-3227(99)00139-5.

Binford, M. W. (1990), Calculation and uncertainty analysis of 210Pb dates for PIRLA project lake sediment cores, *Journal of Paleolimnology*, *3*(3), 253–267, doi:10.1007/BF00219461.

Biscaye, P. E., V. Kolla, and K. K. Turekian (1976), Distribution of calcium carbonate in surface sediments of the Atlantic Ocean, *Journal of Geophysical Research*, *81*(15), 2595–2603, doi:10.1029/JC081i015p02595.

Boessenkool, K. P., I. R. Hall, H. Elderfield, and I. Yashayaev (2007), North Atlantic climate and deep-ocean flow speed changes during the last 230 years, *Geophysical Research Letters*, *34*(13), 2–7, doi:10.1029/2007GL030285.

Böning, C. W., M. Scheinert, J. Dengg, A. Biastoch, and A. Funk (2006), Decadal variability of subpolar gyre transport and its reverberation in the North Atlantic overturning, *Geophysical Research Letters*, *33*(21), 1–5, doi:10.1029/2006GL026906.

Bopp, L., C. Le Quéré, M. Heimann, A. C. Manning, and P. Monfray (2002), Climate-induced oceanic oxygen fluxes: Implications for the contemporary carbon budget, *Global Biogeochemical Cycles*, *16*(2), doi: 10.1029/2001GB001445.

Bower, A. S., B. Le Cann, T. Rossby, W. Zenk, J. Gould, K. Speer, P. L. Richardson, M. D. Prater, and H.-M. Zhang (2002), Directly measured mid-depth circulation in the northeastern North Atlantic Ocean, *Nature*, 419(6907), 603-607, doi: 10.1038/nature01078

Bower, A. S., and W.-J. von Appen (2008), Interannual Variability in the Pathways of the North Atlantic Current over the Mid-Atlantic Ridge and the Impact of Topography, *Journal of Physical Oceanography*, *38*(1), 104–120, doi:10.1175/2007JPO3686.1.

Bower, A., and H. Furey (2017), Iceland-Scotland Overflow Water transport variability through the Charlie-Gibbs Fracture Zone and the impact of the North Atlantic Current, *Journal of Geophysical Research: Ocean.*, doi:10.1002/2017JC012698.

Boyd, P. W., and T. W. Trull (2007), Understanding the export of biogenic particles in oceanic waters: Is there consensus?, *Progress in Oceanography*, *72*(4), 276–312, doi:10.1016/j.pocean.2006.10.007.

Brambilla, E., and L. D. Talley (2008), Subpolar mode water in the northeastern Atlantic: 1. Averaged properties and mean circulation, *Journal of Geophysical Research: Ocean.*, *113*(4), 1–18, doi:10.1029/2006JC0

Brea, S., X. A. Álvarez-Salgado, M. Álvarez, F. F. Pérez, L. Mémery, H. Mercier, and M. J. Messias (2004), Nutrient mineralization rates and ratios in the eastern South Atlantic, *Journal of Geophysical Research*, *109*(5), 1–15, doi:10.1029/2003JC002051.

Brewer, P., and K. Hester (2009), Ocean Acidification and the Increasing Transparency of the Ocean to Low-Frequency Sound, *Oceanography*, *22*(4), 86–93, doi:10.5670/oceanog.2009.99.

Broecker, W. S. (1974), “NO”, a conservative water-mass tracer, *Earth and Planetary Science Letters*, *23*(1), 100–107, doi:10.1016/0012-821X(74)90036-3.

Broecker, W. S., and T. H. Peng (1982), *Tracers in the sea*, doi: 10.1016/0016-7037(83)90075-3

Broeker, W. (1991), The Great Ocean Conveyor, *Oceanography*, *4*(2), 79–89, doi:10.5670/oceanog.1991.07.

Bryden, H. L., H. R. Longworth, and S. A. Cunningham (2005), Slowing of the Atlantic meridional overturning circulation at 25° N, *Nature*, *438*(7068), 655–657, doi:10.1038/nature04385.

Brzezinski, M. A., and D. M. Nelson (1996), Chronic substrate limitation of silicic acid uptake rates in the western Sargasso Sea, *Deep Sea Research Part II: Topical Studies in Oceanography*, *43*(2–3), 437–453, doi:10.1016/0967-0645(95)00099-2.

Buckley, M. W., and J. Marshall (2015), Observations, inferences, and mechanisms of the Atlantic Meridional Overturning Circulation: A review, *Reviews of Geophysics*, *54*, 5–63, doi:10.1002/2015RG000493.Rec

Buesseler, K. O., and C. R. Benitez (1994), Determination of mass accumulation rates and sediment radionuclide inventories in the deep Black Sea, *Deep-Sea Research Part I: Oceanographic Research Papers*, *41*(11–12), 1605–1615, doi: 10.1016/0967-0637(94)90064-7

Buesseler, K. O. et al. (2006), An assessment of particulate organic carbon to thorium-234 ratios in the ocean and their impact on the application of 234Th as a POC flux proxy, *Marine Chemistry*, *100*, 213-233, doi: 10.1016/j.marchem.2005.10.013

Buesseler, K. O. et al. (2008), VERTIGO (VERtical Transport In the Global Ocean): A study of particle sources and flux attenuation in the North Pacific, *Deep-Sea Research Part I: Oceanographic Research Papers*, *55,* 1522-1539, doi: 10.1016/j.dsr2.2008.04.024

Buesseler, K. O., and P. W. Boyd (2009), Shedding light on processes that control particle export and flux attenuation in the twilight zone of the open ocean, *Limnology & Oceanography*, *54*(4), 1210–1232, doi: 10.4319/lo.2009.54.4.1210

Buesseler, K., M. Aoyama, and M. Fukasawa (2011), Impacts of the Fukushima nuclear power plants on marine radioactivity, *Environmental Science and Technology*, *45*(23), 9931–9935, doi:10.1021/es202816c.

Burd, A. B. et al. (2010), Assessing the apparent imbalance between geochemical and biochemical indicators of meso- and bathypelagic biological activity: What the @$#! is wrong with present calculations of carbon budgets?, *Deep Sea Research Part II: Topical Studies in Oceanography*, 57(16), 1557-1571, doi: 10.1016/j.dsr2.2010.02.022.

Caldeira, K., and M. E. Wickett (2003), Oceanography: anthropogenic carbon and ocean pH., *Nature*, *425*(6956), 365, doi:10.1038/425365a.

Carlson, C. A., H. W. Ducklow, and A. F. Michaels (1994), Annual flux of dissolved organic carbon from the euphotic zone in the northwestern Sargasso Sea, *Nature*, *371*(09), 405–408, doi:10.1038/371405a0.

Carlson, C. A., and H. W. Ducklow (1995), Dissolved organic carbon in the upper ocean of the central equatorial Pacific Ocean, 1992: Daily and finescale vertical variations, *Deep-Sea Research Part I: Oceanographic Research Papers*, *42*(2–3), 639–656, doi:10.1016/0967-0645(95)00023-J.

Carlson, C. A., D. A. Hansell, N. B. Nelson, D. A. Siegel, W. M. Smethie, S. Khatiwala, M. M. Meyers, and E. Halewood (2010), Dissolved organic carbon export and subsequent remineralization in the mesopelagic and bathypelagic realms of the North Atlantic basin, *Deep-Sea Research Part I: Oceanographic Research Papers*, 57(16), 1433-1445, doi: 10.1016/j.dsr2.2010.02.013

Carlson, C. A., D. A. Hansell, and C. Tamburini (2011), DOC persistance and its fate after export within the ocean interior, in *Microbial carbon pump in the ocean*, 37. 57–59, doi: 10.1126/science.opms.sb0001.

Carlson, C. A., and D. A. Hansell (2014), DOM Sources, Sinks, Reactivity, and Budgets, in *Biogeochemistry of Marine Dissolved Organic Matter: Second Edition*, pp. 65–126.

Carr, M.-E. et al. (2006), A comparison of global estimates of marine primary production from ocean color, *Deep Sea Research Part II: Topical Studies in Oceanography*, *53*(5–7), 741–770, doi:10.1016/j.dsr2.2006.

Carracedo, L. I., M. Gilcoto, H. Mercier, and F. F. Pérez (2014), Seasonal dynamics in the Azores-Gibraltar Strait region: A climatologically-based study, *Progress in Oceanography*, *122*, 116–130, doi:10.1016/j.pocean.2013.12.005.

Carroll, J., and I. Lerche (2003), Sedimentary Processes - Quantification using radionuclides, in *Radioactivity in the environment*, vol. 5, p. 283, doi: 10.1007/s13398-014-0173-7.2

Carter, B. R., J. R. Toggweiler, R. M. Key, and J. L. Sarmiento (2014), Processes determining the marine alkalinity and calcium carbonate saturation state distributions, *Biogeosciences*, *11*(24), 7349-7362, doi: 10.5194/bg-11-7349-2014.

Cheng, J., Z. Liu, S. Zhang, W. Liu, L. Dong, P. Liu, and H. Li (2016), Reduced interdecadal variability of Atlantic Meridional Overturning Circulation under global warming, *Proceedings of the National Academy of Sciences*, *113*(12), 3175–3178, doi:10.1073/pnas.1519827113.

Chiswell, S. M., and S. D. Nodder (2015), Tilt-induced biases in sediment trap functioning, *Journal of Geophysical Research: Ocean.*, *120*(12), 8381–8391, doi:10.1002/2015JC011350.

Chong, L. S., W. M. Berelson, D. E. Hammond, M. Q. Fleisher, R. F. Anderson, N. E. Rollins, and S. Lund (2016), Biogenic sedimentation and geochemical properties of deep-sea sediments of the Demerara Slope/Abyssal Plain: Influence of the Amazon River Plume, *Marine Geology,* 379, 124-139, doi: 10.1016/j.margeo.2016.05.015.

Ciais, P. et al. (2013), Carbon and other biogeochemical cycles, in *Climate Change 2013: The Physical Science Basis. Contribution of Working Group I to the Fifth Assessment Report of the Intergovernmental Panel on Climate Change*, edited by V. B. and P. M. M. (eds.). [Stocker, T.F., D. Qin, G.-K. Plattner, M. Tignor, S.K. Allen, J. Boschung, A. Nauels, Y. Xia, pp. 465–570, Cambridge University Press, Cambridge, United Kingdom and New York, NY, USA, doi: 10.1017/CBO9781107415324.015.

Clark, L. L., E. D. Ingall, and R. Benner (1998), Marine phosphorus is selectively remineralized, *Nature*, *393*(6684), 426, doi:10.1038/30881.

Cochran, J. K. (1990), 210Pb scavenging in the North Atlantic and North Pacific Oceans, *Earth and Planetary Science Letters*, *97*, 332–352.

Cochran, J. K., and P. Masqué (2004), Natural radionuclides applied to coastal zone processes, in *Marine radioactivity*, pp. 1–23, Elsevier Ltd.

Codispoti, L. A., J. A. Brandes, J. P. Christensen, A. H. Devol, S. W. A. Naqvi, H. W. Paerl, and T. Yoshinari (2001), The oceanic fixed nitrogen and nitrous oxide budgets: Moving targets as we enter the anthropocene? *Scientia Marina,* 65, 85-105, doi: 10.3989/scimar.2001.65s285

Codispoti, L. A. (2007), An oceanic fixed nitrogen sink exceeding 400 Tg-N·a^{-1}; vs the concept of homeostasis in the fixed-nitrogen inventory, *Biogeosciences*, *4*(2), 233–253, doi:10.5194/bg-4-233-2007.

Copin-Montégut, G., and B. Avril (1993), Vertical distribution and temporal variation of dissolved organic carbon in the North-Western Mediterranean Sea, *Deep-Sea Research Part I: Oceanographic Research Papers*, *40*, 1963–1972, doi:10.1016/0967-0637(93)90041-Z.

Crutzen, P. J., and E. F. Stoermer (2000), The Anthropocene, *Global Change Newsletter.*, *41*, 17–18.

Crutzen, P. J. (2002), Geology of mankind, *Nature*, *415*(6867), 23, doi:10.1038/415023a.

Cunningham, S. A. et al. (2007), Temporal variability of the Atlantic meridional overturning circulation at 26.5°N, *Science*, *317*(5840), 935–938, doi:10.1126/science.1141304.

Currie, L. A. (1968), Limits for Qualitative Detection and Quantitative Determination: Application to Radiochemistry, *Analytical Chemistry*, *40*(3), 586–593, doi:10.1021/ac60259a007.

Dai, M., Z. Yin, F. Meng, Q. Liu, and W. J. Cai (2012), Spatial distribution of riverine DOC inputs to the ocean: An updated global synthesis, *Current Opinion in Environmental Sustainability*, *4*(2), 170–178, doi:10.1016/j.cosust.2012.03.003.

Dall'Olmo, G., and K. A. Mork (2014), Carbon export by small particles in the Norwegian Sea, *Geophysical Research Letters*, *41*(8), 2921–2927, doi:10.1002/2014GL059244.

Dall'Olmo, G., J. Dingle, L. Polimene, R. J. W. Brewin, and H. Claustre (2016), Substantial energy input to the mesopelagic ecosystem from the seasonal mixed-layer pump, *Nature Geoscience.*, 1,1-6, doi: 10.1038/ngeo2818.

Daniault, N., P. Lherminier, and H. Mercier (2011), Circulation and Transport at the Southeast Tip of Greenland, *Journal of Physical Oceanography*, *41*(3), 437–457, doi:10.1175/2010JPO4428.1.

Daniault, N. et al. (2016), The northern North Atlantic Ocean mean circulation in the early 21st century, *Progress in Oceanography*, *146*, 142–158, doi:10.1016/j.pocean.2016.06.007.

de Jong, M. F., and L. de Steur (2016), Strong winter cooling over the Irminger Sea in winter 2014–2015, exceptional deep convection, and the emergence of anomalously low SST, *Geophysical Research Letters*, 43(13), 7106-7113, doi: 10.1002/2016GL069596.

De La Rocha, C. L., and U. Passow (2007), Factors influencing the sinking of POC and the efficiency of the biological carbon pump, *Deep-Sea Research Part I: Oceanographic Research Papers*, *54*(5–7), 639–658, doi: 10.1016/j.dsr2.2007.01.004.

del Giorgio, P. A., and C. M. Duarte (2002), Respiration in the open ocean, *Nature*, *420*(6914), 379–384, doi:10.1038/nature01165.

Delaney, M. L. (1998), Phosphorus accumulation in marine sediments and the oceanic phosphorus cycle, *Global Biogeochemical Cycles*, *12*(4), 563, doi:10.1029/98GB02263.

Delworth, T. L., F. Zeng, G. A. Vecchi, X. Yang, L. Zhang, and R. Zhang (2016), The North Atlantic Oscillation as a driver of rapid climate change in the Northern Hemisphere, *Nature Geoscience.*, *9*(7), 509–512, doi:10.1038/ngeo2738.

Deutsch, C., and T. Weber (2012), Nutrient Ratios as a Tracer and Driver of Ocean Biogeochemistry, *Annual Review of Marine Science*, *4*(1), 113–141, doi:10.1146/annurev-marine-120709-142821.

DeVries, T., and T. Weber (2017), The export and fate of organic matter in the ocean: New constraints from combining satellite and oceanographic tracer observations, *Global Biogeochemical Cycles*, 31(3), 535-555, doi:o 10.1002/2016GB005551.

Dickson, R. R., and J. Brown (1994), The production of North Atlantic Deep Water: Sources, rates, and pathways, *Journal of Geophysical Research*, *99*(C6), 12319, doi:10.1029/94JC00530.

Dickson, R., J. Lazier, J. Meincke, P. Rhines, and J. Swift (1996), Long-term coordinated changes in the convective activity of the North Atlantic, *Progress in Oceanography*, *38*(3), 241–295, doi:10.1016/S0079-6611(97)00002-5.

Dittmar, T., and J. Paeng (2009), A heat-induced molecular signature in marine dissolved organic matter, *Nature Geoscience*, *2*(3), 175–179, doi:10.1038/ngeo440.

Dlugokencky, E. J., P. M. Lang, J. W. Mund, A. M. Crotwell, M. J. Crotwell, and K. W. Thoning (2017), Atmospheric Carbon Dioxide Dry Air Mole Fractions from the NOAA ESRL Carbon Cycle Cooperative Global Air Sampling Network, 1968-2016, Version: 2017-07-28, *NOAA/ESRL*. Available from: ftp://aftp.cmdl.noaa.gov/data/trace_gases/co2/flask/surface (Accessed 7 September 2017)

Doney, S. C., V. J. Fabry, R. A. Feely, and J. A. Kleypas (2009), Ocean Acidification: The Other CO_2 Problem, *Annual Review of Marine Science*, *1*(1), 169–192, doi:10.1146/annurev.marine.010908.163834.

Doval, M. ., and D. a Hansell (2000), Organic carbon and apparent oxygen utilization in the western South Pacific and the central Indian Oceans, *Marine Chemistry*, *68*, 249–264, doi:10.1016/S0304-4203(99)00081-X.

Druffel, E. R. M., P. M. Williams, J. E. Bauer, and J. R. Ertel (1992), Cycling of dissolved and particulate organic matter in the open ocean, *Journal of Geophysical Research*, *97*(C10), 15639, doi:10.1029/92JC01511.

Ducklow, H. W., D. K. Steinberg, and K. O. Buesseler (2001), Upper Ocean Carbon Export and the Biological Pump, *Oceanography*, *14*(4), 50–58, doi:10.5670/oceanog.2001.06.

Dunne, J. P., J. L. Sarmiento, and A. Gnanadesikan (2007), A synthesis of global particle export from the surface ocean and cycling through the ocean interior and on the seafloor, *Global Biogeochemical Cycles,* 21(4), 1-16, doi: 10.1029/2006GB002907.

Dürr, H. H., M. Meybeck, J. Hartmann, G. G. Laruelle, and V. Roubeix (2011), Global spatial distribution of natural riverine silica inputs to the coastal zone, *Biogeosciences*, *8*(3), 597–620, doi: 10.5194/bg-8-597-2011.

Dutkiewicz, S., M. Follows, J. Marshall, and W. W. Gregg (2001), Interannual variability of phytoplankton abundances in the North Atlantic, *Deep Sea Research Part II: Topical Studies in Oceanography*, *48*, 2323–2344, doi:10.1016/S0967-0645(00)00178-8.

Eakins, B. W., and G. F. Sharman (2010), Volumes of the World's Oceans from ETOPO1, NOAA National Geophysical Data Center, Boulder, CO. Available from: https://www.ngdc.noaa.gov/mgg/global/etopo1_ocean_volumes.html (Accessed 5 January 2018).

Eden, C., and J. Willebrand (2001), Mechanism of interannual to decadal variability of the North Atlantic circulation, *Journal of Climate*, *14*(10), 2266–2280, doi:10.1175/1520-0442(2001)014

EPICA Community Members (2004), Eight glacial cycles from an Antarctic ice core, *Nature*, *429*(6992), 623–628, doi: 10.1038/nature02599.

Falina, A., A. Sarafanov, H. Mercier, P. Lherminier, A. Sokov, and N. Daniault (2012), On the Cascading of Dense Shelf Waters in the Irminger Sea, *Journal of Physical Oceanography*, *42*(12), 2254–2267, doi: 10.1175/Jpo-D-12-012.1.

Falkowski, P. G., R. T. Barber, and V. Smetacek (1998), Biogeochemical Controls and Feedbacks on Ocean Primary Production, *Science.*, *281*(5374), 200–206, doi:10.1126/science.281.5374.200.

Falkowski, P. et al. (2000), The global carbon cycles: A test of our knowledge of earth as a system, *Science.*, *290*(5490), 291–296, doi:10.1126/science.290.5490.291.

Faul, K. L., A. Paytan, and M. L. Delaney (2005), Phosphorus distribution in sinking oceanic particulate matter, *Marine Chemistry*, *97*(3–4), 307–333, doi:10.1016/j.marchem.2005.04.002.

Fay, A. R., and G. A. McKinley (2014), Global ocean biomes: mean and temporal variability, *Earth System Science Data Discussions*, *7*(1), 107–128, doi:10.5194/essdd-7-107-2014.

Finney, S. C., and L. E. Edwards (2016), The "Anthropocene" epoch: Scientific decision or political statement?, *GSA Today*, *26*(3), 4–10, doi:10.1130/GSATG270A.1.

Fogelqvist, E., J. Blindheim, T. Tanhua, S. Østerhus, E. Buch, and F. Rey (2003), Greenland-Scotland overflow studied by hydro-chemical multivariate analysis, *Deep-Sea Research Part I: Oceanographic Research Papers*, *50*(1), 73–102, doi:10.1016/S0967-0637(02)00131-0.

Föllmi, K. B. (1996), The phosphorus cycle, phosphogenesis and marine phosphate-rich deposits, *Earth-Science Reviews*, *40*(1), 55–124, doi:10.1016/0012-8252(95)00049-6.

Fraga, F., A. F. Ríos, F. F. Pérez, and F. G. Figueiras (1998), Theoretical limits of oxygen : carbon and oxygen : nitrogen ratios during photosynthesis and mineralisation of organic matter in the sea, *Scientia Marina*, *62*(1–2), 161–168, doi:10.3989/scimar.1998.62n1-2161.

Frajka-williams, E., J. L. Bamber, and K. Våge (2016), Greenland melt and the Atlantic meridional overturning circulation, *Oceanography*, *29*, 22–33, doi:https://doi.org/10.5670/oceanog.2016.96.

Francois, R., S. Honjo, R. Krishfield, and S. Manganini (2002), Factors controlling the flux of organic carbon to the bathypelagic zone of the ocean, *Global Biogeochemical Cycles*, *16*(4), 34-1-34–2 doi:10.1029/2001GB001722.

Frankignoulle, M., C. Canon, and J.-P. Gattuso (1994), Marine calcification as a source of carbon dioxide: Positive feedback of increasing atmospheric CO2, *Limnology & Oceanography*, *39*(2), 458–462, doi: 10.4319/lo.1994.39.2.0458.

Fröb, F., A. Olsen, K. Våge, G. W. K. Moore, I. Yashayaev, E. Jeansson, and B. Rajasakaren (2016), Irminger Sea deep convection injects oxygen and anthropogenic carbon to the ocean interior, *Nature Communications,* 7,13244, doi: 10.1038/ncomms13244.

Froelich, P. N., M. L. Bender, and N. A. Luedtke (1982), The marine phosphorus cycle, *American Journal of Science*, *282*(4), 474–511, doi:10.2475/ajs.282.4.474.

Frölicher, T. L., F. Joos, G. K. Plattner, M. Steinacher, and S. C. Doney (2009), Natural variability and anthropogenic trends in oceanic oxygen in a coupled carbon cycle-climate model ensemble, *Global Biogeochemical Cycles,* 23(1), doi: 10.1029/2008GB003316.

Galloway, J. N. et al. (2004), Nitrogen cycles: Past, present, and future, *Biogeochemistry*, *70*(2), 153–226, doi:10.1007/s10533-004-0370-0.

Ganachaud, A., and C. Wunsch (2002), Oceanic nutrient and oxygen transports and bounds on export production during the World Ocean Circulation Experiment, *Global Biogeochemical Cycles*, *16*(4), 5-14, doi: 10.1029/2000GB001333.

Garcia, H. E., and L. I. Gordon (1992), Oxygen solubility in seawater: Better fitting equations, *Limnology & Oceanography*, *37*(6), 1307–1312, doi:10.4319/lo.1992.37.6.1307.

García-Ibáñez, M. I., P. C. Pardo, L. I. Carracedo, H. Mercier, P. Lherminier, A. F. Ríos, and F. F. Pérez (2015), Structure, transports and transformations of the water masses in the Atlantic Subpolar Gyre, *Progress in Oceanography,*135, 18-36, doi: 10.1016/j.pocean.2015.03.009.

García-Ibáñez, M. I., P. Zunino, F. Fröb, L. I. Carracedo, A. F. Ríos, H. Mercier, A. Olsen, and F. F. Pérez (2016), Ocean acidification in the subpolar North Atlantic: Rates and mechanisms controlling pH changes, *Biogeosciences,* 13(12), 3701-3715, doi: 10.5194/bg-13-3701-2016.

García-Ibáñez, M. I., F. F. Pérez, P. Lherminier, P. Zunino, and P. Tréguer (2017), Water mass distributions and transports for the 2014 GEOVIDE cruise in the North Atlantic, *Biogeosciences Discussions*, doi: 10.5194/bg-2017-355.

Garcia-Orellana, J., J. M. Pates, P. Masqué, J. M. Bruach, and J. A. Sanchez-Cabeza (2009), Distribution of artificial radionuclides in deep sediments of the Mediterranean Sea, *Science of the Total Environment*, 407(2), 887-898, doi: 10.1016/j.scitotenv.2008.09.018.

Garcia-Orellana, J., E. Gràcia, A. Vizcaino, P. Masqué, C. Olid, F. Martínez-Ruiz, E. Piñero, J. A. Sánchez-Cabeza, and J. Dañobeitia (2006), Identifying instrumental and historical earthquake records in the in the SW Iberian margin ^{210}Pb turbidite chronology, *Geophysical Research Letters,* 33(24), 1-6, doi: 10.1029/2006GL028417.

Gardner, W. D., S. P. Chung, M. J. Richardson, and I. D. Walsh (1995), The oceanic mixed-layer pump, *Deep-Sea Research Part II: Topical Studies in Oceanography*, *42*(2–3), doi:10.1016/0967-0645(95)00037-Q.

Gattuso, J.-P. et al. (2015), Contrasting futures for ocean and society from different anthropogenic CO2 emissions scenarios, *Science*, *349*(6243), doi:10.1126/science.aac4722.

Geyh, M., and H. Schleicher (1990), *Absolute Age Determination: Physical and Chemical Dating Methods and Their Application*, Springer-Verlag, Berlin.

Giering, S. L. C. et al. (2014), Reconciliation of the carbon budget in the ocean's twilight zone, *Nature*, *507*(7493), 480–483, doi:10.1038/nature13123.

GRDC (2014): Global Freshwater Fluxes into the World Oceans / Online provided by *Global Runoff Data Centre*. 2014 ed. Koblenz: Federal Institute of Hydrology (BfG), 2014.

Godoy, J. M., I. Moreira, C. Wanderley, F. F. Simões Filho, and A. A. Mozeto (1998), An Alternative Method for the Determination of Excess 210Pb in Sediments, *Radiation Protection Dosimetry*, *75*(1–4), 111–115.

Goldberg, E. D. (1963), Geochronology with 210Pb, in *Radioactive Dating. Proceedings of a Symposium*, pp. 21–131, International Atomic Energy Agency, Vienna.

Gourcuff, C., P. Lherminier, H. Mercier, and P. Y. Le Traon (2011), Altimetry combined with hydrography for ocean transport estimation, *Journal of Atmospheric and Oceanic Technology*, *28*(10), 1324–1337, doi:10.1175/2011JTECHO818.1.

Gradstein, F. M., J. G. Ogg, M. D. Schmitz, G. M. Ogg, F. M. Gradstein, and A. All (2012), *The Geologic Time Scale 2012*, doi: 10.1016/B978-0-444-59425-9.01001-5.

Gregory, K. J., and A. S. Goudie (2011), *The SAGE handbook of geomorphology*, doi: 10.4135/9781446201053.

Grist, J. P., R. Marsh, and S. A. Josey (2009), On the relationship between the north Atlantic meridional overturning circulation and the surface-forced overturning streamfunction, *Journal of Climate*, *22*(19), 4989–5002, doi:10.1175/2009JCLI2574.1.

Gruber, N., and J. L. Sarmiento (1997), Global patterns of marine nitrogen fixation and denitrification, *Global Biogeochemical Cycles*, *11*(2), 235, doi:10.1029/97GB00077.

Gruber, N., M. Gloor, S. M. Fan, and J. L. Sarmiento (2001), Air-sea flux of oxygen estimated from bulk data: Implications for the marine and atmospheric oxygen cycles, *Global Biogeochemical Cycles*, *15*(4), 783–803, doi:10.1029/2000GB001302.

Gruber, N. (2004), The Dynamics of the Marine Nitrogen Cycle and its Influence on Atmospheric CO_2 Variations in *The Ocean Carbon Cycle and Climate*, *40*, 97–148, doi:10.1007/978-1-4020-2087-2_4.

Gruber, N. (2008), The Marine Nitrogen Cycle: Overview and Challenges, in *Nitrogen in the Marine Environment*, pp. 1–50, Press, Academic.

Gruber, N., and J. N. Galloway (2008), An Earth-system perspective of the global nitrogen cycle, *Nature*, *451*(7176), 293–296, doi:10.1038/nature06592.

Gruber, N. et al. (2009), Oceanic sources, sinks, and transport of atmospheric CO_2, *Global Biogeochemical Cycles*, *23*(1), 1–21, doi:10.1029/2008GB003349.

Gruber, N. (2011), Warming up, turning sour, losing breath: ocean biogeochemistry under global change, *Philosophical Transactions of the Royal Society, 369*(1943), 1980–1996, doi:10.1098/rsta.201

Guidi, L. et al. (2016), Plankton networks driving carbon export in the oligotrophic ocean, *Nature*, *532*(7600), 465–470, doi:10.1038/nature16942.

Guidi, L., L. Stemmann, G. A. Jackson, F. Ibanez, H. Claustre, L. Legendre, M. Picheral, and G. Gorskya (2009), Effects of phytoplankton community on production, size, and export of large aggregates: A world-ocean analysis, *Limnoly & Oceanography,*54(6), 1951-1963, doi: 10.4319/lo.2009.54.6.1951.

Guilbault, G. G., and M. Hjelm (1989), IUPAC Gold Book, *Pure and Applied Chemistry*, *61*(9), 1657–1664, doi:10.1351/pac198961091657.

Häkkinen, S., and P. B. Rhines (2004), Decline of Subpolar North Atlantic Circulation during the 1990s, *Science,* 304(5670), 555–559, doi:10.1126/science.1094917.

Hansell, D. A., and C. A. Carlson (1998), Net Community Production of dissolved organic carbon, *Global Biogeochemical Cycles*, *12*(3), 443–453.

Hansell, D. A., and C. A. Carlson (2001), Marine dissolved organic matter and the carbon cycle, *Oceanography*, *14*, 41–49.

Hansell, D. A., and C. A. Carlson (2001), Biogeochemistry of total organic carbon and nitrogen in the Sargasso Sea:control by convective overturn, *Deep Sea Research Part II: Topical Studies in Oceanography*, *48*, 1649–1667, doi:10.1016/S096

Hansell, D. A. (2002), DOC in the Global Ocean Carbon Cycle, in *Biogeochemistry of Marine Dissolved Organic Matter*, edited by D. A. Hansell and C. A. Carlson, pp. 685–715, Academic Press, San Diego.

Hansell, D. a., H. W. Ducklow, A. M. Macdonald, and M. O. Baringer (2004), Metabolic poise in the North Atlantic Ocean diagnosed from organic matter transports, *Limnology & Oceanography*, *49*(4), 1084–1, doi: 10.4319/lo.2004.49.4.1084.

Hansell, D. a., D. Kadko, and N. R. Bates (2004), Degradation of Terrigenous Dissolved Organic Carbon in the Western Arctic Ocean, *Science*, *304*(5672), 858–861, doi:10.1126/science.1096

Hansell, D. A., C. A. Carlson, D. J. Repeta, and R. Schlitzer (2009), Dissolved organic matter in the ocean: A controversy stimulates new insights, *Oceanography*, *22*, 202–211, doi:10.5670/oceano

Hansell, D. A., C. A. Carlson, and R. Schlitzer (2012), Net removal of major marine dissolved organic carbon fractions in the subsurface ocean, *Global Biogeochemical Cycles*, *26*(1), 1–9, doi:10.102

Hansell, D. A., and C. A. Carlson (2013), Localized refractory dissolved organic carbon sinks in the deep ocean, *Global Biogeochemical Cycles*, *27*(3), 705–710, doi:10.1002/gbc.20067.

Hansell, D. A. (2013), Recalcitrant Dissolved Organic Carbon Fractions, *Annual Review of Marine Science*, *5*(1), 421–445, doi:10.1146/annurev-marine-120710-100757.

Hansell, D. A., and C. A. Carlson (2015), *Biogeochemistry of Marine Dissolved Organic Matter*.

Hansen, B., and S. Østerhus (2000), North Atlantic Nordic Seas Exchanges, *Progress in Oceanography*, *45*(2), 109–208, doi:10.1016/S0079-6611(99)00052-X.

Hansen, B., and S. Østerhus (2007), Faroe Bank Channel overflow 1995-2005, *Progress in Oceanography*, *75*(4), 817–856, doi:10.1016/j.pocean.2007.09.004.

Hansen, B., S. Østerhus, W. R. Turrell, S. Jónsson, H. Valdimarsson, H. Hátún, and S. M. Olsen (2008), The Inflow of Atlantic Water, Heat, and Salt to the Nordic Seas Across the Greenland–Scotland Ridge, in Arctic–Subarctic Ocean Fluxes, pp. 15–43, Springer Netherlands, Dordrecht.

Harden, S. L., D. J. DeMaster, and C. A. Nittrouer (1992), Developing sediment geochronologies for high-latitude continental shelf deposits: a radiochemical approach, *Marine Geology*, *103*(1–3), 69–97, doi: 10.1016/0025-3227(92)90009-7.

Harlay, J. et al. (2010), Biogeochemical study of a coccolithophore bloom in the northern Bay of Biscay (NE Atlantic Ocean) in June 2004, *Progress in Oceanography*, *86*(3–4), 317–336, doi:10.1016/j.pocean.2010.04.029.

Hartman, S. E., K. E. Larkin, R. S. Lampitt, M. Lankhorst, and D. J. Hydes (2010), Seasonal and inter-annual biogeochemical variations in the Porcupine Abyssal Plain 2003-2005 associated with winter mixing and surface circulation, *Deep-Sea Research Part I: Oceanographic Research Papers*, *57*(15), 1303–1312, doi:10.1016/j.dsr2.2010.01.007.

Hartmann, D. L. et al. (2013), Observations: Atmosphere and surface, in *Climate Change 2013: The Physical Science Basis. Contribution of Working Group I to the Fifth Assessment Report of the Intergovernmental Panel on Climate Change*, vol. 9781107057, edited by B. and P. M. M. Stocker, T.F., D. Qin, G.-K. Plattner, M. Tignor, S.K. Allen, J. Boschung, A. Nauels, Y. Xia, V., pp. 159–254, Cambridge, United Kingdom and New York, NY, USA, doi: 10.1017/CBO9781107415324.008.

Hátún, H., A. B. Sande, H. Drange, B. Hansen, and H. Valdimarsson (2005), Ocean science: Influence of the atlantic subpolar gyre on the thermohaline circulation, *Science.*, *309*(5742), 1841–1844, doi:10.1126/science.1114777.

Hawkings, J., J. Wadham, M. Tranter, J. Telling, E. Bagshaw, A. Beaton, S. L. Simmons, D. Chandler, A. Tedstone, and P. Nienow (2016), The Greenland Ice Sheet as a hot spot of phosphorus weathering and export in the Arctic, *Global Biogeochemical Cycles*, *30*(2), 191–210, doi:10.1002/2015GB005237.

Hawkings, J. R., J. L. Wadham, L. G. Benning, K. R. Hendry, M. Tranter, A. Tedstone, P. Nienow, and R. Raiswell (2017), Ice sheets as a missing source of silica to the polar oceans, *Nature Communications*, 8, 14198, doi: 10.1038/ncomms14198.

Hays, J. D., and A. Perruzza (1972), The significance of calcium carbonate oscillations in eastern equatorial Atlantic deep-sea sediments for the end of the Holocene warm interval, *Quaternary Research*, 2(3), 355-362, doi: 10.1016/0033-5894(72)90058-0.

Heinze, C., S. Meyer, N. Goris, L. Anderson, R. Steinfeldt, N. Chang, C. Le Quéré, and D. C. E. Bakker (2015), The ocean carbon sink - Impacts, vulnerabilities and challenges, *Earth System Dynamics.*, 6(1), 327-358, doi: 10.5194/esd-6-327-2015.

Helm, K. P., N. L. Bindoff, and J. A. Church (2011), Observed decreases in oxygen content of the global ocean, *Geophysical Research Letters*, *38*(23), doi:10.1029/2011GL049513.

Henry, W. (1803), Experiments on the Quantity of Gases Absorbed by Water, at Different Temperatures, and under Different Pressures, *Philosophical Transactions of the Royal Society of London*, *93*(1), 29–274, doi:10.1098/rstl.1803.0004.

Henson, S. A., I. Robinson, J. T. Allen, and J. J. Waniek (2006), Effect of meteorological conditions on interannual variability in timing and magnitude of the spring bloom in the Irminger Basin, North Atlantic, *Deep-Sea Research Part I: Oceanographic Research Papers,* 53(10), 1601-1615, doi: 10.1016/j.dsr.2006.07.009.

Henson, S. A., J. P. Dunne, and J. L. Sarmiento (2009), Decadal variability in North Atlantic phytoplankton blooms, *Journal of Geophysical Research: Ocean.*, *114*(4), doi:10.1029/2008JC005139.

Henson, S. A., R. Sanders, E. Madsen, P. J. Morris, F. Le Moigne, and G. D. Quartly (2011), A reduced estimate of the strength of the ocean's biological carbon pump, *Geophysical Research Letters*, *38*(4), 10-14, doi: 10.1029/2011GL046735.

Henson, S. A., R. Sanders, and E. Madsen (2012a), Global patterns in efficiency of particulate organic carbon export and transfer to the deep ocean, *Global Biogeochemical Cycles*, *26*(1), 1–14, doi: 10.1029/2011GB004099.

Henson, S., R. Lampitt, and D. Johns (2012b), Variability in phytoplankton community structure in response to the North Atlantic Oscillation and implications for organic carbon flux, *Limnology & Oceanography*, *57*(6), 1591–1601, doi:10.4319/lo.2012.57.6.1591.

Henson, S. A., A. Yool, and R. Sanders (2015), Variability in efficiency of particulate organic carbon export: A model study, *Global Biogeochemical Cycles*, *29*(1), 33–45, doi:10.1002/2014GB004965.

Henson, S. A., C. Beaulieu, T. Ilyina, J. G. John, M. Long, R. Séférian, J. Tjiputra, and J. L. Sarmiento (2017), Rapid emergence of climate change in environmental drivers of marine ecosystems, *Nature Communications,* 8(5020), 14682, doi: 10.1038/ncomms14682.

Herndl, G. J., and T. Reinthaler (2013), Microbial control of the dark end of the biological pump, *Nature Geoscences.*, *6*(9), 718–724, doi:10.1038/ngeo1921.

Holfort, J., K. M. Johnson, B. Schneider, G. Siedler, and D. W. R. Wallace (1998), Meridional transport of dissolved inorganic carbon in the South Atlantic Ocean, *Global Biogeochemical Cycles*, *12*(3), 479–499.

Honisch, B. et al. (2012), The Geological Record of Ocean Acidification, *Science*, *335*(6072), 1058–1063, doi:10.1126/science.1208277.

Honjo, S., S. J. Manganini, R. A. Krishfield, and R. Francois (2008), Particulate organic carbon fluxes to the ocean interior and factors controlling the biological pump: A synthesis of

global sediment trap programs since 1983, *Progress in Oceanography,* 76(3), 217-285, doi: 10.1016/j.pocean.2007.11.003.

Hopkinson, C. S., and J. J. Vallino (2005), Efficient export of carbon to the deep ocean through dissolved organic matter, *Nature*, *433*(7022), 142–145, doi:10.1038/nature03191.

Houghton JT, Ding Y, Griggs DJ, Noguer. M, van der Linden PJ, Dai X, Masquel K, and Johnson C (2001), Climate Change 2001: The Scientific Basis, in *Climate Change 2001: The Scientific Basis*, doi:10.1256/004316502320517344.

Hurrell, J. W. (1995), Decadal Trends in the North Atlantic Oscillation: Regional Temperatures and Precipitation, *Science*, *269*(5224), 676–679, doi:10.1126/science.269.5224.676.

Iglesias-Rodríguez, M. D., C. W. Brown, S. C. Doney, J. Kleypas, D. Kolber, Z. Kolber, P. K. Hayes, and P. G. Falkowski (2002), Representing key phytoplankton functional groups in ocean carbon cycle models: Coccolithophorids, *Global Biogeochemical Cycles*, *16*(4), 47-1-47–20, doi:10.1029/2001GB001454.

Iida, Y., A. Kojima, Y. Takatani, T. Nakano, H. Sugimoto, T. Midorikawa, and M. Ishii (2015), Trends in pCO2 and sea–air CO2 flux over the global open oceans for the last two decades, *Journal of Oceanography*, *71*(6), 637–661, doi:10.1007/s10872-015-0306-4.

Ilyina, T., R. E. Zeebe, and P. G. Brewer (2010), Future ocean increasingly transparent to low-frequency sound owing to carbon dioxide emissions, *Nature Geosciences, 3*(1), 18–22, doi:10.1038/ngeo719.

IPCC (2014), Climate Change 2014: Synthesis Report. Contribution of Working Groups I, II and III to the Fifth Assessment Report of the Intergovernmental Panel on Climate Change [Core Writing Team, R.K. Pachauri and L.A. Meyer (eds.)]. IPCC, Geneva, Switzerland, 151 pp.

Irabien, M. J., A. García-Artola, A. Cearreta, and E. Leorri (2015), Chemostratigraphic and lithostratigraphic signatures of the Anthropocene in estuarine areas from the eastern Cantabrian coast (N. Spain), *Quaternary International,* 364, 196-205, doi: 10.1016/j.quaint.2014.08.056

IUPAC (2014), in *Compendium of Chemical Terminology: Gold Book*, doi:10.1351/goldbook.I03352.

Iversen, M. H., and L. K. Poulsen (2007), Coprorhexy, coprophagy, and coprochaly in the copepods *Calanus helgolandicus, Pseudocalanus elongatus,* and *Oithona similis*, *Marine Ecology Progress Series*, *350*, 79–89, doi:10.3354/meps07095.

Jeansson, E., A. Olsen, T. Eldevik, I. Skjelvan, A. M. Omar, S. K. Lauvset, J. E. Ø. Nilsen, R. G. J. Bellerby, T. Johannessen, and E. Falck (2011), The Nordic Seas carbon budget: Sources, sinks, and uncertainties, *Global Biogeochemical Cycles*, *25*(4), 1–16, doi:10.1029/2010GB003961.

Jiang, L. Q., R. A. Feely, B. R. Carter, D. J. Greeley, D. K. Gledhill, and K. M. Arzayus (2015), Climatological distribution of aragonite saturation state in the global oceans, *Global Biogeochemical Cycles*, *29*(10), 1656–1673, doi:10.1002/2015GB005198.

Jiao, N. et al. (2010), Microbial production of recalcitrant dissolved organic matter: long-term carbon storage in the global ocean., *Nature Reviews Microbiology*, *8*(8), 593–9, doi:10.1038/nrmicro2386.

Jiao, N. et al. (2014), Mechanisms of microbial carbon sequestration in the ocean - Future research directions, *Biogeosciences*, *11*(19), 5285–5306, doi:10.5194/bg-11-5285-2014.

Jickells, T. D., P. P. Newton, P. King, R. S. Lampitt, and C. Boutle (1996), A comparison of sediment trap records of particle fluxes from 19 to 48º N in the northeast Atlantic and their relation to surface water productivity, *Deep-Sea Research Part I: Oceanographic Research Papers Pap.*, *43*(7), 971–986.

Jickells, T. D. et al. (2017), A reevaluation of the magnitude and impacts of anthropogenic atmospheric nitrogen inputs on the ocean, *Global Biogeochemical Cycles*, *31*(2), 289–305, doi:10.1002/2016GB005586.

Jochumsen, K., D. Quadfasel, H. Valdimarsson, and S. Jónsson (2012), Variability of the Denmark Strait overflow: Moored time series from 1996-2011, *Journal of Geophysical Research: Ocean.*, *117*(12), doi:10.1029/2012JC008244.

Jochumsen, K., M. Köllner, D. Quadfasel, S. Dye, B. Rudels, and H. Valdimarsson (2015), On the origin and propagation of Denmark Strait overflow water anomalies in the Irminger Basin, *Journal of Geophysical Research: Ocean.*, *120*(3), 1841–1855, doi:10.1002/2014JC010397.

Jochumsen, K., M. Moritz, N. Nunes, D. Quadfasel, K. M. H. Larsen, B. Hansen, H. Valdimarsson, and S. Jonsson (2017), Revised transport estimates of the Denmark Strait overflow, *Journal of Geophysical Research: Ocean.,* 122, doi: 10.1002/2017JC012803.

Johnson, C., M. Inall, and S. Häkkinen (2013), Declining nutrient concentrations in the northeast Atlantic as a result of a weakening Subpolar Gyre, *Deep-Sea Research Part I: Oceanographic Research Papers*, *82*, 95–107, doi:10.1016/j.dsr.2013.08.007.

Jónasdóttir, S. H., A. W. Visser, K. Richardson, and M. R. Heath (2015), Seasonal copepod lipid pump promotes carbon sequestration in the deep North Atlantic., *Proceedings of the National Academy of Sciences,* 112(39), 12122-6, doi: 10.1073/pnas.1512110112.

Jones, S. D., C. Le Quéré, C. Rödenbeck, A. C. Manning, and A. Olsen (2015), A statistical gap-filling method to interpolate global monthly surface ocean carbon dioxide data, *Journal of Advances in Modeling Earth Systems*, *7*(4), 1554–1575, doi:10.1002/2014MS000416.

Jonkers, L., F. Mienis, W. Boer, I. R. Hall, and G. J. A. Brummer (2010a), Intra-annual variability of extremely rapid sedimentation onto Gardar Drift in the northern North Atlantic, *Deep-Sea Research Part I: Oceanographic Research Papers*, 57(8), 1027–1038, doi:10.1016/j.dsr.2010.05.005.

Jonkers, L., G. J. A. Brummer, F. J. C. Peeters, H. M. Van Aken, and M. F. De Jong (2010b), Seasonal stratification, shell flux, and oxygen isotope dynamics of left-coiling *N. pachyderma* and *T. quinqueloba* in the western subpolar North Atlantic, *Paleoceanography*, *25*(2), 1–13, doi:10.1029/2009PA001849.

Jónsson, S., and H. Valdimarsson (2012), Water mass transport variability to the North Icelandic shelf, 19942010, *ICES Journal of Marine Sciences*, *69*(5), 809–815, doi:10.1093/icesjms/fss024.

Joos, F., and R. Spahni (2008), Rates of change in natural and anthropogenic radiative forcing over the past 20,000 years, *Proceedings of the National Academy of Sciences*, *105*(5), 1425–1430, doi:10.1073/pnas.0707386105.

Jørgensen, L., C. a. Stedmon, T. Kragh, S. Markager, M. Middelboe, and M. Søndergaard (2011), Global trends in the fluorescence characteristics and distribution of marine dissolved organic matter, *Marine Chemistry*, *126*, 139–148, doi:10.1016/j.marchem.2011.05.002.

Jumars, P. A., D. L. Penry, J. A. Baross, M. J. Perry, and B. W. Frost (1989), Closing the microbial loop: dissolved carbon pathway to heterotrophic bacteria from incomplete ingestion, digestion and absorption in animals, *Deep-Sea Research Part I: Oceanographic Research Papers*, *36*(4), 483–495, doi:10.1016/0198-0149(89)90001-0.

Kaminski, S., A. Jakobi, and C. Wilhelm (2014), Uncertainty of gamma-ray spectrometry measurement of environmental samples due to uncertainties in matrix composition, density and sample geometry, *Applied Radiation and Isotopes*, *94*, 306–313, doi:10.1016/j.apradiso.2014.08.008.

Kamula, C. M., Z. Z. A. Kuzyk, D. A. Lobb, and R. W. Macdonald (2017), Sources and accumulation of sediment and particulate organic carbon in a subarctic fjard estuary: Pb-210, Cs-137, and delta C-13 records from Lake Melville, Labrador, *Canadian Journal of Earth Sciences*, *54*(9), 993–1006, doi:10.1139/cjes-2016-0167.

Kanzow, T., and W. Zenk (2014), Structure and transport of the Iceland Scotland Overflow plume along the Reykjanes Ridge in the Iceland Basin, *Deep-Sea Research Part I: Oceanographic Research Papers*, *86*, 82–93, doi: 10.1016/j.dsr.2013.11.003.

Karstensen, J., and M. Tomczak (1998), Age determination of mixed water masses using CFC and oxygen data, *Journal of Geophysical Research: Ocean.*, *103*(C9), doi:10.1029/98JC00889.

Keeling, C. D. (1960), The Concentration and Isotopic Abundances of Carbon Dioxide in the Atmosphere, *Tellus*, *12*(2), 200–203, doi:10.3402/tellusa.v12i2.9366.

Keeling, R. F., and T. Peng (1995), Transport of heat, CO_2 and O_2 by the Atlantic's thermohaline circulation, *Philosophical Transactions of the Royal Society*, *348*, 133–142, doi:10.1098/rstb.1995.0055.

Keeling, R. F., A. Körtzinger, and N. Gruber (2010), Ocean Deoxygenation in a Warming World, *Annual Review of Marine Science*, *2*(1), 199–229, doi:10.1146/annurev.marine.010908.163855.

Keen, M. J. (1968), *An introduction to marine geology*, Pergamon Press.

Keil, R. (2017), Anthropogenic Forcing of Carbonate and Organic Carbon Preservation in Marine Sediments, *Annual Review of Marine Science*, *9*(1), 151–172, doi:10.1146/annurev-marine-010816-060724.

Khatiwala, S. et al. (2013), Global ocean storage of anthropogenic carbon, *Biogeosciences*, *10*(4), 2169–2191, doi:10.5194/bg-10-2169-2013.

Kieke, D., and I. Yashayaev (2015), Studies of Labrador Sea Water formation and variability in the subpolar North Atlantic in the light of international partnership and collaboration, *Progress in Oceanography*, 132, 220-232, doi: 10.1016/j.pocean.2014.12.010.

Kirtman, B. et al. (2013), Near-term Climate Change: Projections and Predictability, in *Climate Change 2013: The Physical Science Basis. Contribution of Working Group I to the Fifth Assessment Report of the Intergovernmental Panel on Climate Change*, pp. 953–1028. doi:10.1017/CBO9781107415324.023.

Klaas, C., and D. E. Archer (2002), Association of sinking organic matter with various types of mineral ballast in the deep sea: Implications for the rain ratio, *Global Biogeochemical Cycles*, 16(4), 1-14, doi: 10.1029/2001GB001765.

Kohfeld, K. E., C. Le Quéré, S. P. Harrison, and R. F. Anderson (2005), Role of marine biology in glacial-interglacial CO_2 cycles, *Science, 308*(5718), 74–78, doi:10.1126/science.1105375.

Koide, M., A. Soutar, and E. D. Goldberg (1972), Marine geochronology with ^{210}Pb, *Earth and Planetary Science Letters*, *14*(3), 442–446, doi:10.1016/0012-821X(72)90146-X.

Körtzinger, A., W. Koeve, P. Kähler, and L. Mintrop (2001), C:N ratios in the mixed layer during the productive season in the northeast Atlantic Ocean, *Deep-Sea Research Part I: Oceanographic Research Papers*, *48*(3), 661–688, doi:10.1016/S0967-0637(00)00051-0.

Körtzinger, A., U. Send, D. W. R. Wallace, J. Karstensen, and M. de Grandpre (2008), Seasonal cycle of O_2 and pCO_2 in the central Labrador Sea: Atmospheric, biological, and physical implications, *Global Biogeochemical Cycles*, *22*(1), 1–16, doi:10.1029/2007GB003029.

Krishnaswamy, S., D. Lal, J. M. Martin, and M. Meybeck (1971), Geochronology of lake sediments, *Earth and Planetary Science. Letters*, *11*(1–5), 407–414, doi:10.1016/0012-821X(71)90202-0.

Kroeker, K. J., R. L. Kordas, R. Crim, I. E. Hendriks, L. Ramajo, G. S. Singh, C. M. Duarte, and J. P. Gattuso (2013), Impacts of ocean acidification on marine organisms: Quantifying sensitivities and interaction with warming, *Global Change Biology*, *19*(6), 1884–1896, doi:10.1111/gcb.12179.

Kuhlbrodt, T., A. Griesel, M. Montoya, A. Levermann, M. Hofmann, and S. Rahmstorf (2007), On the driving processes of the Atlantic meridional overturning circulation, *Reviews of Geophysics*, *45*(2), doi:10.1029/2004RG000166.

Kuss, J., and K. Kremling (1999), Particulate trace element fluxes in the deep northeast Atlantic Ocean, *Deep-Sea Research Part I: Oceanographic Research Papers*, *46*(1), 149–169, doi:10.1016/S0967-0637(98)00059-4.

Kuzyk, Z. Z. A., C. Gobeil, and R. W. Macdonald (2013), ^{210}Pb and ^{137}Cs in margin sediments of the Arctic Ocean: Controls on boundary scavenging, *Global Biogeochemical Cycles*, *27*(2), 422–439, doi: 10.1002/gbc.20041.

Kwon, E. Y., F. Primeau, and J. L. Sarmiento (2009), The impact of remineralization depth on the air–sea carbon balance, *Nature Geosciences, 2*(9), 630–635, doi:10.1038/ngeo612.

Laboratoire National Henri Becquerel (2017), Table de radionucleides ^{210}Pb - Data Decay Evaluation Project, Available from: http://www.nucleide.org/DDEP_WG/DDEPdata.htm

Lamborg, C. H., C. R. Hammerschmidt, K. L. Bowman, G. J. Swarr, K. M. Munson, D. C. Ohnemus, P. J. Lam, L.-E. Heimbürger, M. J. a. Rijkenberg, and M. a. Saito (2014a), A global ocean inventory of anthropogenic mercury based on water column measurements, *Nature*, *512*(7512), 65–68, doi:10.1038/nature13563.

Lamborg, C., K. Bowman, C. Hammerschmidt, C. Gilmour, K. Munson, N. Selin, and C.-M. Tseng (2014b), Mercury in the Anthropocene Ocean, *Oceanography*, *27*(1), 76–87, doi:10.5670/oceanog.2014.11.

Lampitt, R. S., and A. N. Antia (1997), Particle flux in deep seas: Regional characteristics and temporal variability, *Deep-Sea Research Part I: Oceanographic Research Papers*, *44*(8), 1377–1403, doi:10.1016/S0967.

Lampitt, R. S., B. Boorman, L. Brown, M. Lucas, I. Salter, R. Sanders, K. Saw, S. Seeyave, S. J. Thomalla, and R. Turnewitsch (2008), Particle export from the euphotic zone: Estimates using a novel drifting sediment trap, ^{234}Th and new production, *Deep-Sea Research Part I: Oceanographic Research Papers*, *55*(11), 1484–1502, doi: 10.1016/j.dsr.2008.07.002.

Lampitt, R. S., I. Salter, B. A. de Cuevas, S. Hartman, K. E. Larkin, and C. A. Pebody (2010), Long-term variability of downward particle flux in the deep northeast Atlantic: Causes and trends, *Deep-Sea Research Part I: Oceanographic Research Papers*, *57*(15), 1346–1361, doi:10.1016/j.dsr2.2010.01.011.

Landolfi, A., C. J. Somes, W. Koeve, L. M. Zamora, and A. Oschlies (2017), Oceanic nitrogen cycling and N_2O flux perturbations in the Anthropocene, *Global Biogeochemical Cycles*, 31, 1236–1255, doi: 10.1002/2017GB005633.

Landschützer, P., N. Gruber, D. C. E. Bakker, and U. Schuster (2014), Recent variability of the global ocean carbon sink, *Global Biogeochemical Cycles*, *28*(9), 927–949, doi:10.1002/2014GB004853.

Landschützer, P., N. Gruber, and D. C. E. Bakker (2016), Decadal variations and trends of the global ocean carbon sink, *Global Biogeochemical Cycles, 30*, 1396–1417, doi:10.1002/2015GB005359.We.

Laruelle, G. G. et al. (2009), Anthropogenic perturbations of the silicon cycle at the global scale: Key role of the land-ocean transition, *Global Biogeochemical Cycles*, *23*(4), doi:10.1029/2008GB003267.

Lauvset, S. K., N. Gruber, P. Landschützer, A. Olsen, and J. Tjiputra (2015), Trends and drivers in global surface ocean pH over the past 3 decades, *Biogeosciences*, *12*(5), 1285–1298, doi:10.519

Lavín, A. M., H. L. Bryden, and G. Parrilla (2003), Mechanisms of heat, freshwater, oxygen and nutrient transports and budgets at 24.5°N in the subtropical North Atlantic, *Deep-Sea*

Research Part I: Oceanographic Research Papers, *50*(9), 1099–1128, doi:10.1016/S0967-0637(03)00095-5.

Laws, E., P. G. Falkowski, W. O. Smith, H. W. Ducklow, and J. J. McCarthy (2000), Temperature effects on export production in the open ocean, *Global Biogeochemical Cycles*, *14*(4), 1231–1246, doi:10

Le Quéré, C. et al. (2016), Global Carbon Budget 2016, *Earth System Science Data*, *8*(2), 605–649, doi:10.5194/essd-8-605-2016.

Lee, K. (2001), Global net community production estimated from the annual cycle of surface water total dissolved inorganic carbon, *Limnology & Oceanography*, *46*(6), 1287–1297, doi:10.4319/lo.2001.46.6.1287.

Legendre, L., R. B. Rivkin, M. G. Weinbauer, L. Guidi, and J. Uitz (2015), The microbial carbon pump concept: Potential biogeochemical significance in the globally changing ocean, *Progress in Oceanography, 134*, 432-450, doi: 10.1016/j.pocean.2015.01.008.

Leorri, E., S. Mitra, M. J. Irabien, A. R. Zimmerman, W. H. Blake, and A. Cearreta (2014), A 700year record of combustion-derived pollution in northern Spain: Tool s to identify the Holocene/Anthropocene transition in coastal environments, *Science of the Total Environment*, *470–471*, 240–247, doi:10.1016/j.scitotenv.2013.09.064.

Lepore, K., S. B. Moran, and J. N. Smith (2009), ^{210}Pb as a tracer of shelf-basin transport and sediment focusing in the Chukchi Sea, *Deep-Sea Research Part I: Oceanographic Research Papers*, *56*(17), 1305–1315, doi: 10.1016/j.dsr2.2008.10.021.

Lewis, S. L., and M. A. Maslin (2015), Defining the Anthropocene, *Nature*, *519*(7542), 171–180, doi:10.1038/nature14258.

Lherminier, P., H. Mercier, C. Gourcuff, M. Alvarez, S. Bacon, and C. Kermabon (2007), Transports across the 2002 Greenland-Portugal Ovide section and comparison with 1997, *Journal of Geophysical Research: Ocean.*, *112*(7), 1–20, doi:10.1029/2006JC003716.

Lherminier, P., H. Mercier, T. Huck, C. Gourcuff, F. F. Perez, P. Morin, A. Sarafanov, and A. Falina (2010), The Atlantic Meridional Overturning Circulation and the subpolar gyre observed at the A25-OVIDE section in June 2002 and 2004, *Deep-Sea Research Part I: Oceanographic Research Papers*, *57*(11), 1374–1391, doi:10.1016/j.dsr.2010.07.009.

Lherminier, P., and G. Sarthou (2017), The 2014 Greenland-Portugal GEOVIDE CTDO2 hydrographic and SADCP data (GO-SHIP A25 and GEOTRACES GA01), *Seanoe*, doi:10.17882/52153.

Li, H., T. Ilyina, W. A. Müller, and F. Sienz (2016), Decadal predictions of the North Atlantic CO_2 uptake, *Nature Communications*, *7*, 11076, doi:10.1038/ncomms11076.

Lima, I. D., P. J. Lam, and S. C. Doney (2014), Dynamics of particulate organic carbon flux in a global ocean model, *Biogeosciences*, *11*(4), 1177–1198, doi:10.5194/bg-11-1177-2014.

Lomas, M. W., and S. B. Moran (2011), Evidence for aggregation and export of cyanobacteria and nano-eukaryotes from the Sargasso Sea euphotic zone, *Biogeosciences*, *8*(1), 203–216, doi:10.5194/bg-8-203-2011.

Longhurst, A., S. Sathyendranath, T. Platt, and C. Caverhill (1995), An estimate of global primary production in the ocean from satelite radiometer data, *Journal of Plankton Research*, *17*(6), 1245–1271.

Loveland, W. D., D. J. Morrissey, and G. T. Seaborg (2005), *Modern Nuclear Chemistry*.

Lozier, M. S., S. Leadbetter, R. G. Williams, V. Roussenov, M. S. C. Reed, and N. J. Moore (2008), The Spatial Pattern and Mechanisms of Heat-Content Change in the North Atlantic, *Science*, *319*(5864), 800–803, doi:10.1126/science.1146436.

Lozier, M. S. (2012), Overturning in the North Atlantic, *Annual Review of Marine Science*, *4*(1), 291–315, doi:10.1146/annurev-marine-120710-100740.

Ludwig, W., P. Amiotte-Suchet, and J. L. Probst (1996), River discharges of carbon to the world's oceans: Determining local inputs of alkalinity and of dissolved and particulate organic carbon, *Comptes Rendus De L Academie Des Sciences Serie Ii Fascicule a-Sciences De La Terre Et Des Planetes*, *323*(12), 1007–1014.

Lumpkin, R., and K. Speer (2007), Global Ocean Meridional Overturning, *Journal of Physical Oceanography*, *37*(10), 2550–2562, doi:10.1175/JPO3130.1.

Lüthi, D. et al. (2008), High-resolution carbon dioxide concentration record 650,000-800,000 years before present, *Nature*, *453*(7193), 379–382, doi:10.1038/nature06949.

Lutz, M. J., K. Caldeira, R. B. Dunbar, and M. J. Behrenfeld (2007), Seasonal rhythms of net primary production and particulate organic carbon flux to depth describe the efficiency of biological pump in the global ocean, *Journal of Geophysical Research: Ocean.*, *112*(10), doi:10.1029/2006JC003706.

Mabit, L. et al. (2014), Fallout ^{210}Pb as a soil and sediment tracer in catchment sediment budget investigations: A review, *Earth-Science Reviews.*, *138*, 335–351, doi:10.1016/j.earscirev.2014.06.007

Mach, D. L., A. Ramirez, and H. D. Holland (1987), Organic phosphorus and carbon in marine sediments, *American Journal of Science*, *287*(5), 429–441, doi:10.2475/ajs.287.5.429.

Macrander, A., U. Send, H. Valdimarsson, S. Jónsson, and R. H. Käse (2005), Interannual changes in the overflow from the Nordic Seas into the Atlantic Ocean through Denmark Strait, *Geophysical Research Letters*, *32*(6), 1–4, doi:10.1029/2004GL021463.

Majkut, J. D., J. L. Sarmiento, and K. B. Rodgers (2014), A growing oceanic carbon uptake: Results from an inversion study of surface pCO_2 data, *Global Biogeochemical Cycles*, *28*(4), 335–351, doi:10.1002/2013GB004585.

Marsay, C. M., R. J. Sanders, S. A. Henson, K. Pabortsava, E. P. Achterberg, and R. S. Lampitt (2015), Attenuation of sinking particulate organic carbon flux through the mesopelagic ocean., *Proceedings of the National Academy of Sciences U. S. A.*, *112*(4), 1089–94, doi:10.1073/pnas.1415311112.

Marshall, J., H. Johnson, and J. Goodman (2001), A study of the interaction of the North Atlantic oscillation with ocean circulation, *Journal of Climate*, *14*(7), 1399–1421, doi:10.1175/1520-0442

Martin, J. H., G. A. Knauer, D. M. Karl, and W. W. Broenkow (1987), VERTEX: carbon cycling in the northeast Pacific, *Deep-Sea Research Part I: Oceanographic Research Papers*, *34*(2), 267–285, doi:10.1016/0198.

Martin, J. H., and S. E. Fitzwater (1988), Iron deficiency limits phytoplankton growth in the north-east Pacific subarctic, *Nature*, *331*(6154), 341–343, doi:10.1038/331341a0.

Martin, J. H., and S. E. Fitzwater (1992), Dissolved organic carbon in the Atlantic, Southern and Pacific oceans, *Nature*, *356*(6371), 699–704.

Martínez-Pérez, A. M., M. Nieto-Cid, H. Osterholz, T. S. Catalá, I. Reche, T. Dittmar, and X. A. Álvarez-Salgado (2017), Linking optical and molecular signatures of dissolved organic matter in the Mediterranean Sea, *Sci. Rep.*, *7*(1), doi:10.1038/s41598-017-03735-4.

Masqué, P., E. Isla, J. A. Sánchez-Cabeza, A. Palanques, J. M. Bruach, P. Puig, and J. Guillén (2002), Sediment accumulation rates and carbon fluxes to bottom sediments at the western Bransfield Strait (Antarctica), *Deep-Sea Research Part I: Oceanographic Research Papers*, *49*(4–5), 921–933, doi:10.1016/S0967-0645(01)00131-X.

Masqué, P., J. Fabres, M. Canals, J. A. Sanchez-Cabeza, A. Sanchez-Vidal, I. Cacho, A. M. Calafat, and J. M. Bruach (2003), Accumulation rates of major constituents of hemipelagic sediments in the deep Alboran Sea: A centennial perspective of sedimentary dynamics, *Marine Geology*, *193*(3–4), 207–233, doi:10.1016/S0025-3227(02)00593-5.

Mastropole, D., R. S. Pickart, H. Valdimarsson, K. Våge, K. Jochumsen, and J. Girton (2017), On the hydrography of Denmark Strait, *Journal of Geophysical Research: Ocean.*, *122*(1), 306–321, doi:10.1002/2016JC012007.

Mayor, D. J., R. Sanders, S. L. C. Giering, and T. R. Anderson (2014), Microbial gardening in the ocean's twilight zone: Detritivorous metazoans benefit from fragmenting, rather than ingesting, sinking detritus, *BioEssays*, *36*(12), 1132–1137, doi:10.1002/bies.201400100.

Mazarrasa, I., N. Marbà, J. Garcia-Orellana, P. Masqué, A. Arias-Ortiz, and C. M. Duarte (2017), Effect of environmental factors (wave exposure and depth) and anthropogenic pressure in the C sink capacity of *Posidonia oceanica* meadows, *Limnology & Oceanography*, doi:10.1002/lno.10510.

Maze, G., H. Mercier, V. Thierry, L. Memery, P. Morin, and F. F. Perez (2012), Mass, nutrient and oxygen budgets for the northeastern Atlantic Ocean, *Biogeosciences*, *9*(10), 4099–4113, doi:10.5194/bg-9-4099-2012.

Mazé, J. P., M. Arhan, and H. Mercier (1997), Volume budget of the eastern boundary layer off the Iberian Peninsula, *Deep-Sea Research Part I: Oceanographic Research Papers*, *44*(9–10), 1543–1574, doi:10.1016/S096

McCarthy, G., E. Frajka-Williams, W. E. Johns, M. O. Baringer, C. S. Meinen, H. L. Bryden, D. Rayner, A. Duchez, C. Roberts, and S. A. Cunningham (2012), Observed interannual variability of the Atlantic meridional overturning circulation at 26.5°N, *Geophysical Research Letters*, *39*(19), doi:10.1029/2012GL052933.

McCarthy, G. D., D. A. Smeed, W. E. Johns, E. Frajka-Williams, B. I. Moat, D. Rayner, M. O. Baringer, C. S. Meinen, J. Collins, and H. L. Bryden (2015), Measuring the Atlantic

Meridional Overturning Circulation at 26ºN, *Progress in Oceanography*, *130*, 91–111, doi:10.1016/j.pocean.2014.10.006.

McCave, I. N., and I. R. Hall (2006), Size sorting in marine muds: Processes, pitfalls, and prospects for paleoflow-speed proxies, *Geochemistry, Geophysics Geosystems*, *7*(10), doi:10.1029/2006GC00

McElroy, M. B. (1983), Marine biological controls on atmospheric CO_2 and climate, *Nature*, *302*(5906), 328–329, doi:10.1038/302328a0.

Medeiros, P. M., M. Seidel, J. Niggemann, R. G. M. Spencer, P. J. Hernes, P. L. Yager, W. L. Miller, T. Dittmar, and D. A. Hansell (2016), A novel molecular approach for tracing terrigenous dissolved organic matter into the deep ocean, *Global Biogeochemical Cycles*, *30*(5), 689–699, doi:10.1002/2015GB005320.

Meehl, G. A. et al. (2014), Decadal climate prediction: an update from the trenches, *Bulletin of the American Meteorological Society*, *95*(2), 243–267, doi:10.1175/BAMS-D-12-00241.1.

Meinshausen, M. et al. (2017), Historical greenhouse gas concentrations for climate modelling (CMIP6), *Geoscientific Model Development*, *10*(5), 2057–2116, doi:10.5194/gmd-10-2057-2017.

Mercier, H. (1986), Determining the general circulation of the ocean: A nonlinear inverse problem, *Journal of Geophysical Research: Ocean.*, *91*(C4), 5103–5109, doi:10.1029/JC091iC04p05103.

Mercier, H. et al. (2015), Variability of the meridional overturning circulation at the Greenland-Portugal OVIDE section from 1993 to 2010, *Progress in Oceanography*, *132*, 250–261, doi:10.1016/j.pocean.2

Miller, P. I., J. F. Read, and A. C. Dale (2013), Thermal front variability along the North Atlantic Current observed using microwave and infrared satellite data, *Deep-Sea Research Part I: Oceanographic Research Papers*, *98*, 244–256, doi:10.1016/j.dsr2.2013.08.014.

Millero, F., R. Woosley, B. DiTrolio, and J. Waters (2009), Effect of Ocean Acidification on the Speciation of Metals in Seawater, *Oceanography*, *22*(4), 72–85, doi:10.5670/oceanog.2009.98.

Miralles, J., O. Radakovitch, and J. C. Aloisi (2005), ^{210}Pb sedimentation rates from the Northwestern Mediterranean margin, *Marine Geology*, *216*(3), 155–167, doi:10.1016/j.margeo.2005.02.020.

Moffa-Sánchez, P., R. Hall, S. Barker, D.J. Thornalley, and I. Yashayaev (2014), Surface changes in the eastern Labrador Sea around the onset of the Little Ice Age, *Paleoceanography 29*(3), 160–175, doi:10.1002/2013PA002523

Moore, C. M. et al. (2013), Processes and patterns of oceanic nutrient limitation, *Nature Geoscience, 6*(9), 701–710, doi:10.1038/ngeo1765.

Moore, W. S., and J. Dymondt (1988), Correlation of ^{210}Pb removal with organic carbon fluxes in the Pacific Ocean, *Nature*, *331*(6154), 339–341, doi:10.1038/331339a0.

Moreira-Coello, V., B. Mouriño-Carballido, E. Marañón, A. Fernández-Carrera, A. Bode, and M. M. Varela (2017), Biological N_2 Fixation in the Upwelling Region off NW Iberia: Magnitude,

Relevance, and Players, *Frontiers in Marine Science*, *4*(303), doi:10.3389/fmars.2017.00303.

Mulder, T., H. Hüneke, and A. J. Van Loon (2011), *Progress in deep-sea sedimentology*, doi: 10.1016/B978-0-444-53000-4.00001-9.

Nagata, T. (2008), Organic Matter-Bacteria Interactions in Seawater, in *Microbial Ecology of the Oceans: Second Edition*, pp. 207–241.

Najjar, G., and R. F. Keeling (2000), Mean annual cycle of the air-sea oxygen flux : A global view, *Global Biogeochemical Cycles*, *14*(2), 573–584, doi: 0886-6236/00/1999GB 900086512.00.

Nakaoka, S., M. Telszewski, Y. Nojiri, S. Yasunaka, C. Miyazaki, H. Mukai, and N. Usui (2013), Estimating temporal and spatial variation of ocean surface pCO_2 in the North Pacific using a self-organizing map neural network technique, *Biogeosciences*, *10*(9), 6093–6106, doi:10.5194/bg-10-6093-2013.

Nelson, D. M., P. Tréguer, M. A. Brzezinski, A. Leynaert, and B. Quéguiner (1995), Production and dissolution of biogenic silica in the ocean: Revised global estimates, comparison with regional data and relationship to biogenic sedimentation, *Global Biogeochemical Cycles*, *9*(3), 359–372, doi:10.1029/95GB01070.

Nelson, D. M., D. J. DeMaster, R. B. Dunbar, and W. O. Smith (1996), Cycling of organic carbon and biogenic silica in the Southern Ocean: Estimates of water-column and sedimentary fluxes on the Ross Sea continental shelf, *Journal of Geophysical Research: Ocean.*, *101*(C8), 18519–18532, doi:10.1029/96JC01573.

Nelson, D. M., and M. A. Brzezinski (1997), Diatom growth and productivity in an oligotrophic mid-ocean gyre: A 3-yr record from the Sargasso Sea near Bermuda, *Limnology & Oceanography*, *42*(6), 473–486, doi:10.4319/lo.1997.42.3.0473.

Neuer, S., V. Ratmeyer, R. Davenport, G. Fischer, and G. Wefer (1997), Deep water particle flux in the Canary Island region: Seasonal trends in relation to long-term satellite derived pigment data and lateral sources, *Deep-Sea Research Part I: Oceanographic Research Papers*, *44*(8), 1451–1466, doi:10.1016/S0967-0637(97)00034-4.

Nieto-Moreno, V., F. Martinez-Ruiz, S. Giralt, D. Gallego-Torres, J. Garcia-Orellana, P. Masque, and M. Ortega-Huertas (2013), Climate imprints during the “Medieval Climate Anomaly” and the “Little Ice Age” in marine records from the Alboran Sea basin, *The Holocene*, *23*(9), 1227–1237, doi:10.1177/0959683613484613.

Nijampurkar, V. N., and H. B. Clausen (1990), A century old record of lead-210 fallout on the Greenland ice sheet, *Tellus B*, *42*(1), 29–38, doi:10.1034/j.1600-0889.1990.00005.x.

Nilsson, J., G. Björk, B. Rudels, P. Winsor, and D. Torres (2008), Liquid freshwater transport and Polar Surface Water characteristics in the East Greenland Current during the AO-02 *Oden* expedition, *Progress in Oceanography*, *78*(1), 45–57, doi:10.1016/j.pocean.2007.06.002.

Noller, J. S., J. M. Sowers, S. M. Colman, and K. L. Pierce (2000), Introduction to Quaternary Geochronology, in *Quaternary Geochronology: Methods and Applications*, p. 582, doi: 10.1029/RF004.

Nondal, G., R. G. J. Bellerby, A. Olsen, T. Johannessen, and J. Olafsson (2009), Optimal evaluation of the surface ocean CO_2 system in the northern North Atlantic using data from voluntary observing ships, *Limnology & Oceanography Methods*, *7*(1), 109–118, doi:10.4319/lom.2009.7.109.

Oberle, F. K. J., P. W. Swarzenski, C. M. Reddy, R. K. Nelson, B. Baasch, and T. J. J. Hanebuth (2016), Deciphering the lithological consequences of bottom trawling to sedimentary habitats on the shelf, *Journal of Marine Systems*, *159*, 120–131, doi:10.1016/j.jmarsys.2015.12.008.

Oguri, K., E. Matsumoto, M. Yamada, Y. Saito, and K. Iseki (2003), Sediment accumulation rates and budgets of depositing particles of the East China Sea, *Deep-Sea Research Part I: Oceanographic Research Papers*, *50*(2), 513–528, doi:10.1016/S0967-0645(02)00465-4.

Oldfield, F., and P. G. Appleby (1984), A combined radiometric and mineral magnetic approach to recent geochronology in lakes affected by catchment disturbance and sediment redistribution, *Chemical Geology*, *44*(1–3), 67–83, doi:10.1016/0009-2541(84)90067-6.

Olsen, A. et al. (2016), The global ocean data analysis project version 2 (GLODAPv2) - An internally consistent data product for the world ocean, *Earth System Science Data*, *8*(2), 297–323, doi:10.5194/essd-8-297-2016.

Orr, J. C. et al. (2005), Anthropogenic ocean acidification over the twenty-first century and its impact on calcifying organisms, *Nature*, *437*(7059), 681–686, doi:10.1038/nature04095.

Oschlies, A., O. Duteil, J. Getzlaff, W. Koeve, A. Landolfi, and S. Schmidtko (2017), Patterns of deoxygenation: sensitivity to natural and anthropogenic drivers., *Philosophical Transactions of the Royal Society., 375*(2102), 20160325, doi:10.1098/rsta.2016.0325.

Østerhus, S., W. R. Turrell, S. Jónsson, and B. Hansen (2005), Measured volume, heat, and salt fluxes from the Atlantic to the Arctic Mediterranean, *Geophysical Research Letters*, *32*(7), 1–4, doi:10.1029/2004GL022188.

Otero, P., X. A. Padín, M. Ruiz-Villarreal, L. M. García-García, A. F. Ríos, and F. F. Pérez (2013), Net sea-air CO_2 flux uncertainties in the Bay of Biscay based on the choice of wind speed products and gas transfer parameterizations, *Biogeosciences*, *10*(5), 2993–3005, doi:10.5194/bg-10-2993-2013.

Palter, J. B., and M. S. Lozier (2008), On the source of Gulf Stream nutrients, *Journal of Geophysical Research: Ocean.*, *113*(6), doi:10.1029/2007JC004611.

Pardo, P. C., F. F. Pérez, A. Velo, and M. Gilcoto (2012), Water masses distribution in the Southern Ocean: Improvement of an extended OMP (eOMP) analysis, *Progress in Oceanography*, *103*, 92–105, doi:10.1016/j.pocean.2012.06.002.

Parekh, P., S. Dutkiewicz, M. J. Follows, and T. Ito (2006), Atmospheric carbon dioxide in a less dusty world, *Geophysical Research Letters*, *33*(3), 2–5, doi:10.1029/2005GL025098.

Park, G. H., R. Wanninkhof, S. C. Doney, T. Takahashi, K. Lee, R. A. Feely, C. L. Sabine, J. Trińlanes, and I. D. Lima (2010), Variability of global net sea-air CO2 fluxes over the last three decades using empirical relationships, *Tellus, Series B: Chemical and Physical Meteorology*, *62*(5), 352–368, doi:10.1111/j.1600-0889.2010.00498.x.

Passow, U., and C. A. Carlson (2012), The biological pump in a high CO_2 world, *Marine Ecology Progress Series*, *470*(2), 249–271, doi:10.3354/meps09985.

Paytan, A., and K. McLaughlin (2007), The oceanic phosphorus cycle, *Chemical Reviews*, *107*(2), 563–576, doi:10.1021/cr0503613.

Pelejero, C., E. Calvo, and O. Hoegh-Guldberg (2010), Paleo-perspectives on ocean acidification, *Trends Ecol. Evol.*, *25*(6), 332–344, doi:10.1016/j.tree.2010.02.002.

Peng, T. -H, and W. S. Broecker (1987), C/P ratios in marine detritus, *Global Biogeochemical Cycles*, *1*(2), 155–161, doi:10.1029/GB001i002p00155.

Pennington, W., R. S. Cambray, J. D. Eakins, and D. D. Harkness (1976), Radionuclide dating of the recent sediments of Blelham Tarn, *Freshwater Biology*, *6*(4), 317–331, doi:10.1111/j.1365-2427.1976.tb01617.x.

Pérez, F. F., M. Vázquez-Rodríguez, E. Louarn, X. A. Padín, H. Mercier, and A. F. Ríos (2008), Temporal variability of the anthropogenic CO_2 storage in the Irminger Sea, *Biogeosciences*, *5*(6), 1669–1679, doi:10.5194/bg-5-1669-2008.

Pérez, F. F., M. Vázquez-Rodríguez, H. Mercier, A. Velo, P. Lherminier, and A. F. Ríos (2010), Trends of anthropogenic CO_2 storage in North Atlantic water masses, *Biogeosciences*, *7*(5), 1789–180, doi: 10.5194/bg-7-1789-2010.

Pérez, F. F., H. Mercier, M. Vázquez-Rodríguez, P. Lherminier, A. Velo, P. C. Pardo, G. Rosón, and A. F. Ríos (2013), Atlantic Ocean CO_2 uptake reduced by weakening of the meridional overturning circulation, *Nature Geosciences, 6*(2), 146–152, doi:10.1038/ngeo1680.

Pérez, F. F. et al. (2018), Meridional overturning circulation conveys fast acidification to the deep Atlantic Ocean, *Nature*, doi:10.138/nature25493.

Peterson, B. J., R. M. Holmes, J. W. Mcclelland, C. J. Vo, R. B. Lammers, A. I. Shiklomanov, I. A. Shiklomanov, and S. Rahmstorf (2002), Increasing River Discharge to the Arctic Ocean, *Science*, *298*(December), 2171–2174.

Pickart, R. S., M. A. Spall, M. H. Ribergaard, G. W. K. Moore, and R. F. Milliff (2003), Deep convection in the Irminger sea forced by the Greenland tip jet, *Nature*, *424*(6945), 152–156, doi:10.1038/nature01729.

Piron, A., V. Thierry, H. Mercier, and G. Caniaux (2016), Argo float observations of basin-scale deep convection in the Irminger sea during winter 2011-2012, *Deep-Sea Research Part I: Oceanographic Research Papers*, *109*, 76–90, doi:10.1016/j.dsr.2015.12.012.

Piron, A., V. Thierry, H. Mercier, and G. Caniaux (2017), Gyre scale deep convection in the subpolar North-Atlantic Ocean during winter 2014-2015, *Geophysical Research Letters*, doi:10.1002/2016GL071895.

Polimene, L., S. Sailley, D. Clark, A. Mitra, and J. I. Allen (2017), Biological or microbial carbon pump? The role of phytoplankton stoichiometry in ocean carbon sequestration, *Journal of Plankton Research*, *39*(2), 180–186, doi:10.1093/plankt/fbw091.

Pollard, R. T., M. J. Griffttths, S. A. Cunningham, J. F. Read, F. F. Pérez, and A. F. Ríos (1996), Vivaldi 1991 - A study of the formation, circulation and ventilation of Eastern North Atlantic Central Water *Progress in Oceanography*, *37*(2), 167–192, doi:10.1016/S0079-6611(96)00008-0.

Pondaven, P., D. Ruiz-Pino, J. N. Druon, C. Fravalo, and P. Tréguer (1999), Factors controlling silicon and nitrogen biogeochemical cycles in high nutrient, low chlorophyll systems (the Southern Ocean and the North Pacific): Comparison with a mesotrophic system (the North Atlantic), *Deep-Sea Research Part I: Oceanographic Research Papers*, *46*(11), 1923–1968, doi:10.1016/S0967-0637(99)00033-3.

Pörtner, H.-O., D. M. Karl, P. W. Boyd, W. W. L. Cheung, S. E. Lluch-Cota, Y. Nojiri, D. N. Schmidt, and P. O. Zavialov (2014), Part A: Global and Sectoral Aspects. (Contribution of Working Group II to the Fifth Assessment Report of the Intergovernmental Panel on Climate Change), in *Climate Change 2014: Impacts, Adaptation, and Vulnerability.*, edited by T. E. B. Field, C.B., V.R. Barros, D.J. Dokken, K.J. Mach, M.D. Mastrandrea, S. M. M. Chatterjee, K.L. Ebi, Y.O. Estrada, R.C. Genova, B. Girma, E.S. Kissel, A.N. Levy, and and L. L. W. P.R. Mastrandrea, p. 1132, Cambridge University Press, 2014)., Cambridge, United Kingdom and New York, NY, USA, doi: 10.1017/CBO9781107415324.004.

Poulton, A. J., R. Sanders, P. M. Holligan, M. C. Stinchcombe, T. R. Adey, L. Brown, and K. Chamberlain (2006), Phytoplankton mineralization in the tropical and subtropical Atlantic Ocean, *Global Biogeochemical Cycles*, *20*(4), 1–10, doi:10.1029/2006GB002712.

Povinec, P. P., P. Bailly Du Bois, P. J. Kershaw, H. Nies, and P. Scotto (2003), Temporal and spatial trends in the distribution of ^{137}Cs in surface waters of Northern European Seas - A record of 40 years of investigations, *Deep-Sea Research Part I: Oceanographic Research Papers*, *50*(17–21), 2785–2801, doi:10.1016/S0967-0645(03)00148-6.

Primeau, F. (2005), Characterizing Transport between the Surface Mixed Layer and the Ocean Interior with a Forward and Adjoint Global Ocean Transport Model, *Journal of Physical Oceanography*, *35*(4), 545–564, doi:10.1175/JPO2699.1.

Puig, P., J. Martín, P. Masqué, and A. Palanques (2015), Increasing sediment accumulation rates in la Fonera (Palamós) submarine canyon axis and their relationship with bottom trawling activities, *Geophysical Research Letters*, *42*(19), 8106–8113, doi:10.1002/2015GL065052.

Quintana, B., and F. Fernández (1998), Continuous component determination in γ-ray spectra, *Nuclear Instruments and Methods in Physics Research, Section A: Accelerators, Spectrometers, Detectors and Associated Equipment*, *411*(2–3), 475–493, doi:10.1016/S0168-9002(98)00334-9.

Quintana, B., P. Álvarez-Iglesias, R. Santamaría, B. Rubio, and M. Pérez-Arlucea (2006), Low-level gamma spectrometry for pollution assessment in San Simón Bay (Vigo, Spain), in

Journal of Physics: Conference Series, vol. 41, pp. 400–407, doi: 10.1088/1742-6596/41/1/044.

Quintana, B., M. C. Pedrosa, L. Vázquez-Canelas, R. Santamaría, M. A. Sanjuán, and F. Puertas (2017), A method for the complete analysis of NORM building materials by γ-ray spectrometry using HPGe detectors, *Applied Radiation and Isotopes,* doi:http://dx.doi.org/10.1016/j.apradiso.2017.07.045.

Ragueneau, O. et al. (2000), A review of the Si cycle in the modern ocean: Recent progress and missing gaps in the application of biogenic opal as a paleoproductivity proxy, *Global and Planetary Change*, *26*(4), 317–365, doi:10.1016/S0921-8181(00)00052-7.

Ragueneau, O., N. Dittert, P. Pondaven, P. Tr, and L. Corrin (2002), Si/C decoupling in the world ocean: is the Southern Ocean different?, *Deep-Sea Research Part II: Topical Studies in Oceanography, 49*, 3127–3154.

Rahman, S., R. C. Aller, and J. K. Cochran (2017), The missing silica sink: revisiting the marine sedimentary Si cycle, *Global Biogeochemical Cycles*, 1559–1578, doi:10.1002/2017GB005746.

Raven, J. A., and P. G. Falkowski (1999), Oceanic sinks for atmospheric CO_2, *Plant, Cell and Environment*, *22*(6), 741–755, doi:10.1046/j.1365-3040.1999.00419.x.

Raven, John, K. Caldeira, H. Elderfield, O. Hoegh-Guldberg, P. Liss, U. Riebesell, J. Shepherd, C. Turley, and A. Watson (2005), Ocean acidification due to increasing atmospheric carbon dioxide, *Philosophical Transactions of the Royal Society*, (June), 1–68.

Rebesco, M., F. J. Hernández-Molina, D. Van Rooij, and A. Wåhlin (2014), Contourites and associated sediments controlled by deep-water circulation processes: State-of-the-art and future considerations, *Marine Geology*, *352*, 111–154, doi:10.1016/j.margeo.2014.03.011.

Rebesco, M. et al. (2016), Evolution of a high-latitude sediment drift inside a glacially-carved trough based on high-resolution seismic stratigraphy (Kveithola, NW Barents Sea), *Quaternary Science Reviews*, *1*

Redfield, A. C. (1934), On the proportions of organic derivatives in sea water and their relation to the composition of plankton, in *James Johnstone Memorial Volume*, pp. 176–192, Liverpool Univ. Press

Redfield, A. C., B. H. Ketchum, and F. A. Richards (1963), The influence of organisms on the composition of sea-water, in *The sea ideas and observations on progress in the study of the seas.*

Rhein, M. et al. (2013), Observations: Ocean, in *Climate Change 2013: The Physical Science Basis. Contribution of Working Group I to the Fifth Assessment Report of the Intergovernmental Panel on Climate Change*, edited by B. and P. M. M. Stocker, T.F., D. Qin, G.-K. Plattner, M. Tignor, S.K. Allen, J. Boschung, A. Nauels, Y. Xia, V., Cambridge University Press, Cambridge, United Kingdom and New York, NY, USA.

Ribeiro, S., A. Amorim, F. Abrantes, and M. Ellegaard (2016), Environmental change in the Western Iberia Upwelling Ecosystem since the preindustrial period revealed by

dinoflagellate cyst records, *The Holocene*, *26*(6), 874–889, doi:10.1177/0959683615622548.

Riley, J. S., R. Sanders, C. Marsay, F. A. C. Le Moigne, E. P. Achterberg, and A. J. Poulton (2012), The relative contribution of fast and slow sinking particles to ocean carbon export, *Global Biogeochemical Cycles*, *26*(1), doi:10.1029/2011GB004085.

Rintoul, S. R., and C. Wunsch (1991), Mass, heat, oxygen and nutrient fluxes and budgets in the North Atlantic Ocean, *Deep-Sea Research Part I: Oceanographic Research Papers*, *38*, 355–377, doi:10.1016/S0198-0149(12)80017-3.

Ríos, A. F., L. Resplandy, M. I. García-Ibáñez, N. M. Fajar, A. Velo, X. A. Padin, R. Wanninkhof, R. Steinfeldt, G. Rosón, and F. F. Pérez (2015), Decadal acidification in the water masses of the Atlantic Ocean, *Proceedings of the National Academy of Sciences*, *112*(32), 9950–9955, doi:10.1073/pnas.1504613112.

Rivero-Calle, S., C. E. Del Castillo, A. Gnanadesikan, A. Dezfuli, B. Zaitchik, and D. G. Johns (2016), Interdecadal *Trichodesmium* variability in cold North Atlantic waters, *Global Biogeochemical Cycles*, *30*(11), 1620–1638, doi:10.1002/2015GB005361.

Robbins, J. A., and D. N. Edgington (1975), Determination of recent sedimentation rates in Lake Michigan using Pb-210 and Cs-137, *Geochimica et Cosmochimica Acta*, *39*(3), 285–304, doi:10.1016/0016-7037(75)90198-2.

Robbins, J. A. (1978), Geochemical and geophysical applications of radioactive lead isotopes, in *Biochemistry of Lead*, edited by N. J.O., pp. 85–393, Elsevier, Amsterdam.

Robson, J., P. Ortega, and R. Sutton (2016), A reversal of climatic trends in the North Atlantic since 2005, *Nature Geoscience*, *9*(7), 513–517, doi:10.1038/ngeo2727.

Rödenbeck, C., D. C. E. Bakker, N. Metzl, A. Olsen, C. Sabine, N. Cassar, F. Reum, R. F. Keeling, and M. Heimann (2014), Interannual sea–air CO_2 flux variability from an observation-driven ocean mixed-layer scheme, *Biogeosciences*, *11*(17), 4599–4613, doi:10.5194/bg-11-4599-2014.

Rödenbeck, C. et al. (2015), Data-based estimates of the ocean carbon sink variability - First results of the Surface Ocean pCO_2 Mapping intercomparison (SOCOM), *Biogeosciences*, *12*(23), 7251–72, doi: 10.5194/bg-12-7251-2015.

Roessler, A., M. Rhein, D. Kieke, and C. Mertens (2015), Long-term observations of North Atlantic Current transport at the gateway between western and eastern Atlantic, *Journal of Geophysical Research: Ocean.*, *120*(6), 4003–4027, doi:10.1002/2014JC010662.

Romera-Castillo, C., R. T. Letscher, and D. A. Hansell (2016), New nutrients exert fundamental control on dissolved organic carbon accumulation in the surface Atlantic Ocean, *Proceedings of the National Academy of Sciences*, (3), 201605344, doi:10.1073/pnas.1605344113.

Rosengard, S. Z., P. J. Lam, W. M. Balch, M. E. Auro, S. Pike, D. Drapeau, and B. Bowler (2015), Carbon export and transfer to depth across the Southern Ocean Great Calcite Belt, *Biogeosciences*, *12*(13), 3953-3971, doi: 10.5194/bg-12-3953-2015.

Rosón, G., A. F. Ríos, F. F. Pérez, A. Lavín, and H. Bryden (2003), Carbon distribution, fluxes, and budgets in the subtropical North Atlantic Ocean (24.5º N), *Journal of Geophysical Research*, *108*(C5), 3144-3157, doi:10.1029/1999jc000047.

Rossby, T. (1999), On gyre interactions, *Deep-Sea Research Part I: Oceanographic Research Papers*, *46*(1–2), 139–164, doi:10.1016/S0967-0645(98)00095-2.

Rost, B., and U. Riebesell (2004), Coccolithophores and the biological pump: Responses to environmental changes, in *Coccolithophores: From Molecular Processes to Global Impact*, pp. 99–125.

Ruddiman, W. F. (2003), The Anthropogenic Greenhous Era Began Thousands of Years Ago, *Climatic Change*, *61*, 261–293, doi:10.1007/s10584-005-7278-0.

Ruddiman, W. F. (2013), The Anthropocene, *Annual Review of Earth and Planetary Sciences*, *41*(1), 45–68, doi:10.1146/annurev-earth-050212-123944.

Ruttenberg, K. C. (2013), The Global Phosphorus Cycle, in *Treatise on Geochemistry: Second Edition*, vol. 10, pp. 499–558.

Sabine, C. L. et al. (2004), The oceanic sink for anthropogenic CO_2, *Science*, *305*, 367–371, doi:10.1126/science.1097403.

Sambrotto, R. N., G. Savidge, C. Robinson, P. Boyd, T. Takahashi, D. M. Karl, C. Langdon, D. Chipman, J. Marra, and L. Codispoti (1993), Elevated consumption of carbon relative to nitrogen in the surface ocean, *Nature*, *363*(6426), 248–250, doi:10.1038/363248a0.

Sanchez-Cabeza, J. a, P. Masqué, and I. Ani-Ragolta (1998), Lead-210 and polonium-210 analysis in sediments and soils by microwave acid digestion., *Journal of Radioanalytical and Nuclear Chemistry*, *227*(1–2), 19–22, doi:10.1007/BF02386425.

Sanchez-Cabeza, J. A., I. Ani-Ragolta, and P. Masqué (2000), Some considerations of the ^{210}Pb constant rate of supply (CRS) dating model, *Limnology & Oceanography*, *45*(4), 990–995, doi:10.4319/lo.2000.45.4.0990.

Sanchez-Cabeza, J. A., and A. C. Ruiz-Fernández (2012), ^{210}Pb sediment radiochronology: An integrated formulation and classification of dating models, *Geochim. Cosmochim. Acta*, *82*, 183–200, doi:10.1016/j.gca.2010.12.024.

Sanders, R., L. Brown, S. Henson, and M. Lucas (2005), New production in the Irminger Basin during 2002, *Journal of Marine Systems*, *55*(3–4), 291–310, doi:10.1016/j.jmarsys.2004.09.002.

Sanders, R. et al. (2014), The Biological Carbon Pump in the North Atlantic, *Progress in Oceanography*, *129*(PB), 200–218, doi:10.1016/j.pocean.2014.05.005.

Sarafanov, A., A. Falina, A. Sokov, and A. Demidov (2008), Intense warming and salinification of intermediate waters of southern origin in the eastern subpolar North Atlantic in the 1990s to mid-2000s, *Journal of Geophysical Research: Ocean.*, *113*(12), 1–8, doi:10.1029/2008JC004975.

Sarafanov, A., A. Falina, H. Mercier, P. Lherminier, and A. Sokov (2009), Recent changes in the Greenland-Scotland overflow-derived water transport inferred from hydrographic

observations in the southern Irminger Sea, *Geophysical Research Letters*, *36*(13), 1–6, doi:10.1029/2009GL038385.

Sarafanov, A., H. Mercier, A. Falina, A. Sokov, and P. Lherminier (2010), Cessation and partial reversal of deep water freshening in the northern North Atlantic: Observation-based estimates and attribution, *Tellus, Series A: Dynamic Meteorology and Oceanography*, *62*(1), 80–90, doi:10.1111/j.1600-0870.2009.00418.x.

Sarafanov, A., A. Falina, H. Mercier, A. Sokov, P. Lherminier, C. Gourcuff, S. Gladyshev, F. Gaillard, and N. Daniault (2012), Mean full-depth summer circulation and transports at the northern periphery of the Atlantic Ocean in the 2000s, *Journal of Geophysical Research: Ocean.*, *117*(1), doi:10.1029/2011JC007572.

Sarmiento, J. L., P. Monfray, E. Maier-Reimer, O. Aumont, R. J. Murnane, and J. C. Orr (2000), Sea-air CO_2 fluxes and carbon transport: A comparison of three ocean general circulation models, *Global Biogeochemical Cycles*, *14*(4), 1267–1281, doi:10.1029/1999GB900062.

Sarmiento, J. L., and N. Gruber (2006), *Ocean Biogeochemical Dynamics*, Princeton, NJ: Princeton University Press.

Sasse, T. P., B. I. McNeil, and G. Abramowitz (2013), A new constraint on global air-sea CO_2 fluxes using bottle carbon data, *Geophysical Research Letters*, *40*(8), 1594–1599, doi:10.1002/grl.50342.

Schelske, C. L., A. Peplow, M. Brenner, and C. N. Spencer (1994), Low-background gamma counting: applications for ^{210}Pb dating of sediments, *Journal of Paleolimnology*, *10*(2), 115–128, doi:10.1007/BF006825

Schlesinger, W. H., and E. S. Bernhardt (2013), *Biogeochemistry: An Analysis of Global Change, Third Edition*.

Schmitz, W. J., and M. S. McCartney (1993), On the North Atlantic Circulation, *Reviews of Geophysics*, *31*(1), 29–49, doi:10.1029/92RG02583.

Schmitz, W. J. (1996), On the World Ocean Circulation: Volume I Some Global Features/North Atlantic Circulation, *Woods Hole Oceanographic Institution Technical Report WHOI-96-03*, *I*, 148, doi:10.1575/1912/355.

Scholten, J. C., J. Fietzke, S. Vogler, M. M. Rutgers van der Loeff, A. Mangini, W. Koeve, J. Waniek, P. Stoffers, A. Antia, and J. Kuss (2001), Trapping efficiencies of sediment traps from the deep Eastern North Atlantic: The ^{230}Th calibration, *Deep-Sea Research Part I: Oceanographic Research Papers*, *48*(10), 2383–2408, doi:10.1016/S0967-0645(00)00176-4.

Schuster, U. et al. (2013), An assessment of the Atlantic and Arctic sea–air CO_2; fluxes, 1990–2009, *Biogeosciences*, *10*(1), 607–627, doi:10.5194/bg-10-607-2013.

Seibold, E., and W. Berger (2017), *The Sea Floor: An Introduction to Marine Geology*, Springer Textbooks.

Sharp, J. H., C. A. Carlson, E. T. Peltzer, D. M. Castle-Ward, K. B. Savidge, and K. R. Rinker (2002), Final dissolved organic carbon broad community intercalibration and preliminary

use of DOC reference materials, *Marine Chemistry*, *77*(4), 239–253, doi:10.1016/S0304-4203(02)00002-6.

Sharples, J., J. J. Middelburg, K. Fennel, and T. D. Jickells (2017), What proportion of riverine nutrients reaches the open ocean?, *Global Biogeochemical Cycles*, *31*(1), 39–58, doi:10.1002/2016GB005483.

Sholkovitz, E. R., and D. R. Mann (1984), The pore water chemistry of Pu-239,-240 and Cs-137 in sediments of Buzzards Bay, Massachusetts, *Geochimica et Cosmochimica Acta*, *48*(1979), 1107–1114.

Shutler, J. D., P. E. Land, J. F. Piolle, D. K. Woolf, L. Goddijn-Murphy, F. Paul, F. Girard-Ardhuin, B. Chapron, and C. J. Donlon (2016), FluxEngine: A flexible processing system for calculating atmosphere-ocean carbon dioxide gas fluxes and climatologies, *Journal of Atmospheric and Oceanic Technology, 33*(4), 741–756, doi:10.1175/JTECH-D-14-00204.1.

Siegel, D. A., K. O. Buesseler, S. C. Doney, S. F. Sailley, M. J. Behrenfeld, and P. W. Boyd (2014), Global assessment of ocean carbon export by combining satellite observations and food-web models, *Global Biogeochemical Cycles*, *28*(3), 181–196, doi:10.1002/2013GB004743.

Siegenthaler, U., E. Monnin, K. Kawamura, R. Spahni, J. Schwander, B. Stauffer, T. F. Stocker, J. M. Barnola, and H. Fischer (2005), Supporting evidence from the EPICA Dronning Maud Land ice core for atmospheric CO_2 changes during the past millennium, *Tellus*, *57B*(1), 51–57, doi:10.1111/j.1600-0889.2005.00131.x.

Siegert, H., and H. Janssen (1990), Precise determination of gamma-ray peak areas, *Nuclear Installations and Methods in Physics Research, 286*(3), 415–420, doi:10.1016/0168-9002(90)90889-E.

Sigman, D. M., and E. A. Boyle (2000), Glacial/Interglacial Variations in Atmospheric Carbon Dioxide, *Nature*, *407*(6806), 859–869, doi:10.1038/35038000.

Smeed, D. A. et al. (2014), Observed decline of the Atlantic meridional overturning circulation 2004-2012, *Ocean Science*, *10*(1), 29–38, doi:10.5194/os-10-29-2014.

Smeed, D. A., G. D. Mccarthy, D. Rayner, B. I. Moat, W. Johns, M. O. Baringer, and C. S. Meinen (2016), Atlantic meridional overturning circulation observed by the RAPID-MOCHA-WBTS (RAPID-Meridional Overturning Circulation and Heatflux Array-Western Boundary Time Series) array at 26N from 2004 to 2015., British Oceanographic Data Centre - Natural Environment Research Council, UK, doi:10.5285/35784047-9b82-2160-e053-6c86abc0c91b.

Smethie Jr., W. M., and R. a Fine (2001), Rates of North Atlantic Deep Water formation calculated from chlorofluorocarbon inventories, , *Deep-Sea Research Part I: Oceanographic Research Papers*, *48*(2001), 189–215.

Smith, S. V., and J. T. Hollibaugh (1993), Coastal metabolism and the oceanic organic carbon balance, *Reviews of Geophysics*, *31*(1), 75–89, doi:10.1029/92RG02584.

Soetaert, K., P. M. J. Herman, J. J. Middelburg, C. Heip, H. S. DeStigter, T. C. E. van Weering, E. Epping, and W. Helder (1996), Modeling ^{210}Pb-derived mixing activity in ocean margin sediments: Diffusive versus nonlocal mixing, *Journal of Marine Research*, *54*, 1207–1227, doi:10.1357/0022240963213808.

Solomon, S., D. et al. (2007), Summary for Policymakers. In: Climate Change 2007: The Physical Science Basis. Contribution of Working Group I to the Fourth Assessment Report of the Intergovernmental Panel on Climate Change, *New York Cambridge Univ. Press*, 996, doi:10.1038/446727a.

Sommerfield, C. K. (2006), On sediment accumulation rates and stratigraphic completeness: Lessons from Holocene ocean margins, *Continental Shelf Research*, *26*(17–18), 2225–2240, doi:10.1016/j.csr.2006.07.015.

Srokosz, M. a., and H. L. Bryden (2015), Observing the Atlantic Meridional Overturning Circulation yields a decade of inevitable surprises, *Science*, *348*(6241), 1255575–1255575, doi:1 10.1126/science.1255575.

Steffen, W., J. Grinevald, P. Crutzen, and J. McNeill (2011), The Anthropocene: conceptual and historical perspectives, *Philosophical Transactions of the Royal Society*, *369*(1938), 842–867, doi: 10.1098/rsta.2010.0327.

Steffen, W. et al. (2016), Stratigraphic and Earth System approaches to defining the Anthropocene, *Earth's Future*, *4*(8), 324–345, doi:10.1002/2016EF000379.

Steinberg, D. K., B. A. S. Van Mooy, K. O. Buesseler, P. W. Boyd, T. Kobari, and D. M. Karl (2008), Bacterial vs. zooplankton control of sinking particle flux in the ocean's twilight zone, *Limnology & Oceanography*, *53*(4), 1327–1338, doi:10.4319/lo.2008.53.4.1327.

Steinfeldt, R., M. Rhein, J. L. Bullister, and T. Tanhua (2009), Inventory changes in anthropogenic carbon from 1997-2003 in the Atlantic Ocean between 20°S and 65°N, *Global Biogeochemical Cycles*, *23*(3), 1–11, doi:10.1029/2008GB003311.

Stendardo, I., and N. Gruber (2012), Oxygen trends over five decades in the North Atlantic, *Journal of Geophysical Research: Ocean.*, *117*(11), 1–18, doi:10.1029/2012JC007909.

Susan Lozier, M. et al. (2017), Overturning in the Subpolar North Atlantic Program: A New International Ocean Observing System, *Bulletin of the American Meteorological Society*, *98*(4), 737–752, doi:10.1175/BAMS-D-16-0

Sutton, A. J. et al. (2016), Using present-day observations to detect when anthropogenic change forces surface ocean carbonate chemistry outside preindustrial bounds, *Biogeosciences*, *13*(17), 5065-5083, doi: 10.5194/bg-13-5065-2016.

Szmytkiewicz, A., and T. Zalewska (2014), Sediment deposition and accumulation rates determined by sediment trap and ^{210}Pb isotope methods in the outer puck bay (Baltic Sea), *Oceanologia*, *56*(1), 85–106, doi:10.5697/oc.56-1.085.

Tagklis, F., A. Bracco, and T. Ito (2017), Physically driven patchy O_2 changes in the North Atlantic Ocean simulated by the CMIP5 Earth system models, *Global Biogeochemical Cycles*, *31,* 1218-1235, doi:10.1002/2016GB005617.

Takahashi, T., W. S. Broecker, and S. Langer (1985), Redfield ratio based on chemical data from isopycnal surfaces, *Journal of Geophysical Research*, *90*(C4), 6907, doi:10.1029/JC090iC04p06907.

Takahashi, T. et al. (2002), Global sea-air CO_2 flux based on climatological surface ocean pCO_2, and seasonal biological and temperature effects, *Deep-Sea Research Part I: Oceanographic Research Papers*, *49*(9–10), 1601-1622, doi: 10.1016/S0967-0645(02)00003-6.

Takahashi, T. et al. (2009), Climatological mean and decadal change in surface ocean pCO_2, and net sea-air CO_2 flux over the global oceans, *Deep-Sea Research Part I: Oceanographic Research Papers*, *56*(8–10), 554-577, doi: 10.1016/j.dsr2.2008.12.009.

Talley, L. D. (2013), Closure of the global overturning circulation through the Indian, Pacific and Southern Oceans: schematics and transports, *Oceanography*, *26*, doi:http://dx.doi.org/10.5670/o

Tanhua, T., and R. F. Keeling (2012), Changes in column inventories of carbon and oxygen in the Atlantic Ocean, *Biogeosciences*, *9*(11), 4819–4833, doi:10.5194/bg-9-4819-2012.

Thierry, V., E. de Boisséon, and H. Mercier (2008), Interannual variability of the Subpolar Mode Water properties over the Reykjanes Ridge during 1990-2006, *Journal of Geophysical Research: Ocean.*, *113*(4), 1–14, doi: 10.1029/2007JC004443.

Thomson, J., S. Colley, R. Anderson, G. T. Cook, and A. B. MacKenzie (1993), ^{210}Pb in the sediments and water column of the Northeast Atlantic from 47 to 59ºN along 20ºW, *Earth and Planetary Science Letters*, *115*(1–4), 75–87, doi:10.1016/0012-821X(93)90214-T.

Tian, R. C., D. Deibel, R. B. Rivkin, and A. F. Vézina (2004), Biogenic carbon and nitrogen export in a deep-convection region: Simulations in the Labrador Sea, *Deep-Sea Research Part I: Oceanographic Research Papers*, *51*(3), 413–437, doi:10.1016/j.dsr.2003.10.015.

Tomczak, M. (1981), A multi-parameter extension of temperature/salinity diagram techniques for the analysis of non-isopycnal mixing, *Progress in Oceanography*, *10*(3), 147–171, doi:10.1016/0079-6611(81)90010-0.

Tomczak, M., and D. G. B. Large (1989), Optimum multiparameter analysis of mixing in the thermocline of the eastern Indian Ocean, *Journal of Geophysical Research*, *94*(C11), 16141, doi:10.1029/JC094iC11p16141.

Tomczak, M. (1999), Some historical, theoretical and applied aspects of quantitative water mass analysis, *Journal of Marine Research*, *57*(2), 275–303, doi:10.1357/002224099321618227.

Torres-Valdés, S., T. Tsubouchi, S. Bacon, A. C. Naveira-Garabato, R. Sanders, F. A. McLaughlin, B. Petrie, G. Kattner, K. Azetsu-Scott, and T. E. Whitledge (2013), Export of nutrients from the Arctic Ocean, *Journal of Geophysical Research: Ocean.*, *118*(4), 1625–1644, doi:10.1002/jgrc.20063.

Torres-Valdés, S., S. C. Painter, A. P. Martin, R. Sanders, and J. Felden (2014), Data compilation of fluxes of sedimenting material from sediment traps in the Atlantic ocean, *Earth System Science Data*, *6*(1), 123–145, doi:10.5194/essd-6-123-2014.

Torres-Valdés, S., T. Tsubouchi, E. Davey, I. Yashayaev, and S. Bacon (2016), Relevance of dissolved organic nutrients for the Arctic Ocean nutrient budget, *Geophysical Research Letters*, *43*(12), 6418–6426, doi:10.1002/2016GL069245.

Tréguer, P., D. M. Nelson, A. J. Van Bennekom, D. J. DeMaster, A. Leynaert, and B. Queguiner (1995), The Silica Balance in the World Ocean: A Reestimate, *Science*, *268*(5209), 375–379, doi:10.1126/science.268.5209.375.

Tréguer, P. J., and C. L. De La Rocha (2013), The World Ocean Silica Cycle, *Annual Review of Marine Science*, *5*(1), 477–501, doi:10.1146/annurev-marine-121211-172346.

Turner, J. T. (2015), Zooplankton fecal pellets, marine snow, phytodetritus and the ocean's biological pump, *Progress in Oceanography*, *130*, 205–248, doi:10.1016/j.pocean.2014.08.005.

Tyrrell, T. (1999), The relative influence of nitrogen and phosphorus on oceanic primary production, *Nature*, *400*, 525–531, doi:10.1038/22941.

Tyrrell, T., and R. E. Zeebe (2004), History of carbonate ion concentration over the last 100 million years, *Geochimica et Cosmochimica Acta*, *68*(17), 3521–3530, doi:10.1016/j.gca.2004.02.018.

Tziperman, E., and H. Gildor (2003), On the mid-Pleistocene transition to 100-kyr glacial cycles and the asymmetry between glaciation and deglaciation times, *Paleoceanography*, *18*(1), 1-1-1–8, doi: 10.1029/2001pa000627.

Våge, K., R. S. Pickart, A. Sarafanov, Ø. Knutsen, H. Mercier, P. Lherminier, H. M. van Aken, J. Meincke, D. Quadfasel, and S. Bacon (2011), The Irminger Gyre: Circulation, convection, and interannual variability, *Deep-Sea Research Part I: Oceanographic Research Papers*, *58*(5), 590–614, doi:10.1016/j.dsr.2011.03.001.

Vajda, N., J. LaRosa, R. Zeisler, P. Danesi, and G. Kis-Benedek (1997), A novel technique for the simultaneous determination of ^{210}Pb and ^{210}Po using a crown ether, *Journal of Environmental Radioactivity*, *37*(3), 355–372, doi:10.1016/S0265-931X(95)00059-J.

Valsala, V., and S. Maksyutov (2010), Simulation and assimilation of global ocean pCO_2 and air-sea CO_2 fluxes using ship observations of surface ocean pCO_2 in a simplified biogeochemical offline model, *Tellus, Series B: Chemical and Physical Meteorology*, *62*(5), 821–840, doi:10.1111/j.1600-0889.2010.00495.x.

Van Aken, H. M. (2000), The hydrography of the mid-latitude northeast Atlantic Ocean: I: The deep water masses. *Deep-Sea Research Part I: Oceanographic Research Papers*, *47,* 757-788, doi: 10.1016/S0967-0637(99)00092-8.

Vázquez-Rodríguez, M., F. F. Pérez, A. Velo, A. F. Ríos, and H. Mercier (2012), Observed acidification trends in North Atlantic water masses, *Biogeosciences*, *9*(12), 5217–5230, doi:10.5194/bg-9-5217-2012.

Villa-Alfageme, M., F. De Soto, F. A. C. Le Moigne, S. L. C. Giering, R. Sanders, and R. García-Tenorio (2014), Observations and modeling of slow-sinking particles in the twilight zone, *Global Biogeochemical Cycles*, *28*(11), 1327–1342, doi:10.1002/2014GB004981.

Villa-Alfageme, M., F. C. de Soto, E. Ceballos, S. L. C. Giering, F. A. C. Le Moigne, S. Henson, J. L. Mas, and R. J. Sanders (2016), Geographical, seasonal, and depth variation in sinking particle speeds in the North Atlantic, *Geophysical Resarch Letters.*, *43*(16), 8609–8616, doi:10.1002/2016GL069233.

Visbeck, M., E. P. Chassignet, R. G. Curry, T. L. Delworth, R. R. Dickson, and G. Krahmann (2003), The ocean's response to North Atlantic Oscillation variability, *Geophysical Monograph Series*, *134*, 113–145, doi:10.1029/134GM06.

Vladimir I. Vernadsky (1926), *The Biosphere*, 1998th Edition, edited by M. A. S. McMenamin, Copernicus.

Volk, T., and M. I. Hoffert (1985), Ocean carbon pumps: Analysis of relative strength and efficiencies in ocean-driven atmospheric CO_2 changes, *Geophysical Monograph Series*, *32*, 99–110, doi:10.1029/GM032p0099.

Walker, M. (2005), *Quaternary dating methods*, edited by John Wiley & Sons Ltd.

Walsh, J. J., K. L. Carder, and F. E. Müller-Karger (1992), Meridional fluxes of dissolved organic matter in the north Atlantic Ocean, *Journal of Geophysical Research*, *97*(C10), 15625, doi:10.1029/92JC01177.

Waniek, J. J., N. P. Holliday, R. Davidson, L. Brown, and S. A. Henson (2005), Freshwater control of onset and species composition of Greenland shelf spring bloom, *Marine Ecology Progress Series*, *288*, 45–57, doi:10.3354/meps288045.

Wassmann, P. (1998), Retention versus export food chains: Processes controlling sinking loss from marine pelagic systems, *Hydrobiologia*, 363,. 29–57, doi: 10.1023/A:1003113403096.

Waters, C. N. et al. (2016), The Anthropocene is functionally and stratigraphically distinct from the Holocene, *Science, 351*(6269), aad2622, doi:10.1126/science.aad2622.

Waters, C. N., J. A. Zalasiewicz, M. Williams, M. A. Ellis, and A. M. Snelling (2014), A stratigraphical basis for the Anthropocene?, *Geological Society, London, Special Publications*, *395*(1), 1–21, doi:10.1144/SP395.18.

Willey, J. D., R. J. Kieber, M. S. Eyman, and B. G. Avery (2000), Rainwater dissolved organic carbon: Concentrations and global flux, *Global Biogeochemical Cycles*, *14*, 139–148, doi:10.1029/1999GB900036.

Williams, M. et al. (2016), The Anthropocene: A conspicuous stratigraphical signal of anthropogenic changes in production and consumption across the biosphere, *Earth's Future*, *4*(3), 34–53, doi: 10.1002/2015EF000339.

Willis, J. K. (2010), Can in situ floats and satellite altimeters detect long-term changes in Atlantic Ocean overturning?, *Geophysical Research Letters*, *37*(6), n/a-n/a, doi:10.1029/2010GL042372.

Wolf-Gladrow, D. A., R. E. Zeebe, C. Klaas, A. Körtzinger, and A. G. Dickson (2007), Total alkalinity: The explicit conservative expression and its application to biogeochemical processes, *Marine Chemistry*, *106*(1–2 SPEC. ISS.), 287–300, doi:10.1016/j.marchem.2007.01.006.

Woosley, R. J., F. J. Millero, and R. Wanninkhof (2016), Rapid anthropogenic changes in CO_2 and pH in the Atlantic Ocean: 2003-2014, *Global Biogeochemical Cycles*, *30*(1), 70–90, doi:10.1002/2015GB0

Wunsch, C. (2002), What is the thermohaline circulation?, *Science*, *298*(November), 1179–81, doi:10.1126/science.1079329.

Yang, S., and N. Gruber (2016), The anthropogenic perturbation of the marine nitrogen cycle by atmospheric deposition: Nitrogen cycle feedbacks and the ^{15}N Haber-Bosch effect, *Global Biogeochemical Cycles*, *30*(10), 1418–1440, doi:10.1002/2016GB005421.

Yashayaev, I. (2007), Hydrographic changes in the Labrador Sea, 1960-2005, *Progress in Oceanography*, *73*(3–4), 242–276, doi:10.1016/j.pocean.2007.04.015.

Yashayaev, I., and B. Dickson (2008), Transformation and Fate of Overflows in the Northern North Atlantic, in *Arctic–Subarctic Ocean Fluxes*, edited by and P. R. R. R. Dickson, J. Meincke, pp. 505–526, Springer Netherlands.

Yashayaev, I., and J. W. Loder (2016), Recurrent replenishment of Labrador Sea Water and associated decadal-scale variability, *Journal of Geophysical Research: Ocean.*, *121*(11), 8095–8114, doi:10.1002/2016JC012046.

Yashayaev, I., and J. W. Loder (2017), Further intensification of deep convection in the Labrador Sea in 2016, *Geophysical Research Letters*, *44*(3), 1429–1438, doi:10.1002/2016GL071668.

Zaborska, A., J. L. Carroll, C. Papucci, and J. Pempkowiak (2007), Intercomparison of alpha and gamma spectrometry techniques used in ^{210}Pb geochronology, *Journal of Environmental Radioactivity*, *93*(1), 38–50, doi: 10.1016/j.jenvrad.2006.11.007.

Zaborska, A., J. Carroll, C. Papucci, L. Torricelli, M. L. Carroll, J. Walkusz-Miotk, and J. Pempkowiak (2008), Recent sediment accumulation rates for the Western margin of the Barents Sea, *Deep Sea Research Part II: Topical Studies in Oceanography*, *55*(20–21), 2352–2360, doi:10.1016/j.dsr2.2008.05.026.

Zachos, J. C. et al. (2005), Paleoclimate: Rapid acidification of the ocean during the paleocene-eocene thermal maximum, *Science*, *308*(5728), 1611–1615, doi:10.1126/science.1109004.

Zalasiewicz, J. et al. (2015), When did the Anthropocene begin? A mid-twentieth century boundary level is stratigraphically optimal, *Quaternary International*, *383*, 196–203, doi:10.1016/j.quaint.2014.11.045.

Zalasiewicz, J. et al. (2017), The Working Group on the Anthropocene: Summary of evidence and interim recommendations, *Anthropocene*, *19*, 55–60, doi:10.1016/j.ancene.2017.09.001.

Zalewska, T., J. Woroń, B. Danowska, and M. Suplińska (2015), Temporal changes in Hg, Pb, Cd and Zn environmental concentrations in the southern Baltic Sea sediments dated with 210Pb method, *Oceanologia*, *57*(1), 32–43, doi:10.1016/j.oceano.2014.06.003.

Zeebe, R. E., J. C. Zachos, K. Caldeira, and T. Tyrrell (2008), Oceans: Carbon emissions and acidification, *Science*, *321*(5885), 51–52, doi:10.1126/science.1159124.

Zeebe, R. E. (2012), History of Seawater Carbonate Chemistry, Atmospheric CO_2, and Ocean Acidification, *Annual Review of Earth and Planetary Sciences, 40*(1), 141–165, doi:10.1146/annurev-earth-042711-105521.

Zehr, J. P., and R. M. Kudela (2011), Nitrogen Cycle of the Open Ocean: From Genes to Ecosystems, *Annual Review of Marine Science*, *3*(1), 197–225, doi:10.1146/annurev-marine-120709-142819.

Zeng, J., Y. Nojiri, P. Landschützer, M. Telszewski, and S. Nakaoka (2014), A global surface ocean fCO_2 climatology based on a feed-forward neural network, *Journal of Atmospheric and Oceanic Technology*, *31*(8), 1838–1849, doi:10.1175/JTECH-D-13-00137.1.

Zhang, R. (2010), Latitudinal dependence of Atlantic meridional overturning circulation (AMOC) variations, *Geophysical Research Letters*, *37*(16), doi:10.1029/2010GL044474.

Zunino, P., M. I. Garcia-Ibañez, P. Lherminier, H. Mercier, A. F. Ríos, and F. F. Pérez (2014), Variability of the transport of anthropogenic CO_2 at the Greenland-Portugal OVIDE section: Controlling mechanisms, *Biogeosciences*, *11*, 2375–2389, doi:10.5194/bg-11-2375-2014.

Zunino, P., P. Lherminier, H. Mercier, X. A. Padín, A. F. Ríos, and F. F. Pérez (2015), Dissolved inorganic carbon budgets in the eastern subpolar North Atlantic in the 2000s from in situ data, *Geophysical Research Letters*, 1–9, doi:10.1002/2015GL066243.Received.

Zunino, P., P. Lherminier, H. Mercier, N. Daniault, M. I. García-ibáñez, and F. F. Pérez (2017), The GEOVIDE cruise in May–June 2014 reveals an intense Meridional Overturning Circulation over a cold and fresh subpolar North Atlantic, *Biogeosciences*, *14*, 5323–5342, doi:https://doi.org/10.5194/bg-14-5323-2017.

Appendix

Appendix I. Acronyms, abbreviations and symbols

θ: Potential temperature.

σ_i: Potential density referenced to (*i)* dbar.

σ_{MOC}: Potential density that constitutes the limit between the upper and lower limbs of the Meridional Overturning Circulation.

ρ: In situ density.

ε: In Part II, the DOC measurement error.

λ: The disintegration constant of an isotope, the probability that a nuclei of a radionuclide will decay per unit of time.

$^{210}Pb_{excess}$: The difference between the total ^{210}Pb measured and the $^{210}Pb_{supported}$.

$^{210}Pb_{supported}$: The fraction of ^{210}Pb that comes from the radioactive decay of ^{226}Ra.

A: The inventory of $^{210}Pb_{excess}$ in a core.

Ac: Chemical symbol of actinium.

AT: Total alkalinity.

At: Chemical symbol of astatine.

AABW: Antarctic Bottom Water.

ADCP: Acoustic Doppler Current Profiler.

AIW: Arctic Intermediate Water.

Am: Chemical symbol of anthropogenic radionuclide americium. Their isotope ^{241}Am appears in the Part IV.

$A_{missing}$: Missing inventory of $^{210}Pb_{excess}$ in a core.

AMOC: Atlantic Meridional Overturning Circulation.

AOU: Apparent Oxygen Utilization.

ASH: Aragonite Saturation Horizon.

Bi: Chemical symbol of bismuth.

B_{DIC}: In Part III, represents the change in the pool of DIC by unit of time.

B_{DICorg}: Represents the change in the pool of DIC mediated by organic carbon production by unit of time. It is one of the biogeochemical unknowns optimized inside the inverse model of Part III.

B_{CaCO3}: In Part III, represents the change in the pool of calcium carbonate by unit of time. It is one of the biogeochemical unknowns optimized inside the inverse model of Part III.

BOCATS: Biennial Observation of Carbon, Acidification, Transport and Sedimentation in the North Atlantic.

C_{ant}: Anthropogenic carbon dioxide.

CE: Current Era

C_{org}: Organic carbon.

C_t: Total dissolved carbon.

$CaCO_3$: Calcium carbonate.

CCHDO: CLIVAR & Carbon Hydrographic Data Office.

CGFZ: Charlie-Gibbs Fracture Zone.

CH_4: Methane.

CLIVAR: Climate and Ocean: Variability, Predictability, and Change.

CO_2: Carbon dioxide.

CO_3^{2-}: Carbonate ion.

CRM: Certified Reference Material.

Cs: Chemical symbol of anthropogenic radionuclide cesium. Their isotope ^{137}Cs appears in the Part IV.

CF:CS: Constant Flux Constant Sedimentation, a type of dating model based on ^{210}Pb decay.

CIC/CA: Constant Initital Concentration/Constant Activity, a type of dating model based on ^{210}Pb decay.

CRS: Constant Rate of Supply, a type of dating model based on ^{210}Pb decay.

CTD: Conductivity–Temperature–Depth.

DDEP: Data Decay Evaluation Project. http://www.nucleide.org/DDEP.htm

DIC: Dissolved inorganic carbon.

DOC: Dissolved organic carbon.

DSOW: Denmark Strait Overflow Water.

DWBC: Deep Western Boundary Current.

E_{Corg}: Net exportation of organic carbon.

E_{CaCO3}: Net exportation of carbonates. In Part III it is assumed that all the exportation of inorganic carbon corresponds exclusively to calcium carbonate, then $E_{CaCO3} = E_{Cinorg}$.

EGC: East Greenland Current.

ENA: East North Atlantic.

ENACW: East North Atlantic Central Water, subpolar (ENACWP) and subtropical (ENACWT) varieties.

ERRC: East Reykjanes Ridge Current.

ESM: Eriador Seamount.

eSPNA: Eastern Subpolar North Atlantic, the region defined in this work as the marine area at north of the OVIDE section and at south of the Greenland-Iceland-Scotland sills.

EPICA: European Project for Ice Coring in Antarctica

Fe: Chemical symbol of iron.

$F^{O2\ air\text{-}sea}$: Represents the flux of oxygen in the air-sea interface by unit of time. It is one of the biogeochemical unknowns optimized inside the inverse model of Part III.

Galea: Gamma Line Expert Analyser

GEOVIDE: The 2014 OVIDE cruise, that belongs to the international GEOTRACES study of the marine biogeochemical cycles of trace elements and their isotopes that took place along the OVIDE section in the North Atlantic and in the Labrador Sea.

GLODAP: Global Data Analysis Project.

GOSHIP: Global Ocean Ship-based Hydrographic Investigations Project.

G-I-S sills: Greenland–Iceland–Scotland sills.

H^+: Hydrogen ions.

HCO_3^-: Bicarbonate ion.

H_2CO_3: Carbonic acid.

Hg: Chemical symbol of mercury.

HPGE: Hyper-pure germanium, the material of the detectors used in Part IV.

IAEA: International Atomic Energy Agency.

IAP: Iberian Abyssal Plain.

ICE: In Part IV, it references the sediment core located at the Iceland Basin

IcSPMW: Subpolar Mode Water formed in the Iceland Basin.

IRM: In Part IV, it references the sediment core located at the Irminger Basin

IrSPMW: Subpolar Mode Water formed in the Irminger Basin.

IPCC: Intergovernmental Panel on Climate Change.

ISOW: Iceland–Scotland Overflow Water.

J: Joule, unit of energy in the International System of Units.

K: Chemical symbol of potassium.

k_0: Solubility constant of carbon dioxide.

k_1: First equilibrium constant of dissociation of carbonic acid.

k_2: Second equilibrium constant of dissociation of carbonic acid.

keV: Kiloelectronvolt

kyr: Kiloyears, thousand years.

LADCP: Lowered Acoustic Doppler Current Profilers.

LDW: Lower Deep Water.

LNHB: Laboratoire National Henri Becquerel.

LRI: Laboratorio de radiaciones ionizantes, name of the Department of University of Salamanca where gamma-meaurements where done.

LSW: Labrador Sea Water, classical (cLSW) and upper (uLSW) varieties.

MAR: Mid-Atlantic Ridge.

MOC: Meridional Overturning Circulation.

MOCσ: Meridional Overturning Circulation computed in density coordinates.

MW: Mediterranean Water.

NH_4^+: Amonium.

NAC: North Atlantic Current.

NACW: North Atlantic Central Water.

NADW: North Atlantic Deep Water.

NAO: North Atlantic Oscillation.

NEADW: North East Atlantic Deep Water, upper ($NEADW_U$) and lower ($NEADW_L$) varieties.

NO_3: Nitrate.

O_2: Oxygen.

O_3: Ozone.

OMP: Optimum MultiParameter (analysis), classical (cOMP) and extended (eOMP).

OVIDE: Observatoire de la Variabilité Interannuelle et Décennale en Atlantique Nord.

Pa: Chemical symbol of protactinium.

PANGAEA: Open Access library aimed at archiving, publishing and distributing georeferenced data from earth system reseach (www.pangaea.de).

Pb: Chemical symbol of lead. The natural radionuclide ^{210}Pb is the central element of the dating technique applied in the Part IV.

PETM: Paleocene-Eocene Thermal Maximum.

pH: Potential of hydrogen, $-\log_{10}[H^+]$.

pCO_2: Partial pressure of CO_2.

pCO_2^{atm}: Partial pressure of CO_2 in the atmosphere.

pCO_2^{sw}: Partial pressure of CO_2 in seawater.

Pg-C: Petagrams (10^{15} g) of carbon.

PIW: Polar Intermediate Water.

PlankTOM: Plankton Type Ocean Model, a global marine biogeochemistry model that represents lower-trophic marine ecosystems based on plankton functional types.

Po: Chemical symbol of polonium.

PO_4: Phosphate.

ppm: Parts per million.

r^2: Correlation coefficient.

QuikSCAT: From Quick Scatterometer, is an Earth observation satellite carrying the SeaWinds scatterometer. Its mission is to measure the surface wind speed and direction over the ice-free global ocean.

Ra: Chemical symbol of radium.

RAPID: A monitoring program of the Atlantic Meridional Overturning Circulation at 26.5ºN since 2004 through a set of mooring arrays (http://rapid.ac.uk).

Rn: Chemical symbol of radon.

RCP: Representative Concentration Pathway

RR: Reykjanes Ridge

S: Salinity.

s: Sediment accumulation rates.

SEANOE: Sea scientific open data edition (http://www.seanoe.org).

SADCP: Shipboard Acoustic Doppler Current Profilers.

SAIW: Subarctic Intermediate Water.

SDR: Standard deviation of the residuals.

SiO_4: Silicate.

SOCOM: Surface Ocean pCO_2 Mapping intercomparison. http://www.bgc-jena.mpg.de/SOCOM/

SPMW: Subpolar Mode Water, of 7ºC ($SPMW_7$) and 8ºC ($SPMW_8$) varieties.

SPNA: Subpolar North Atlantic.

std: Standard deviation.

Sv: Sverdrup (1 Sv = 10^6 $m^3 \cdot s^{-1}$).

SWT: Source Water Type.

Tg-C: Teragrams (10^{12} g) of carbon.

Th: Chemical symbol of thorium.

Ti: Chemical symbol of titanium.

Tl: Chemical symbol of thallium.

U: Chemical symbol of uranium.

v: Transoceanic section orthogonal velocity.

WEB: Western European Basin.

WNACW: West North Atlantic Central Water.

WOCE: World Ocean Circulation Experiment.

X_i: Fraction of a source water type in a water sample.

XRF Core scanner: X-ray reflectance core scanner

yr: Year.

Appendix II: List of figures

Appendix III: List of tables

Appendix IV: Resumen en castellano

La emisión a la atmósfera de gases de efecto invernadero, especialmente CO_2, debido a las actividades antropogénicas, es el principal agente del cambio climático [*IPCC,* 2014]. El océano tiene un papel crucial en el sistema climático terrestre: modera el efecto invernadero por su capacidad para absorber CO_2, y contribuye al transporte y distribución de calor desde el ecuador a los polos por su circulación a gran escala. A día de hoy, el océano ha captado entre un 25-30% del carbono antropogénico (C_{ant}) [*Sabine et al.,* 2004*; Khatiwala et al.,* 2013], alterando significativamente la química oceánica en un conjunto de cambios conocidos colectivamente bajo la expresión "acidificación oceánica" [*Caldeira & Wickett,* 2003*; Raven et al.,* 2005*; Doney et al.,* 2009].

El carbono es la molécula central de la química orgánica, y por tanto, de la vida en la Tierra. Como base fundamental de cualquier tejido vivo, el carbono está estrechamente interrelacionado con el resto de elementos químicos indispensables para la vida: oxígeno, nitrógeno, fósforo… La comprensión y cuantificación de los flujos de los elementos químicos entre los seres vivos y el ambiente se describe en términos de ciclos biogeoquímicos [*Vernadsky,* 1926]. Entender los ciclos biogeoquímicos de nutrientes es necesario para predecir los efectos actuales y futuros que los cambios naturales y/o antropogénicos puedan provocar en la productividad marina [*Benitez-Nelson,* 2000]. El actual exceso de carbono en el océano que provoca la acidificación oceánica, ¿ha alterado también los principales ciclos biogeoquímicos marinos? ¿Está alterado el ciclo biológico del carbono? Esta es la hipótesis de trabajo desarrollada a lo largo de esta tesis.

Con la intención de evaluar el estado actual del ciclo del carbono en el Atlántico Norte, es necesario conocer el conjunto de procesos físicos y biológicos que determinan su distribución vertical en la columna de agua (bombas de carbono). Comenzando por los fenómenos de captación, el intercambio neto de CO_2 entre el océano y la atmósfera es debido a diferencias en la presión parcial del CO_2 en la interfase océano-atmósfera [*Takahashi et al.,* 2009]. Este intercambio obedece a la Ley de Henry [*Henry,* 1803], de tal forma que las aguas más frías presentan mayor solubilidad para los gases y por lo tanto mayores concentraciones de CO_2 (bomba de solubilidad). Una mayor captación de CO_2 genera alteraciones en el sistema del carbonato en agua de mar, provocando una disminución del pH a la vez que una atenuación en la capacidad de absorción de CO_2. El progresivo incremento en C_{ant} está provocando un cambio en el equilibrio ácido-base del sistema del carbono hacia condiciones más acidificantes. Desde el inicio de la Revolución Industrial, el pH superficial del océano ha descendido en 0.1

unidades de pH, y se predice que para el año 2100 la disminución en el medio marino será de alrededor de 0.3 unidades de pH [*Caldeira & Wickett,* 2003*; Ciais et al.,* 2013].

Los fenómenos físicos representados por la circulación oceánica también tienen un papel fundamental en la distribución de trazadores biogeoquímicos en medio marino. En la circulación del Atlántico Norte, las corrientes cálidas pierden progresivamente calor hacia la atmósfera a medida que se dirigen hacia latitudes altas, enfriándose y ganando densidad hasta que llegan a hundirse, formando masas de agua profundas que regresan hacia el sur en profundidad. Este fenómeno circulatorio, conocido como recirculación meridional (MOC), favorece la acumulación de C_{ant} en el Atlántico [*Pérez et al.,* 2013], y lo convierten en el océano que acumula las mayores concentraciones de C_{ant} en relación a su superficie y el único en el que la señal antropogénica es detectable, incluso en las masas de agua más profundas [*Sabine et al.,* 2004*; Khatiwala et al.,* 2013*; Vázquez-Rodriguez et al.,* 2012*; García-Ibañez et al.,* 2016].

A una escala temporal decenal, la variabilidad en la circulación del MOC muestra correlación con la variación en el índice de Oscilación del Atlántico Norte (NAO) –la diferencia en presión atmosférica superficial entre los centros de altas presiones de Azores y las bajas de Islandia-. Está demostrado que la NAO guarda relación con la actividad convectiva que propicia la formación de masas de agua saturadas de CO_2 en el Atlántico Norte [*Schüster & Watson,* 2007*; Pérez et al.,* 2008]. A principios de los 90, una serie de fases NAO positivas generaron fenómenos de convección excepcionalmente altos, provocando capas de mezcla por debajo de los 2000 m [*Yashayaev*, 2007] y las mayores tasas de almacenaje de C_{ant} [*Pérez et al.,* 2010*; Vázquez-Rodríguez et al.,* 2012]. Recientemente, en los inviernos de 2014 a 2016, fases NAO extremadamente altas han coincidido con fenómenos de convección profunda en el giro subpolar del Atlántico Norte [*de Jong & de Steur,* 2016*; Fröb et al.,* 2016*; Piron et al.,* 2017], introduciendo gran cantidad de aguas recientemente ventiladas y con elevadas concentraciones de oxígeno y de C_{ant} en el océano profundo [*Fröb et al.,* 2016*; Pérez et al.,* 2018]. La circulación y la mezcla oceánica transportan hacia el interior del océano las masas de agua superficial saturadas con gases tanto de origen natural (CO_2 y O_2) como de origen antropogénico (CFCs o C_{ant}). Estos procesos físicos en su conjunto se conocen como la bomba física.

En el ciclo del carbono natural actúan otros componentes, como la bomba biológica de carbono. Los productores primarios marinos convierten carbono inorgánico disuelto (DIC) en carbono orgánico particulado (POC). La fijación de carbono en material biogénico y su posterior exportación desde la capa fótica al océano profundo representa la bomba biológica [*Broecker & Peng,* 1982]. El transporte vertical de POC disminuye con la profundidad a medida que la materia orgánica es respirada (remineralizada) de nuevo a DIC o transformada en carbono orgánico disuelto (DOC), y la eficiencia de la bomba biológica puede ser evaluada como la fracción del flujo que llega hasta una profundidad dada [*Torres-Valdés et al.,* 2014]. La cuantificación de la magnitud de CO_2 atmosférico secuestrado por la bomba biológica de carbono es un conocimiento clave para una adecuada evaluación del balance de carbono

oceánico [*Falkowski et al.,* 1998*; Sabine et al.,* 2004*, Körtzinger et al.,* 2001]. Si la bomba biológica no existiera, las concentraciones atmosféricas actuales de CO_2 serían hasta un 50% más altas (más de 600 ppm) [*Parekh et al.,* 2006]. La producción marina neta, la máxima cantidad de carbono fijada fotosintéticamente disponible para ser exportada, es de ~50 Pg-C·año^{-1} a escala global [*Longhurst et al.,* 1995*; Behrenfeld and Falkowski,* 1997*; Falkowski et al.,* 1998], con un valor de alrededor de ~13 Pg-C·año^{-1} para el Océano Atlántico [*Carr et al.,* 2006]. Sólo una fracción del carbono orgánico es exportado de la zona fótica. Estimaciones actuales con diferentes técnicas oscilan alrededor de un valor global de ~10-12 Pg-C·año^{-1} [*Falkowski et al.,* 1998*; Henson et al.,* 2015*; Laws et al.,* 2000*; Sambrotto et al.,* 1993], con una magnitud cercana a 1.5 Pg-C·año^{-1} teniendo lugar en el Atlántico Norte [*Dunne et al.,* 2007*; Laws et al.,* 2000*; Sanders et al.,* 2014]. Una gran parte del material exportado de la capa fótica va a ser respirado en el océano profundo [*del Giorgio and Duarte,* 2002*; Arístegui et al.,* 2003], y a 2000 m de profundidad el flujo vertical global es de tan solo ~0.3-0.7 Pg-C·año^{-1} [*Guidi et al.,* 2015*; Henson et al.,* 2012a*; Honjo et al.,* 2008*; Lutz et al.,* 2007]. Considerando un área de 41.5 x 10^6 km^2 [*Eakins & Sharman,* 2010], y un flujo vertical medio a 2000 m de ~1.5-2 g-C·m^2·año^{-1} [*Honjo et al.,* 2008, *Henson et al.,* 2012a], una primera aproximación de la magnitud para el Atlántico Norte sería entre ~62-83 Tg-C·año^{-1}. La magnitud de la bomba biológica no es la misma en todas las zonas del océano [*Honjo et al.,* 2008], y los datos de exportación de partículas al océano profundo indican que el giro subpolar del Atlántico Norte se caracteriza por un importante flujo de carbono orgánico particulado que es a menudo más del doble que la media global [*Jickells et al.,* 1996*; Kuss & Kremling,* 1999*; Scholten et al.,* 2001*; Antia et al.,* 2001]. Dentro de la heterogeneidad global, y a modo de generalización, puede decirse que menos de un 3% de la producción primaria neta llega a profundidades mayores de 1000 metros [*de la Rocha & Passow,* 2007] y ni siquiera un 1% del CO_2 fijado por fotosíntesis en la capa fótica llega a ser sedimentado en el océano profundo constituyendo un sumidero de carbono a largo plazo [*Martin et al.,* 1987*; Ducklow et al.,* 2001; *Poulton et al.,* 2006*; Lampitt et al.,* 2010*; Legendre et al.,* 2015*;*]. En el Atlántico Norte, para una producción primaria media de ~200-250 g-C·m^2·año^1 [*Henson et al.,* 2012a], el porcentaje exportado supondría un 0.7-0.9%, es decir, en el rango esperado.

Los sucesivos ciclos de síntesis y mineralización de la materia orgánica producen un conjunto de sustancias orgánicas en fase disuelta que constituye un reservorio o *pool* de materia orgánica disuelta que también puede ser acumulado en la zona fótica y exportado hacia el océano interior por la circulación oceánica [*Hansell et al.,* 2009], donde los procesos de remineralización bacteriana convierten el DOC en carbono inorgánico [*Ducklow et al.,* 2001]. La exportación de DOC desde el giro subpolar resulta de interés por ser un componente esencial en la bomba biológica – con una contribución que puede llegar a suponer hasta el 20% del total [*Hansell et al.,* 2002]- y es un proceso que se ve afectado por los forzamientos físicos que ocurren en la región subpolar [*Carlson et al.,* 2010].

Aunque el carbono es el elemento central de la tesis, el transporte y balance de nutrientes y oxígeno en el Atlántico Norte también será evaluado. La distribución de nutrientes y oxígeno en

el océano está controlada por la interacción de procesos físicos y biológicos. Los procesos biológicos median la transformación de los nutrientes entre formas inorgánicas y formas orgánicas. Los procesos físicos redistribuyen los trazadores biogeoquímicos en la columna de agua a través de transporte y mezcla vertical. La combinación de los procesos físicos y biológicos se refleja en las distribuciones del oxígeno, y los macronutrientes nitrato, fosfato y silicato. Para los macronutrientes, la distribución oceánica refleja el balance entre el déficit en la capa fótica por el consumo de nutrientes que pasan desde forma inorgánica disuelta a forma orgánica en los procesos de generación de materia orgánica; y el incremento de los nutrientes en profundidad debido a remineralización/respiración, es decir, el paso contrario desde forma orgánica a forma inorgánica. Para el oxígeno, la distribución también está alterada con respecto a la fotosíntesis/remineralización, pero con signo contrario: producción de oxígeno en capas superficiales y consumo por respiración en profundidad. Además, y a diferencia de los nutrientes, el balance oceánico de oxígeno se ve afectado por el importante proceso físico del flujo en la interfase océano-atmósfera [*Ganachaud & Wunsch,* 2002]. Asumiendo que la distribución a escala de cuenca de los trazadores implica el promediado de procesos biogeoquímicos a escala temporal y espacial, es posible realizar balances cuantitativos a partir de la combinación de transportes advectivos horizontales que son independientes de las asunciones sobre comportamiento biogeoquímico [*Ganachaud & Wunsch,* 2002].

El Océano Atlántico es el océano más muestreado y estudiado en la historia de la oceanografía. El conocimiento sobre sus procesos circulatorios ha mejorado notablemente a lo largo del siglo XXI con la repetición de secciones transoceánicas, datos de corrientes obtenidos con fondeos, boyas perfiladoras derivantes (notablemente desde la puesta en marcha del programa de boyas ARGO) o datos de altimetría obtenidos mediante satélite [*Hansen and Østerhus,* 2000*; Willis,* 2010*; Sarafanov et al.,* 2012*; Roessler et al.,* 2015*; Daniault et al.,* 2016]. Hasta ahora se ha prestado la mayor parte de la atención a los transportes de calor, masa y salinidad [*Lumpkin and Speer,* 2007*; Lozier et al.,* 2008], mientras que el número de balances biogeoquímicos a escala de cuenca es aún escaso [*Álvarez et al.,* 2002*; Maze et al.,* 2012].

En el área que nosotros vamos a denominar Atlántico Norte subpolar oriental (por sus siglas en inglés, eSPNA), definida como la zona al norte de la sección OVIDE y al sur del límite topográfico submarino que conecta Groenlandia-Islandia-Escocia ("*G-I-S sills*"), *Maze et al.,* [2012] realizaron un balance de masa, nutrientes y oxígeno. El eSPNA es una región clave en la circulación de retorno atlántica (AMOC), con importantes repercusiones en los ciclos biogeoquímicos y en la regulación climática. Con los datos de asimilación de nutrientes y usando relaciones estequiométricas constantes para describir las relaciones fotosíntesis/respiración de la materia orgánica marina (C:N:P:O de 106:16:1:-150, *Anderson,* 1995), *Maze et al.,* [2012] llegaron a la consideración de que el eSPNA es una zona netamente autotrófica de producción de materia orgánica en la que se fijan 40 Tg-C·año^{-1}. En el eSPNA se han realizado estudios sobre los transportes y balances de nutrientes básicos (nitrógeno y fósforo) y de oxígeno [*Álvarez et al.,* 2002*,* 2003*; Maze et al.,* 2012], así como de DIC y C_{ant}

[*Pérez et al.,* 2013*; Zunino et al.,* 2015]. Sin embargo, ambos enfoques aún no han sido combinados.

El planteamiento de esta tesis es la realización de un balance completo e integrador de los flujos de nutrientes, oxígeno y carbono en sus componentes naturales, orgánica e inorgánica, y antropogénicas, manteniendo la coherencia biogeoquímica entre el conjunto de los trazadores. Además, como aspecto innovador del proyecto al que está adscrito la tesis (BOCATS, Observación bienal del carbono, acidificación, transporte y sedimentación en el Atlántico Norte, CTM2013-41048-P) se cuantificará la interacción actual entre la columna de agua con el sedimento en términos de flujos de carbono recientes. Con la intención de conectar las escalas temporales de los procesos biogeoquímicos potencialmente afectados por el cambio climático antropogénico con los procesos geológicos que actúan generalmente a escalas de tiempo mucho más largas, nos centraremos en la época geológica actual propuesta recientemente, el Antropoceno. El Antropoceno sugiere que la Humanidad ha alterado los procesos naturales de la Tierra llegando a convertirse en una fuerza geológica global por sí misma [*Crutzen & Stoermer,* 2000]. Aunque el Antropoceno aún no ha sido reconocido por la Comisión Internacional de Estratigrafía (ICS) ni por la Unión Internacional de Ciencias Geológicas (IUGS), está empezando a ser un término común no sólo en el ámbito geológico, sino también en la valoración del impacto antropogénico en el clima y los ciclos biogeoquímicos [*Falkowski et al.,* 2000*; Codispoti et al.,* 2001*; Andersson et al.,* 2006*; Lamborg et al.,* 2014b*; Landolfi et al.,* 2017]. Bajo esta premisa utilizaremos el concepto de Antropoceno en la parte de la tesis que integra la cuantificación de los flujos de carbono hacia el sedimento oceánico.

El primer componente del ciclo del carbono analizado fue el componente orgánico. En el ciclo de carbono oceánico, la fracción de carbono orgánico disuelto (DOC) representa prácticamente la totalidad del *pool* de carbono orgánico total (TOC) porque la fracción particulada (POC) es minoritaria y puede asumirse que está en estado estacionario. La escasez de datos de DOC medidos en el océano en general, y en el Atlántico Norte en particular, dificulta una correcta evaluación cuantitativa de la importancia relativa del DOC en el ciclo del carbono total [*Hansell et al.,* 2004]. Para solucionar esta problemática, aquí se muestra una evaluación realizada mediante la combinación de unos adecuados transportes de masas de agua a lo largo de secciones transoceánicas con medidas reales de concentración de DOC ([DOC]) de alta calidad, permitiendo realizar una valoración cuantitativa del papel que tiene la AMOC en la exportación de DOC.

Con muestras de [DOC] analizadas en la campaña OVIDE 2002 y un reciente modelo de mezcla de masas de agua desarrollado para el giro subpolar del Atlántico Norte [*García-Íbañez et al.,* 2015], se realizó una caracterización del contenido tipo en [DOC] para cada masa de agua existente en la sección OVIDE mediante un sistema de inversión lineal. Una vez definido la [DOC] tipo para cada masa de agua, la combinación de la estructura de masas de agua resuelta por medio de un análisis multiparamétrico optimizado extendido (eOMP) [*García-Íbañez et al.,* 2015] con los campos de velocidades absolutas para la sección OVIDE

[*Lherminier et al.,* 2007*,* 2010], se pudo calcular el transporte de DOC para las campañas en las que no había sido medido. Combinando los transportes en la sección OVIDE con datos de transportes de masas de agua y medidas de DOC disponibles en la literatura para el límite norte del eSPNA (el límite topográfico submarino que comunica Groenlandia-Islandia-Escocia) [*Hansen & Ø*sterhus*,* 2000; *Jeansson et al.,* 2011*; Jochumsen et al.,* 2012], se generó el balance de carbono orgánico en el eSPNA. La combinación de datos propios provenientes de la sección OVIDE con datos disponibles públicamente para los límites del eSPNA es una característica habitual a lo largo de esta tesis en la elaboración de los balances.

En la evaluación de la componente orgánica del ciclo del carbono se separó la contribución de la rama superficial y de la rama profunda de la AMOC en el transporte total de DOC. Encontramos que cuando se considera la advección de DOC en el eSPNA, el DOC está en balance (8±77 kmol·s^{-1}), es decir, que la producción de DOC en el eSPNA está equilibrada con su consumo. Con respecto a la caracterización del contenido en [DOC] de las masas de agua, nuestros resultados confirman que las aguas de desbordamiento nórdicas (masa de agua de desbordamiento de Islandia–Escocia, ISOW; y masa de agua de desbordamiento de Dinamarca–Escocia, DSOW) son relativamente ricas en DOC, y añaden importantes cantidades de DOC a las aguas profundas del Atlántico Norte. Se muestra que una característica significativa del ciclo del DOC en el eSPNA es su exportación desde la rama superficial a la rama profunda de la AMOC. Los fenómenos de formación de aguas profundas que conectan las dos ramas de la AMOC generan una considerable exportación de DOC no-refractario (197 Tg-C·año^{-1}) hacia profundidad. Este relativamente rápido transporte vertical contribuye al secuestro de carbono de una manera análoga al transporte vertical de DIC. El DOC inyectado a las capas profundas en nuestra región de estudio es más lábil que la mayoría del DOC profundo observado en el Atlántico Sur y el Océano Pacífico, siendo por lo tanto más susceptible a la remineralización (consumo).

Una vez determinado que el balance de DOC está equilibrado en el eSPNA, y motivados por la constatación de que en el eSPNA las dos ramas de la AMOC llevan similares [DOC] medias ponderadas por velocidad, se reconstruyeron los transportes de DOC a latitudes subtropicales. Siguiendo una estrategia similar de combinación de transportes de masas de agua (del proyecto RAPID de monitoreo de la AMOC) y concentraciones de [DOC] medidas [*Hansell et al.,* 2004], se evaluó el transporte de DOC en las ramas superficial y profunda de la AMOC en 24.5-26.5ºN. Se encontró que 62 Tg-C·año^{-1} son consumidos en la rama profunda de la AMOC en su trayecto en dirección sur desde latitudes subpolares a latitudes subtropicales. Este consumo representa el 72% de todo el DOC exportado por el Océano Atlántico. Este consumo implica que gran parte de la exportación neta de DOC mediada por la recirculación meridional en el eSPNA, la fuente principal de DOC nuevo al océano profundo a nivel global, es remineralizada en un rango temporal decenal. Este proceso tiene repercusión en las comunidades microbianas profundas y en la dinámica composicional de la materia orgánica. La contribución del DOC al secuestro de carbono en el Atlántico Norte es considerable y representa casi una tercera parte de la captación de CO_2 atmosférico en la región.

Una vez evaluado el componente orgánico de manera individualizada, continuamos con el núcleo principal de la tesis, que coincide con el objetivo de síntesis del proyecto BOCATS al que está adscrita: la elaboración de un balance biogeoquímico integrador centrado en el carbono y basado en la serie temporal más larga disponible para la sección OVIDE (2002-2016). Si el ciclo del carbono global está alterado por las emisiones antropogénicas, es necesaria una precisa evaluación cuantitativa de su estado actual y de su posible impacto en los ciclos biogeoquímicos con los que está interrelacionado. En la parte III de la tesis se muestra una evaluación cuantitativa del ciclo del carbono a través de la resolución conjunta de una serie de balances biogeoquímicos. Este estudio combina datos hidrográficos de alta calidad para la sección OVIDE, con campos de velocidades y concentraciones de los trazadores en alta resolución, con diversas fuentes públicas de datos. A través de un método de optimización matemático [*Mercier,* 1986], se desarrolló un modelo de inversión lineal en caja simple. Entre los siguientes trazadores biogeoquímicos: variables del sistema del carbono (DIC y alcalinidad), nutrientes (nitrato, fosfato, silicato) y oxígeno disuelto, se establecen relaciones basadas en ratios estequiométricos, se plantea y resuelve un modelo con veintiuna ecuaciones y dieciséis incógnitas, y se estiman las fuentes y sumideros de carbono, nutrientes y oxígeno en el eSPNA. Esta aproximación permite una valoración integrada de los ciclos biogeoquímicos dentro de un mismo modelo, utilizando relaciones estequiométricas conocidas entre los elementos químicos en la composición de la materia orgánica como factores de conversión (ratios de Redfield). La evaluación se apoya sobre una robusta caracterización de la circulación media en el Atlántico Norte [*Daniault et al.,* 2016] y las estimaciones cuantitativas de transportes de trazadores, permitiendo una valoración integrada e independiente de asunciones sobre el comportamiento biogeoquímico y con una salida que mantiene la consistencia biogeoquímica entre todos los trazadores.

El modelo reafirma que a escala temporal decenal el eSPNA es un importante sumidero de carbono atmosférico. El balance biogeoquímico confirma que el eSPNA es una región netamente autotrófica donde la producción de materia orgánica supera a la respiración, y en la cual existe una exportación a sedimento de 101±27 $kmol \cdot s^{-1}$ de carbono orgánico y 20±27 $kmol \cdot s^{-1}$ de carbono inorgánico. La conexión entre la rama superficial de la AMOC que va hacia el norte y la rama profunda que va hacia el sur está mediada por procesos de formación de masas de agua profundas que conllevan una exportación a largo plazo de los trazadores a través del océano profundo. De manera análoga, los procesos de formación de aguas profundas son los responsables de la captación de 856±74 $kmol \cdot s^{-1}$ de oxígeno desde la atmósfera y la pérdida de calor que tiene lugar en el eSPNA. El transporte de aguas recientemente ventiladas, con una alta concentración de oxígeno disuelto, fluyendo hacia el sur con la rama profunda de la AMOC es la causa del transporte de oxígeno hacia el ecuador observado en el Atlántico Norte y es el principal mecanismo de oxigenación del Océano Atlántico profundo. La pronosticada desoxigenación oceánica causada por el calentamiento global no es detectada en nuestra región de estudio. La no-detección de desoxigenación puede deberse, al menos, a dos motivos complementarios: en un océano heterogéneo, la

desoxigenación a escala global puede ocurrir sin que se alteren los niveles de oxígeno de una localización concreta, y/o series temporales más largas son necesarias para detectar tendencias en las desviaciones del contenido en oxígeno, especialmente en regiones dinámicas con gran variabilidad natural, como es el eSPNA.

Con respecto al consumo neto de macronutrientes, nuestros transportes indican que el nitrato y el fosfato están en balance, y no existe una significativa exportación de esos nutrientes desde el eSPNA hacia zonas subtropicales. Para el macronutriente silicato parece existir un desequilibrio en el eSPNA que implicaría que la zona actúa como un sumidero de silicato. Esta posibilidad aún necesita ser contrastada con una mayor cantidad y calidad de datos de transportes. La contribución del DOC a la exportación total de carbono es especialmente relevante en nuestra región de estudio, particularmente en la cuenca del Irminger. Las condiciones hidrográficas y la localización de la cuenca del Irminger, justo en la confluencia de las dos ramas de la AMOC, donde se hunden alrededor de 10 Sv (1 Sv=10^6 $m^3 \cdot s^{-1}$) formando aguas profundas, lo convierten en un sitio especialmente relevante en el secuestro a largo plazo de trazadores biogeoquímicos. El Irminger, representando el 16% en área, supone un 48% del flujo de carbono orgánico total y un 46% del flujo de carbono inorgánico total que tiene lugar en el eSPNA.

Por último, el sumidero de carbono detectado con el balance biogeoquímico de la columna de agua fue contrastado con los flujos obtenidos desde el análisis de sedimentos profundos. Utilizando muestras de sedimentos superficiales obtenidas durante la campaña OVIDE/BOCATS 2016 y una innovadora técnica para establecer cronologías absolutas, se ha obtenido una primera estimación cuantitativa de los flujos de carbono hacia sedimentos profundos en las cuencas subpolares de Irminger e Islandia.

La evaluación de procesos biogeoquímicos en sedimentos superficiales profundos requiere precisas técnicas de datación. La geocronología basada en espectrometría gamma de alta resolución y bajo fondo con dos detectores simultáneos de germanio hiper-puro (HPGe) es una técnica suficientemente precisa y sensible como para datar sedimentos pelágicos profundos. El papel cuantitativo de las cuencas de Irminger e Islandia como sumideros de carbono durante el Antropoceno se evaluó combinando una cronología basada en el radionúclido natural ^{210}Pb junto a análisis sedimentológicos y de composición elemental. La tasa media de sedimentación para el canal central del Irminger es de 1.0 ±0.13 $mm \cdot yr^{-1}$, y para la cuenca de Islandia es de 0.96±0.08 $mm \cdot yr^{-1}$. En las dos cuencas la tasa de sedimentación es considerablemente alta para tratarse de sedimentos marinos profundos. Al aplicar el modelo de datación basado en una tasa constante de aportes (modelo CRS), es posible evaluar la evolución temporal de las tasas de sedimentación de los sedimentos datados. Con la excepción de determinados eventos breves de mayor deposición, los dos registros sedimentarios mostraron una tasa de sedimentación bastante constante, lo cual implica que las condiciones de sedimentación se han mantenido relativamente estables durante el Antropoceno.

La combinación de una precisa cronología con caracterizaciones geoquímicas del sedimento permite la cuantificación de flujos de elementos hacia el sedimento. La variabilidad interanual en la tasa de sedimentación y en los indicadores de aportes terrígenos y biogénicos sugieren la existencia de cambios de escala temporal breve en las corrientes de fondo y/o en la productividad biológica en el Atlántico Norte subpolar durante el Antropoceno. Los indicadores geoquímicos apoyan un incremento en la productividad biológica, con una mayor relevancia de la fracción biogénica desde los últimos 50 años aproximadamente en las dos cuencas, pero aún es demasiado pronto para poder inferir una tendencia robusta en el flujo de carbono desde el inicio del Antropoceno. Los cálculos de flujos de carbono concluyen que durante el Antropoceno 38±5 $g \cdot C_{inorg} \cdot m^{-2} \cdot año^{-1}$ y 5.4±0.7 $g \cdot C_{org} \cdot m^{-2} \cdot año^{-1}$ sedimentan en la cuenca del Irminger, mientras que 53±6 $g \cdot C_{inorg} \cdot m^{-2} \cdot año^{-1}$ y 6.4±0.7 $g \cdot C_{org} \cdot m^{-2} \cdot año^{-1}$ lo hacen en la cuenca de Islandia. Esta acumulación en el sedimento supone la existencia de un considerable sumidero de carbono en el área, cuantificado en más de 26 $Tg\text{-}C \cdot año^{-1}$ en el Irminger y 48 $Tg\text{-}C \cdot yr^{-1}$ en la cuenca de Islandia. Considerando de manera conjunta estas dos relevantes cuencas del giro subpolar del Atlántico Norte, la cantidad anual de carbono orgánico conservado en los sedimentos es de 8 $Tg\text{-}C_{org} \cdot año^{-1}$.

En resumen, una aproximación integradora es una necesidad no sólo para comprender el ciclo del carbono, sino también para cuantificarlo. La combinación de observaciones procedentes de diferentes metodologías y el aprovechamiento de bases de datos de acceso público junto a nuevas modelizaciones permitió analizar los flujos de carbono en una región dinámicamente compleja. La relevancia del Atlántico norte como un área sumidero de carbono ha sido una vez más corroborada bajo un conjunto de enfoques diferentes. Siguiendo el orden de la investigación, concluimos que: (i) la exportación de DOC mediada por la AMOC supone una fracción significativa (~30%) del sumidero de carbono total y ha de ser considerada en los actuales modelos del ciclo del carbono oceánico y en los estudios llevados a cabo por las comunidades microbiológicas y biogeoquímicas. (ii) Los transportes y balances de carbono, nutrientes y oxígeno en el Atlántico norte subpolar descritos en este trabajo pueden tomarse como referencia en las futuras evaluaciones del ciclo del carbono en el Atlántico y deberían ser utilizadas para probar y/o constreñir las salidas de modelos oceánicos globales. Por último (iii), es factible evaluar los flujos actuales de carbono hacia sedimentos marinos profundos con la combinación de técnicas de datación de alta resolución y análisis geoquímicos.

El aumento continuado en los niveles de CO_2 atmosférico, unido al conjunto de perturbaciones antropogénicas en el ciclo natural de los elementos, requerirá futuras evaluaciones de la asunción de que el ciclo biológico del carbono está en estado estacionario. Los resultados de esta tesis pueden verse como una aproximación al intento de integrar los componentes orgánicos e inorgánicos, así como los naturales y antropogénicos, del ciclo del carbono en el Atlántico Norte con sus flujos entre los reservorios de la atmósfera, el océano y los sedimentos. La combinación de distintas fuentes de datos con un conjunto de relaciones biogeoquímicas bien establecidas para la composición elemental de la materia orgánica permite la evaluación de balances biogeoquímicos oceánicos de una manera integradora. Este estudio también

sugiere la posibilidad de que las comunidades bentónicas tengan un papel relevante en los flujos de carbono que aún no está debidamente cuantificado.

En la actualidad, la creciente necesidad de predecir escenarios de cambio climático hace que el estudio de las Ciencias de la Tierra esté liderado a través de aproximaciones desde el modelado. Los cambios potenciales en múltiples indicadores con impacto biogeoquímico en los ecosistemas oceánicos (oxígeno, nutrientes, producción primaria, pH…) son casi rutinariamente modelados, pero no siempre debidamente validados. Proponemos que el tipo de enfoque mostrado aquí puede ser aplicado a evaluar datos provenientes de salidas de modelos, con la idea de comprobar si los modelos mantienen la coherencia biogeoquímica. Este tipo de estudios son de utilidad para mejorar nuestra comprensión del ciclo del carbono global y del Atlántico en particular.